COMPUTATIONAL MODELLING OF HARDNESS AND SOFT IMPRESSER TESTING OF MATERIALS

JINHUA HU

A thesis submitted in partial fulfillment of the
requirements of The Nottingham Trent University
for the degree of Doctor of Philosophy in Engineering

This research project was carried out in the:
School of the Built Environment

June 2005

ABSTRACT

Hardness testing is a traditional, widely used experimental method to evaluate material properties. Recent years have seen significant improvements in indentation equipment and a growing need to measure the mechanical properties of materials at small scales. Much research work has been carried out in this area using experimental methods. Until recently, it has not been possible to model in detail the deformation behaviour around an indentation, and phenomenologically based simplified models have been used. These have been very successful in some respects, but have distinct limitations. Commercial Finite Element software packages, and hardware technology, have been developed within the last several years to now be able to model the indentation process, which combines non-linear geometric behaviour and non-linear material models with contact analysis, in a reasonable time. Since it is a very complicated modelling problem, there are a number of issues that remain unresolved and which require further investigation.

In the present study, the initial research concentrated upon evaluating different commercially available FE software programs to determine their suitability with regard to modelling indentation. ABAQUS was identified as the most appropriate software. Thereafter, the geometry, mesh, contact and loading conditions were investigated to establish the appropriate parameters to enable reliable results to be obtained. It was found that the hardness values were relatively robust with regard to the details of the FE model, particularly mesh and contact conditions, but the detailed parameters, such as local deformations and stresses could be very sensitive. The established parameters were then used in the modelling of indentation in a ceramic (single crystal MgO), in a multilayered coating system (Al and TiB_2 on a steel substrate), and indentation creep in a Yttria stabilized cubic Zirconia and MgO.

The soft impresser test involves placing a 'sharp' cone in contact with a flat substrate and applying a load sufficient to cause the cone to plastically deform to conform to the surface of the substrate. Its main advantage with regard to the diamond pyramid indentation test is that it induces far less plastic deformation into the substrate, which renders the analysis less problematical, and it can be used to apply repeated loads at one position. A parallel study was thus undertaken to model soft impresser testing by establishing the appropriate parameters and applying the results to analyse soft impresser testing of Ceria stabilised Zirconia, including repeated loading (fatigue) and sliding.

CONTENTS

ABSTRACT I

LIST OF SYMBOLS VIII

ACKNOWLEDGEMENT XI

1 INTRODUCTION 1

1.1 General 1

1.2 Aims and Objectives 2

1.3 Research methodology 3

1.4 Publications to date 3

2 BACKGROUND 5

2.1 Hardness 5

2.1.1 Hardness definition 5

2.1.2 Indenter geometries 8

2.1.3 Indention size effect 9

2.2 Contact mechanics 10

2.3 Soft impresser technique 11

2.4 Dimensional analysis 11

2.4.1 II theorem 12

2.4.2 Dimensional analysis in the rigid conical indentation loading curve 13

2.4.3 Relationships between hardness and mechanical properties of solids 14

2.4.4 Unloading curve 15

2.4.5 Work of indentation 16

2.5 Introduction to the finite element method 17

2.5.1 Summary of the history of the finite element method 17

2.5.2 The finite element method 18

2.6 Application of FEM in indentation 20

2.6.1 Hard impresser modelling 21

2.6.1.1 General 21

2.6.1.2 Indenter geometries 28

2.6.1.3 Mesh effects 29

2.6.1.4 Material properties 30

2.6.1.5 Friction 30

2.6.1.6 Sliding 31
2.6.1.7 Coatings 32
2.6.1.8 Creep 34
2.6.1.9 Indentation cracking 35
2.6.2 Soft impresser modelling 36
2.6.2.1 Constant pressure assumption 36
2.6.2.2 Soft impresser modelling 36
2.7 Summary 36
3 FINITE ELEMENT ANALYSIS IN SOLID MECHANICS: BASIC THEORY 37
3.1 The configuration of an object 37
3.2 The constitutive relation for elasto-plastic FEM 38
3.3 Finite element formulation 40
3.3.1 Virtual work rate equation 40
3.3.2 U.L formulation 40
3.3.2.1 Strain increments 40
3.3.2.2 Constitutive relation in incremental form 42
3.3.2.3 Incremental tangent equation of elements 44
3.3.3 Numerical implementation of the elasto-plastic incremental constitutive relations 47
3.3.3.1 Stress computation 47
3.3.3.2 Determination of the loading state 48
3.3.3.3 Integration technology 49
3.3.3.4 Correction of the consistency condition 51
3.3.3.5 General procedure for stress computation 51
3.4 Summary 53
4 FINITE ELEMENT MODELLING: PRELIMINARY STUDIES 54
4.1 Localised constant pressure 54
4.1.1 Problem description 54
4.1.2 Analytical results 54
4.1.3 FE analysis 55
4.1.3.1 Introduction of four different element formulations 55
4.1.3.2 Comparison of different element types 57
4.2 Hertzian contact 58
4.2.1 Problem description 58

4.2.2 FEM contact model 59
4.2.3 Comparison of results 60
4.3 Coatings 61
4.3.1 Problem description 62
4.3.2 Comparison of results 62
4.4 Summary 63
5 FE MODELLING OF RIGID INDENTATION HARDNESS 64
5.1 Geometry and FEM model 64
5.2 Material properties 65
5.2.1 En08 65
5.2.2 MgO 66
5.3 Effect of FE variables 66
5.3.1 Element size 66
5.3.2 Comparison between ABAQUS and other commercial FE software 67
5.4 Effect of indenter angle 69
5.5 Model size effect 70
5.6 Indentation size and indenter tip radius effect 72
5.7 Effect of friction coefficient 74
5.7.1 Effect of friction coefficient on deformation 74
5.7.2 Effect of friction coefficient on hardness 75
5.7.3 Effect of friction coefficient on the normal contact pressure 75
5.7.4 Effect of friction coefficient on the maximum first principal stress 78
5.8 Effect of indenter rigidity 79
5.8.1 Effect of indenter rigidity on calculated hardness 80
5.8.2 Effect of indenter rigidity on calculated elastic modulus 81
5.9 Effect of material properties of the substrate 82
5.9.1 Effect of the yield stress 82
5.9.2 Effect of the tangent modulus 83
5.9.3 Effect of Young's modulus 83
5.10 Effect of load application method 84
5.11 Loading behaviour 85
5.12 Unloading behaviour 87
5.13 Extracting the elastic modulus 87
5.14 2D modelling vs. 3D modelling 90

5.15 Dimensional analysis 91
5.16 Summary 93
6 FE MODELLING OF HARDNESS TESTS ON MgO 94
6.1 Material model of MgO 94
6.1.1 Anisotropic elastic properties of MgO 94
6.1.2 MgO plastic material model 95
6.2 Modelling process 97
6.3 Hardness results for MgO 97
6.4 Summary 99
7 FE MODELLING OF THE HARDNESS OF ALTERNATING Al AND TiB_2 MULTILAYER COATINGS 100
7.1 Introduction 100
7.2 FE model 101
7.3 Material properties 102
7.4 Measurements of hardness and elastic modulus 103
7.5 FE modelling process 104
7.6 Comparison between the explicit method and the implicit method 104
7.7 Results 107
7.7.1 Deformation of the coatings 107
7.7.2 Equivalent stress 108
7.7.3 Equivalent Plastic Strain in the substrate 109
7.8 Hardness and elastic modulus 109
7.9 Hardness and elastic modulus variations with number of layers 112
7.9.1 Hardness variation with number of layers 112
7.9.2 Elastic modulus variation with number of layers 116
7.10 Summary 117
8 RIGID INDENTATION CREEP MODELLING 120
8.1 Finite element modelling of diamond indentation creep in YCPZ 121
8.1.1 Introduction 121
8.1.2 Indentation creep modelling procedure 121
8.1.2.1 Analytical Approach 121
8.1.2.2 Formulation of procedure to apply to experimental data 122
8.1.2.3 Calculate 'constants' from experimental data 123
8.1.2.4 Implementation of the creep model in ABAQUS 123

8.1.3 Analytical indentation creep analysis in YCPZ 124
8.1.4 FE modelling of indentation creep in YCPZ 126
8.1.4.1 FE model 126
8.1.4.2 Results 126
8.1.5 Summary for FE indentation creep modelling in YCPZ 129
8.2 Finite element modelling of diamond indentation creep in MgO 130
8.2.1 Indentation creep modelling procedure 130
8.2.1.1 Analytical approach 130
8.2.1.2 Formulation of procedure to apply to experimental data 131
8.2.1.3 Calculate 'constants' from experimental data 131
8.2.1.4 Implementation of the creep model in ABAQUS 131
8.2.2 Analytical indentation creep analysis in MgO 132
8.2.3 FE modelling of indentation creep in MgO 134
8.2.3.1 FE model 134
8.2.3.2 Results 135
8.2.4 Summary for the FE indentation creep modelling in MgO 139
8.3 Summary 139
9 SOFT IMPRESSER MODELLING 140
9.1 Soft impresser test 140
9.2 Preliminary modelling 141
9.2.1 Mesh formulation 141
9.2.1.1 Substrate mesh 142
9.2.1.2 Soft impresser mesh 147
9.2.2 Effect of friction coefficient 149
9.2.3 Effect of soft impresser material properties 158
9.2.3.1 Effect of soft impresser elastic modulus 158
9.2.3.2 Effect of soft impresser work hardening rate 159
9.2.4 Preliminary modelling summary 160
9.3 Soft Impresser flattening and re-locating analysis 161
9.3.1 Geometric model and FE model 161
9.3.2 Material model 162
9.3.3 Modelling procedure 162
9.3.4 Results 164
9.3.4.1 Results for two elastic substrates 164

9.3.4.2 Results for the elasto-plastic substrates 165
9.3.5 Analysis of results 167
9.3.6 Summary for the soft impresser flattening and re-locating analysis 167
9.4 Cyclic soft impresser modelling with reference to CeTZP 169
9.4.1 Modelling procedure 170
9.4.2 Results 170
9.4.2.1 Variation of the maximum principal stress 170
9.4.2.2 Variation of the shear stress 175
9.4.2.3 Comparison between experimental observations and FEA results 178
9.4.3 Cyclic soft impresser modelling summary 181
9.5 Sliding 181
9.5.1 Geometric model and FE model 181
9.5.2 Modelling procedure 182
9.5.3 Results 183
9.5.4 Soft impresser sliding summary 188
9.6 Extracting the elastic modulus 189
9.7 Summary 191
10 SUMMARY and DISCUSSION 193
10.1 Introduction 193
10.2 Development of the finite element models 194
10.3 FE modelling of rigid indentation hardness 197
10.4 FE modelling of hardness tests on MgO 202
10.5 FE modelling of the hardness of alternating Al and TiB_2 multilayer coatings 203
10.6 Rigid indentation creep modelling 204
10.7 Soft impresser modelling 205
11 CONCLUSIONS and FURTHER WORK 207
11.1 Conclusions 207
11.2 Further work 215
REFERENCES 216
BIBLIOGRAPHY 224
APPENDICES 225
APPENDIX A Calculation of Elastic Constants for MgO 225
APPENDIX B_1 Fortran resource file of the analytical creep model for MgO 226
APPENDIX B_2 Abaqus creep user subroutine for MgO at T=293K 229

APPENDIX C Useful notes for the use of ABAQUS 231

BIBLIOGRAPHY FOR APPENDICES 239

ACKNOWLEDGEMENT

I wish to dedicate this thesis to my grandmother Dezhen Wang. She took care of me for many years without any complaints and I will have no chance to repay her. I wish her to rest peacefully in heaven. I also would like to thank my father Zifa Hu and my previous supervisor Professor Huixue Sun, who introduced me into the FEA field, for their help and guidance throughout many years.

The work presented in this thesis was accomplished under the supervision of Professor John Leslie Henshall and Dr Anton Ianakiev. I would like to acknowledge their help. Professor Henshall gave me this opportunity to study in the hardness indentation field and research for a PhD. I would like to thank Professor Henshall especially for his constant guidance and support and constructive suggestions. I have been impressed by his knowledge, kindness, patience, the detailed amendments to my papers and thesis and efficient work, etc. He is one of the best supervisors that I have met throughout my life of studying.

Certainly, some credits should go to my wife Deng Juan, who worked hard during the last three years, which improved our living level to some extent, though I had to look after my 4-year old daughter Xiaoqian Hu on my own in the last seven months. Also I'd like to express my gratitude to the nursery teachers, such as Miss Diana Meeks, Mrs Jan Callaway and Miss Elaine Corlins in Sycamore Infant and Nursery School for taking care of my daughter.

Many other academic, secretarial, and technical members of staff, such as Mrs Corlett Doreen, Miss Julie Bradshaw and Mr Gary Griffiths, etc., have facilitated the realisation of this thesis and I express my gratitude to them all.

Several of my best friends, such as Dr Xinjian Duan, Dr Wenguang Jiang and Dr Xuejun Ren, etc., are always there ready for help and I'd like to thank them as well.

Finally, I am very grateful to the Nottingham Trent University for the provision of a research scholarship and the School of the Built Environment for the facilities provided.

Jinhua Hu

20/04/2005

CHAPTER 1
INTRODUCTION

1.1 General

The diamond pyramid indentation test has been used for some time to study deformation in materials. It has mainly been used as a quality control procedure for metallic materials. However in recent years its use has been extended to be able to derive information regarding the mechanisms of plastic deformation in nominally brittle materials (Brookes et al, 1972; Henshall et al, 1992; Guillou et al, 1990) and also time-dependent plastic deformation (Li et al, 1991), to provide a quantitative measure of localised fracture behaviour (Lawn and Evans, 1997; Guillou et al, 1992) and monitoring of the load-displacement behaviour at very low loads (Pethica et al, 1983).

Until recently, it has not been possible to model in detail the deformation behaviour around an indentation, and phenomenologically based simplified models have been used. These have been very successful in some respects, but have distinct limitations. Commercial Finite Element software packages, and hardware technology, have been developed within the last 10 years to now be able to model the indentation process, which combines non-linear geometric behaviour and non-linear material models with contact analysis, in a reasonable time. This has thus become an active research area (Cheng et al, 2001; Zhang and Subhash, 2001; Bull, 2001; DeFazio et al, 2001). Since it is a very complicated modelling problem, there are a number of issues that remain unresolved and which require further investigation. For example, the modelling to date has concentrated on metals, and reproducing the macroscopic aspects of the behaviour, principally indentation depth, using 2-D axisymmetric models.

The soft impresser test involves placing a 'sharp' cone in contact with a flat substrate and applying a load sufficient to cause the cone to plastically deform to conform to the surface of the substrate. This test method enables the elucidation of the mechanical properties of materials which are very difficult to determine by other means, and has been principally applied to the study of ceramic and ultrahard materials. Its main advantage with regard to the diamond pyramid indentation test is that it induces far less plastic deformation into the substrate, which renders the analysis less problematical, and it can be used to apply repeated loads at one position, i.e. to assess fatigue resistance in ceramic and ultrahard materials (Brookes et al, 1990; Maerky et al, 1997; Henshall et al,

1999). The majority of the analyses that have been presented to date (Brookes et al, 1990; Maerky et al, 1997; Fagan, 2000) have assumed that the loading due to the soft impresser can be considered as a uniform pressure, which is simply the applied load divided by the contact area. Some preliminary FE modelling of the actual contact situation would suggest that this approximation is not generally correct (Henshall et al, 1999). Therefore further analysis of the mechanics of this test method is required.

1.2 Aims and Objectives

The aims of this project are:

1. Numerical Modelling, using the Finite Element Method, of the Classical Indentation Process involving Penetration of a Pointed Rigid (Diamond) Indenter into Metals and Ceramics.
2. Numerical Modelling, using primarily the Finite Element Method, of the recently developed Soft Impresser Test Technique to simulate plastic deformation in Ceramics and Metals.

The objectives are:

1. Review, plus continuous updating, of the relevant literature.
2. Investigate the capability of commercial finite element software to be able to analyse the stress distributions at/near the surface for situations with well accepted analytical solutions for monolithic substrates and one FEA solution for a coated substrate.
3. Use the FEA software package(s) identified as acceptable in objective 2 to model a diamond hardness indentation in a steel of known hardness and uniaxial stress-strain data. The modelling will investigate the following variables:
    - Mesh size
    - Mesh geometry
    - Element Type
    - Contact Element Type
    - Friction coefficient
    - Model size
    - Applied load
    - Indenter tip radius
    - Indenter Rigidity

4. Compare the results of the diamond indentation modelling with available literature results where these are sufficiently detailed.
5. Use the FEA procedures identified in the previous objectives to model plastic deformation in a ceramic substrate subjected to diamond pyramid indentation.
6. Use FEA to model a series of diamond pyramid indentation tests for a multilayer coated substrate.
7. Model the effects of time dependent deformation for a series of diamond pyramid indentation results using FEA.
8. Model the soft impresser test methodology to investigate the influence of experimental conditions and test procedure on the stress distributions in the substrate.
9. Investigate the possibility of using FEA to analyse the extension of the soft impresser test method to repeated loading and sliding.

1.3 Research Methodology

1. Familiarise with the relevant published works as presented in Chapters 2 and 3;
2. Develop and validate appropriate FEA modelling procedures, as described in Chapters 4 and 5;
3. Investigate the applicability of the developed FEA modelling procedures with modifications as appropriate, to model the following:
   - diamond indentation in a ceramic material, MgO (Chapter 6),
   - diamond indentation in multilayer coatings (Chapter 7),
   - time dependent deformation under diamond indentation conditions in ceramics (Chapter 8),
4. Investigate the applicability of FEA to analyse the stress distributions in a substrate subjected to loading by a softer deformable impresser under static conditions, repeated loading, and sliding (Chapter 9).
5. The results are described and discussed in each chapter, and there is also an overall summary and discussion of the present research findings in Chapter 10.

1.4 Publications to Date

The following presentations and publications have been achieved to date:

J L Henshall, J Hu, and C Griffiths, 'Finite Element Modelling of Diamond Pyramid Indentations', Proceedings of the International Conference on Applied Mechanics and Materials (ICAMM 2003), January 21-23, 2003, Durban, South Africa, Editors S Adali, E V Morozov and V E Verijenko, 1-6. (Keynote presentation)

J Hu and J L Henshall, 'Finite Element Modelling of diamond indentation in MgO' 3rd Materials Research Conference. 22 June 2004, London.

J Hu and J L Henshall, 'FE modelling of the hardness of alternating Al and TiB_2 multilayer coatings' The 2nd International Conference on Technological Advances of Thin Films & Surface Coatings 13 – 17 July 2004, Meritus Mandarin, Singapore.

CHAPTER 2
BACKGROUND

This chapter provides an overview of previous and current work on hardness, contact mechanics, the soft impresser technique and the application of FEM in indentation. The first section presents the general concepts of hardness and the types of indenter geometry. The second section is concerned with contact mechanics. In the third section, previous research using the soft impresser method is reviewed. Subsequently, the dimensional analysis in the rigid indentation is introduced. Finally, an introduction to finite element methods and the application of FEM in indentation are presented.

2.1 Hardness

2.1.1 Hardness definition

Hardness testing was originally concerned with scratch hardness, which assesses the hardness of solids with regard to their ability to scratch other solids, and forms the basis of the semi-quantitative Mohs hardness scale. However, nowadays, the most common technique to determine the hardness of a material is the well established indentation technique (*e.g.* Tabor, 1951; Mott, 1956). This is generally based on the formation of a permanent indentation in the surface of the tested material by a rigid indenter. The Shore hardness test for rubbers is an exception to this since it is more a measure of the elastic behaviour rather than permanent deformation (Kucherskii & Kaporovskii, 1995). These tests have been supplemented by the instrumented nanoindentation test in recent years, which can be used to determine both elastic and plastic behaviour (Malkow et al, 2001).

Tabor (1951) was the first to provide a semi-quantitative relationship between hardness measurements and other material properties. He showed, using a rigid perfectly plastic analysis, that the hardness H is related to the flow stress in simple compression Y by the relation

$$H = CY \qquad (2.1)$$

where C is a constant, which is approximately equal to three for polycrystalline isotropic metals, but can have much higher values for single crystals (Swain & Lawn, 1969; Tabor, 1970).

Subsequently, more sophisticated analyses for the deformation processes occurring during indentation tests were derived for elasto-plastic materials. The most widely accepted model, developed by Johnson (1970), is

$$p_{av} = \frac{2}{3} Y (1 + \ln \frac{E \tan(90 - \theta)}{3Y}) \qquad (2.2)$$

where p_{av} is the average contact pressure (equivalent to the "true" hardness) and θ is the semi cone angle of the indenter. Johnson took the angle for θ to be 70.3°, which gives the same volume of material displaced for a conical indentation as for a Vickers indentation. This formula works surprisingly well for materials with well defined constant strain hardening, as long as neither significant piling-up nor sinking-in of the material occurs.

The recent ISO standard (BS EN ISO 14577, 2002) has defined two measures of hardness. The Martens Hardness, *HM*, is the force divided by the surface area of the indenter penetrating beyond the zero point of contact. For a perfect rigid Vickers indenter this gives,

$$HM = P / A_s = P / (26.43 * h^2) \qquad (2.3)$$

where P, A_s and h are defined in Figure 2.1(a). The Indentation Hardness, H_{IT}, is given by:

$$H_{IT} = P_{\max} / A_p \qquad (2.4)$$

where P_{max} and A_p are defined in Figure 2.1(a). The latter definition is claimed to be in accord with the definition initially proposed by Meyer. The Martens Hardness definition does not take into account any sinking-in or piling-up of material around the indenter.

Figure 2.1(b) shows an example of a load-displacement curve from a hardness test. In this figure, the area enclosed by the loading curve and the unloading curve is the plastic work, W_p, which is irreversible. The area under the unloading curve is the elastic work, W_e, which is reversible. The area under the loading curve is the total work, W_{tot}, i.e. $W_{tot}=W_p+W_e$.

The quantitative correlation in actual materials between the depth as measured in a depth sensing indenter, and the residual impression diagonals, as conventionally measured for a pyramidal indenter is not entirely clear. It has also been proposed by Henshall et al (1993) on physical grounds that the volume of the indentation is a better reflection of the deformation that occurs, and thus an equivalent hardness, could be defined as follows:

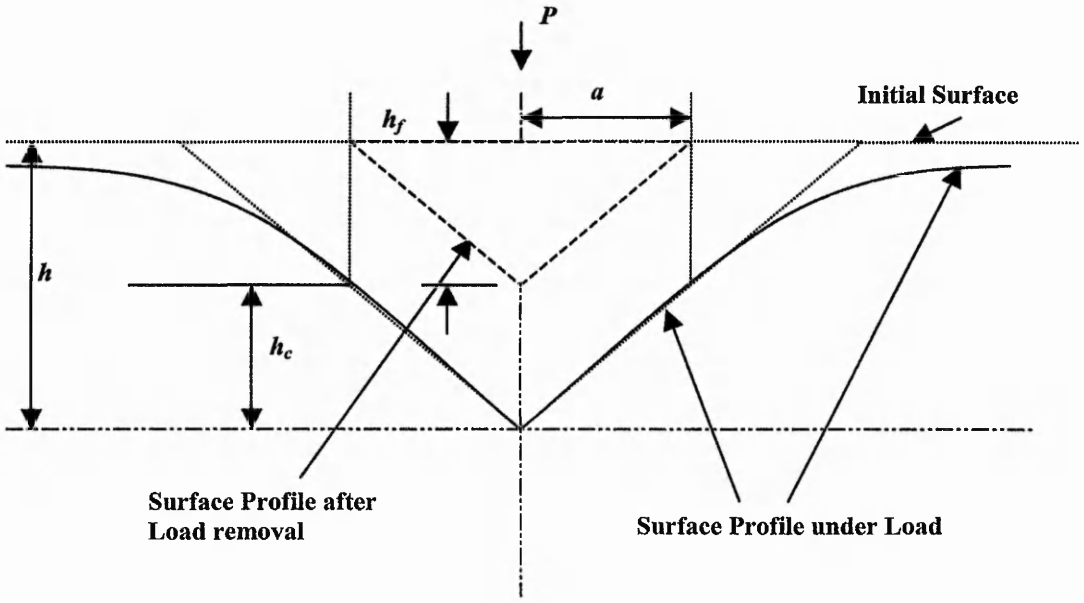

(a)

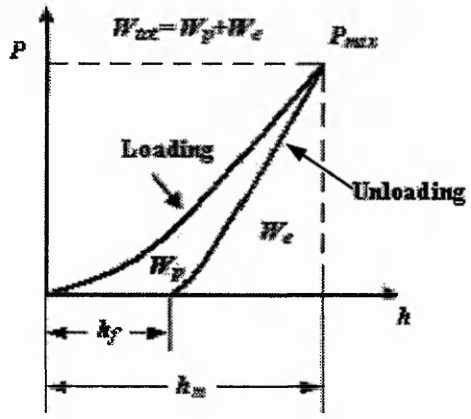

(b)

Figure 2.1 (a) A schematic diagram of indentation process, and definition of measured parameters. P = test force, P_{max} = maximum test force, h = indentation depth under the applied test force, h_c = depth of contact of the indenter with the test piece at P_{max}, h_f = permanent indentation depth after removal of the test force. a is the radius of the projected contact surface between the indenter and the test piece. A_s is the surface area of the indenter at distance h from the tip, and A_p is the projected area of the indenter at distance h_c from the tip (Griffiths et al, 2001), and (b) A typical load-displacement curve.

$$H_{vol} = \frac{P_{\max}}{k_1 * V^{2/3}} \qquad (2.5)$$

where, H_{vol} could be termed the Volumetric Hardness and would provide a more physically based representation of hardness, and k_1 is a constant which depends on the indenter geometry.

In the FE models it is also possible to calculate the average contact pressure H_{cp}, which can be used as a measure of hardness. The average contact pressure can be calculated from the following formulation:

$$H_{cp} = \frac{\sum_{i=1}^{nc} p_i^{el} A_i^{el}}{\sum_{i=1}^{nc} A_i^{el}} \tag{2.6}$$

where, p_i^{el} is the normal contact pressure on the ith element, A_i^{el} is the area of the ith element after deformation, and nc is the total number of contact elements that are in the closed contact condition under the current load.

2.1.2 Indenter geometries

In practice various indenter geometries are typically used, including spherical (Brinell hardness), conical (Rockwell hardness) and pyramidal indenters (Guillou, 1992). Sharp pyramidal indenters are generally more suited to studying brittle materials because they do not encourage as much fracture as conical or spherical indenters, which induce significant circumferential tensile stresses. The most common pyramidal indenters are Knoop, Vickers and Berkovich, which have respectively a rhombohedral, square and triangular based tip. Figure 2.2 shows the geometries of the Knoop, Vickers and Berkovich indenters.

The hardness values are related to the applied mean contact pressure, calculated as the ratio of the load to either the contact or projected area of the indentation. The formulae to calculate their corresponding hardnesses are given by

$$H_K = 14.23\frac{F}{l^2} \tag{2.7}$$

$$H_V = 1.854\frac{F}{d^2} \tag{2.8}$$

$$H_B = 1.732\frac{F}{d_B^{\,2}} \tag{2.9}$$

where F is the applied load in kg, and l, d and d_B are respectively the length of long diagonal of the Knoop, the mean diagonal length of the Vickers and the mean height of the Berkovich. Diamond Pyramidal Hardness values are traditionally expressed in kg/mm^2 but GPa are also used.

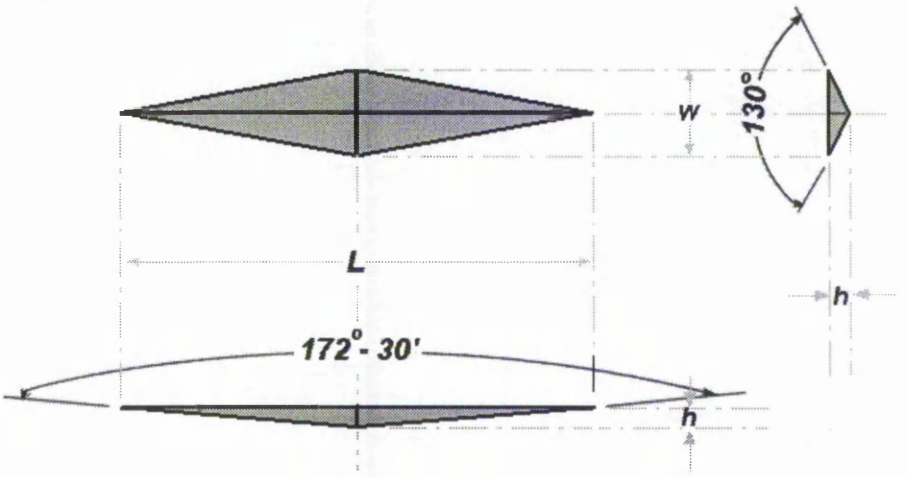

(a) Knoop indenter

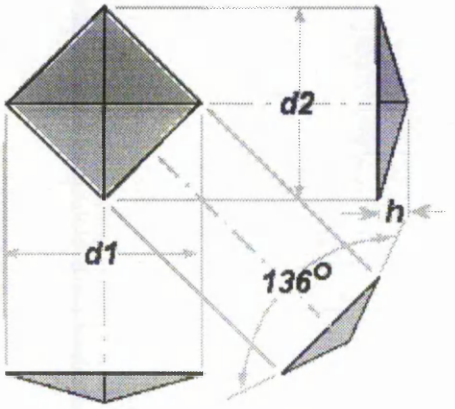

(b) Vickers indenter

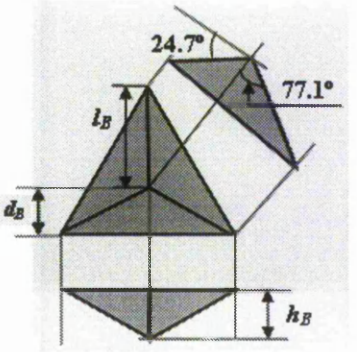

(c) Berkovich indenter

Figure 2.2 Sharp pyramidal indenters

2.1.3 Indentation-size effect

The Indentation-Size Effect, ISE, i.e. the observed decrease in microhardness with increasing load, has been reported to occur in a wide range of materials (Mott, 1956;

Buckle, 1973; Brookes, 1983; Sargent, 1986; Bull et al, 1989; Atkinson, 1991; Li and Bradt, 1992). There have been several possible explanations advanced to explain this phenomenon, as summarised in Ren et al (2002), but none of these has been accepted as a full interpretation of the experimental data. The existence of ISE will be borne in mind throughout the present study wherever appropriate, but it will not form a particular focus within the present modelling investigations.

2.2 Contact mechanics

Contact mechanics is concerned with the deformations, and thus stresses, which arise when two surfaces are brought into contact. A thorough presentation of the different aspects of contact mechanics can be found in Johnson (1985). One of these aspects, *i.e.* Hertzian contact, is briefly discussed in this section.

Since Hertz first investigated the beautiful cone-shaped fractures produced in contacts between glass lenses in the 1880s, indentation mechanics has become extensively used in the analysis and characterization of fracture and deformation properties of materials, *e.g.* indentation of ceramics with spheres: a century after Hertz (Lawn, 1998). Johnson (1982) has reviewed the developments stemming from Hertz's work.

The frictionless elastic contact between a sphere and a flat plane has received particular attention. The radius of the circular contact obtained when the sphere is pressed onto the plane with a normal load P is defined by

$$a = \left(\frac{3PR}{4E^*} \right)^{1/3} \tag{2.10}$$

where R is the radius of the sphere and E^* is an equivalent elastic modulus defined by

$$\frac{1}{E^*} = \frac{1-\nu_1^{\,2}}{E_1} + \frac{1-\nu_2^{\,2}}{E_2} \tag{2.11}$$

where E_1 and E_2, and ν_1 and ν_2 represent respectively the Young's moduli and the Poisson's ratios of the materials of the spherical indenter and the plane.

The average contact pressure p_{av} is

$$p_{av} = \left(\frac{6PE^{*2}}{\pi^3 R^2} \right)^{1/3} \tag{2.12}$$

The maximum tensile stress σ_{max} in the specimen occurs at the edge of the contact circle

$$\sigma_{max} = \frac{1}{2}(1-2\nu_2)p_{av} \tag{2.13a}$$

or

$$\sigma_{max} = (1-2\nu_2)\left(\frac{3PE^{*2}}{4\pi^3 R^2}\right)^{1/3} \qquad (2.13b)$$

which contributes to the cone cracking. When this maximum tensile stress σ_{max} reaches a critical value, a ring crack would initiate at the surface of brittle materials, just outside the periphery of the contact area. This ring crack subsequently develops into a Hertzian cone crack beneath the surface.

2.3 Soft impresser technique

In the last two decades, the soft impresser technique has proven very successful in investigating the plasticity of hard materials. More recently, it has been adapted to study the cyclic deformation processes preceding fatigue fracture. The soft impresser test technique is similar to a conventional indentation hardness test except that the 'impresser' is softer than the substrate and deforms with significant plasticity on contact, rather than vice versa. The analyses of the mechanics of the soft impresser test to date have been based upon simplifying assumptions, such as ignoring the local plastic deformation (Brookes et al, 1990; Maerky et al, 1997; Henshall et al, 1999), and assuming a constant pressure distribution (Brookes et al, 1990; Maerky et al, 1997; Fagan et al, 2000). These assumptions are not likely to significantly affect the mechanics in certain specific cases, but obviously may lead to significant deviations in general.

Therefore, the present research has developed numerical models of the soft impresser technique using a commercial Finite Element software package. The goals of the models will be to investigate the influence of differing experimental test procedures, such as lubricating the interface or not, on the stress/strain patterns developed in the substrates, and a more complete quantitative explanation of the existing experimental observations on the deformation and incipient fracture behaviour in ceramics. The extension of the modelling to study the mechanics of fatigue and sliding wear will also be investigated.

2.4 Dimensional analysis (Cheng and Cheng, 2004)

Dimensional analysis is routinely used as a convenient analytical tool in fluid mechanics. It has been used to a much lesser extent in solid mechanics. However,

Cheng and Cheng (1997, 2004) have developed a formulation relevant to indentation hardness. An introduction to this approach is presented in the following sections.

2.4.1 Π theorem

Assume there exists a dependent quantity z, which is a function of the independent variables z_1 to z_n, i.e.

$$z = f(z_1,...,z_n) \tag{2.14}$$

Let there be i dimensionally independent quantities in this relation with $i \le n$. Without loss of generality, these may be set to be z_1 to z_i. The remaining $(n-i)$ variables are then dimensionally dependent.

Consequently, their dimensions can be expressed as

$$[z] = [z_1]^{\alpha_1} \ldots [z_i]^{\alpha_i}$$

$$[z_{i+j}] = [z_1]^{\alpha_{j1}} \ldots [z_i]^{\alpha_{ji}}, \; j = 1,\ldots,n-i \tag{2.15}$$

Hence, the following $n-i+1$ quantities formed out of the original $n+1$ z's are dimensionless.

$$\Pi = \frac{z}{z_1^{\alpha_1} \cdots z_i^{\alpha_i}}$$

$$\Pi_j = \frac{z_{i+j}}{z_1^{\alpha_{j1}} \cdots z_i^{\alpha_{ji}}}, \; j = 1,\cdots,n-i \tag{2.16}$$

The existence of the exponents in the above expressions is guaranteed by the fact that z as well as z_{i+j} are dimensionally dependent on z_k ($k = 1,\cdots,i$). Note that the construction of the Π_j's ensures that they are all independent, since each of them contains an element that is not present in any of the other Π_j's.

Equation (2.14) can then be written in terms of the new variables Π and Π_j as:

$$\Pi = f(z_1,\cdots,z_i,\Pi_1,\cdots,\Pi_{n-i}) \tag{2.17}$$

Now by passing from one system of basic units to another the values of z_1 to z_i can be made arbitrarily large or small while the values of the Π's remain unchanged. Consequently the requirement that physical relations be objective and independent of units forbids the appearance of the z's in the above equation. Hence,

$$\Pi = f(\Pi_1,\cdots,\Pi_{n-i}) \tag{2.18}$$

Equation (2.18) differs from (2.14) in that the number of variables is reduced by i, the

number of dimensionally independent quantities, and all the variables in Equation (2.18) are dimensionless. This is known as the Π-theorem (Buckingham 1914). The Π-theorem is intuitively obvious since it is clear that physical laws should not depend on the choice of units. When $n-i$ is small, this advantage can be quite significant as will be seen when considering indentation modelling in later sections.

2.4.2 Dimensional analysis in the rigid conical indentation loading curve

Dimensional analysis can be applied to conical indentation in an isotropic elastic-plastic solid obeying a power-law work-hardening rule with uniaxial tension stress-strain curves which are assumed to be given by:

$$\sigma = E\varepsilon, \text{ for } \varepsilon \le \frac{Y}{E}$$

$$\sigma = C_1\varepsilon^n, \text{ for } \varepsilon \ge \frac{Y}{E} \qquad (2.19)$$

where Y is the initial yield stress, C_1, the strength coefficient, $C_1 = Y(E/Y)^n$ and n, the strain-hardening exponent, is dimensionless. For most metals n has a value between 0.1 and 0.5 (Dieter, 1976).

Assume the indenter is rigid and the friction coefficient between the indenter and the specimen surface is zero. The first step in the dimensional analysis is to select the dependent variable and identify all the independent variables and parameters. Select the force on the indenter, F, as the dependent variable and the indenter's displacement, h, as the independent variable. The mechanical properties of the materials, i.e. Young's modulus (E), Poisson's ratio (ν), initial yield strength (Y), and work hardening exponent (n), are independent parameters. The indenter half angle (θ), which characterizes the indenter geometry, is also an independent parameter. After identifying all the independent variables and parameters, a general expression, f_L, for the loading curve is,

$$F = f_L(E,\nu,Y,n,h,\theta) \qquad (2.20)$$

The next step is to identify, among the six governing parameters, E, ν, Y, n, h, and θ, the ones with independent dimensions. This is accomplished by noting that two of them, namely E and h, have independent dimensions (i.e., dimensions of stress and length). The dimensions of Y, ν, n, θ, and F are then given by $[Y]=[E]$, $[\nu]=[E]^0[h]^0$, $[n]=[E]^0[h]^0$, $[\theta]=[E]^0[h]^0$, $[F]=[E][h]^2$.

Now it is possible to take the third step in the dimensional analysis. By applying the Π-theorem in dimensional analysis, this results in:

$$\Pi_\alpha = \frac{F}{Eh^2} \quad \text{and} \quad \Pi_1 = \frac{Y}{E} \tag{2.21}$$

Thus, from Equation (2.18),

$$\Pi_\alpha = \Pi_\alpha(\Pi_1, \nu, n, \theta) \tag{2.22a}$$

Or equivalently,

$$F = Eh^2 \Pi_\alpha(\frac{Y}{E}, \nu, n, \theta) \tag{2.22b}$$

Based on the above dimensional analysis, several important observations can be made for a rigid conical indenter with a given half angle, θ, indenting into an elastic–plastic solid with work hardening.

Firstly, the force on the indenter, F, is proportional to the square of the indenter displacement, h. This square dependence is common to conical indentation in purely elastic (i.e., when $Y \to \infty$), rigid-plastic (i.e., $E \to \infty$), elastic-perfectly plastic (i.e., $n \to 0$), and elastic–plastic solid with work-hardening. The coefficient of the square dependence is of course different for these cases. Secondly, the parameter, F / Eh^2, is a function of Y / E, ν, and n, for a given θ. Thirdly, the original problem of a function of six parameters is reduced by 2, the number of parameters with independent dimensions in Equation (2.20). It is now a function of four parameters, thus simplifying the original problem of six parameters and allowing a systematic evaluation of the effects of each parameter. Finally, the numerical values of the function $\Pi = \Pi(\Pi_1, \nu, n, \theta)$ cannot be known from dimensional analysis alone and must be obtained either through experiments or modelling. Using a finite element analysis software program, ABAQUS (1998), the function $\Pi = \Pi(\Pi_1, \nu, n, \theta)$ has been calculated over a wide range of parameter space (Cheng and Cheng, 1998, 1999; Giannakopoulos, 1994; Larsson, 1996).

2.4.3 Relationships between hardness and mechanical properties of solids

Several hardness definitions exist in the standards or protocols for indentation measurements.

The one commonly used in recent instrumented indentation literature is given by Equation (2.4).

For a conical indenter

$$A_p = \frac{\pi h_c^2}{\cot^2 \theta} \tag{2.23}$$

In general, the contact depth is a function of all the independent parameters, i.e.

$$h_c = g(E, \nu, Y, n, h, \theta) \tag{2.24}$$

As has been noted in the previous section, the dimensions of Y, ν, n, h and h_c can be expressed in terms of the dimension of E and h, the two parameters with independent dimensions. Applying the Π-theorem in dimensional analysis gives:

$$\Pi_\beta = \frac{h_c}{h} \quad \text{and} \quad \Pi_1 = \frac{Y}{E} \tag{2.25}$$

Therefore from Equation (2.18):

$$\Pi_\beta = \Pi_\beta(\Pi_1, \nu, n, \theta) \tag{2.26-a}$$

or equivalently,

$$h_c = h\Pi_\beta(\frac{Y}{E}, \nu, n, \theta) \tag{2.26-b}$$

Using Equations (2.22), (2.23) and (2.26), the ratio of hardness to the elastic modulus is given by

$$\frac{H}{E} = \frac{\cot^2 \theta}{\pi}\left[\frac{\Pi_\alpha((Y/E), \nu, n, \theta)}{\Pi_\beta^2((Y/E), \nu, n, \theta)}\right] \tag{2.27}$$

The above equation shows that hardness, H, is a multiple function of a material's mechanical properties and it is independent of indentation depth h for conical indentation in the class of elastic-plastic solids that obey Equation (2.19).

2.4.4 Unloading curve

Since unloading takes place after loading during which the indenter reaches a maximum depth, h_m, there is one additional independent parameter, h_m, in the unloading equation. Thus, the force, F, should be expressed as

$$F = f_U(E, \nu, Y, n, h, h_m, \theta)$$

By applying the Π-theorem in dimensional analysis, this results in:

$$\Pi_\gamma = \frac{F}{Eh^2}, \ \Pi_1 = \frac{Y}{E} \text{ and } \Pi_2 = \frac{h}{h_m} \tag{2.28}$$

Thus, from Equation (2.18),

$$\Pi_\gamma = \Pi_\gamma(\Pi_1, \Pi_2, \nu, n, \theta) \tag{2.29a}$$

or equivalently,

$$F = Eh^2 \Pi_\gamma(\frac{Y}{E}, \frac{h}{h_m}, \nu, n, \theta) \qquad (2.29b)$$

Equation (2.29) shows that during the unloading stage, the force, F, is not proportional to the square of the indenter displacement, h.

At the final indentation depth, h_f, the force on the indenter first becomes zero during unloading, i.e.,

$$F = Eh_f{}^2 \Pi_\gamma(\frac{Y}{E}, \frac{h_f}{h_m}, \nu, n, \theta) = 0 \qquad (2.30a)$$

or,

$$\Pi_\gamma(\frac{Y}{E}, \frac{h_f}{h_m}, \nu, n, \theta) = 0 \qquad (2.30b)$$

Equation (2.30) shows that h_f / h_m is a function of Y/E, ν, n and θ, i.e.

$$\frac{h_f}{h_m} = f(\frac{Y}{E}, \nu, n, \theta) \qquad (2.31)$$

2.4.5 Work of indentation

By integrating the loading and unloading curves (Figure 2.1(b)), the work of indentation can be obtained. From Equation (2.22), the total work, W_{tot}, is given by

$$W_{tot} = \int_0^{h_m} F dh = \frac{Eh_m{}^3}{3} \Pi_\alpha(\frac{Y}{E}, \nu, n, \theta) \qquad (2.32)$$

From Equation (2.29), substituting h_f / h_m by x, the elastic work, W_e, is given by

$$W_e = \int_{h_f}^{h_m} F dh = Eh_m{}^3 \int_{h_f/h_m}^1 x^2 \Pi_\gamma(\frac{Y}{E}, x, \nu, n, \theta) dx \qquad (2.33)$$

where the integral, $\int_{h_f/h_m}^1 x^2 \Pi_\gamma(\frac{Y}{E}, x, \nu, n, \theta) dx$, can be designated as $\Pi_u(\frac{Y}{E}, \nu, n, \theta)$ since h_f / h_m is also a function of Y/E, ν, n and θ as seen from Equation (2.31). Therefore, Equation (2.33) can be rewritten as follows,

$$W_e = \int_{h_f}^{h_m} F dh = Eh_m{}^3 \Pi_u(\frac{Y}{E}, \nu, n, \theta) \qquad (2.34)$$

From Equations (2.32) and (2.34), the plastic work W_p can be obtained,

$$W_p = W_{tot} - W_e = \frac{Eh_m{}^3}{3}(\Pi_\alpha(\frac{Y}{E}, \nu, n, \theta) - 3\Pi_u(\frac{Y}{E}, \nu, n, \theta)) \qquad (2.35)$$

From Equations (2.32), (2.34) and (2.35),

$$\frac{W_e}{W_{tot}} = 3\frac{\Pi_u(\frac{Y}{E},\nu,n,\theta)}{\Pi_\alpha(\frac{Y}{E},\nu,n,\theta)} \qquad (2.36)$$

$$\frac{W_p}{W_{tot}} = 1-3\frac{\Pi_u(\frac{Y}{E},\nu,n,\theta)}{\Pi_\alpha(\frac{Y}{E},\nu,n,\theta)} \qquad (2.37)$$

Equations (2.27), (2.31), (2.36), and (2.37) show that h_f/h_m, W_e/W_{tot}, W_p/W_{tot} and H/E are all functions of Y/E, ν, n and θ. It is instructive to investigate the connections between them. The relationships between them are considered further in Section 2.6.1.1 below.

2.5 Introduction to the finite element method

2.5.1 Summary of the history of the finite element method (Cook, 1989)

In 1906, researchers suggested a "lattice analogy" for stress analysis (Hrennikoff, 1941). The continuum was replaced by a regular pattern of elastic bars. The properties of the bars were chosen in a way that caused displacements of the joints to approximate displacements of points in the continuum. This method sought to capitalize on well-known methods of structural analysis.

Courant appears to have been the first to propose the finite element method as it is known today. In a 1941 mathematics lecture, published in 1943, he used the principle of stationary potential energy and piecewise polynomial interpolation over triangular sub-regions to study the Saint-Venant torsion problem (Courant, 1943). Courant's work was ignored until engineers had independently developed it.

None of the foregoing work was of much practical value at the time because there were no computers available to generate and solve large sets of simultaneous algebraic equations. It is no accident that the development of the finite element methods coincided with major advances in digital computers and programming languages.

By 1953 engineers had written stiffness equations in matrix format and solved the equations with digital computers (Levy, 1953). Most of this work took place in the aerospace industry. At that time, a large problem was one with 100 DOF. In 1953, at the Boeing Airplane Company, Turner suggested that triangular plane stress elements be used to model the skin of a delta wing (Clough, 1980). This work, published almost

simultaneously with similar work in England (Turner, 1956; Argyris, 1960), marks the beginning of widespread use of finite elements. Much of this early work went unrecognized because of company policies against publication (Robinson, 1985).

The name "finite element method" was coined by Clough in 1960 (Clough, 1960). The practical value of the method was soon obvious. New elements for stress analysis applications were developed, largely by intuition and physical argument. In 1963, the finite element method gained respectability when it was recognized as having a sound mathematical foundation: it can be regarded as the solution of a variational problem by minimization of a functional. Thus the method was seen as applicable to all field problems that can be cast in a variational form. Papers about the application of finite elements to problems of heat conduction and seepage flow appeared in 1965.

Large general-purpose finite element computer programs emerged during the late 1960s and early 1970s. Examples include ANSYS, ASKA, and NASTRAN. Each of these programs included several kinds of elements and could perform static, dynamic, and heat transfer analysis. Additional capabilities were soon added. Also added were preprocessors (for data input) and postprocessors (for results evaluation). These processors rely on graphics and make it easier, faster, and cheaper to do finite element analysis. Graphics development became intensive in the early 1980s as hardware and software for interactive graphics became available and affordable.

A general-purpose finite element program typically contains over 100,000 lines of code and usually resides on a mainframe or a superminicomputer. However, in the mid-1980s, adaptations of general-purpose programs began to appear on personal computers. Hundreds of analysis and analysis-related programs are now available, large and small, general and specific, cheap and expensive, for lease or for purchase. A detailed description of the finite element method is presented in Chapter 3. A brief overview, and discussion of its application to indentation modelling is presented in the following sections.

2.5.2 The finite element method (Cook, 1989; Chandrakant, 1972)

In brief, the basis of the finite element method is the representation of a body or a structure by an assemblage of subdivisions called finite elements, Figure 2.3. These elements are considered interconnected at joints, which are called nodes or nodal points. Simple functions are chosen to approximate the distribution or variation of the actual displacements over each element. Such assumed functions are called displacement

functions or displacement models. The unknown magnitudes or amplitudes of the displacement functions are the displacements (or the derivatives of the displacements) at the nodal points.

Hence, the final solution will yield the approximate displacements at discrete locations in the body, the nodal points. A displacement model can be expressed in various simple forms, such as polynomials or trigonometric functions. Since polynomials offer ease in mathematical manipulations, they have been employed commonly in finite element applications.

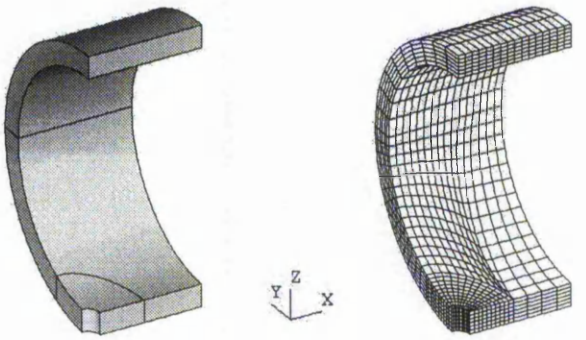

Figure 2.3 Three-dimensional region represented as an assemblage of 8-node solid elements

A variational principle of mechanics, such as the principle of minimum potential energy, is usually employed to obtain the set of equilibrium equations for each element. The potential energy of a loaded elastic body or structure is represented by the sum of the internal energy stored as a result of the deformations and the potential energy of the external loads. If the body is in a state of equilibrium, this energy is a minimum. This is a simple statement of the principle of minimum potential energy.

For many engineering problems, it is not possible to obtain analytical mathematical solutions. An analytical solution is a mathematical expression that gives the values of the desired unknown quantity at any location in a body. Analytical solutions can be obtained only for certain simplified situations. For problems involving complex material properties, a complex geometrical shape, large geometrical deformation or a complex boundary, the engineer resorts to numerical methods, that provide approximate, but acceptable, solutions.

The finite element method is a numerical procedure for analyzing structures and continua. It originated as a method of stress analysis. Today finite elements are also used to analyze problems of heat transfer, fluid flow, electric and magnetic fields, etc. Some problems that previously were intractable are now solved routinely. Finite element procedures are used widely in the design of buildings, electric motors, heat engines, cars, ships, airframes and spacecraft.

A typical structural finite element analysis involves the following steps:

1. Divide the structure or continuum into finite elements, termed discretization.
2. Formulate the properties of each element. This means determining nodal loads associated with all element deformation states that are allowed.
3. Assemble the elements to obtain the finite element model of the structure.
4. Apply the known force, moment, displacement and/or rotational loads.
5. Specify how the structure is supported. This step usually involves setting several nodal displacements to known values, which are often zero.
6. Solve simultaneous linear algebraic equations to determine nodal degrees of freedom (DOF), i.e. nodal displacements.
7. Calculate element strains from the nodal DOF and the element displacement field interpolation, and finally calculate stresses from strains.

The power of the finite element method resides principally in its versatility. The method can be applied to various physical problems. The body analyzed can have arbitrary shape, loads and support conditions. The mesh can mix elements of different types, shapes and physical properties.

However, a general purpose program has extensive documentation. Good understanding of these documents is necessary. A computer, a reliable problem, and intelligent use are essential. Experience and good engineering judgment are needed in order to define a good model. Many input data are required and voluminous output must be sorted and understood.

2.6 Application of FEM in indentation

Indentation is a very complex deformation process. It usually comprises geometric nonlinearity, material nonlinearity and contact nonlinearity. Meanwhile, hardness itself is recognized as a complex function of fundamental material properties such as elastic modulus, Poisson's ratio, yield stress, strain hardening, and time dependent plasticity. For certain materials, additional factors such as surface energy, fracture toughness,

pressure induced phase changes, anisotropic crystal structure and grain size must be taken into account as well. The combination of all these effects makes the problem too formidable to be addressed analytically, and for this reason it was left unresolved for a long time. Due to the significant development of the computational technology, it is now possible to carry out a detailed investigation of indentation tests with the aid of the Finite Element Method.

To this end, considerable theoretical and numerical approaches were drawn from previous work over several decades. The present review is carried out from the following two viewpoints, i.e. indentation modelling using an assumed rigid indenter or an elastic indenter and soft impresser modelling. In order to describe these more concisely, indentation modelling using an assumed rigid indenter or an elastic indenter is termed 'hard impresser modelling', which is a counterpart to the soft impresser modelling. Most of the previous work was based on hard impresser modelling, as summarized by Mackerle (2001). There is only limited work on soft impresser modelling. This review will begin with hard impresser modelling.

2.6.1 Hard impresser modelling

2.6.1.1 General

Akyus and Merwin (1968) first carried out a finite element analysis of indentation by a cylindrical punch of elastic-perfectly plastic solids in plane strain. Lee et al (1972) carried out finite element analyses of a ball indentation. They concluded that the computed load-displacement curve, plastic zone development and indentation pressures are in good agreement with those obtained experimentally for heat-treated steel SAE 4340. Bourcier et al (1985) performed numerical and experimental studies of sub-micron indentations. Tanega and Hurkx (1986) presented an iterative procedure to estimate the plastic part of the stress-strain curves for a ductile metal coating from Brinell indentation tests. However, their method cannot be applied for hard materials. A finite element study of bulk materials has been conducted by Bhattacharya and Nix (1988). They showed that the basic features of the indentation experiment could be described using the finite element technique in conjunction with relatively simple material behaviour. They first successfully simulated the load vs. depth response of a nanoindentation test by using finite element modelling. Their results demonstrated that it is possible to extract Young's modulus, E, and hardness, H, respectively, from the slope of the linear portion of the unloading curve and from simulated data along the

loading curve. Cai and Zhou (1992) demonstrated, using finite element analyses, that at very low loads elastic recovery does not account for the apparent variation in hardness. Edlinger et al (1993) describe in detail the numerical treatment of contact conditions, including the influence of friction between the rigid indenter and the indented surface. By using a spherical indenter they investigated the hardenability of a material as well, and observed piling-up and sinking-in phenomena. Giannakopoulos et al (1994) attempted to explore the theoretical foundation for the Vickers test based on the 3D finite element modelling. In order to capture the influence of the yield stress and the piling-up (or sinking-in) of material on the average pressure, as well as the influence of different types of strain hardening at large strains, they assumed that the influence of the yield stress and pile-up could be described up to first order through a series expansion resulting in the relation for the average contact pressure (load divided by the true projected contact area), i.e.

$$p_{av} = 0.265\sigma_u(1+Y/\sigma_u)(1+\ln\frac{E\tan 22^\circ}{3Y})(1-\frac{u_{2\max}}{h}) \qquad (2.38)$$

Where, σ_u is the maximum stress in uniaxial compression. Y is the initial yield stress, and $u_{2\max}$ is the maximum (positive) surface displacement due to material pile-up.

The load-indentation depth relation was given as

$$P = 1.06(\tan 22^\circ)^{-2}\sigma_u(1+Y/\sigma_u)(1+\ln\frac{E\tan 22^\circ}{3Y})h^2 \qquad (2.39)$$

The above two formulae were obtained based on the small strain formulation for the non-hardening case, i.e. no strain hardening was considered when the stress is larger than σ_u.

Larsson et al (1996) analyzed the Berkovich indentation of elastic and elasto-plastic materials numerically, using 3D finite element modelling and experimentally. They derived formulae for hardness and total indentation load from the small strain numerical results and for low strain hardening. For hardness,

$$p_{av} = 0.245Y(1+\sigma_{ref}/Y)(1+\ln\frac{E\tan 24.7^\circ}{3Y}) \qquad (2.40)$$

where σ_{ref} is the stress level at a plastic strain of 30%.

For the total indentation load,

$$P = 1.273(\tan 24.7^\circ)^{-2}Y(1+\sigma_{ref}/Y)(1+\ln\frac{E\tan 24.7^\circ}{3Y})h^2 \qquad (2.41)$$

The universal formulae for hardness and total indentation load derived from the numerical results by these authors were in good agreement with their experimental findings. They also numerically checked the formulae for determining the elastic stiffness at initial unloading and found that the formulae are reliable regardless of the plastic hardening present, at least for the range of moderate hardening investigated.

Murakami and co-workers (1994, 1997) established a particular formulation of the three-dimensional finite element method for the elastic-plastic analysis of a triangular pyramidal indentation. They analysed triangular pyramidal indentations in 0.46% carbon steel and 70/30 brass as well as the curve for the calculated load-penetration depth with relation to geometrical similarity. The calculated Vickers hardness values correlate well with the experimental results. In addition, their analysis predicted the extension of the plastic zone induced by indentation, the stresses at the maximum load, and the residual stresses present after complete removal of the load. They found that at the maximum load there were no tensile stresses in the vicinity of the indenter, however, after removal of the load, large tensile residual stresses were present at the diagonal edge. They also compared the effect of hardening rules, e.g. between the isotropic hardening rule and the kinematic hardening rule. Their results indicated that the hardening rule has a marked effect on the unloading indentation displacement. However, it has little effect on the analytical values of the Vickers hardness.

Jayaraman et al (1998) proposed a method to determine the stress-strain curve of hard materials from ultra-low-load indentation tests using geometrically similar indenters. The hardness-flow stress, and characteristic plastic strain-cone angle correlations, for conical indenters, were obtained from a number of calculations with different stress-strain curves using the finite element code ABAQUS. They obtained the following equation, which is valid only for $H_{IT}/E < 0.16$, to determine the flow stress from the hardness values

$$\frac{H_{IT}}{E} = 1.7\left(\frac{\sigma}{E}\right)^{0.92} \tag{2.42}$$

The general equation relating h_c/h and H_{IT}/E^* for a 70.3° conical indenter obtained in their work is

$$\frac{h_c}{h} = \frac{1}{0.91 + 4.93 H_{IT}/E^*} \tag{2.43}$$

where, h_c is the contact depth, and E^* is the equivalent elastic modulus of the indenter-specimen system, $E^* = \left[\frac{1-\nu^2}{E} + \frac{1-\nu_{indenter}^2}{E_{indenter}}\right]^{-1}$.

Finally, they concluded that the hardness-flow stress correlation, i.e. Equation (2.42), employing a simple axisymmetric model, is close to that obtained using a more complex, three dimensional analysis after comparison with the results from Equation (2.38) for different material properties.

Giannakopoulos and Suresh (1999) presented a step-by-step method for sharp indentation tests to estimate local and bulk mechanical properties, such as Young's modulus, compressive yield strength, strain hardening exponent, strength at a plastic strain of 0.29, and hardness.

The contact pressure, $p_{av} = P_{\max}/A_{\max}$, can be identified with the hardness of the indented material; $P_{\max}$ is the maximum indentation load which makes the indenter penetrate the material by a depth h_m, thereby creating a true (projected) contact area $A_{\max}$ on the indented surface.

The load-penetration depth $(P-h)$ relationship for a sharp indenter from the three-dimensional finite element simulations of elasto-plastic indentation, combined with experimental data, was found to have the following form:

$$P = Ch^2 = M_1\sigma_{0.29}\left\{1+\frac{\sigma_y}{\sigma_{0.29}}\right\}\left\{M_2 + \ln\left(\frac{E^*}{\sigma_y}\right)\right\}h^2 \quad \text{for } 0.5 \le \frac{p_{av}}{\sigma_y} \le 3.0 \quad (2.44)$$

where σ_y is the yield strength and $\sigma_{0.29}$ is the stress corresponding to the characteristic plastic strain of 0.29 for the indented material in uniaxial compression. The constants in this equation are $M_1 = 7.143$ and $M_2 = -1$ for the Vickers pyramid indenter with an included tip angle of 136°. The corresponding values for the Berkovich indenter are $M_1 = 6.618$ and $M_2 = -0.875$ with an included angle of 130.6°. Circular conical indenters also follow the same results as the Vickers or Berkovich depending on the apex angle of the cone. If p_{av}/σ_y falls outside the bounds given in Equation (2.34), the indentation response is either elastic (for $p_{av}/\sigma_y < 0.5$) or elastic-perfectly plastic (for $p_{av}/\sigma_y = 3$).

A relationship between $A_{\max}$ and h_m was derived for the elasto-plastic materials by accounting for the effects of strain hardening on piling-up and sinking-in (Giannakopoulos et al, 1994):

$$\frac{A_{\max}}{h_m^2} = 9.96 - 12.64(1-S^*) + 105.42(1-S^*)^2 - 229.57(1-S^*)^3 + 157.67(1-S^*)^4 \quad (2.45)$$

where, $S^* = p_{av}/E^*$.

$$E^* = \left[\frac{1-\nu^2}{E} + \frac{1-\nu_{indenter}^2}{E_{indenter}}\right]^{-1} = \frac{1}{c^*\sqrt{A_{\max}}}\left(\frac{dP}{dh}\right) \quad (2.46)$$

The ratio of the residual depth of penetration, h_f, upon complete unloading to the maximum penetration depth, h_m, prior to unloading, is indicative of the extent of plastic deformation and strain hardening (Suresh et al, 1997, 1998; Giannakopoulos et al, 1994), such that

$$\frac{\sigma_{0.29}}{0.29E^*} = 1 - 0.142\frac{h_f}{h_m} - 0.957\left(\frac{h_f}{h_m}\right)^2 \quad (2.47)$$

This result holds for Vickers and Berkovich, as well as circular conical, indenters.

From elasto-plastic finite element analyses of the sharp indentation, h_f/h_m can also be described as

$$\frac{h_f}{h_m} = 1 - d^*\frac{p_{av}}{E^*} = 1 - d^*S^* \quad (2.48)$$

where, $d^* = 5$ for the Vickers pyramid indenter and $d^* = 4.678$ for the Berkovich indenter; the conical indenter has the results similar to Vickers or Berkovich depending on the included apex angle.

Combining Equations (2.45) and (2.48) readily provides a unique relationship between $A_{\max}$ and h_m.

Alternatively, S^* can be computed by applying the following equation:

$$\frac{W_e}{W_{tot}} = d^*S^* \quad (2.49)$$

where, W_e is the elastic work and W_{tot} is the total work. W_e and W_{tot} can be found graphically from the $P-h$ curve.

This method is expected to be valid provided that the diameter of the impression made by the indenter spans at least five grains. For thin films on substrates, it must

additionally be ensured that the contact diameter is typically smaller than about one third of the film thickness in order that the indentation response is not influenced by the substrate.

However, there is a question remaining here as to whether the stress-strain relationships can be uniquely determined from the loading-unloading curves alone. Cheng and Cheng (1999) first examined the essential features of indentation loading and unloading curves using the scaling relationships for conical indentation in elastic-plastic solids. Using these features, they showed that essentially the same loading-unloading curves can be constructed from different stress-strain relationships (Figure 2.4). They concluded that stress-strain relationships may not be uniquely determined from loading and unloading

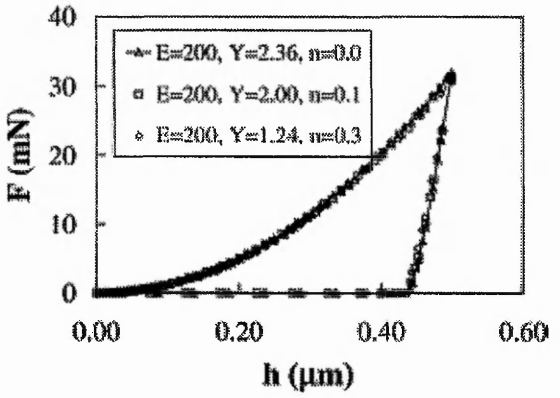

Figure 2.4 An example showing that the same loading-unloading curves can be constructed from different stress-strain relationships (Cheng and Cheng, 2004)

curves alone using a conical or pyramidal indenter. Hardness and elastic modulus, however, can be obtained from these curves alone. Finally, they pointed out that the possibilities of using several conical indenters of different angles to obtain stress-strain relationships should also be investigated both experimentally and theoretically.

Futakawa et al (2001) presented a technique for determining the constitutive equation in elastic-plastic materials from indentation test data using multiple indenters with different apex angles. Finite element analyses were carried out to evaluate the effects of yield stress, work hardening coefficient, work hardening exponent, and the apex angle of the indenter on the load-depth curves obtained from the indentation tests. As a result, the characterized curves describing the relationship between the yield stress, work hardening coefficient, and the work hardening exponent were established. Identification of the constants for a constitutive equation was made on the basis of the relationship between the characterized curves and the hardness given by the load-depth curves.

Cheng and Cheng (2002) summarized and extended their recent results (Cheng and Cheng, 1998a, b, 1999, 2000, 2001) obtained using a scaling approach to indentation modelling, which provides some insights into instrumented indentation measurements. They first derived the scaling relationships for the loading and unloading curves, contact depth, and hardness for indentation in elastic-plastic solids with work hardening. Using these relationships and extensive finite-element computations, they found three approximately linear relationships between H_{IT}/E^*, W_p/W_{tot} and h_f/h_m, i.e.

$$\frac{W_p}{W_{tot}} = (1+\gamma)\frac{h_f}{h_m} - \gamma \quad \text{for } \frac{h_f}{h_m} > 0.4 \tag{2.50}$$

where $\gamma = 0.27$.

$$\frac{h_f}{h_m} = 1 - \lambda\frac{H_{IT}}{E^*} \tag{2.51}$$

where $\lambda = 1.50\tan(\theta) + 0.327 \quad \text{for } 60^\circ \le \theta \le 80^\circ$

$$\frac{H_{IT}}{E^*} = \kappa\frac{W_e}{W_{tot}} \tag{2.52}$$

where $\kappa = 1/(\lambda(1+\gamma))$ for $60^\circ \le \theta \le 80^\circ$.

Cao and Lu (2005a) proposed a closed-form expression for the size dependent sharp indentation loading curve based on dimensional analysis and the finite deformation Taylor-based nonlocal theory (TNT) of plasticity. The key issue was to link the results of FEM based on TNT plasticity with those obtained using conventional FEM by taking as the effective strain gradient, η, that presented in the work of Nix and Gao (1998), thus avoiding large-scale finite element computations using strain gradient plasticity theories.

Cao and Lu (2005b) established a reverse algorithm to extract the plastic properties of engineering metals from size-dependent indentation loading curves. Furthermore, they investigated the properties of the reverse problem, i.e. the existence, uniqueness and stability of the solution. They also emphasized that their model was based on the plasticity theories which link geometrically necessary dislocations to continuum plasticity via the Taylor model. For size effects due to other mechanisms such as geometrical constraints (Arzt, 1998), surface layers, tip effects and so on which cannot be explained by the effects of GND, their present method might produce poor results.

2.6.1.2 Indenter geometries

Lichinchi et al (1998) simulated Berkovich indentation experiments with the ABAQUS finite element software package. The investigated system was titanium nitride on high speed steel as an example of a hard film on a soft substrate. They used an axisymmetric model in which the conical indenter had the same contact area as the Berkovich indenter. The friction coefficient between the indenter and the specimen surface was assumed to be zero. Subsequently, they compared the loading-unloading curves for a bulk TiN sample between an axisymmetric model and a three-dimensional model. The curves were practically identical. They concluded that the axisymmetric model with a conical indenter, which has the same area function of the real tip, is an effective tool for simulating the nanoindentation procedure with a Berkovich indenter.

The effect of the substrate on coating hardness measurements was analyzed for the TiN/HSS system through the evolution of the plastic deformation field. The initiation of plastic deformation in the substrate at the interface zone corresponded to a penetration depth of the indenter equal to 15% of the film thickness. They proposed that this relative penetration of the indenter represents a critical point from which the load data begin to be affected by the lower stiffness of the substrate. Consequently, at this stage the hardness of the film decreases with respect to the real value. Finally, they concluded that the general criterion that the film should not be penetrated more than 10-20% of its thickness is still applicable for TiN on HSS.

Xue Z. et al (2002) studied the influence of indenter tip radius on the micro-indentation hardness based on the theory of mechanism-based strain gradient (MSG) plasticity. Their finite element modelling shows that for conical indenters with spherical tips, the dependence of indentation hardness on the contact radius is not monotonic; spherical contact and conical contact give increasing and decreasing indentation hardness, respectively (Figure 2.5). The effect of indenter tip radius disappears once the contact radius exceeds one half of the indenter radius.

Yu et al (2004) carried out finite element simulations of sub-50 nm shallow nanoindentations with a 90° cube corner indenter. They proposed a nonlinear regression method for estimating the tip radius of an indenter by taking into account that initially the contact is only with the spherical surface of the tip and subsequently also includes

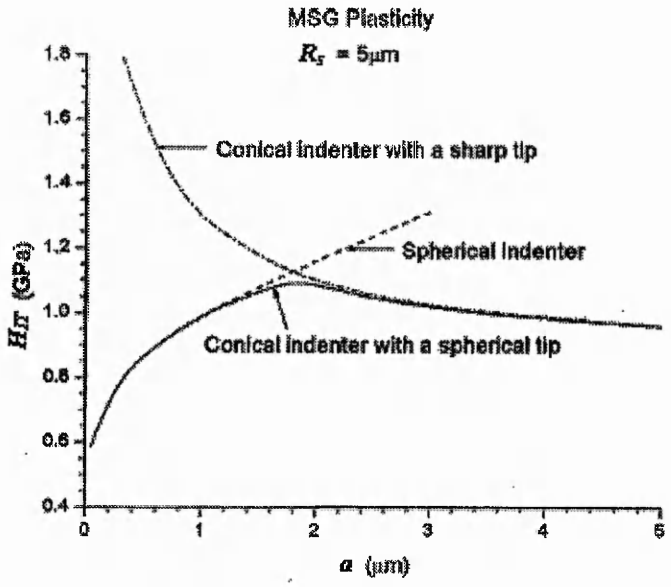

Figure 2.5 The indentation hardness H_{IT} predicted by MSG plasticity theory versus the contact radius a for a spherical indenter with radius $R_s = 5$ μm; a sharp, conical indenter with semi cone angle $\theta = 72°$ and a conical indenter $\theta = 72°$ with a spherical tip $R_s = 5$ μm. The indented material is a polycrystalline copper. (Xue Z. et al, 2002)

contact with the equivalent conical surface. This effective tip radius determined from the regression is then used to define the geometry of the tip of the corresponding ideal conical indenter in the finite element method. They found that it is necessary to consider the roundness of the tip in the area function calibration and modelling, otherwise the predicted yield strength found from successive iterations to best-fit the load-displacement curves could be 10 times larger than its real value.

2.6.1.3 Mesh effects

Lausen and Simo (1992) designed a specific mesh for the axisymmetric indentation modelling problem. They mentioned that the meshing was very fine near the indenter in order to resolve the contact conditions and allow accurate contact area determination, but was also sufficiently large so that it approximated a semi-infinite solid. The transition regions were used right at the material surface under the indenter to assure good resolution of the contact area. They pointed out that the presence of these very small elements at the material surface was found to have virtually no effect on the contact load for a given indentation depth, but was crucial in order to assure that the area was accurately calculated, leading to reasonable calculation of hardness.

Sung (2000) also carried out a detailed examination on the effect of mesh geometry by comparing the results between FEA and theory.

2.6.1.4 Material properties

Matsuda (2002) analysed the Vickers hardness H_V of elastic linear hardening materials with various Young's moduli E, yield stresses Y and strain-hardening moduli TM using a 3D finite element method. One eighth of the specimen was analysed. The indenter was modelled as a frictionless rigid square pyramid. The effects of the factors ($E/Y, H_V/Y$) on the surface profiles of the Vickers indentation were initially studied. Subsequently a method was proposed to predict the stress-strain curves of elastic-plastic materials. Finally, it was concluded that: 1) the type of the indentation changes from piling-up to sinking-in with increase in the ratio H_V/Y, i.e. the strain-hardening modulus to the yield stress; 2) as H_V/Y increases, the ratio h_m/d of the maximum pile-up height to the diagonal of the indentation decreases and the ratio r/d increases, where d is the indentation diagonal length, h_m is the maximum pile-up height, and r is the distance from the centre of the indentation to the maximum pile-up.

2.6.1.5 Friction

Atkinson and Shi (1989) proposed on the basis of Vickers indentation tests conducted with or without a lubricant, that friction is the principal factor causing the load dependence of hardness values. Bradt and co-workers (1992) also proposed in their initial papers that friction was the main factor affecting the Indentation Size Effect (ISE), although this viewpoint was modified in later publications. More recently, Ren et al (2002) have provided support for Almond and Roebuck's (1983) contention that friction is not a significant factor affecting hardness values.

With regard to numerical modelling, Matsuda and Kaneta (1996) found in their simulation of the Vickers hardness of electroplated nickel that, in the case of a soft coating on a harder substrate, the hardness could be markedly affected by the friction coefficient. Bucaille et al (2003) extended Dao's (2001) approach and studied the influence of the included angle of conical indenters ($\theta = 70.3, 60, 50$ and 42.3°) and the friction coefficient on the force penetration curves based on a finite element analysis, using ABAQUS, on elasto-plastic materials. Based on this analysis, a more general method for determining the plastic properties of metals was suggested. It was concluded that friction has no significant influence on the normal force for included angles equal to, or higher than, 60°.

Tsou et al (2005) have presented several experimental results to demonstrate the existence of the friction force between the tip of the indenter and the test sample. They also investigated the effect of the sliding friction on thin film mechanical property measurements. They reported that the friction effect is influenced by the indentation depth according to the experimental results. In addition, they reported that the interface friction force is more significant for a brittle material due to its larger elastic restoring force and that ignoring the friction effect may lead to significant error when extracting the elastic modulus of thin films from the indentation test.

Bolzon et al (2004) performed a parametric study by assuming friction coefficients equal to 0, 0.05, 0.15, 0.3 and 0.5. Their results show that the friction coefficient has practically no influence on the load versus displacement indentations curves for the experimental set up considered by them; a significant influence was noted on the specimen residual deformations, particularly on the piling-up portion of the indented material around the imprint. Remarkable differences are evidenced in the measurable displacements especially when the friction coefficient varies in the range of 0-0.3.

Mata and Alcalá (2004) examined frictional effects on sharp indentation of strain hardening solids. The role of friction on the development of pileup and sinking-in around the contact boundary was estimated quantitatively. They concluded that friction has the largest influence on the contact response of solids exhibiting considerable piling-up effects, whereas materials developing moderate pileup or sinking-in are less sensitive to friction. Finally, they devised a methodology to assess the influence of the friction coefficient on mechanical properties extracted through indentation experiments.

2.6.1.6 Sliding

Krichen et al (1996) investigated the fretting conditions in a contact between poly (methylmethacrylate) and a rigid counterface using both experiments and finite elements computations. Two-dimensional computations were carried out assuming a plane strain state. The computation of the microdisplacements in the contact area during a tangential loading allowed the determination of the critical displacement for transition from partial sliding to gross sliding conditions. These conditions were mapped in friction maps as a function of the contact loading parameters (i.e., normal load and displacement amplitude) and the friction coefficient. Their analysis was performed assuming that the polymer behaved elastically and that the friction obeyed Coulomb's law. The fretting loading was simulated in two steps:

i) a normal indentation step involving a downward displacement of the rigid cylindrical indenter.

ii) A tangential loading step obtained by simultaneously moving the boundaries of the mesh.

They concluded that FE simulations have been proved to be an efficient way for predicting the initial fretting conditions in a contact involving PMMA and a rigid counterface.

Giannakopoulos and Suresh (1998) presented three-dimensional finite element analyses of fretting contact fatigue between a sphere and a flat surface. Their results showed that the magnitude, as well as distribution of the fields, changed markedly with the sign of the superimposed mean stress. Their computational model was also used to simulate the evolution of fretting damage in prior experiments conducted on a bearing steel and an aluminium alloy with the sphere on flat surface fretting arrangement.

McColl et al (2004) presented a finite element-based method for simulating both the fretting wear and the evolution of fretting variables with number of wear cycles in a cylinder-on-flat fretting configuration for aeroengine transmission components. The measured and predicted worn surface profiles were found to correlate well for the low normal load case. Under high normal loads, the predicted maximum wear depth was under-estimated and the width of the scar was over-estimated. The differences were attributed to the use of stroke for wear coefficient calculation and the effect of debris, which was not modelled. They found that during the first 1000 wear cycles, the half contact width increases significantly, by about 100%, while the peak contact pressure decrease dramatically to about 40% of the initial peak Hertzian value; subsequent changes in these variables were at a slower rate. The contact pressure distribution was shown to evolve to a uniform distribution across the increased contact width. The slip between the contacting bodies was shown to increase slightly with wear, concomitant with the decreasing contact pressure.

2.6.1.7 Coatings

There is a commonly used rule of thumb that the indentation depth has to be within about 10% of the thickness of the thin film for Vickers indentation in order to limit the error induced by the substrate to be less than 2% (Peggs and Leigh, 1983).

Depth-sensing indentation techniques have been used widely to study the mechanical properties of thin films on substrates.

Tsui et al (1999a) studied the indentation plastic displacement field using ANSYS, which is a general commercial FEM software, for the case of soft films (a Titanium/Aluminium multilayered thin film) on hard substrates (Silicon) and the case of hard films (a Titanium/Aluminium multilayered thin film) on soft substrates (an Aluminium alloy) respectively. In their models, the multilayered film was assumed as a homogeneous solid. For the case of soft films on hard substrates, they observed pileup for indentations with depths larger than 30% of the total film thickness. For shallow indentations, pileup was significantly overestimated due to the existence of pores. For the case of hard films on soft substrates (Tsui et al, 1999b), they observed sinking-in effects in all of the indentations. Based on their experimental results, the amount of sinking-in of the hard film-soft substrate composite is larger than the bulk substrate and film alone. This was confirmed by their finite element analyses. Their results also indicate that the plastic deformation around the plane strain indentations is dominated by the soft aluminium substrate. Finally, they concluded that the large tensile stress near the indentation apex created voids and caused reduction of the film density. They pointed out that the indentation voids may pose difficulties in extracting the intrinsic film properties from the indentation properties of the composites, even if the 'substrate effect' is fully understood and characterized.

He and Veprek (2003) applied finite element modelling to simulate the mechanical response of superhard coatings on soft substrates under indentation. In these situations, they found that the diamond tip cannot be treated as rigid any more. The Doerner-Nix and Oliver-Pharr methods were found to give quite different data when applied to derive hardness from the load-displacement curves. The substrate influence was found to be severe even for relatively thick (~5μm) coatings. They suggested that in order to get the film hardness with no substrate influence, indentation experiments should be made within ~5% the film thickness, rather than the 10% rule-of-thumb.

Panich and Sun (2004) studied the effect of penetration depth on indentation response of soft coatings on hard substrates using finite element analysis (ABAQUS). The Berkovich indenter was modelled as an axisymmetric conical indenter with the same projected area-depth function. They concluded that the frequently used one-tenth 'rule of thumb' does not apply to soft coating property measurement. For the wide range of coatings investigated by them, the coating hardness can be safely measured if the indentation is less than 30% of the coating thickness. With very soft coatings, an

indentation depth approaching the thickness of the coating can even be used without inducing significant substrate effect.

Yoo et al (2004) investigated the effect of the radius of the spherical indenter on the critical nano-indentation depth (CID) to ensure the reliable measurement of thin film properties using ABAQUS/Explicit for a Si hard thin film/Al soft substrate layered system. They found that the CID based on the 10% load-error tolerable limit was fairly low, e.g. about 2-3% of the thickness of film, t, when the indenter radius was large ($R/t = 33.3$). The CID then increased gradually with a decrease in R/t, followed by a rapid increase in slope when R/t was below about 3.33. They also commented that in their preliminary study, that when the speed-up technique (increasing the speed of the indentation) was employed for the explicit method (ABAQUS/Explicit), the computational time was 50 times faster than the implicit method (ABAQUS/Standard) without loss of numerical accuracy. Therefore, they used the explicit method with the speed-up technique to carry out the finite element analyses.

2.6.1.8 Creep

The hardness creep test provides a simple and non-destructive method for investigating the mechanical properties of solids (Tabor, 1985), and it also gives information about the time-dependent flow (creep) of materials (Atkins et al, 1966; Walker, 1973; Carter et al, 1988a, b; Hooper and Brookes, 1984; Sargent and Ashby, 1989). In the latter case, the hardness indenter maintains its load over a period of time under well controlled conditions, and changes in indentation size are monitored. An important result of this is that most materials, including ceramics and even diamond, are found to creep at temperatures well below half their melting point.

Indentation hardness-creep is influenced by a large number of variables such as the material's plastic deformation properties, diffusion constants, the normal-acting load on the indenter, duration of the indentation, etc. Mainly based on a power-law creep approach (Atkins et al, 1966; Walker, 1973; Carter and Henshall et al, 1988a, b; Hooper and Brookes, 1984; Sargent and Ashby, 1989), equations of hardness change as a function of dwell time were obtained. However, several difficulties arose when these equations were used to interpret experimental results, particularly when applied to low temperature indentation creep. Li et al (1991) analyzed all the possible mechanisms which may contribute to indentation creep, and thereby obtained rate-equations for each mechanism.

Becker et al (1994) presented an indentation creep example to demonstrate the versatility and accuracy of Finite Element solutions.

Yue et al (2000) explored the possibilities of determining creep parameters for a simple Norton law material from indentation creep testing following the procedure outlined by Becker et al (1994). The creep indentation test technique was analysed in terms of indentation rates at constant loads using creep finite element analysis. They concluded that the indentation creep behaviour generally depended on geometry, dimensions and boundary conditions. Their examples showed that if the constitutive law for creep of a material is given by a simple power law equation then creep indentation testing yields a power law relation between indentation rate and the indentation load. A FEM assisted procedure was proposed by them to translate the parameters of indentation creep into uniaxial creep parameters for cases where the indentation creep response is controlled by only one material.

2.6.1.9 Indentation cracking

Indentation cracking can be used to determine the fracture properties of the materials. Cracking occurs frequently on loading as well as unloading of the specimens during pyramid indentation of high hardening and pressure-sensitive hard metals, glasses and ceramics (Larsson and Giannakopoulos, 1998). Larsson and Giannakopoulos (1998) presented a detailed investigation on indentation induced tensile stresses from which cracking initiation and propagation sequences can be inferred. Their analysis was carried out using the three-dimensional finite element method and included a parametric study of both the Vickers and the Berkovich indentation tests, without explicit modelling of the cracks.

Zhang and Subhash (2001) presented a three-dimensional finite element model for simultaneous and sequential double Vickers indentations on brittle materials using ABAQUS. The induced damage due to double indentations was investigated using an "elastic–plastic-cracking" constitutive model that takes into account "tensile cracking and compressive yielding" behaviour in ceramics.

Muchtar et al (2003) simulated the cracking processes during the indentation testing of brittle solids by means of the finite element method using elements exhibiting cohesive post-failure behaviour and alumina as the model material. Their results showed that at low indentation loads, median cracks could nucleate at full loading but Palmqvist cracks only nucleate in the unloading stage, and these may not join up even after full unloading.

At high indentation loads, both median and Palmqvist cracks nucleate early during the loading stage and coalesce to form a half-penny crack on further loading. The indentation process was simulated using ABAQUS/Explicit in a quasi-static manner to ensure the inertia effects did not dominate and affect the solution since ABAQUS/Explicit treats problems dynamically.

2.6.2 Soft impresser modelling

2.6.2.1 Constant pressure assumption

Fagan et al (2000) carried out elastic finite element analysis using ANSYS to predict the stress distribution in a diamond-coated substrate. They used a uniform normal load assumption for the soft impresser problem. In order to ensure that the finite element results were reliable, they tested their model by systematically increasing the mesh density and plotting sample output. They assumed the models have converged when an increase in mesh density did not result in a significant change in output. They mentioned that a very fine graduated mesh near the edge of the contact region was used. Their results demonstrated that the performance of a coating can be related to the ratio of coating thickness to contact radius (t/a). For example, for the silicon substrate most of the protection is achieved when the t/a ratio is about 0.1, and for the diamond coating there is no advantage in using coatings with t/a ratios greater than 1.3.

2.6.2.2 Soft impresser modelling

Numerical modelling of the soft impresser test technique has been very limited, i.e. Lacerda et al (1999) and Henshall et al (1999) have developed an elastic axisymmetric boundary element code to investigate contact stresses in layered axisymmetric bodies induced by a flat steel cone for the soft impresser technique test, and compared the results to those from Finite Element Analysis.

2.7 Summary

This chapter provides an overview of previous and current work on hardness, contact mechanics, the soft impresser technique, the dimensional analysis in the rigid indentation and the application of FEM in indentation.

The above review shows that FE modelling has been implemented extensively in indentation tests. However, much important research still remains to be done. Furthermore, no significant FE modelling of the soft impresser has been undertaken at the present time.

CHAPTER 3
FINITE ELEMENT ANALYSIS IN SOLID MECHANICS: BASIC THEORY

This chapter is concerned with the basic theory of the finite element method. The concept of the configuration of an object is presented in the first section. The subsequent section presents the constitutive relations for the elasto-plastic finite element method. Finally, the finite element formulation and the numerical implementation of the elasto-plastic incremental constitutive relations are introduced.

3.1 The configuration of an object (Xiao and Li, 1994)

In small deformation solid mechanics, the change in geometry of an object can be ignored since the deformation is very small. However, when the deformation is very large, i.e. finite deformation, the change in an object's location in space must be considered.

In order to describe the two different states, the reference configuration and the deformed configuration are introduced here. At any given time, the region in space occupied by an object is termed as that object's configuration. If the mechanical characteristics of an object at different times $t = 0, t_1 \ldots t_{m-1} (m = 1,2,\ldots)$ were known, any time before t_m can be taken as the reference configuration. Usually the initial configuration is taken as the reference configuration.

When $t = 0$, assume the initial configuration of an object is V_0 with reference to a specific Cartesian coordinate system $\{x_i\}$. The location of a random particle P on this object is $x_i (i = 1,2,3)$. Assume the object deforms at a subsequent time t. The configuration of this object at this time is called the deformed configuration. Another Cartesian coordinate system $\{\bar{x}_i\}$ can be used to describe this configuration. Particle P of the initial configuration has moved to point Q after deformation. The location of particle Q is $\bar{x}_i (i = 1,2,3)$. If it is assumed that the coordinate system $\{x_i\}$ coincides with the coordinate system $\{\bar{x}_i\}$, the deformed configuration can be shown in Figure 3.1.

Obviously, for the same point, the relationship between the two coordinates is

$$\bar{x}_i = \bar{x}_i (x_j, t) \qquad (3.1)$$

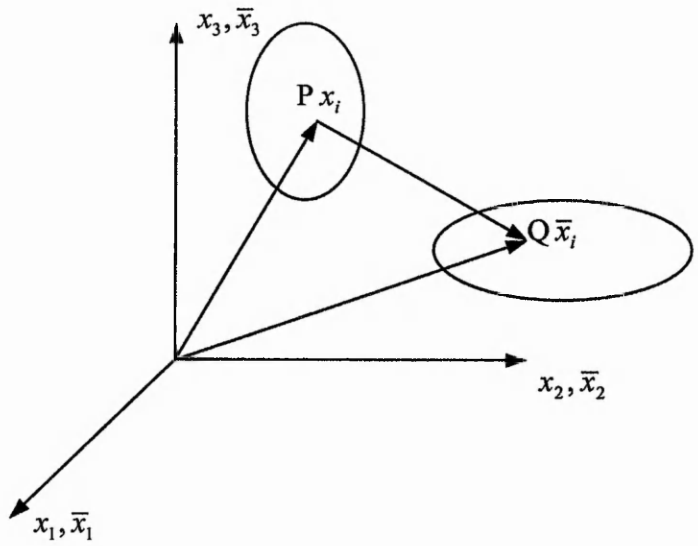

Figure 3.1 Configuration description of a point P which moves to Q

Assume the deformation and movement of the object are continuous, then every particle x_i in V_0 only corresponds with one particle $\bar{x}_i$ in V_t, and vice versa. Then this function can be considered as a mono-valued, continuous and differentiable function. Its Jacobian matrix is not equal to zero, i.e.

$$J = \left| \frac{\partial \bar{x}_i}{\partial x_j} \right| \neq 0 \qquad (3.2)$$

and $$x_i = x_i(\bar{x}_j) \qquad (3.3)$$

3.2 The constitutive relation for elasto-plastic FEM (Xiao and Li, 1994; Washizu, 1982)

Since the elasto-plastic constitutive relation of metals has nonlinear character and it is affected by its deformation process and loading path, it is a transient relation. The deformed configuration can use Euler parameters, i.e. Cauchy stress tensor and Almansi strain tensor, to describe the constitutive relationship. However, the material derivative $\dot{\tau}_{ij}$ of the Cauchy stress tensor is not an objective tensor. In order to satisfy the objective condition of the constitute equation, the Jaumann stress tensor needs to be used.

The relation between the Jaumann stress variation rate tensor τ_{ij}^{V} and the Almansi strain rate tensor $\dot{e}_{ij}$ is

$$\tau_{ij}^{V} = D_{ijkl}\dot{e}_{ij} \qquad (3.4)$$

where D_{ijkl} is the elasto-plastic tensor.

According to plastic flow theory, for isotropic hardening metal materials, D_{ijkl} can be determined by the Prandtl-Reuss equations

$$\dot{\sigma}_{ij} = \frac{E}{1+\nu}\left[\left(\delta_{ik}\delta_{jl} + \frac{\nu}{1-2\nu}\delta_{ij}\delta_{kl}\right)\dot{\varepsilon}_{kl} - \alpha^*\dot{\lambda}\sigma'_{ij}\right] \tag{3.5}$$

where $\dot{\lambda} = \dfrac{1}{\frac{2}{3}\bar{\sigma}^2\left(1+\frac{2}{3}H\frac{1+\nu}{E}\right)}\sigma'_{kl}\dot{\varepsilon}_{kl}$ (3.6)

$$H = \frac{d\bar{\sigma}}{d\bar{\varepsilon}^p} \tag{3.7}$$

α^*=1 where $\bar{\sigma} = c_s$ and $\sigma'_{ij}d\varepsilon_{ij} \geq 0$,

α^*=0 where $\bar{\sigma} < c_s$ or where

$\bar{\sigma} = c_s$ and $\sigma'_{ij}d\varepsilon_{ij} < 0$.

Where the parameter c_s specifies the final state of strain hardening, and its value may vary from point to point throughout the body.

Equation (3.5) was derived based on small deformation theory.

In order to use Equation (3.5) in the finite deformation analysis, $\dot{\sigma}_{ij}$ and $\dot{\varepsilon}_{kl}$ should be replaced by τ^V_{ij} and $\dot{e}_{kl}$ respectively. Substituting these into Equation (3.5),

$$\tau^V_{ij} = \frac{E}{1+\nu}\left[\left(\delta_{ik}\delta_{jl} + \frac{\nu}{1-2\nu}\delta_{ij}\delta_{kl}\right) - \alpha^*\frac{\tau'_{ij}\tau'_{kl}}{\frac{2}{3}\bar{\tau}^2\left(1+\frac{2}{3}H_E\frac{1+\nu}{E}\right)}\right]\dot{e}_{kl} \tag{3.8}$$

Comparing Equation (3.4) with Equation (3.8),

$$D_{ijkl} = \frac{E}{1+\nu}\left[\left(\delta_{ik}\delta_{jl} + \frac{\nu}{1-2\nu}\delta_{ij}\delta_{kl}\right) - \alpha^*\frac{\tau'_{ij}\tau'_{kl}}{\frac{2}{3}\bar{\tau}^2\left(1+\frac{2}{3}H_E\frac{1+\nu}{E}\right)}\right] \tag{3.9}$$

Thus, for the isotropic 3D plastic deformation of metals, the more universal constitutive Equation (3.9) is obtained from the constitutive Equation (3.5), which is only suitable for small displacements and small deformations.

3.3 Finite element formulation

Here, the finite element formulation will be introduced based on the Lagrangian formulation. For the Lagrangian formulation, if the initial configuration is taken as the reference configuration, it is named as the total Lagrangian formulation, which can be abbreviated as the T. L formulation; if the previous configuration were taken as the reference configuration, it is named as the updated Lagrangian formulation, which can be abbreviated as the U. L formulation.

The virtual work rate equation in Cartesian coordinates will be described first.

3.3.1 Virtual work rate equation

The virtual work rate equation based on the Eulerian Formulation is

$$\int_V \tau_{ij}\delta\dot{e}_{ij}dV = \int_{S_\sigma} p_i\delta v_i dS + \int_V F_i\delta v_i dV \qquad (3.10)$$

where, V is the volume of the deformed object, p_i are the surface traction forces on surface S_σ, F_i are the body forces, τ_{ij} are the Cauchy stresses, δv_i are the virtual velocity increments, and $\delta\dot{e}_{ij}$ are virtual strain rate increments. Equation (3.10) was described by Eulerian parameters based on the deformed configuration. From this equation, the virtual work rate equation using the Lagrangian formulation and Kirchhoff stress components S_{ij} and Green strain material derivative components $\dot{E}_{ij}$, i.e.

$$\int_V S_{ij}\delta\dot{E}_{ij}dV_0 = \int_{S_{0\sigma}} p_i^0\delta v_i dS_0 + \int_V F_i^0\delta v_i dV_0 \qquad (3.11)$$

where, F_i^0 and p_i^0 are the the gravitational force per volume and the surface force vector components on surface $S_{0\sigma}$ based on the initial configuration.

3.3.2 U.L formulation

3.3.2.1 Strain increments

Assume the initial configuration V_0 has been known already and the configuration V_t at time = t has been computed using the iterative method. The U. L formulation takes the configuration V_t at time t as the reference configuration, which has initial strain $\{E^t\}$ and initial stress $\{S^t\}$. The unknown configuration $V_{t+\Delta t}$ at time $=t+\Delta t$ needs to be computed based on V_t. Assume the coordinates are X_i for any point in V_t. For this point, assume the displacements are $\{u^t\}$, Green strains are $\{E^t\}$ and Kirchhoff stresses are

$\{S^t\}$ referring to the initial configuration V_0. Assume the displacement increments, Green strain increments and Kirchhoff stress increments from time=t to time=$t+\Delta t$ are $\{\Delta u\}$, $\{\Delta E\}$ and $\{\Delta S\}$ respectively. For the corresponding point, the displacement $\{u\}$, Green strain $\{E\}$ and Kirchhoff stress $\{S\}$ at time = $t+\Delta t$ are

$$\{u\}=\{u^t\}+\{\Delta u\} \tag{3.12}$$

$$\{E\}=\{E^t\}+\{\Delta E\} \tag{3.13}$$

$$\{S\}=\{S^t\}+\{\Delta S\} \tag{3.14}$$

where, $\{\Delta u\}=\{\Delta u_1 \quad \Delta u_2 \quad \Delta u_3\}^T$

$$\{E\}=\{E_{11} \quad E_{22} \quad E_{33} \quad 2E_{12} \quad 2E_{23} \quad 2E_{31}\}^T$$

$$\{S\}=\{S_{11} \quad S_{22} \quad S_{33} \quad S_{12} \quad S_{23} \quad S_{31}\}^T$$

The Green strain increments are

$$\Delta E_{ij}=\frac{1}{2}\left(\frac{\partial \Delta u_i}{\partial X_j}+\frac{\partial \Delta u_j}{\partial X_i}+\frac{\partial \Delta u_k}{\partial X_i}\frac{\partial \Delta u_k}{\partial X_j}\right) \tag{3.15}$$

If ΔE_{ij}^L and ΔE_{ij}^N are used to denote the linear part and nonlinear part of the strain increments respectively, the strain increments can be written as

$$\Delta E_{ij}=\Delta E_{ij}^L+\Delta E_{ij}^N \tag{3.16}$$

where, $\Delta E_{ij}^L=\frac{1}{2}\left(\frac{\partial \Delta u_i}{\partial X_j}+\frac{\partial \Delta u_j}{\partial X_i}\right)$ (3.17)

$$\Delta E_{ij}^N=\frac{1}{2}\frac{\partial \Delta u_k}{\partial X_i}\frac{\partial \Delta u_k}{\partial X_j} \tag{3.18}$$

Its matrix form is

$$\{\Delta E\}=\{\Delta E^L\}+\{\Delta E^N\} \tag{3.19}$$

where

$$\{\Delta E^L\}=[L]\{\Delta u\} \tag{3.20}$$

$$\{\Delta E^N\}=\frac{1}{2}[\Delta\theta]\{\Delta\theta\} \tag{3.21}$$

$$[L]=\begin{bmatrix} \frac{\partial}{\partial X_1} & 0 & 0 & \frac{\partial}{\partial X_2} & 0 & \frac{\partial}{\partial X_3} \\ 0 & \frac{\partial}{\partial X_2} & 0 & \frac{\partial}{\partial X_1} & \frac{\partial}{\partial X_3} & 0 \\ 0 & 0 & \frac{\partial}{\partial X_3} & 0 & \frac{\partial}{\partial X_2} & \frac{\partial}{\partial X_1} \end{bmatrix}^T$$

$$\{\Delta\theta\}=\begin{bmatrix} \{\Delta\theta_1\}^T & \{\Delta\theta_2\}^T & \{\Delta\theta_3\}^T \end{bmatrix}^T$$

$$[\Delta\theta]=\begin{bmatrix} \{\Delta\theta_1\}^T & \{0\}^T & \{0\}^T \\ \{0\}^T & \{\Delta\theta_2\}^T & \{0\}^T \\ \{0\}^T & \{0\}^T & \{\Delta\theta_3\}^T \\ \{\Delta\theta_2\}^T & \{\Delta\theta_1\}^T & \{0\}^T \\ \{0\}^T & \{\Delta\theta_3\}^T & \{\Delta\theta_2\}^T \\ \{\Delta\theta_3\}^T & \{0\}^T & \{\Delta\theta_1\}^T \end{bmatrix}$$

$$\{\Delta\theta_i\}=\begin{bmatrix} \frac{\partial\Delta u_1}{\partial X_i} & \frac{\partial\Delta u_2}{\partial X_i} & \frac{\partial\Delta u_3}{\partial X_i} \end{bmatrix}^T \qquad (3.22)$$

3.3.2.2 Constitutive relation in incremental form

The incremental relationship between the Kirchhoff stress tensor and the Green strain tensor is required in the U.L formulation.

The relation between the Green strain rate tensor $\dot{E}_{ij}$ and the Almansi strain rate tensor $\dot{e}_{ij}$ is

$$\dot{E}_{ij}=\frac{\partial x_\alpha}{\partial X_i}\frac{\partial x_\beta}{\partial X_j}\dot{e}_{\alpha\beta} \qquad (3.23)$$

The relation between the material derivative of the Kirchhoff stress tensor and the Jaumann derivative of the Cauchy stress is

$$\dot{S}_{ij}=\frac{\rho_0}{\rho}\frac{\partial X_i}{\partial x_\alpha}\frac{\partial X_j}{\partial x_\beta}(\tau^V_{\alpha\beta}+\tau_{\alpha\beta}\dot{e}_{kk}-\tau_{\alpha p}\dot{e}_{p\beta}-\tau_{\beta p}\dot{e}_{p\alpha}) \qquad (3.24)$$

Substituting Equation (3.4) into Equation (3.24) and assuming that the volume remains constant during plastic deformation, the following equation can be obtained

$$\dot{S}_{ij}=\frac{\partial X_i}{\partial x_\alpha}\frac{\partial X_j}{\partial x_\beta}(D_{\alpha\beta kl}\dot{e}_{kl}-\tau_{\alpha p}\dot{e}_{p\beta}-\tau_{\beta p}\dot{e}_{p\alpha}) \qquad (3.25)$$

Substituting Equation (3.23) into Equation (3.25), results in

$$\dot{S}_{ij} = \frac{\partial X_i}{\partial x_\alpha}\frac{\partial X_j}{\partial x_\beta} D_{\alpha\beta kl}\frac{\partial X_m}{\partial x_k}\frac{\partial X_n}{\partial x_l}\dot{E}_{mn} - \frac{\partial X_j}{\partial x_\beta}\frac{\partial X_n}{\partial x_\beta} S_{im}\dot{E}_{mn} - \frac{\partial X_i}{\partial x_\alpha}\frac{\partial X_n}{\partial x_\alpha} S_{jm}\dot{E}_{mn} \quad (3.26)$$

Since the configuration V_t at time=$t+\Delta t$ is not known, the variation x_α in Equation (3.26) is also unknown, therefore, the relation between $\dot{S}_{ij}$ and $\dot{E}_{mn}$ cannot be computed directly. For the nonlinear finite element method, an approximate solution can be obtained by assuming all of the initial values of current variations as those from a previous balanced configuration. The values of current variations are improved iteratively subsequently. According to this method, in Equation (3.26), let $x_i = X_i$, Equation (3.26) becomes

$$\dot{S}_{ij} = D_{ijmn}\dot{E}_{mn} - \tau_{im}\dot{E}_{mj} - \tau_{jm}\dot{E}_{mi} \quad (3.27)$$

The incremental form of the constitutive equation can be obtained by multiplying by dt on both sides of the above equation,

$$\Delta S_{ij} = D_{ijmn}\Delta E_{mn} - \tau_{im}\Delta E_{mj} - \tau_{jm}\Delta E_{mi} \quad (3.28)$$

Its matrix form is

$$\{\Delta S\} = ([D]_{ep} - [\tau_d])\{\Delta E\} \quad (3.29)$$

Applying Equation (3.9) to the above equation,

$$[D]_{ep} = \frac{E}{1+\nu} *$$

$$\begin{bmatrix}
A - B\tau'^2_{11} & & & & & \\
C - B\tau'_{22}\tau'_{11} & A - B\tau'^2_{22} & & & \textit{Symmetric} & \\
C - B\tau'_{33}\tau'_{11} & C - B\tau'_{33}\tau'_{22} & A - B\tau'^2_{33} & & & \\
-B\tau'_{12}\tau'_{11} & -B\tau'_{12}\tau'_{22} & -B\tau'_{12}\tau'_{33} & \frac{1}{2} - B\tau'^2_{12} & & \\
-B\tau'_{23}\tau'_{11} & -B\tau'_{23}\tau'_{22} & -B\tau'_{23}\tau'_{33} & -B\tau'_{23}\tau'_{12} & \frac{1}{2} - B\tau'^2_{23} & \\
-B\tau'_{31}\tau'_{11} & -B\tau'_{31}\tau'_{22} & -B\tau'_{31}\tau'_{33} & -B\tau'_{31}\tau'_{12} & -B\tau'_{31}\tau'_{23} & \frac{1}{2} - B\tau'^2_{31}
\end{bmatrix} \quad (3.30)$$

where, $A = \frac{1-\nu}{1-2\nu}$, $B = \alpha^* \beta$, $C = \frac{\nu}{1-2\nu}$

$$\beta = \frac{1}{\frac{2}{3}\bar{\tau}^2\left(1 + \frac{2}{3}H_E\frac{1+\nu}{E}\right)}$$

$$H_E = \frac{d\bar{\sigma}}{d\bar{\varepsilon}^p}$$

From the uniaxial tension $\varepsilon - \sigma$ curve, the instantaneous tangent modulus can be determined,

$$E_t = \frac{d\sigma}{d\varepsilon} = \frac{d\bar{\sigma}}{d\bar{\varepsilon}}$$

$$E = \frac{d\sigma}{d\varepsilon_e}$$

Thus H_E can be determined as

$$H_E = \frac{d\bar{\sigma}}{d\bar{\varepsilon}^p} = \frac{d\sigma}{d\varepsilon_p} = \frac{d\sigma}{d\varepsilon - d\varepsilon_e}$$

$$H_E = \frac{E_t E}{E - E_t} \tag{3.31}$$

$$[\tau_d] = \begin{bmatrix} 2\tau_{11} & & & & & \\ 0 & 2\tau_{22} & & & \textit{Symmetry} & \\ 0 & 0 & 2\tau_{33} & & & \\ \tau_{12} & \tau_{12} & 0 & \frac{1}{2}(\tau_{11}+\tau_{22}) & & \\ 0 & \tau_{23} & \tau_{23} & \frac{1}{2}\tau_{31} & \frac{1}{2}(\tau_{22}+\tau_{33}) & \\ \tau_{31} & 0 & \tau_{31} & \frac{1}{2}\tau_{23} & \frac{1}{2}\tau_{12} & \frac{1}{2}(\tau_{11}+\tau_{33}) \end{bmatrix} \tag{3.32}$$

3.3.2.3 Incremental tangent equation of elements

1) Strain increments of elements

The strain increments at any point in an element can be described using the nodal displacement increments,

$$\{\Delta u\} = [N]\{\Delta u\}^e \tag{3.33}$$

where, $[N]$ is the shape function and $\{\Delta u\}^e$ is the nodal displacement increments.

Substituting Equation (3.33) into Equation (3.20),

$$\{\Delta E^L\} = [B^L]\{\Delta u\}^e \tag{3.34}$$

where, $[B^L] = [L][N]$, $[B^L]$ is referred to as the linear geometric matrix.

Substituting Equation (3.33) into Equation (3.22), results in

$$\{\Delta \theta_i\} = [G_i]\{\Delta u\}^e \tag{3.35a}$$

which can also be written as

$$\{\Delta\theta\} = [G]\{\Delta u\}^e \tag{3.35b}$$

where , $[G_i] = \begin{bmatrix}[G_i]^{(1)} & [G_i]^{(2)} & \dots & [G_i]^{(n)}\end{bmatrix}$, n is the number of nodes.

$$[G_i]^{(k)} = \begin{bmatrix} \dfrac{\partial N^{(k)}}{\partial X_i} & 0 & 0 \\ 0 & \dfrac{\partial N^{(k)}}{\partial X_i} & 0 \\ 0 & 0 & \dfrac{\partial N^{(k)}}{\partial X_i} \end{bmatrix} \quad (k = 1,2,\dots,n)$$

$$[G] = \begin{bmatrix} [G_1]^{(1)} & [G_1]^{(2)} & \dots & [G_1]^{(n)} \\ [G_2]^{(1)} & [G_2]^{(2)} & \dots & [G_2]^{(n)} \\ [G_3]^{(1)} & [G_3]^{(2)} & \dots & [G_3]^{(n)} \end{bmatrix}$$

Substituting Equation (3.35b) into Equation (3.21) gives

$$\{\Delta E^N\} = [B^N]\{\Delta u\}^e \tag{3.36}$$

where, $[B^N] = \frac{1}{2}[\Delta\theta][G]$, and $[B^N]$ is the non-linear geometric matrix.

From Equations (3.19), (3.34) and (3.36), these give

$$\{\Delta E\} = [B]\{\Delta u\}^e \tag{3.37}$$

where now the geometric matrix $[B] = [B^L] + [B^N]$.

2) Elemental stress and its increments

When solving analyses based on the U.L formulation, taking the configuration V_t as the reference configuration, the Cauchy stress is equal to the Kirchhoff stress at time = t, hence Equation (3.14) can be written as

$$\{S\} = \{\tau\} + \{\Delta S\} \tag{3.38}$$

where, $\{\tau\}$ is the Cauchy stress at time = t at any point in element e in the reference configuration taking $\{X_i\}$ as the Lagrangian coordinates.

Substituting Equation (3.37) into Equation (3.29), results in

$$\{\Delta S\} = ([D]_{ep} - [\tau_d])[B]\{\Delta u\}^e \tag{3.39}$$

3) Incremental stiffness equation for elements

Applying the virtual rate equation of Equation (3.11) to element e in configuration V_t and considering the nodal force $\{f\}^e$, then the matrix form of the incremental virtual work equation for this element at time $= t + \Delta t$ can be derived

$$\int_e \{\delta\Delta E\}^T \{S\} dV = (\{\delta\Delta u\}^e)^T \{f\}^e + \int_{S\sigma e} \{\delta\Delta u\}^T \{p\} dS + \int_e \{\delta\Delta u\}^T \{F\} dV \qquad (3.40)$$

Substituting Equation (3.29) and Equation (3.38) into the above equation, results in

$$\int_e \{\delta\Delta E\}^T (\{\tau\} + ([D]_{ep} - [\tau_d])\{\Delta E\}) dV = (\{\delta\Delta u\}^e)^T \{f\}^e + \int_{S\sigma e} \{\delta\Delta u\}^T \{p\} dS + \int_e \{\delta\Delta u\}^T \{F\} dV \qquad (3.41)$$

Substituting Equations (3.33), (3.34), (3.35), (3.36) and (3.37) into Equation (3.41), results in

$$([k_0]^e + [k_\sigma]^e + [k_{NL}]^e)\{\Delta u\}^e = \{f\}^e + \{P\}^e - \{r\}^e \qquad (3.42)$$

where, $[k_0]^e = \int_e [B^L]^T ([D]_{ep} - [\tau_d])[B^L] dV$

$$[k_\sigma]^e = \int_e [G]^T [\tau][G] dV$$

$$[\tau] = \begin{bmatrix} \tau_{11}[I]_{3\times3} & & symmetry \\ \tau_{12}[I]_{3\times3} & \tau_{22}[I]_{3\times3} & \\ \tau_{13}[I]_{3\times3} & \tau_{23}[I]_{3\times3} & \tau_{33}[I]_{3\times3} \end{bmatrix}$$

$$[k_{NL}]^e = \int_e ([B^L]^T ([D]_{ep} - [\tau_d])[B^N] + 2[B^N]^T ([D]_{ep} - [\tau_d])[B^L] + 2[B^N]^T ([D]_{ep} - [\tau_d])[B^N]) dV$$

$$\{r\}^e = \int_e [B^L]^T \{\tau\} dV$$

$$\{P\}^e = \int_{S\sigma e} [N]^T \{p\} dS + \int_e [N]^T \{F\} dV$$

$[k_0]^e$ is the small displacement stiffness matrix, $[k_\sigma]^e$ is the initial stress stiffness matrix, and $[k_{NL}]^e$ is the large displacement stiffness matrix.

Equation (3.42) can also be written as:

$$[k]^e \{\Delta u\}^e = \{q\}^e - \{r\}^e \qquad (3.43)$$

where, $[k]^e$ is the tangent stiffness matrix, $[k]^e = [k_0]^e + [k_\sigma]^e + [k_{NL}]^e$, and $\{q\}^e$ is the nodal load, $\{q\}^e = \{f\}^e + \{P\}^e$.

Assembling all of the elemental equations, the whole stiffness equation can be obtained. The whole stiffness equation has the same form as the elemental stiffness matrix, i.e.

$$[K]\{\Delta u\} = \{Q\} - \{R\} \qquad (3.44)$$

where, $[K]$ is the tangent stiffness matrix, $\{\Delta u\}$ are the nodal displacement increments, $\{Q\}$ are the nodal loads, and $\{R\}$ are the nodal force induced by the initial stress.

3.3.3 Numerical implementation of the elasto-plastic incremental constitutive relations (Chen and Han, 1998)

3.3.3.1 Stress computation

Equation (3.29) gives the incremental constitutive equation based on the U.L formulation. In finite element analysis, since the applied load increments are finite, as well as the corresponding stress and strain increments in a load step, it is necessary to use numerical integration for Equation (3.29). It is of key importance to apply a suitable numerical algorithm for stress computation. An inappropriate algorithm may not only result in an inaccurate stress solution, but may also delay the convergence of the equilibrium iteration, and even lead to divergence of the iteration. Since stress computation consumes a significant share of the total computing time, the efficiency of an algorithm is essential.

Stress computations are required at all of the Gaussian integration points. Only the computation at one Gaussian point will be considered herein to illustrate the methodology. Assume at a typical load step, e.g. $(m+1)^{\text{th}}$ step, the stress ${}^{m}\{\sigma\}$, strain ${}^{m}\{\varepsilon\}$, ${}^{m}\varepsilon_p$ and work hardening parameter ${}^{m}k$ at the m^{th} step are known. For a typical iterative step i assume the i^{th} approximation of the displacement, ${}^{m+1}\{U\}^{(i)}$, for the $(m+1)^{\text{th}}$ load step has been calculated. Then the corresponding strain and strain increments at a Gaussian point are

$$ {}^{m+1}\{\varepsilon\}^{(i)} = [B]^{m+1}\{U\}^{(i)} \tag{3.45} $$

$$ \{\Delta\varepsilon\} = {}^{m+1}\{\varepsilon\}^{(i)} - {}^{m}\{\varepsilon\} \tag{3.46} $$

Defining a trial stress increment based on elastic behaviour, i.e.

$$ \{\Delta\sigma^e\} = [D]_e\{\Delta\varepsilon\} \tag{3.47} $$

Assume at the end of the m^{th} load step, that the stress state at a Gaussian point is in the elastic state, satisfying $f({}^{m}\{\sigma\}, {}^{m}k) < 0$, where $f(\sigma, k)$ is the loading function, and it enters into an elasto-plastic state at the $(m+1)^{\text{th}}$ step, i.e. $f({}^{m}\{\sigma\} + \{\Delta\sigma^e\}, {}^{m}k) > 0$. Hence, there exists a scaling factor r, which obeys $f({}^{m}\{\sigma\} + r\{\Delta\sigma^e\}, {}^{m}k) = 0$. Correspondingly, the strain can be divided into two parts as well, i.e. $r\{\Delta\varepsilon\}$ and

$(1-r)\{\Delta\varepsilon\}$. The first part corresponds to pure elastic response, and the second part corresponds to elasto-plastic response. Hence, the stress increments can be integrated as:

$$\begin{aligned}\{\Delta\sigma\} &= \int_{m\{\varepsilon\}}^{m+1\{\varepsilon\}^{(i)}} [D]_e(\{d\varepsilon\} - \{d\varepsilon^p\}) \\ &= \int_{m\{\varepsilon\}}^{m\{\varepsilon\}+r\{\Delta\varepsilon\}} [D]_e\{d\varepsilon\} + \int_{m\{\varepsilon\}+r\{\Delta\varepsilon\}}^{m\{\varepsilon\}+\{\Delta\varepsilon\}} [D]_e(\{d\varepsilon\} - \{d\varepsilon^p\}) \\ &= r\{\Delta\sigma^e\} + \int_{m\{\varepsilon\}+r\{\Delta\varepsilon\}}^{m\{\varepsilon\}+\{\Delta\varepsilon\}} [D]_e(\{d\varepsilon\} - \{d\varepsilon^p\}) \end{aligned} \quad (3.48a)$$

or

$$\{\Delta\sigma\} = r\{\Delta\sigma^e\} + \int_{m\{\varepsilon\}+r\{\Delta\varepsilon\}}^{m\{\varepsilon\}+\{\Delta\varepsilon\}} [D]_{ep}\{d\varepsilon\} \quad (3.48b)$$

Finally, the stress that corresponds to ${}^{m+1}\{U\}^{(i)}$ can be obtained

$${}^{m+1}\{\sigma\}^{(i)} = {}^{m}\{\sigma\} + \{\Delta\sigma\} \quad (3.49)$$

In the following two sections, the determination of the proportional factor r and the applied numerical integration methodology will be discussed in more detail.

3.3.3.2 Determination of the loading state

The first step in the stress computation is to determine the loading state of a Gaussian point, i.e. for the strain increments $\{\Delta\varepsilon\}$, the point is in a plastic loading state, elastic loading state, or in an unloading state. Only for the case that constitues a plastic loading state, are the elasto-plastic constitutive relations used to determine the corresponding stress increments. Therefore, it can be divided into two cases to discuss. The first case is at the end of the m^{th} loading step, the Gaussian point is in the elastic state; the second case is at the end of the m^{th} loading step, the Gaussian point is in the elasto-plastic state.

1) In the first case at the end of the m^{th} loading step, the Gaussian point is in the elastic state, i.e. $f({}^{m}\{\sigma\}, {}^{m}k) < 0$.

The trial stress increments $\{\Delta\sigma^e\}$ defined by Equation (3.47) can be used to check whether this point is likely to enter into the plastic state at the $(m+1)^{\text{th}}$ step. If $f({}^{m}\{\sigma\} + \{\Delta\sigma^e\}, {}^{m}k) \le 0$, then this point remains in the elastic state at the $(m+1)^{\text{th}}$ step. Applying the elastic stress-strain relation,

$$\{\Delta\sigma\} = \{\Delta\sigma^e\} \quad (3.50)$$

If $f({}^m\{\sigma\}+\{\Delta\sigma^e\},{}^mk)>0$ then this point enters into an elasto-plastic state at the $(m+1)$ th step. Thus, there exists such a scaling factor r, which gives

$$f({}^m\{\sigma\}+r\{\Delta\sigma^e\},{}^mk)=0 \tag{3.51}$$

The scaling factor r in Equation (3.51) can be solved using either an analytical method or a numerical method.

2) In the second case at the end of m^{th} loading step, the Gaussian point is in an elasto-plastic state, i.e. $f({}^m\{\sigma\},{}^mk)=0$. In this case, the loading criterion function L

$$L=\left\{\frac{\partial f}{\partial\{\sigma\}}\right\}^T[D]_e\{\Delta\varepsilon\} \tag{3.52}$$

can be used to determine the loading state. If $L\le 0$, then this Gaussian point is in an unloading or neutral loading state, therefore the elastic constitutive equation should be used

$$\{\Delta\sigma\}=\{\Delta\sigma^e\} \tag{3.53}$$

If $L>0$, then this Gaussian point is in a plastic loading state, therefore numerical integration must be applied for Equation (3.48) to obtain $\{\Delta\sigma\}$, with now $r=0$. The following section will describe this in detail.

3.3.3.3 Integration methodology

For Equation (3.48), two kinds of integration methods can be applied, i.e. explicit method and implicit method. For the two kinds of computational methods, in order to achieve the required precision, the strain increments that constitute the elasto-plastic stress-strain response need to be subdivided further. Assume these to be subdivided as m_{sub} sub-increments, $\{\Delta\tilde{\varepsilon}\}$,

$$\{\Delta\tilde{\varepsilon}\}=(1-r)\{\Delta\varepsilon\}/m_{sub} \tag{3.54}$$

The explicit method will be discussed initially.

Equation (3.47) may be re-rewritten in differential form,

$$\{d\sigma\}=[D]_e(\{d\varepsilon\}-\{d\varepsilon^p\}) \tag{3.55}$$

and, $$\{d\varepsilon^p\}=d\lambda\left\{\frac{\partial g}{\partial\{\sigma\}}\right\}=\frac{L}{h}\left\{\frac{\partial g}{\partial\{\sigma\}}\right\} \tag{3.56a}$$

$$L=\left\{\frac{\partial f}{\partial\{\sigma\}}\right\}^T[D]_e\{\Delta\tilde{\varepsilon}\} \tag{3.56b}$$

or,

$$\{d\varepsilon^p\} = [P]\{d\varepsilon\} \tag{3.56c}$$

$$\text{where, } [P] = P(\{\varepsilon\},\{\varepsilon^p\},\varepsilon_p) = \frac{1}{h}\left\{\frac{\partial g}{\partial\{\sigma\}}\right\}\left\{\frac{\partial f}{\partial\{\sigma\}}\right\}^T [D]_e \tag{3.56d}$$

The initial conditions are

$$\{\varepsilon\} = {}^m\{\varepsilon\} + r\{\Delta\varepsilon\} \tag{3.57a}$$

$$\{\sigma\} = {}^m\{\sigma\} + r\{\Delta\varepsilon\} \tag{3.57b}$$

$$\{\varepsilon^p\} = {}^m\{\varepsilon^p\} \quad \varepsilon_p = {}^m\varepsilon_p \tag{3.57c}$$

For every strain sub-increment $\{\Delta\tilde{\varepsilon}\}$ the procedure for the explicit method is

1) Utilize Equation (3.56) to determine the plastic strain sub-increment $\{\Delta\tilde{\varepsilon}^p\}$;

2) Utilize Equation (3.55) to calculate the stress sub-increment $\{\Delta\tilde{\sigma}\}$:

$$\{\Delta\tilde{\sigma}\} = [D]_e(\{\Delta\tilde{\varepsilon}\} - \{\Delta\tilde{\varepsilon}^p\})$$

3) Update the stress, strain and hardening parameters:

$$\{\sigma\} \leftarrow \{\sigma\} + \{\Delta\tilde{\sigma}\}$$

$$\{\varepsilon\} \leftarrow \{\varepsilon\} + \{\Delta\tilde{\varepsilon}\}$$

$$\{\varepsilon^p\} \leftarrow \{\varepsilon^p\} + \{\Delta\tilde{\varepsilon}^p\}$$

$$\varepsilon_p \leftarrow \varepsilon_p + \Delta\tilde{\varepsilon}_p, \quad k \leftarrow k(\varepsilon_p)$$

In this program, the computed stress precision mainly depends on the computing precision of plastic strain sub-increment. Denoting

$$[P_i] = P(\{\varepsilon\} + r_i\{\Delta\tilde{\varepsilon}\}, \{\varepsilon^p\} + r_i\{\Delta\tilde{\varepsilon}^p\}_{i-1}, \varepsilon_p + r_i(\Delta\tilde{\varepsilon}_p)_{i-1}) \tag{3.58}$$

Three algorithms for computing $\{\Delta\tilde{\varepsilon}^p\}$ are:

1 The Euler forward method:

$$\{\Delta\tilde{\varepsilon}^p\} = [P_1]\{\Delta\tilde{\varepsilon}\}$$

$$r_1 = 0$$

2 The second-order Runge-Kutta method:

$$\{\Delta\tilde{\varepsilon}^p\} = w_1\{\Delta\bar{\varepsilon}_1^p\} + w_2\{\Delta\bar{\varepsilon}_2^p\}$$

$$\{\Delta\bar{\varepsilon}_i^p\} = [P_i]\{\Delta\tilde{\varepsilon}\}$$

$$r_1 = 0 \quad r_2 = 1 \quad w_1 = w_2 = \frac{1}{2}$$

3 The fourth-order Runge-Kutta method:

$$\{\Delta\tilde{\varepsilon}^p\} = w_1\{\Delta\bar{\varepsilon}_1^p\} + w_2\{\Delta\bar{\varepsilon}_2^p\} + w_3\{\Delta\bar{\varepsilon}_3^p\} + w_4\{\Delta\bar{\varepsilon}_4^p\}$$

$$\{\Delta\bar{\varepsilon}_i^p\} = [P_i]\{\Delta\tilde{\varepsilon}\}$$

$$r_1 = 0 \quad r_2 = r_3 = \frac{1}{2} \quad r_4 = 1$$

$$w_1 = w_4 = \frac{1}{6} \quad w_2 = w_3 = \frac{1}{3}$$

In a practical program, it is not nessary to form the matrix $[P_i]$, Equation (3.56a) can be used directly to calculate $\{\Delta\tilde{\varepsilon}^p\}$. It should also be noted that in the procedure for computing stress sub-increments, Equation (3.48a) was applied instead of Equation (3.48b). This is because by using Equation (3.48a), it is easier to formulate different algorithms, furthermore, for a work hardening material, it is necessary to calculate the plastic strain. Here, the elasto-plastic matrix $[D]_{ep}$ is not relevant within the stress computation. $[D]_{ep}$ is only computed when the stiffness matrix of the structure is required to be determined separately.

3.3.3.4 Correction of the consistency condition

In a plastic loading process, the consistency condition, $df = 0$, must be satisfied. However, in the numerical computation of the incremental constitutive relation, many approximations have been made, therefore the consistency condition is often invalid. In order to satisfy the consistency condition, it is necessary to amend the stress vector. Such a correction is often realised by applying a corrected stress vector in the direction normal to the yield surface. The corrected stress vector $\{\delta\sigma\}$ is

$$\{\delta\sigma\} = a\left\{\frac{\partial f}{\partial\{\sigma\}}\right\} \tag{3.59}$$

where, a is a small scalar to be determined, ensuring that the yield condition is satisfied at the subsequent location,

$$f(\{\sigma\} + \{\delta\sigma\}, \varepsilon_p) = f(\{\sigma\} + a\left\{\frac{\partial f}{\partial\{\sigma\}}\right\}, \varepsilon_p) = 0 \tag{3.60}$$

Similar to the scaling factor r, scalar a may be computed from Equation (3.47) by an analytical method or a numerical method.

3.3.3.5 General procedure for stress computation

Here a typical procedure to compute stress will be introduced briefly. The symbol IPEL denotes the state of a Gaussian point under consideration. IPEL 0 indicates the Gaussian

point is in an elastic state; IPEL 1 indicates the Gaussian point is in an elasto-plastic state.

1 Compute strain increments $\{\Delta\varepsilon\}$ and the trial stress increments $\{\Delta\sigma^e\}$, assuming elastic behavior:

$$\{\Delta\varepsilon\}={}^{m+1}\{\varepsilon\}^{(i)}-{}^{m}\{\varepsilon\}$$

$$\{\Delta\sigma^e\}=[D]_e\{\Delta\varepsilon\}$$

2 Determine the loading state

If IPEL=1, the Gaussian is in an elasto-plastic state previously. Compute the loading criterion function L according to Equation (3.52).

If $L>0$, $r\leftarrow 0$, plastic loading.

If $L\leq 0$, $r\leftarrow 1$, IPEL$\leftarrow 0$, unloading or neutral loading.

If IPEL=0, the Gaussian point is in an elastic state previously.

Compute the yield function f:

$$f\leftarrow f({}^{m}\{\sigma\}+\{\Delta\sigma^e\},\varepsilon_p)$$

If $f\leq 0$, $r\leftarrow 1$, remains in the elastic state. Go to step 5.

If $f>0$, IPEL$\leftarrow 1$, enters into an elasto-plastic state.

Determine r such that $f({}^{m}\{\sigma\}+r\{\Delta\sigma^e\},{}^{m}k)=0$

$$\{\sigma\}\leftarrow{}^{m}\{\sigma\}+r\{\Delta\sigma\}$$

3 Compute strain sub-increments

$$\{\Delta\tilde{\varepsilon}\}=\frac{1-r}{m_{sub}}\{\Delta\varepsilon\}$$

4 Integrate numerically, loop from 1 to m_{sub}.

Determine the plastic strain sub-increments $\{\Delta\tilde{\varepsilon}^p\}$ and $\Delta\tilde{\varepsilon}_p$

$$\{\Delta\tilde{\sigma}\}=[D]_e(\{\Delta\tilde{\varepsilon}\}-\{\Delta\tilde{\varepsilon}^p\})$$

$$\{\sigma\}\leftarrow\{\sigma\}+\{\Delta\tilde{\sigma}\},\quad \varepsilon_p\leftarrow\varepsilon_p+\Delta\tilde{\varepsilon}_p$$

Check the subsequent yield condition. If $\left|f(\{\sigma\},\varepsilon_p)\right|>\varepsilon_f$, where ε_f is the prescribed tolerance for the yield function. Determine the corrected stress vector $\{\delta\sigma\}$, and $\{\sigma\}\leftarrow\{\sigma\}+\{\delta\sigma\}$.

5 ${}^{m+1}\{\sigma\}^{(i)}\leftarrow\{\sigma\}$

If necessary, compute the elasto-plastic matrix $[D]_{ep}$.

3.4 Summary

The basic theory of finite element was presented in this chapter. The concept of the configuration of an object was presented first. Then the constitutive relation for the elasto-plastic finite element method was presented. Subsequently, the finite element formulation was derived. Finally, numerical implementation of the elasto-plastic incremental constitutive relations was introduced.

CHAPTER 4
FINITE ELEMENT MODELLING: PRELIMINARY STUDIES

In order to investigate the accuracy and validity of the finite element modelling implemented in this study, it is necessary to verify the FEM results with available analytical and/or experimental results first. Three relevant situations are considered in this chapter:

i) The problem of an elastic half-space subjected to uniform pressure over a circular area. This has been studied since the analytical solution is available, and the analyses of the soft impresser results to date have assumed this pressure distribution,

ii) The Hertzian contact problem, since several authors have assumed that this pressure distribution can be used in FE modelling of contact, regardless of friction, plastic deformation or other factors, and

iii) The analysis of stress distributions in a coating subjected to contact, which is of considerable significance in determining the effectiveness of a given coating on a substrate when subjected to wear.

4.1 Localised constant pressure

4.1.1 Problem description

For the problem of an elastic half-space subjected to uniform pressure p_{uni} over a circular area of radius a, there exists an analytical solution derived by Love (1929). In this section the following numerical values have been used, p_{uni} = 809 MPa, a = 0.04 mm, E = 248 GPa, and ν = 0.23. These values are related to the experimental soft impresser testing of MgO (Guillou et al, 1992). The focus of this study is the maximum tensile stress that occurs at the edge of the contact pressure area. This is of relevance to the observed formation of cracks in ceramics at the edge of the contact zone in soft impresser testing, and is difficult to determine numerically since the stress distributions at the surface are discontinuous at the edge of the applied pressure region.

4.1.2 Analytical results

Love (1929) derived the stress field throughout an elastic half-space subjected to uniform pressure p over a circular area of radius a. The stress field results can be simplified (Johnson, 1985), when considering only the stresses on the surface. For both

inside and outside the contact area, the direct stresses at the surface σ_r, σ_θ and σ_z are principal stresses. Within the contact area, the stress components are all compressive:

$$\begin{cases} \sigma_r = \sigma_\theta = -\dfrac{1+2\nu}{2} p_{uni} \\ \sigma_z = -p_{uni} \end{cases} \quad (4.1)$$

Outside the contact area, the radial and circumferential stresses are of equal magnitude and are tensile and compressive respectively:

$$\begin{cases} \sigma_r = -\sigma_\theta = \dfrac{1-2\nu}{2} \dfrac{a^2}{r^2} p_{uni} \\ \sigma_z = 0 \end{cases} \quad (4.2)$$

The maximum tensile stress occurs at $r = a$, $\sigma_{r\max} = \dfrac{1-2\nu}{2} p_{uni}$.

Thus, for the particular values presented above:

$$\sigma_{r\max} = \frac{1-2\nu}{2} p_{uni} = \frac{1-2*0.23}{2} * 809 = 218.4\ MPa .$$

4.1.3 FE analysis

4.1.3.1 Introduction of four different element formulations (ANSYS, 2001)

This problem was modelled as an axisymmetric problem with the commercial FEM software ANSYS. The quadrilateral elements investigated have been plane 42 (4-noded), plane 182 (4-noded), plane 82 (8-noded), plane 183 (8-noded), visco 106 (4-noded), and visco 108 (8-noded). There are two problems with conventional displacement-based elements: shear locking and volumetric locking.

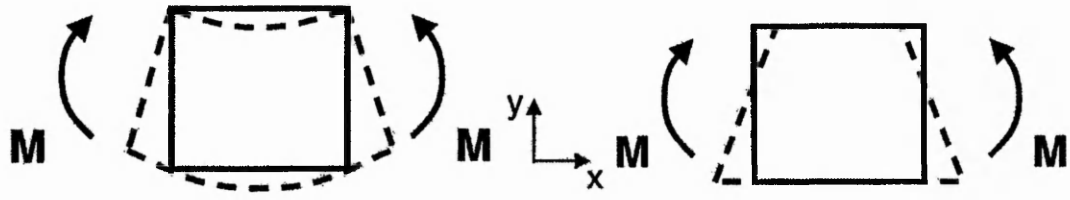

a) Pure bending deformation for a differential volume, top and bottom edges become arcs, $\gamma_{xy} = 0$.

b) Fully integrated lower order element deformation, top and bottom edges remain straight, $\gamma_{xy} \neq 0$.

Figure 4.1 Shear locking illustration (ANSYS, 2001)

Fully integrated lower order elements exhibit "overstiffness", known as shear locking, in bending. This formulation includes shear strains in bending which do not physically

exist, called parasitic shear (Figure 4.1). This is a property of the geometry, when thin members are subject to bending.

Volumetric locking occurs in fully integrated elements when the material behaviour is nearly or fully incompressible. In this case, spurious pressure stresses would develop in the element, which cause the element to have an "overstiffness" for deformations that should not cause any volume change.

In the 18X series of solid elements there are four different element technologies: B-Bar (Selective Reduced Integration, Full integration), URI (Uniform Reduced Integration), Enhanced Strain, and Mixed U-P. Whereas higher-order 18X elements (plane 183, solid 186-187) always use URI; B-Bar and enhanced strain are not applicable to higher-order elements.

In the B-bar element formulation, the volumetric and deviatoric components of the geometric matrix, $[B]$, are not evaluated at the same order of integration. Only the volumetric component $[B_v]$ has reduced integration. The deviatoric component $[B_d]$ still has full integration. That is why this method is called selective reduced integration.

$$[B]=[B_v]+[B_d] \tag{4.3}$$

It is also known as the B-bar method because $[B]$ is averaged on the volumetric term.

$$\Delta\varepsilon=[\overline{B}]\Delta u \tag{4.4}$$

where $[\overline{B}]=[\overline{B}_v]+[B_d]$

$$[\overline{B}_v]=\frac{\int[B_v]dV}{V} \tag{4.5}$$

The fact that the volumetric term $[B_v]$ has reduced integration allows it to be 'softer' since it is not fully integrated. This allows for the solution of nearly incompressible behaviour and overcomes volumetric locking. However, because the deviatoric term $[B_d]$ remains the same as the full integration formulation, parasitic shear strains still exist, so this formulation is still susceptible to shear locking.

URI uses an integration rule one order lower than needed for numerically exact integration. It is similar to selective reduced integration, but both volumetric and deviatoric terms have reduced integration. This formulation leads to a more flexible formulation which helps eliminate shear and volumetric locking. Unfortunately, the reduced integration of the deviatoric terms causes modes of deformation which have zero strain energy, called zero energy or hourglass modes. By themselves, these are

uncontrollable modes of deformation which lead to physically unrealistic behaviour. Moreover, more elements may be required to capture stress gradients due to the reduced integration.

Enhanced strain formulation (also known as Incompatible modes or Assumed strain) adds internal degrees of freedom to lower-order quad/hex elements. The displacement gradient tensor is modified with these extra 'enhanced' terms, hence the name "Enhanced strain". It is useful when shear or volumetric locking is encountered.

Mixed U-P elements (also termed Hybrid or Herrmann elements) are used to treat volumetric locking by interpolating (and solving) hydrostatic pressure as an additional DOF. Mixed U-P technology is independent of the others, so it can be used in conjunction with B-Bar, enhanced Strain, or URI.

Higher-order elements do not suffer from shear locking. However, they require more computational time than the lower-order elements.

4.1.3.2 Comparison of different element types

Figure 4.2 shows the overall geometry and a typical mesh for the FEM model. The model is 2D axisymmetric, with edge lengths of 1000 μm and has zero displacements assigned to the nodes on the two sides as shown. An APDL (ANSYS Parametric Design Language) program was written to investigate efficiently the influence of element type and mesh size. Table 4.1 shows that the 4-node plane 182 with enhanced strain option is the most robust element. It gives a maximum radial stress value close to the analytical result; moreover, it is not as sensitive with regard to the mesh size compared with the other elements. 4-node plane 42 with extra displacement shapes, 8-node plane 183 and 8-node plane 82 also give reasonable results.

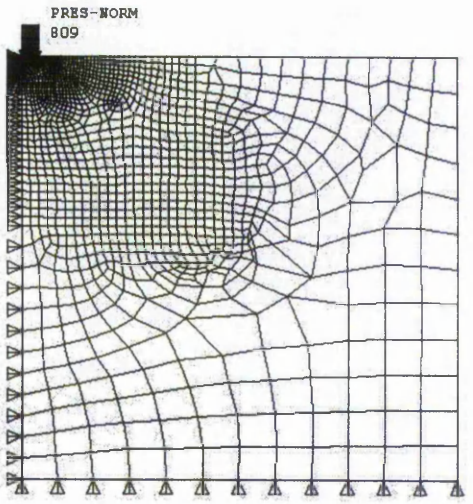

Figure 4.2 FEM model

Table 4.1 The variation of the maximum radial stress σ_r (MPa) with different element types and mesh refinement

Element		Local Mesh Size μm		
		0.1	0.2	0.4
4-node 42	Excluding extra displacement shapes	228.3	229	238.4
	Including extra displacement shapes	223.0	221.6	230.8
8-node 82		220.4	218.4	242.7
4-node 182	Reduced Integration	196.0	180.3	154.7
	Full Integration	205.2	196.9	184.7
	Enhanced Strain	218.7	218.1	224.0
8-node183		217.2	215.4	238.9
4-node 106		203.5	191.7	173.5
8-node 108		208.2	200.7	186.8
Analytical		218.4		

4.2 Hertzian contact

4.2.1 Problem description

The contact problem of an elastic spherical indenter compressing an elastic substrate was investigated using a 2D axisymmetric model with contact. Figures 4.3 and 4.4 are the model geometry and the mesh used, respectively. Both the radius and height of the substrate were 1539 μm. The radius of the sphere was 100 μm. Figure 4.5 shows the detailed mesh around the contact region. The mesh size in the two bodies within the contact region, is only 0.25 μm. The elastic moduli of the indenter and the substrate are 600 and 200 GPa respectively. The Poisson's ratios for both are 0.3. The loads were

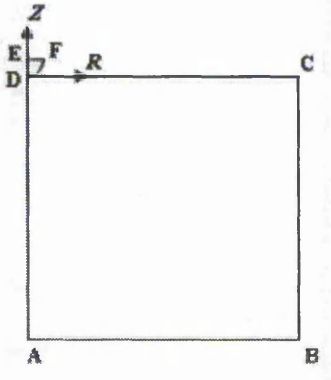

Figure 4.3 Geometry model

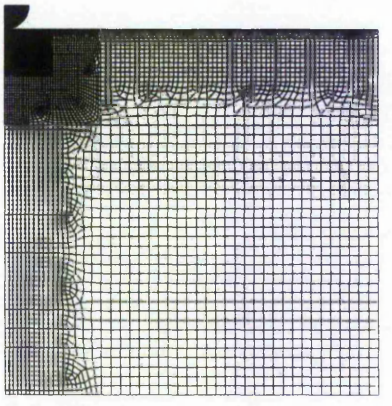

Figure 4.4 FEM model

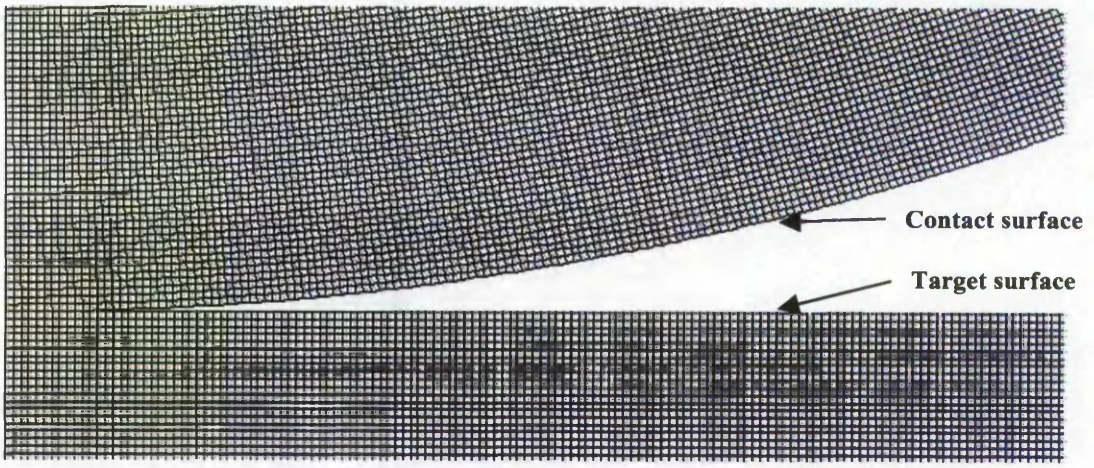

Figure 4.5 FEM contact model

applied as fixed displacements to the top surface of the curved body, with the lower edge (AB) being constrained in the z direction, and the left hand edge (r = 0) being constrained in the r direction.

From Hertzian theory (Johnson, 1985), the stresses inside the loaded circle in the surface, i.e. $z = 0$ are,

$$\sigma_r / p_{av} = \frac{1-2\nu}{2}(a^2/r^2)(1-(1-r^2/a^2)^{3/2}) - \frac{3}{2}(1-r^2/a^2)^{1/2} \qquad (4.6)$$

$$\sigma_\vartheta / p_{av} = -\frac{1-2\nu}{2}(a^2/r^2)(1-(1-r^2/a^2)^{3/2}) - 3\nu(1-r^2/a^2)^{1/2} \qquad (4.7)$$

$$\sigma_z / p_{av} = -(1-r^2/a^2)^{1/2} \qquad (4.8)$$

Outside the contact circle, the stresses are,

$$\sigma_r / p_{av} = -\sigma_\theta / p_{av} = (1-2\nu)a^2/2r^2 \qquad (4.9)$$

4.2.2 FEM contact model

The contact condition was established between the indenter and the substrate using surface-to-surface contact elements (Figure 4.5). Both bodies behave elastically, the substrate surface is flat whereas the other surface is curved, so the curved surface was defined as the contact surface, and the substrate surface was defined as a target surface. Examination of the results of the analysis showed that no penetration occurred between the two surfaces.

All contact problems require the use of an effective stiffness between the two contact surfaces. The amount of penetration between the two surfaces depends on this stiffness. Higher stiffness values decrease the amount of penetration but can lead to convergence difficulties. Ideally, the stiffness should be high enough to give acceptably small contact

penetration, but also low enough such that the problem will be well-behaved in terms of convergence or matrix ill-conditioning (ANSYS, 2001). In ANSYS the two most important real constants are the normal contact stiffness *FKN* and the penetration tolerance *FTOLN*. Determining a good stiffness value requires some experimentation. To arrive at a 'good' stiffness value, the following procedure has been developed (ANSYS, 2001):

1. Use a low value to start. In general, it is better to underestimate this value rather than overestimate it.
2. Run the analysis up to a fraction of the final load (just enough to get the contact fully established).
3. Check the penetration and the number of equilibrium iterations used in each substep.
4. Adjust *FKN* or *FTOLN* as necessary, and run the full analysis.

According to the above procedure, the scaled real contact stiffness factor *FKN* was determined as 1 and the scaled contact tolerance factor *FTOLN* as 0.02 in this case. The other real constants have less effect and thus it is more straightforward to determine acceptable values. The radius *PINB* of the 'Pinball' region was 1 and the initial closure factor *ICONT* was 0.03 respectively.

4.2.3 Comparison of results

Table 4.2 shows the variation of the maximum radial stress in the substrate as well as the comparison of the maximum radial stress between FEA and theory. It is shown in Table 4.2 that the relative difference between FEA and theory decreases as the displacement *uz* increases up to 2 μm, then it increases and maintains a constant value of around 18 %.

This reveals that, firstly, the results are dependent on mesh size, i.e. the mesh size is

Table 4.2 The variation of the maximum radial stress σ_r in the substrate

Displacement *uz* μm		0.2	0.3	0.4	0.5	1	2	3	4
σ_r, MPa	Analytical	627.5	768.9	888.2	993.5	1407.4	1995.4	2448.2	2831.4
	FEA	518.5	668.0	813.5	925.5	1367.0	2020.7	2908.7	3341.5
	Relative difference %	17.4	13.1	8.4	6.8	2.9	1.3	18.8	18.0

not appropriate for a small displacement, and secondly, there is a marked discrepancy between FEA and theory when the displacement is equal to, or large than, 3 μm.

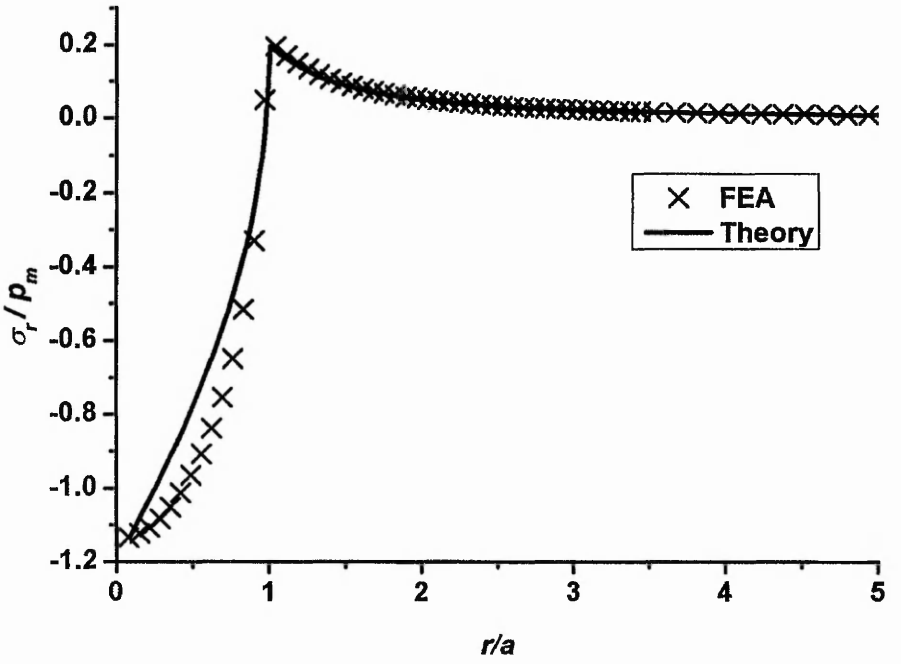

Figure 4.6 Comparison of radial stress in the surface (z=0)
between FEA and Theory when the indentation depth h = 2 μm

By comparing the radial stress in the surface (z=0) between FEA and theory when the displacement uz = 2 μm (Figure 4.6), it can be seen that the radial stress in the surface from FEA agrees well with that from theory outside the contact edge, but there are some discrepancies in the radial stress in the surface between FEA and theory inside the contact edge.

4.3 Coatings

The mechanical surface properties of many materials can be improved by depositing appropriate coatings (Lichinchi, 1998). Frequently, it is required to determine the mechanical properties of the deposited films in situ. In this case the comparison is based on the analysis of the soft impressor method, which has been used to measure the effectiveness of diamond coatings of different thicknesses on a silicon substrate (Fagan Park and Wang, 2000).

4.3.1 Problem description

Figures 4.7 and 4.8 show the model geometry and mesh for the diamond on silicon coating system. A uniform pressure p was applied over a circle of radius a. The coating was assumed to be perfectly bonded to the substrate. Table 4.3 shows the material properties.

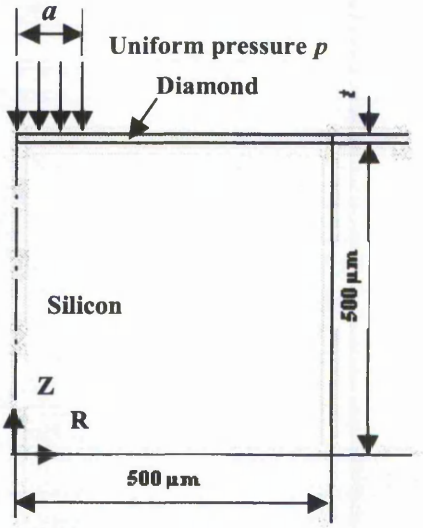

Figure 4.7 Geometry model

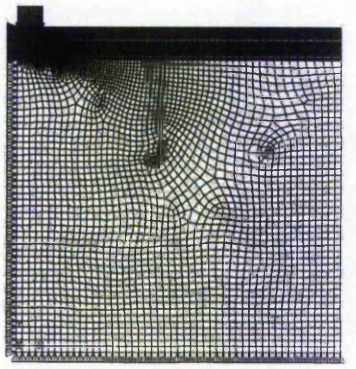

Figure 4.8 FEM model

Table 4.3 Material properties

	Diamond	Silicon
Young's modulus (GPa)	1050	110
Poisson's ratio	0.1	0.2

4.3.2 Comparison of results

Table 4.4 The variation in maximum tensile stress in the diamond with coating thickness

Coating thickness µm	Applied pressure p MPa	Thickness to contact radius ratio	Maximum tensile stress in the diamond coating			Maximum tensile surface stress in the diamond coating		
			σ_1 MPa	σ_1/p		σ_1 MPa	σ_1/p	
				This work	Fagan et al		This work	Fagan et al
0	1600	0	487	0.304	0.322	487	0.304	0.322
2	1630	0.05	1931	1.185	1.114	1931	1.185	1.114
3.5	2740	0.09	3127	1.141	1.088	3127	1.141	1.088
12	3470	0.3	2911	0.839	0.77	2739	0.789	0.746
22	6160	0.56	7349	1.193	1.114	2751	0.446	0.486
48	8000	1.22	5983	0.748	0.743	669	0.0836	0.143
90	8000	2.28	2584	0.323	0.3	1269	0.159	0.286

Figure 4.9 shows the variation of maximum tensile stress to applied pressure ratio with coating thickness to contact radius ratio in the diamond coating. Table 4.4 presents the

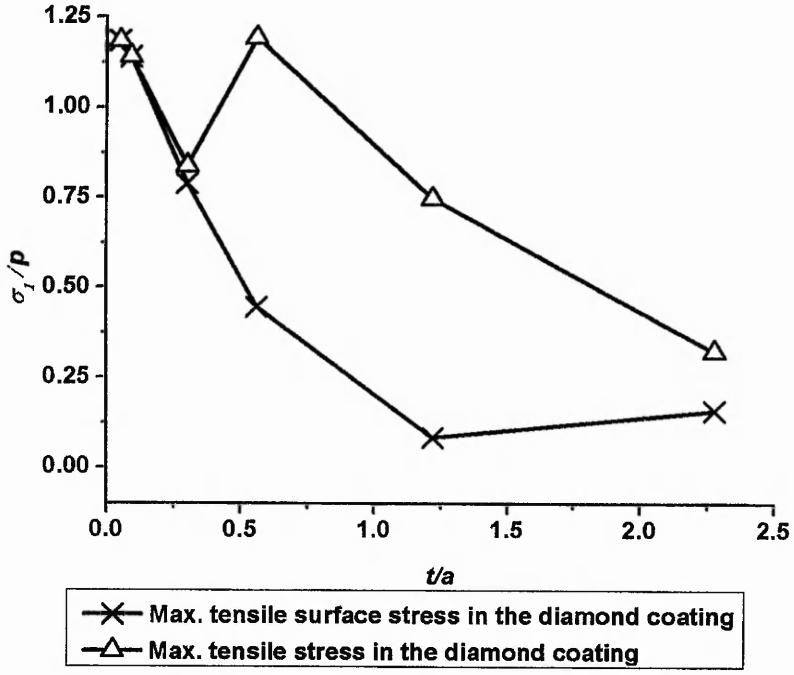

Figure 4.9 Maximum tensile stress to applied pressure ratio with coating thickness to contact radius ratio

variation in the maximum tensile stress in the diamond with coating thickness as well as the comparison of σ_1 / p between this work and Fagan, Park and Wang (2000). The results generally show reasonably good agreement, except for the maximum tensile surface stress for the thicker coatings.

4.4 Summary

Three basic problems, i.e. i) the problem of an elastic half-space subjected to uniform pressure over a circular area; ii) the Hertzian contact problem; iii) the stress analysis of a coated substrate, were calculated in this chapter using ANSYS in order to ensure the correctness of the finite element modelling implemented in this work.

1) From the analysis of an elastic half-space subjected to uniform pressure over a circular area, it was found that element plane 182 with enhanced strain integration option gave the most satisfactory results.
2) The Hertzian contact problem was used to find appropriate contact parameter values for the FEA.
3) The coating analysis results are consistent with those of Fagan, Park and Wang (2000).

CHAPTER 5
FE MODELLING OF RIGID INDENTATION HARDNESS

FEM modelling can be used to quantitatively estimate material hardness and evaluate the deformation properties, such as elasto-plastic deformation and creep, of materials. In order to establish a reliable and effective FEM indentation model, some relevant factors, such as mesh size, model size, friction coefficient, applied load, indenter tip radius, indenter angle, indenter rigidity, etc., were investigated using a 2D axisymmetric FEM model in most cases. In addition, the effect of the material properties of the substrate was studied. Subsequently, the loading behaviour, and the unloading behaviour, were investigated based on five materials. Following from these analyses, a method to extract the elastic modulus was proposed. This is followed by a comparison between a 2D model and 3D model. Finally, a dimensional analysis of the relationships between H/E^*, W_p/W_{tot} and h_f/h_m was implemented.

5.1 Geometry and FEM model

A 2D axisymmetric model was used to enable the analyses to be performed with a sufficiently refined mesh adjacent to the indenter. The indenter was modelled as a sharp, rigid cone with semi-apical included angle of 70.3°. This is a good representation for Vickers and Berkovich indentation hardnesses (Lichinchi et al, 1998; Carlsson and Larsson, 2001). The simulations were carried out with commercial software, ABAQUS, based on conventional J_2 plasticity theory. The FE model is shown in Figure 5.1. The radius and the height of the substrate are both 1000 μm. The axisymmetric element type used here is CAX4I, which is the 4-node bilinear element with incompatible mode. The substrate mesh was very fine in the contact region (Figure 5.2). It was specially refined at the contact edge, since the deformation of the mesh at this point would obviously influence the precision of hardness and stresses. A surface-to-surface contact pair was established between the indenter and the substrate. For the tangential behaviour, the penalty friction formulation was used; for the normal behaviour, the augmented Lagrange formulation was used. The friction coefficient was taken as 0.5 unless otherwise specified. The bottom line ($z = 0$) of the substrate was constrained along the radial and axial directions, i.e. R and Z respectively, and the axisymmetric line ($r = 0$)

was constrained in the radial direction only. A force load or displacement load was applied on the reference point of the rigid indenter.

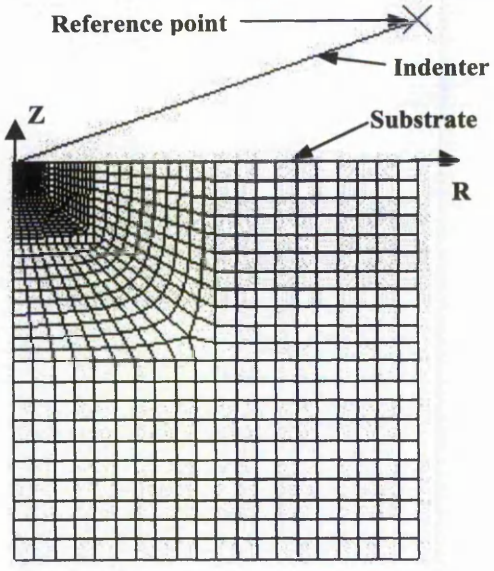

Figure 5.1 FE model

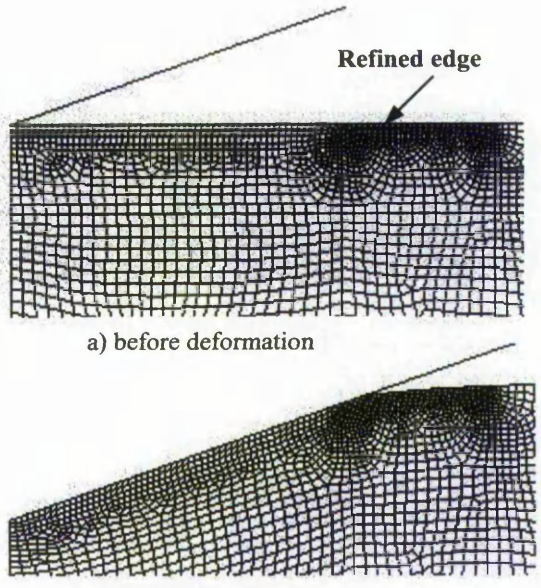

a) before deformation

b) after deformation

Figure 5.2 Detail of the contact edge

5.2 Material properties

The indenter was assumed to be rigid. Two typical materials, i.e. EN08 steel and single crystal MgO, have been used to define the material properties of the substrate.

5.2.1 En08

The En08 steel is described by an elasto-plastic multilinear isotropic hardening deformation behaviour. The true stress vs. true strain curve was derived from a uniaxial tensile test, Figure 5.3 (Ren, 2001). Its initial yield stress is 625.2 MPa. The Young's

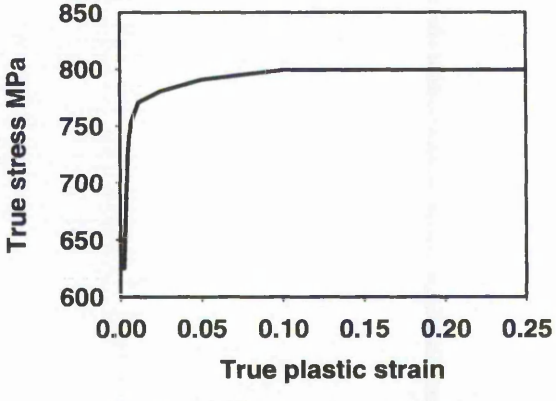

Figure 5.3 The experimental true stress vs. true plastic strain curve for En08

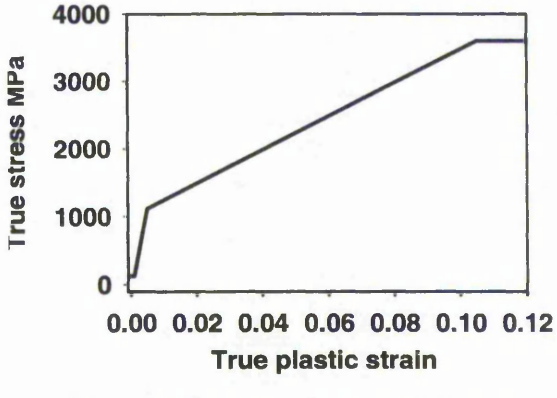

Figure 5.4 The assumed true stress vs. true plastic strain curve for MgO (see section 6.1.2)

modulus and the average Vickers hardness value of the substrate are 206 GPa and 2450 MPa respectively. The Poisson's ratio is 0.3.

5.2.2 MgO

The elastic modulus and Poisson's ratio for single crystal MgO (001) <100> were 248 GPa and 0.23 respectively (*cf* Table 6.2). The indentation hardness test has been used to obtain information concerning the plastic deformation behaviour of ceramics and ultrahard materials, since it is generally not possible to test these in conventional uniaxial tensile or compressive tests. Magnesium oxide has been used for many studies on indentation behaviour since the dislocation patterns can be revealed by etch pitting. A force load, F_Z = -3.13N, was applied on the indenter for the MgO indentation modelling in this chapter unless otherwise specified. The experimental values and physical reasoning concerning the details of the MgO stress strain curve (Figure 5.4) are described in detail in section 6.1.2.

5.3 Effect of FE variables

5.3.1 Element size

Different element sizes were investigated to determine a suitable mesh geometry. Table 5.1 presents the results from a selection of the mesh geometries that were evaluated. The substrate material model was En08. A sharp rigid indenter was used with a final applied displacement of 0.12 mm. The convergence criteria were also varied to determine appropriate values which gave consistent values for the parameters presented in Table 5.1. The number of elements refers to the number of elements in the high mesh density region, *cf* Figure 5.1. As can be seen from Table 5.2 the hardness values for the final three meshes give values for the standard deviations which are ~1% of the average values, which is considered to be very good agreement. The values for the maximum equivalent stress are also very consistent. The parameter for which there is the greatest variation is the maximum principal stress, σ_1. It was found that not only the value for this parameter, but also its location, were dependent on the mesh geometry. Therefore, overall consideration of the results leads to the conclusion that the most reasonable mesh method is to use a medium mesh density and refine the mesh around the point at the edge of contact under full load.

Table 5.1 Mesh size influence (En08 substrate)

Local mesh number of elements		1200	4800	7500	10800	5026 (refined edge)
Local mesh size μm		6.25	3.125	2.5	2.1	3.07 (0.347, around edge)
Under load	Max. σ_{eqv} MPa	795	797.6	798	798	797
	Max. σ_1 MPa	230	234	239	244	353
	Location of max. σ_1	r = 82 μm z =-33 μm	r = 77 μm z =-30 μm	r = 78 μm z =-30 μm	r = 79 μm z =-30 μm	edge
	H_{IT} MPa	2122	2513	2415	2357	2393
	HM MPa	2453	2729	2637	2592	2585
Unloaded	Max. σ_{eqv} MPa	789	786	791	791	794
	Max. σ_1 MPa	275	326	401	404	424
	Location of max. σ_1	edge	edge	edge	edge	edge
	H_{IT} MPa	2106	2486	2396	2338	2372
	HM MPa	2662	2912	2885	2831	2823

Note: σ_{eqv} is the Von Mises effective stress, and σ_1 is the first principal stress.

Table 5.2 Average and standard deviations of the relevant parameters for the last 3 columns

Parameter	Loading Condition	Average of last 3 Columns	Standard Deviation
Max. σ_{eqv} MPa	under load	798	1
	unloaded	792	2
Max. σ_1 MPa	under load	(353)*	
	unloaded	410	13
H_{IT} MPa	under load	2388	29
	unloaded	2369	29
HM MPa	under load	2605	28
	unloaded	2846	34

* This value is taken from the final column only

5.3.2 Comparison between ABAQUS and other commercial FE software

There are several commercial FE packages. Attempts were made to analyse this indentation problem using ABAQUS and ANSYS plus also MSC.MARC, ADINA, and LSDYNA. The three latter programs were found to be generally inappropriate for the

range of analyses considered in this thesis. Thus, a detailed comparison between ABAQUS and ANSYS was undertaken. Table 5.3(a), based on the model described in sections 5.1, 5.2 and 5.3.1 with En08 as the substrate, shows values for selected parameters as examples to demonstrate that many of the FE results are very similar for ABAQUS and ANSYS, when using the same model.

Table 5.3(a) Comparison between ANSYS and ABAQUS

	Under load		Unloaded	
	ABAQUS	ANSYS	ABAQUS	ANSYS
Displacement mm	0.12	0.12	0.12	0.12
Resultant force N	9.6509	9.6609	-	-
Contact radius mm	0.03588	0.03587	0.03604	0.03603
Piling-up height mm	0.8488e-3	0.8349e-3	0.001299	0.001287
H_{IT} MPa	2385	2390	2365	2369

Table 5.3(b) Comparison between ANSYS and ABAQUS

	Displacement μm	10	20	30	40	50	60	70	80
ANSYS (Results-1)	Max. σ_1 MPa	891	543	886	490	906	434	916	501
ANSYS (Results-2)	Max. σ_1 MPa	838	1507	1425	1007	1172	1249	1327	1533
ABAQUS	Max. σ_1 MPa	1398	1307	1221	1106	1210	1398	1246	1261

Table 5.3(c) Flow stress vs. total strain data used for Results-1 (ANSYS) for MgO

Flow Stress MPa	Total Strain
124	0.0005
124.5	0.0015
1116.5	0.0055
3596.5	0.1055

In Table 5.3(b), where MgO was used as the substrate, the same plastic material model (*cf* Figure 5.4 and Table 5.3c) was used for Results-1 (ANSYS) and ABAQUS. The results in Table 5.3(b) show that the calculated values for the maximum principal stress from ANSYS (results-1) exhibit a much greater variation than the values calculated by ABAQUS.

Table 5.3(d) Results from a uni-axial constant pressure model using ANSYS†

Applied pressure MPa		124	124.5	1116.5	1141.3	3596.5
Calculated Equivalent Stress MPa		124	124.5	1116.5	1141.3	3596.5
Material model (Table 5.3(c))	Equivalent total strain	0.0005	0.0015	0.0312‡	-	0.1055
Modified material model	Equivalent total strain	0.0005	0.0015	0.00638‡	0.0065	0.1055

† ANSYS 5.7 to ANSYS 9.0

‡ These values should be equal to 0.0055.

This was investigated further by considering a simple uniaxial constant pressure compression model. When using the plastic material model as shown in Table 5.3(c) in ANSYS, the calculated stress-strain data were found to be inconsistent with the inputted material constitutive model; an example of which is shown in Table 5.3(d). These results were not expected and are obviously incorrect in part. The equivalent analysis in ABAQUS gave calculated stress-strain data which were consistent with the inputted material model. When an additional data point, i.e. (0.0065, 1141.3), which is very close to the data point (0.0055, 1116.5), was interpolated between the two adjacent stress-strain data points, i.e. (0.0055, 1116.5) and (0.105, 3596.5), this discrepancy can be controlled to a tolerable extent as shown by the strain values in the modified material model row in Table 5.3(d). In table 5.3(b), the results shown in the row designated ANSYS (Results-2), which were obtained using the modified material model, give much closer results to those from ABAQUS than the original material model, i.e. ANSYS (Results-1). A similar problem was also encountered in ANSYS for En08 with the last few material data points, possibly as a consequence of their work hardening rates being relatively low.

This would suggest that the results from ABAQUS are more robust. Therefore ABAQUS was selected as the preferred FE package, although a substantial amount of modelling was also undertaken in ANSYS prior to ABAQUS being available for use by the author.

5.4 Effect of indenter angle

Five different indenter angles, i.e., 60°, 68°, 70.3°, 75°, and 80°, were studied. The material used for the substrate was the En08 steel. The value of Y/E for En08 is 0.003. The stress vs. strain curve for this material cannot be described by a single power law equation, e.g. Equation (2.19). The work hardening exponent is about 0.16 when the

strain is less than 0.0097. When the strain is greater than 0.0097, the work hardening exponent is about 0.01.

The FE model parameters are the same as those described in section 5.3.1. The displacement load method was used. Table 5.4 shows that H_{IT} decreases gradually, whereas HM increases very markedly, when the indenter angle increases from 60° to 80°. The hardness that is generally discussed in the literature is the Indentation Hardness, i.e., H_{IT}.

It can be seen from these results that although the FEA H_{IT} and Johnson's hardness values have generally the same form, there is a significant difference in the actual values. The results based on the analysis of Cheng and Li (2000) appear to be very different. These results would indicate that it is not possible to use a simplified equation to predict quantitatively the variation of hardness with indenter angle. It is also of interest to note that the FEA results give a value of $H/Y = 3.9$, which is very close to the 'rule-of-thumb' estimate for steels of $H/Y = 4$.

Table 5.4 Influence of indenter angle on calculated hardness

Cone semi-angle	Present FEA				Analytical	
	HM MPa		H_{IT} MPa		H_{IT} MPa	
	under load	unloaded	under load	unloaded	Johnson (1970)	Cheng and Li (2000)*
60	1103	1171	2448	2430	2146	1438
68	2107	2326	2447	2428	1998	
70.3	2611	2915	2442	2421	1947	1998
75	4345	5004	2415	2396	1826	
80	8918	10838	2335	2318	1652	2128

* The values for Cheng and Li require interpolation from graphical figures presented in their paper, and are thus relatively imprecise.

5.5 Model size effect

In this section, the FE model was based on that described in sections 5.1, 5.2 and 5.3.1, with the exception that the overall model size was varied. The ratio of width:height was maintained as 1. Tables 5.5 and 5.7 show that the model size has only limited influence on the calculated hardness values, especially when the model size is more than 20 times the indentation depth. However, Tables 5.6 and 5.8 show that the model size has a marked influence on the calculated elastic modulus (the method for calculating the elastic modulus is described in detail in section 5.13). The relative error in the

calculated elastic modulus is less than 5% when the ratio of the model size to the indentation depth is greater than 50. These results show that a model size of more than one hundred times the indentation depth is required to give accurate elastic modulus values, and would suggest that experimentally tested specimens should also have a thickness of more than one hundred times the indentation depth.

Table 5.5 The influence of model size on the calculated hardness of En08

Model size / Indentation depth		10	20	30	50	100	333
Model size μm		30	60	90	150	300	1000
Under load	*HM*	2437	2566	2596	2604	2617	2611
	H_{IT}	2381	2452	2437	2442	2449	2442
Unloaded	*HM*	2654	2848	2895	2915	2938	2917
	H_{IT}	2363	2431	2416	2421	2428	2421

Table 5.6 The influence of model size on the calculated elastic modulus of En08

Model size / Indentation depth	10	20	30	50	100	333
Model size μm	30	60	90	150	300	1000
Calculated Elastic Modulus GPa	262	231	223	215	211	206
Relative difference %	27.3	12.2	8.05	4.54	2.39	3.24e-3

Table 5.7 The influence of model size on the calculated hardness of MgO

Model size / Indentation depth		10	20	30	50	100	333
Model size μm		30	60	90	150	300	1000
Under load	*HM*	4978	4974	4984	4982	4995	4965
	H_{IT}	7355	7445	7472	7480	7499	7473
Unloaded	*HM*	6060	6212	6276	6312	6340	6328
	H_{IT}	7180	7259	7283	7290	7307	7282

Table 5.8 The influence of model size on the calculated elastic modulus of MgO

Model size / Indentation depth	10	20	30	50	100	333
Model size	30	60	90	150	300	1000
Calculated Elastic Modulus GPa	275	272	263	256	253	249
Relative difference %	10.8	9.86	6.12	3.15	2.03	0.375

Various ratios of the model size to the indentation depth have been used in the published papers concerned with FE modelling of hardness and elastic modulus (Table 5.9). From the present results, Tables 5.5 and 5.7, a model size of more than 20 times

the indentation depth is needed to give acceptable hardness values, and for elastic moduli the ratio is closer to 100 times. As can be seen from Table 5.9 there are a number of studies in which the model size:indentation depth ratio may not be sufficient to give good results. Moreover, the effect of the model size on the calculated elastic modulus does not appear to have been investigated to date in the literature.

Table 5.9 Model sizes used in some published papers

Reference	Model size / Indentation depth
Bolzon et al, 2004	6.25
Bucaille & Felder, 2002	10
Ning et al, 2004	22
Murakami & Matsuda, 1994	34
Cheng & Cheng, 1999	35
Strange & Varshneya, 2001	50
Giannakopoulos et al, 1994	50
Marx & Balke, 1997	139
He & Veprek, 2003	200
Hay et al, 1999	2060

5.6 Indentation size and indenter tip radius effect

In all the situations considered in the preceding sections in this chapter the indenter has been modelled as sharp. However, in practice all real indenters will have a radius at their tip. Therefore it is of interest to model an indenter with a tip radius to investigate if it affects the results. The model and mesh geometries where the same as outlined previously, sections 5.1, 5.2 and 5.3.1, with the exception that a range of tip radii from 0 to 3 μm were analysed. Tables 5.10 and 5.11 show the results for En08 and MgO respectively. It can be noted that *HM* increases markedly with an increase in the indenter tip radius, although the effect becomes less significant as the indentation depth increases, whereas H_{IT} is hardly affected. The significance with regard to experimental work is that in practice the reported values for *HM* will generally be higher than the true value, whereas the H_{IT} values should be close to the actual material value.

Tables 5.10 and 5.11 also show when the indenter tip radius equals zero, there is no indentation size effect for both Martens hardness *HM* and Indentation Hardness H_{IT}.

Table 5.10 Effect of indentation depth and indenter tip radius on the hardness of En08

Indentation depth μm	Hardness		Tip radius μm			
			0	1	2	3
1	*HM*	Under load	2610	2939	3291	3679
		Unloaded	2896	3285	3706	4172
	H_{IT}	Under load	2459	2457	2437	2444
		Unloaded	2441	2439	2418	2425
2	*HM*	Under load	2617	2782	2949	3124
		Unloaded	2913	3111	3310	3520
	H_{IT}	Under load	2441	2443	2442	2444
		Unloaded	2422	2423	2422	2424
3	*HM*	Under load	2613	2723	2833	2944
		Unloaded	2919	3035	3166	3300
	H_{IT}	Under load	2442	2444	2444	2443
		Unloaded	2422	2424	2424	2423
4	*HM*	Under load	2697	2698	2782	2866
		Unloaded	2907	3019	3118	3217
	H_{IT}	Under load	2441	2439	2441	2441
		Unloaded	2421	2419	2421	2421

Table 5.11 Effect of indentation depth and indenter tip radius on the hardness of MgO

Indentation depth μm	Hardness		Tip radius μm			
			0	1	2	3
1	*HM*	Under load	5016	5655	6333	7040
		Unloaded	6288	7176	8168	9229
	H_{IT}	Under load	7461	7542	7520	7494
		Unloaded	7274	7355	7335	7310
2	*HM*	Under load	5019	5335	5661	5996
		Unloaded	6307	6704	7200	7670
	H_{IT}	Under load	7488	7479	7472	7464
		Unloaded	7301	7295	7288	7280
3	*HM*	Under load	5017	5231	5446	5662
		Unloaded	6297	6561	6880	7188
	H_{IT}	Under load	7459	7460	7457	7451
		Unloaded	7274	7276	7273	7267
4	*HM*	Under load	5018	5175	5335	5498
		Unloaded	6300	6495	6737	6964
	H_{IT}	Under load	7477	7470	7470	7470
		Unloaded	7291	7283	7283	7283

When the indenter tip radius equals 1, 2 or 3 μm respectively, H_{IT} still exhibits no indentation size effect; however, *HM* has a marked indentation size effect. The larger

the indenter tip radius is, the more significant is the indentation size effect in *HM*. The effect of the indenter tip radius on H_{IT} is similar to the conclusion drawn by Lu and Bogy (1994), i.e. the hardness values obtained using indenters with a nonzero tip radius present a weak tip effect and indentation size effect. Xue et al (2002) concluded that the effect of indenter tip radius on indentation hardness disappears once the contact radius exceeds one half of the indenter radius. In the present investigation, the minimum ratio of the contact radius to the indenter radius is equal to 0.93 for MgO, when the indenter radius is 3 μm and the indentation depth is 1 μm. Thus the conclusion of the present study with regard to the effect of the indenter tip radius on H_{IT} is consistent with Xue et al (2002). For the results presented above, H_{IT} exhibits no indentation size effect, which is different from the findings of Xue et al (2002). These authors have proposed that the reason for this is that classical continuum plasticity theory, which was used in the present modelling, cannot explain the observed indentation size effect (Xue et al, 2002).

5.7 Effect of Friction coefficient

5.7.1 Effect of friction coefficient on deformation

(a) friction coefficient μ=0 (b) friction coefficient μ=0.5

Figure 5.5 Effect of friction coefficient on deformation for En08

The effect of the value of friction coefficient is considered in this section. The model used is the same as that described in section 5.3.1, except for the variation in friction coefficient.

Figure 5.5(a) shows that the elements in the vicinity of the indenter tip for a friction coefficient $\mu = 0$ are highly deformed. This very severe distortion is highly localized and is unlikely to affect non-localised parameters such as the total applied force or the hardness estimates, or localized parameters, such as the stresses, at positions away from the tip region, but it will probably have a significant influence on the values of stress etc. in this vicinity. The calculated values of stresses, for example, from the elements close to the indenter tip would not be considered to be reliable. When $\mu = 0.5$, the

elements in the same region maintain a more regular shape during the whole indentation process.

As noted above, section 2.6, most FE analyses are undertaken assuming frictionless contact. Where figures showing the deformed mesh have been presented (e.g. Mata and Alcalá, 2004) similar highly localized deformation to that shown in figure 5.5(a) is apparent.

5.7.2 Effect of friction coefficient on hardness

Tables 5.12 and 5.13 show that, for En08, the Martens Hardness *HM* is larger than Indentation Hardness H_{IT}; whereas, for MgO, the Martens Hardness *HM* is smaller than Indentation Hardness H_{IT}. This is because, for EN08, the Martens Hardness does not take into account the pile-up in the En08 substrate at the edge of the indentation. Thus the apparent hardness of the substrate will be an overestimate. On the other hand for MgO, the Martens Hardness does not take into account the sinking-in in the MgO substrate at the edge of the indentation. This will result in an underestimate for the Martens Hardness of the substrate. Tables 5.12 and 5.13 show that the friction coefficient has little influence on the Martens Hardness. However, it has a noticeable influence on the Indentation Hardness for two friction coefficient zones, i.e. a low friction coefficient zone [0 - 0.1] and a high friction coefficient zone [0.1 - 0.5].

5.7.3 Effect of friction coefficient on the normal contact pressure

The friction coefficient has a marked influence on the distribution of the contact pressure (Figures 5.6 and 5.7). For En08, the contact pressure decreases linearly from the central region to the contact edge when the friction coefficient $\mu = 0$; whereas it increases sharply first from the central region, then is almost constant towards the contact edge when $\mu = 0.5$ (Figure 5.6). For MgO, when $\mu = 0$ the contact pressure decreases gradually first from the central region, then is almost constant toward the contact edge; finally it increases gradually; whereas when $\mu = 0.5$ it increases initially rapidly from the central region, and then increases more gradually towards the contact edge (Figure 5.7).

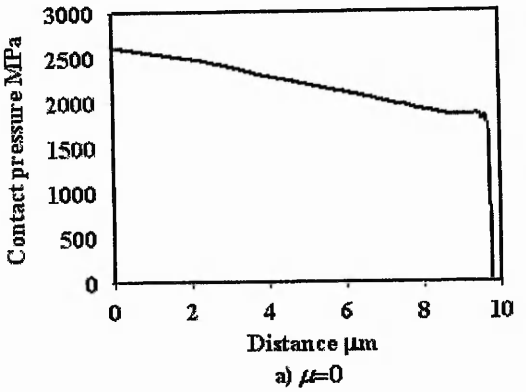

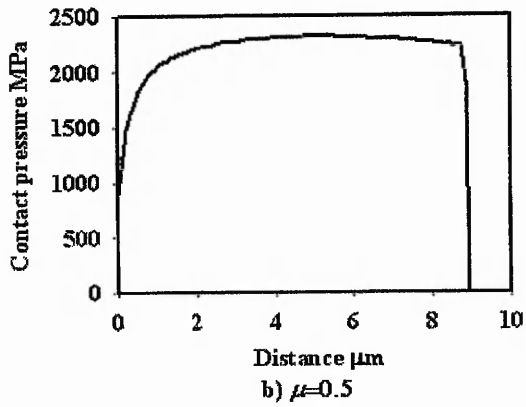

Figure 5.6 Contact pressure distribution of EN08

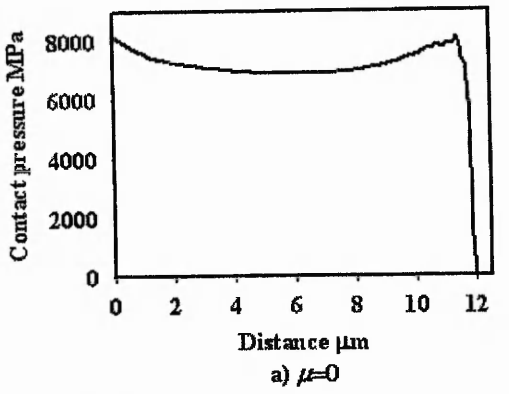

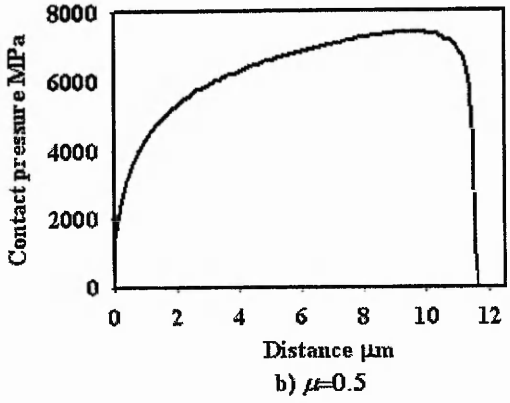

Figure 5.7 Contact pressure distribution of MgO

Table 5.12 Effect of friction coefficient on hardness (EN08)

Friction coefficient		0	0.1	0.2	0.3	0.4	0.5
HM MPa	under load	2613	2647	2583	2580	2579	2579
	unloaded	2930	2983	2905	2900	2899	2899
H_{IT} MPa	under load	2088	2339	2428	2462	2463	2463
	unloaded	2079	2324	2407	2440	2441	2441

Table 5.13 Effect of friction coefficient on hardness (MgO)

Friction coefficient		0	0.1	0.2	0.3	0.4	0.5
HM MPa	under load	4972	4987	4968	4966	4965	4965
	unloaded	6235	6340	6360	6332	6328	6328
H_{IT} MPa	under load	7237	7473	7468	7473	7473	7473
	unloaded	7122	7322	7287	7283	7283	7282

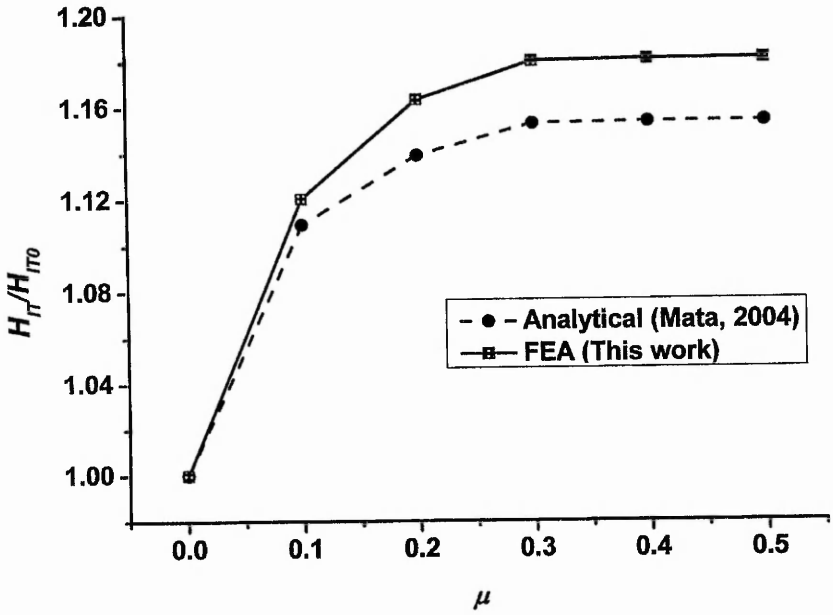

Figure 5.8 Comparison of effect of friction coefficient on H_{IT} for En08 between FEA and theory

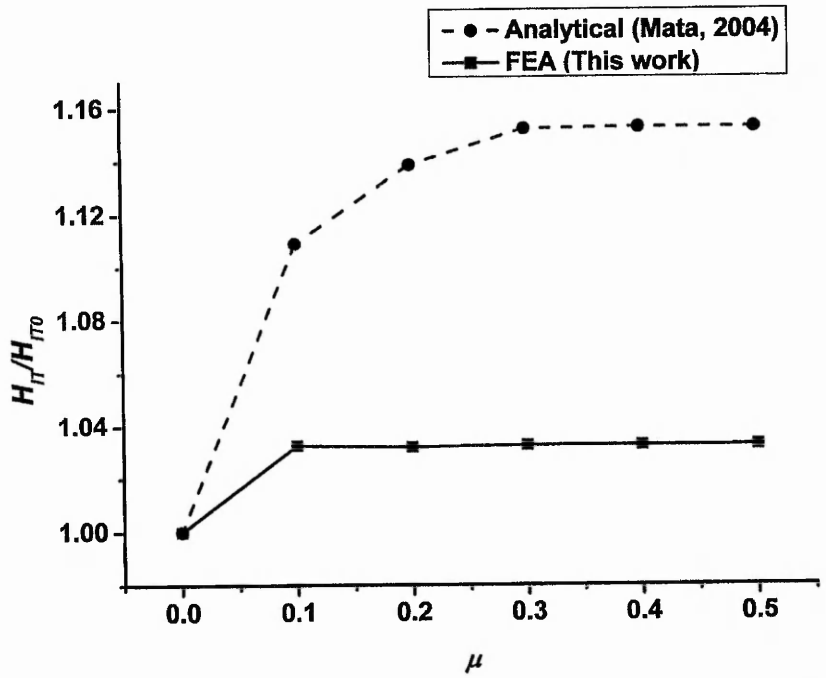

Figure 5.9 Comparison of effect of friction coefficient on H_{IT} for MgO between FEA and theory

Figures 5.8 and 5.9 show a comparison of the effect of friction coefficient on H_{IT} between the present FEA data and the analytical results of Mata (2004) for En08 and MgO respectively. In both cases the trends in the FEA and analytical results are consistent, i.e. H_{IT} increases with increasing friction coefficient up to a value of 0.2-0.3,

and then it becomes constant as the friction coefficient is increased further. For En08, the actual numerical values of the results from the FEA agree quite well with those from the analytical analysis (Mata, 2004). However, for MgO, the results have a more significant discrepancy between the numerical values for the FEA and the analytical analysis (Mata, 2004), which may not be surprising since the analytical analysis was developed for metallic materials.

5.7.4 Effect of friction coefficient on the maximum first principal stress

Table 5.14 The effect of friction coefficient on the maximum 1st principal stresses outside the contact edge for En08

Friction coefficient		0	0.1	0.2	0.3	0.4	0.5
Maximum 1st principal stress just outside the contact edge	under load	295	368	489	585	556	557
	unloaded	710	567	505	561	572	566

Table 5.15 The effect of friction coefficient on the maximum 1st principal stresses inside the contact edge for En08

Friction coefficient		0	0.1	0.2	0.3	0.4	0.5
Maximum 1st principal stress just inside the contact edge	under load	-948	-1135	-1317	-1482	-1508	-1505
	unloaded	324	288	93	80	89	136

Table 5.16 The effect of friction coefficient on the maximum 1st principal stresses outside the contact edge for MgO

Friction coefficient		0	0.1	0.2	0.3	0.4	0.5
Maximum 1st principal stress just outside the contact edge	under load	4023	1035	1600	1690	1675	1699
	unloaded	982	789	751	741	716	666

Table 5.17 The effect of friction coefficient on the maximum 1st principal stresses inside the contact edge for MgO

Friction coefficient		0	0.1	0.2	0.3	0.4	0.5
Maximum 1st principal stress just inside the contact edge	under load	-60	-231	-338	-772	-671	-620
	unloaded	1253	1552	1774	1721	1752	1780

The first principal stress is an important factor with regard to the fracture behaviour of brittle materials. Tables 5.14 to 5.17 show the effect that the friction coefficient has on the maximum 1st principal stress values in the substrates, both under full load and after unloading, for En08 and MgO both outside, but close to the contact edge, and within the contact zone, respectively.

For En08, Tables 5.14 and 5.15 show that the maximum 1st principal stress occurs outside the contact edge. The maximum tensile value occurs in the frictionless case just outside the contact zone. As the friction coefficient increases the values converge. The values under load increase with increasing friction coefficient until it reaches 0.3, whereas for the unloaded case the value decreases between 0 and 0.1, and then remains reasonably constant. Tables 5.16 and 5.17 show that for MgO the maximum 1st principal stress occurs for friction coefficient values greater than 0.1 inside the contact edge when unloaded. However, the maximum 1st principal stress values outside the contact edge when under load, for friction coefficients greater than 0.2, are also high, and very close to the highest values shown in Table 5.17.

Overall, it can be seen that there appears to be basically two regimes of friction coefficient values affecting the maximum 1st principal stress values. For high friction coefficients, i.e. 0.2 and above, the values are generally independent of the friction coefficient. For lower friction values, the results are generally quite different from the high friction values and would generally be affected by the friction coefficient value.

The other conclusion that can be drawn is that for En08, where pile-up occurs, the maximum 1st principal stress occurs when $\mu = 0$, whereas for MgO it occurs when $\mu > 0.2$. Further studies would be required to determine if this observation holds in general.

5.8 Effect of indenter rigidity

In this case, the indenter was modelled with a sharp tip as either a rigid body, an elastic solid, or an elasto-plastic solid. For En08, the elastic modulus and Poisson's ratio of the indenters were 206 GPa and 0.3 respectively. For MgO, two types of elastic indenters were used, one with an elastic modulus of 1141 GPa and Poisson's ratio of 0.07, which corresponds to a diamond indenter, and the other with an elastic modulus of 366.9 GPa and Poisson's ratio of 0.22, which correspond to the elastic properties of TiB2. In this section, the ratio of the indentation hardness of the indenter to that of the corresponding substrate was termed the Hardness Ratio. Three types of elasto-plastic indenters, with different Hardness Ratios, were used for En08 and MgO respectively (Tables 5.18-5.21).

For the cases with hardness ratios of 1.5 and 2, elastic perfectly plastic material models were assumed for the elasto-plastic indenters. The indentation hardness values for the substrates were 2428 MPa for En08 and 7468 MPa for MgO (Tables 5.12 and 5.13). The friction coefficient was assumed to be 0.2. Thus, the yield stresses for the elasto-plastic indenters can be calculated from Equation (5.2). For the case with hardness ratio = 1, the indenter and the substrate have the same material properties. The mesh for the flexible indenters is similar to, but slightly coarser than, the one for the soft impresser as described in section 9.2.1.2. The other details of the analysis are as described in sections 5.1, 5.2 and 5.3.1.

5.8.1 Effect of indenter rigidity on calculated hardness

Table 5.18 The effect of indenter rigidity on calculated hardness for En08

Indenter	Rigid	Elastic	Elasto-plastic	Elasto-plastic	Elasto-plastic
Elastic modulus of the indenter GPa	∞	206	206	206	206
Hardness ratio	∞	∞	2	1.5	1
H_{IT} MPa	2442	2450	2450	2447	2108

Table 5.18 shows that when the hardness ratio is greater than 1.5, the indenter rigidity has no effect on the calculated indentation hardness. When the hardness ratio is equal to 1, the calculated indentation hardness is about 14% lower than that for the rigid indentation case. In addition, it should be noted that in this case the indenter itself underwent substantial plastic deformation.

Table 5.19 The effect of indenter rigidity on calculated hardness for MgO

Indenter	Rigid	Elastic_1	Elastic_2	Elasto-plastic	Elasto-plastic	Elasto-plastic
Elastic modulus of the indenter	∞	1141	366.9	366.9	366.9	248
Hardness ratio	∞	∞	∞	2	1.5	1
H_{IT} MPa	7471	7452	7226	7226	7095	5295

Table 5.19 shows that for MgO, the indenter rigidity has a comparatively more marked effect on the calculated indentation hardness. For the case with hardness ratio = 1, the indenter deformed plastically and the calculated indentation hardness is substantially lower than that for the rigid indentation case. When the hardness ratio is equal to 1.5,

the indenter still deformed plastically to some extent and the calculated indentation hardness is about 5% lower than that for the rigid indentation case. For the case with hardness ratio = 2, the indenter exhibits virtually no plastic deformation (except for two elements around the indenter tip) and the calculated indentation hardness is still about 3.3% lower than that for the rigid indentation case. This is as a result of the elastic deformation of the indenter, since it is equal to the value from the elastic indenter case with the same elastic modulus. Only in the elastic indenter case with the same material properties as a diamond, can the equivalent indentation hardness value be obtained as that for the rigid indentation case.

5.8.2 Effect of indenter rigidity on calculated elastic modulus

In section 5.13, the revised method determined in the present investigation for calculating the elastic modulus is described in detail for the rigid indentation case. For the deformable indenters, Equation (5.17) can be written as

$$E_r = S_c /(2\gamma_h R_c) \tag{5.1}$$

where, E_r is the reduced modulus, which is defined as

$$\frac{1}{E_r} = \frac{1-\nu^2}{E} + \frac{1-\nu_i^2}{E_i} \tag{5.2}$$

where E and E_i, and ν and ν_i represent respectively the Young's moduli and the Poisson's ratios of the materials of the indenter and the substrate.

Table 5.20 The effect of indenter rigidity on calculated elastic modulus for En08

Indenter	Rigid	Elastic	Elasto-plastic	Elasto-plastic	Elasto-plastic
Elastic modulus of the indenter	∞	206	206	206	206
Hardness ratio	∞	∞	2	1.5	1
γ_h	1.07104	1.022	1.022	1.022	1.022
E GPa	205.2	205.9	205.9	205.4	205.2

Tables 5.20 and 5.21 show that the indenter rigidity has virtually no effect on the calculated elastic modulus. Thus the method (Equation (5.1)) for calculating the elastic modulus of a material can be extended to the elasto-plastic indenter case, which implies

that the soft impresser technique can also be used to measure the elastic modulus of a material. This will be discussed further in section 9.6.

The results also demonstrated that for the cases with deformable indenters, it is not appropriate to calculate the constant γ_h using Equations (5.18)-(5.20), which were proposed by Hay, Bolshakov and Pharr (1999). In this work, the appropriate values for γ_h, as presented in Tables 5.20 and 5.21, were determined based on the FE indentation modelling for the elastic indenter case. The same value of γ_h was used for all the present elasto-plastic indenter cases.

Table 5.21 The effect of indenter rigidity on calculated elastic modulus for MgO

Indenter	Rigid	Elastic_1	Elastic_2	Elasto-plastic	Elasto-plastic	Elasto-plastic
Elastic modulus of the indenter	∞	1141	366.9	366.9	366.9	248
Hardness ratio	∞	∞	∞	2	1.5	1
γ_h	1.08314	1.05	1.034	1.034	1.034	1.034
E GPa	248.7	248.1	248.0	247.4	246.9	245.6

5.9 Effect of material properties of the substrate

Although, as discussed above, it is not feasible to undertake a parametric study of all the variables involved in modelling indentation hardness, it was considered appropriate to undertake a very limited investigation into the effects of variations in the elastic modulus, yield stress and tangent modulus (using a bilinear isotropic material model) for the substrate. The basic model was as described in sections 5.1, 5.2 and 5.3.1. The Poisson's ratio for the substrate was 0.3 and the friction coefficient was 0.2 in all cases.

5.9.1 Effect of the yield stress

In these analyses, the yield stress was given values of 200, 400 and 625 MPa, with the elastic modulus at 206 GPa, without considering work hardening. Table 5.22 shows that in this case both HM and H_{IT} increase with increasing yield stress. The values calculated for HM are higher when unloaded than loaded, which is expected as a result of the elastic recovery, and the ratio of hardness to yield stress decreases with the increasing yield stress. The values calculated for H_{IT} are essentially the same for both the loaded

and unloaded cases, and the ratio H_{IT}/Y is approximately constant with a value of 3.12 when E/Y varies from 329.6 to 1030. This latter result is consistent with Tabor's experimental observations that for plasticity dominated indentations, the ratio of hardness to yield stress is ~3 (Tabor, 1951).

Table 5.22 The effect of yield stress on calculated hardness

Yield stress Y MPa	200		400		625	
E/Y	1030		515		329.6	
Loading status	under load	unloaded	under load	unloaded	under load	unloaded
HM	808	837	1520	1626	2228	2463
HM/Y	4.04	4.19	3.8	4.06	3.56	3.94
H_{IT}	626	625	1252	1246	1952	1938
H_{IT}/Y	3.13	3.12	3.13	3.12	3.12	3.10

5.9.2 Effect of the tangent modulus

Table 5.23 shows that for a yield stress of 625 MPa and tangent modulus variations between 0 and 625 MPa, the hardness increases with the increasing tangent modulus and thus the ratio of hardness to yield stress increases with the increasing tangent modulus for both HM and H_{IT}.

Table 5.23 The effect of tangent modulus on calculated hardness

Tangent modulus MPa	0		312.5		625	
Loading status	under load	unloaded	under load	unloaded	under load	unloaded
HM	2228	2463	2259	2501	2311	2567
HM/Y	3.56	3.94	3.61	4.0	3.70	4.11
H_{IT}	1952	1938	2111	2094	2236	2217
H_{IT}/Y	3.12	3.10	3.38	3.35	3.58	3.55

5.9.3 Effect of Young's modulus

It can be noted from the results shown in table 5.24 that for an elastic perfectly plastic material model for a range of elastic moduli and yield stresses that when E/Y=constant, H/Y is also constant. Table 5.24 also shows that H/Y increases with increasing E/Y. These results also show that for $E/Y \leq 200$, the value of $H_{IT}/Y < 3.1$.

The following equations can be obtained by regression from the data in table 5.24.

$$\frac{H_{IT}}{Y} = 3.18086 * (1 - 7.12089 * \frac{Y}{E}) \quad \text{when under load} \quad (5.3)$$

$$\frac{HM}{Y} = 0.6822 * (1 + 1.1125 * \ln(\frac{E \tan 19.7^{\circ}}{3Y})) \quad \text{when under load} \quad (5.4)$$

$$\frac{H_{IT}}{Y} = 3.1697 * (1 - 8.44671 * \frac{Y}{E}) \quad \text{when unloaded} \quad (5.5)$$

$$\frac{HM}{Y} = 2.454 * (1 + 0.1595 * \ln(\frac{E \tan 19.7^{\circ}}{3Y})) \quad \text{when unloaded} \quad (5.6)$$

The values for the constants in Equation (5.4) are very close to those proposed by Johnson (1970) for this situation.

Table 5.24 Effect of *E/Y*

E/Y		50		200			666.7	
E GPa		100	200	200	400	600	200	1333.3
Y MPa		2000	4000	1000	2000	3000	300	2000
HM MPa	under load	3942	7885	3222	6443	9666	1178	7852
	unloaded	6311	12623	3755	7511	11266	1242	8282
HM/Y	under load	1.97		3.22			3.93	
	unloaded	3.16		3.76			4.14	
H_{IT} MPa	under load	5435	10870	3089	6178	9268	935	6231
	unloaded	5260	10521	3055	6110	9166	931	6210
H_{IT}/Y	under load	2.72		3.09			3.12	
	unloaded	2.63		3.06			3.10	

5.10 Effect of load application method

If a force load is applied on the indenter, especially for an elastic or elasto-plastic indenter material, then it has been found that small equation solver pivot terms occur and the analysis has considerable difficult in converging at the initial indentation stage. Even if a range of additional FEM solution techniques, e.g. adding a weak spring between the indenter and the substrate, are adopted to eliminate the rigid movement of the indenter, convergence is still difficult to achieve. In this respect it can be noted that most of the previous published papers, *cf* section 2.6, apply a controlled displacement load to the indenter. However, in some cases, e.g. a creep problem, a fixed force load must be used instead of a controlled displacement.

In order to overcome this convergence difficulty problem, the force-displacement load switch method has been implemented, i.e. the displacement is applied to a specified

indentation depth first, which should be large enough to guarantee that there would be no convergence difficulty when the loading method is switched from displacement to force control, then force controlled loading is continued until the maximum load is applied. The solution can be switched back to displacement load control to implement an unloading step if one is required.

5.11 Loading behaviour

Table 5.25 Material properties for Al HE15 (Ref. U, Ref. V), Brass, Steel, and Copper

Al HE15 (Ref. U)	Elastic modulus GPa	70							
	Poisson's ratio	0.33							
	Plastic Strain %	0	1.67	4.69	11.38	13.14	14.81	17.18	
	Plastic Flow Stress MPa	258.88	326.37	389.22	469.21	481.43	489.92	502.53	
Al HE15 (Ref. V)	Elastic modulus GPa	70							
	Poisson's ratio	0.33							
	Plastic Strain %	0	1.129	1.465	4.158	9.188			
	Plastic Flow Stress MPa	414.15	427.42	441.47	485.91	517.81			
Steel (Ref. C)	Elastic modulus GPa	210							
	Poisson's ratio	0.3							
	Plastic Strain %	0	1.739	3.669	5.131	7.054	9.979	12.69	14.04	20.06
	Plastic Flow Stress MPa	212.6	231.1	322.8	363.6	397.3	440.1	472.6	498.2	498.2
Brass 60/40	Elastic modulus GPa	110							
	Poisson's ratio	0.34							
	Plastic Strain %	0	0.7323	3.161	7.682	11.17	16.73		
	Plastic Flow Stress MPa	294.4	296.78	380.07	447.34	483.85	511.07		
Copper	Elastic modulus GPa	124							
	Poisson's ratio	0.32							
	Plastic Strain %	0	0.1514	1.151	2.992	4.729			
	Plastic Flow Stress MPa	287.3	291.5	298.9	307.3	310.5			

The load-displacement relationship was studied extensively by many researchers using FEM (Giannakopoulos et al, 1994; Larsson et al, 1996; Murakami et al, 1994, 1997; Jayaraman et al, 1998; Giannakopoulos and Suresh, 1999). It was studied in this work as well by the indentation modelling of five different materials, i.e. Aluminium alloy HE15 solution treated (Ref. U), Aluminium alloy HE15 heat treated (Ref. V), Brass 60/40, Steel (Ref. C) and Copper. Uniaxial tension tests were performed on cylindrical specimens in a Hounsfield Tensometer to give the plastic material properties shown in Table 5.25. Standard values were assumed for the elastic properties. An isotropic multilinear plastic work hardening material model was used for these materials.

The dimensional analysis, section 2.4, showed that the force on the indenter, P, is generally proportional to the square of the indenter displacement, h. Several formulae have been proposed to describe the relationship between the indentation load P and the penetration depth h, e.g., Equations (2.39), (2.41), and (2.44). In this work, the following formulae were used to study the loading behaviour for the above five materials, i.e.,

$$P = c_1(\sigma_u + \sigma_y)(c_2 + \ln(\frac{E^*}{\sigma_y}))h^2 \qquad (5.7)$$

$$P = c_1' H_{IT}(c_2' + \ln(\frac{E^*}{H_{IT}}))h^2 \qquad (5.8)$$

$$P = c_3(\tan 19.7^\circ)^{-2}(\sigma_y + \sigma_u)(1 + \ln\frac{E\tan 19.7^\circ}{3\sigma_y})h^2 \qquad (5.9)$$

$$P = c_3'(\tan 19.7^\circ)^{-2} H_{IT}(1 + \ln\frac{E\tan 19.7^\circ}{H_{IT}})h^2 \qquad (5.10)$$

where, c_1, c_2, c_3, c_1', c_2' and c_3' are constants.

Table 5.26 gives the constants in the above P-h equations for the five materials in table 5.25 as determined by regression fitting of the relevant data.

5.12 Unloading behaviour

The dimensional analysis showed that during the unloading stage, the force, P, applied on the indenter, is not proportional to the square of the indenter displacement, h. It has been suggested by Oliver and Pharr (1992) that the unloading curves can be described by an equation of the form:

$$P = b_h(h - h_f)^m \qquad (5.11)$$

Table 5.26 Constants in Equations (5.7)-(5.10) for the five materials in Table 5.25

	Equation (5.7)		Equation (5.8)		Equation (5.9)	Equation (5.10)
	c_1	c_2	c_1'	c_2'	c_3	c_3'
Al HE15 (Ref. U)	4.223	6.981	3.547	4.931	2.042	1.333
Al HE15 (Ref. V)	4.261	6.837	3.619	5.015	2.16	1.404
Steel	4.198	7.535	3.498	5.208	1.852	1.202
Brass 60/40	4.306	7.333	3.597	5.167	2.075	1.334
Copper	4.591	8.066	3.871	5.897	2.333	1.498
Average	4.316	7.350	3.626	5.244	2.092	1.354
Standard Error	0.071	0.218	0.065	0.171	0.078	0.049

Table 5.27 Constants in Equation (5.12) for the five materials described in Table 5.25

		Al HE15 (Ref. U)	Al HE15 (Ref. V)	Steel	Brass 60/40	Copper
Equation (5.12)	c_4	8.076	7.543	12.03	9.139	12.91
	m	1.325	1.297	1.314	1.298	1.396

where b_h and m are constants.

The following equation was proposed for the unloading curves

$$P = c_4 E^* \tan\theta (h - h_f)^m \qquad (5.12)$$

where, c_4 and m are constants, and θ is half the included angle of the indenter, which is $\theta = 70.3°$ in this case.

Table 5.27 gives the constants in Equation (5.12) for the five materials described in Table 5.24. The computed exponents m for the above five materials range from 1.297 to 1.396, which is consistent with the observations of Oliver and Pharr (1992), where m was found to vary between 1.25 and 1.51.

5.13 Extracting the elastic modulus

It is useful to compare the elastic modulus derived from FEA with the elastic modulus input into the model. The Oliver-Pharr method (Pharr et al, 1992) assumes that there is sinking-in of the material instead of pileup. Therefore, the Oliver-Pharr method, i.e.,

$$P = \frac{2}{\pi} \frac{E}{1-\nu^2} \tan\phi \, h^2 \qquad (5.13)$$

can be expected to underestimate the true contact area (Strange and Varshneya, 2001). Some insight into the causes of overestimation of Young's modulus is provided by the work of Hay, Bolshakov and Pharr (1999). The corrected load-displacement relationship proposed by them is

$$P = \gamma_h \frac{2}{\pi} \frac{E}{1-\nu^2} \tan\phi \, h^2 \qquad (5.14)$$

where, γ_h is a constant.

However, one basic assumption, i.e. $h_c / h = 2/\pi$, used to derive the above equation may not be true generally. If it is now assumed that $R_c / h = \mathrm{C''}$ instead, where, R_c is the contact radius, and C" is a material dependent constant.

Thus, the following equation is obtained,

$$P = \gamma_h \frac{E}{1-\nu^2} \mathrm{C''} h^2 \qquad (5.15)$$

and the indentation contact stiffness S_c is,

$$S_c = \gamma_h \frac{2E}{1-\nu^2} \mathrm{C''} h = \gamma_h \frac{2E}{1-\nu^2} R_c \qquad (5.16)$$

The derived elastic modulus E is given by,

$$E = S_c (1-\nu^2)/(2\gamma_h R_c) \qquad (5.17)$$

where, the contact stiffness S_c can be obtained based on the unloading curve. The contact radius R_c can be interpolated based on the contact pressure of the last two contact nodes in the FEA.

Three separate methods, i.e. contact radius matching, modified indenter shape and comparison to finite element simulations, for modifying the solution were presented by Hay, Bolshakov and Pharr (1999):

For the contact radius matching method,

$$\gamma_h = 1 + \frac{1-2\nu}{4(1-\nu)\tan\phi} \qquad (5.18)$$

For the modified indenter shape method,

$$\gamma_h = \pi \frac{\pi/4 + 0.15483073 \cot\phi \frac{1-2\nu}{4(1-\nu)}}{(\pi/2 - 0.83119312 \cot\phi \frac{1-2\nu}{4(1-\nu)})^2} \qquad (5.19)$$

and for the simplified modified indenter shape method,

$$\gamma_h = 1 + \frac{1-2\nu}{4(1-\nu)\tan\phi}(3-\frac{\pi}{2}) \qquad (5.20)$$

Table 5.28 Elastic modulus derived from FEA for En08 and MgO

		Equation (5.13)	Equation (5.18)	Equation (5.19)	Equation (5.20)
EN08	γ_h	1	1.05115	1.06707	1.07310
	E	219.5	208.8	205.7	204.5
	Relative difference %	6.5	1.4	0.16	0.72
MgO	γ_h	1	1.06278	1.08314	1.08972
	E	271.3	255.2	250.4	248.9
	Relative difference %	9.4	2.9	0.99	0.38

Table 5.29 Elastic modulus derived from FEA

		Equation (5.13)	Equation (5.18)	Equation (5.19)	Equation (5.20)
Aluminium alloy HE15 ref U.	γ_h	1	1.04542	1.05927	1.06492
	E	74.1	70.9	69.9	69.6
	Relative difference %	5.8	1.2	0.09	0.62
Aluminium alloy HE15 ref V.	γ_h	1	1.04542	1.05927	1.06492
	E	77.0	71.7	70.8	70.4
	Relative difference %	7.1	2.4	1.1	0.55
Brass 60/40	γ_h	1	1.04340	1.05653	1.06203
	E	116.3	111.5	110.1	109.5
	Relative difference %	5.7	1.32	0.06	0.45
Steel ref. C 0.2%C-0.25%C	γ_h	1	1.05115	1.06707	1.07310
	E	224.6	213.7	210.5	209.3
	Relative difference %	7.0	1.8	0.24	0.33
Copper	γ_h	1	1.04739	1.06193	1.06773
	E	132.1	126.1	124.4	123.7
	Relative difference %	6.5	1.71	0.31	0.23

Two types of materials, i.e. En08 steel and MgO ceramic, were studied here in the first instance. Indentation of En08 will incur pileup, whereas MgO will incur sinking-in.

Table 5.28 shows that both Equations (5.19) and (5.20), i.e. the modified indenter shape method, can give accurate elastic modulus values for either a piling-up material or a sinking-in material.

Furthermore, this analysis has been extended to include the five other materials described in Table 5.25. The results are presented in Table 5.29. It can be seen that Equations (5.19) and (5.20) also give good agreement between the input and calculated modulus values in all cases.

5.14 2D modelling vs. 3D modelling

Table 5.30 Comparison of hardness between 2D modelling and 3D modelling

	HM			*H_{IT} from 2D and HV from3D*		
	Under load	Unloaded	Hardness equation	Under load	Unloaded	Hardness equation
2D	2526	2831	*P/(26.03*h^2)*	2574	2552	*P/(πR_c^2)*
3D	2514	2831	*P/(26.424*h^2)*	2573	2556	*2Psin(68°)/d^2*

For the 2D modelling, the included half angle of the conical indenter is 70.3° so that the 2D model has the same area-to-depth ratio as that of a 3D Vickers indentation. This procedure has generally been shown to give calculated hardness values which are the same for a frictionless case (Lichinchi et al, 1998). However, it was decided that it would be appropriate to consider this equivalence for a frictional case in the present study. Thus a 3D model of one-eighth of a Vickers indenter was developed.

The analyses were performed using sharp indenters, En08 substrate material properties with friction coefficient = 0.5. The analyses were performed to the same displacement. The element sizes for the 2D model were the same as that for the 3D model such that the results between them are comparable (Figure 5.10 and 5.11). However, this mesh is much coarser than that used in previous sections for 2D analyses, in order to save computational time for the 3D model.

From the results shown in table 5.30 it is clear that H_{IT}, $H_{IT} = F/(\pi R_c^2)$, from the 2D model is equivalent to the Vickers hardness, $HV = \dfrac{2F\sin 68^\circ}{d^2}$, from the 3D model.

Also, HM, $HM = F/(26.03h^2)$, from the 2D model is equivalent to HM, $HM = F/(26.424h^2)$, from the 3D model.

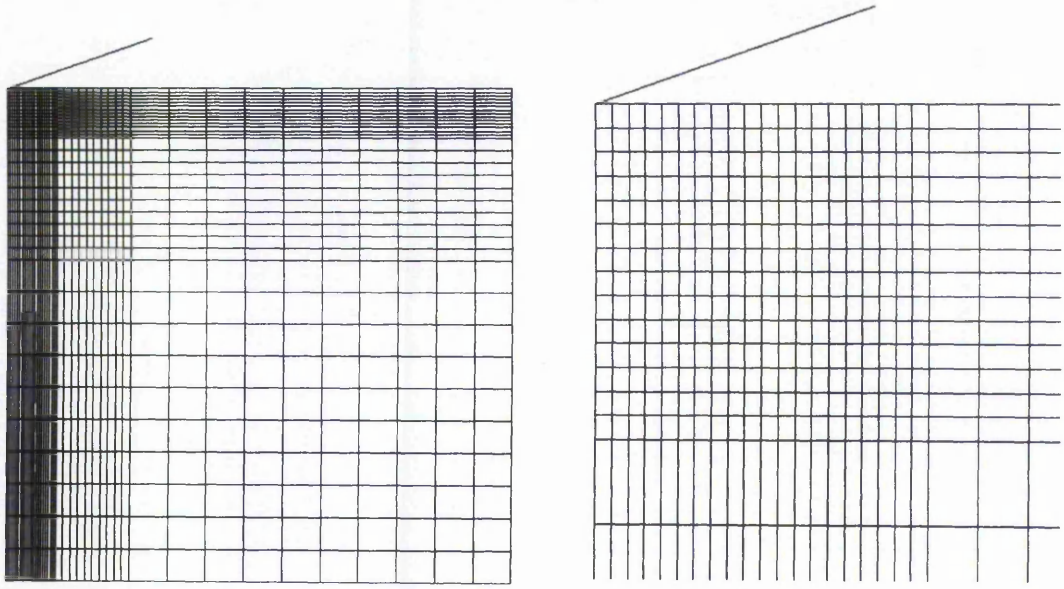

(a) The whole mesh model

(b) Detailed mesh beneath the indenter

Figure 5.10 2D mesh model

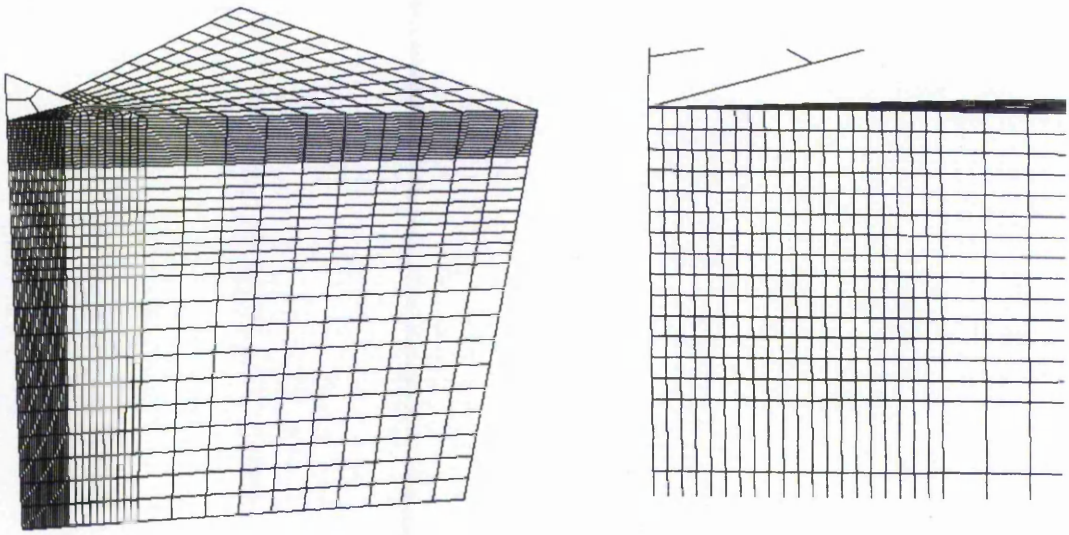

(a) The whole mesh model

(b) Detailed mesh beneath the indenter

Figure 5.11 3D mesh model

5.15 Dimensional analysis

For a conical cone indenter with semi-apical included angle of 70.3°, based on Cheng and Cheng's (2002) work, the relationships between H_{IT}/E^*, W_p/W_{tot} and h_f/h_m are:

$$\frac{W_p}{W_{tot}} = 1.27\frac{h_f}{h_m} - 0.27 \qquad for\ \frac{h_f}{h_m} > 0.4 \qquad (5.21)$$

$$\frac{h_f}{h_m} = 1 - 4.5163\frac{H_{IT}}{E^*} \tag{5.22}$$

$$\frac{H_{IT}}{E^*} = 0.1743\frac{W_e}{W_{tot}} \tag{5.23}$$

In Cheng and Cheng's work, the friction coefficient was assumed to be zero. An equivalent analysis is developed herein, but with the effect of friction coefficient being taken into account. During loading, the force F is given by

$$F = Eh^2\Pi_\alpha(\frac{Y}{E}, \nu, n, \theta, \mu), \tag{5.24}$$

and the contact depth h_c is

$$h_c = h\Pi_\beta(\frac{Y}{E}, \nu, n, \theta, \mu) \tag{5.25}$$

During unloading, the force is

$$F = Eh^2\Pi_\gamma(\frac{Y}{E}, \frac{h}{h_m}, \nu, n, \theta, \mu) \tag{5.26}$$

The friction coefficient was assumed to be 0.15. The indentation modelling and Vickers indentation experiments were performed for the five materials described in Table 5.25. A conical indenter with semi-apical included angle of 70.3° was used. The data for H_{IT}/E^*, W_p/W_{tot} (W_e/W_{tot}) and h_f/h_m can be obtained from the FE analyses (Tables 5.31-5.33). Subsequently, the relationships between the parameters can be determined using regression, to give the values shown in Equations (5.27)-(5.29).

Table 5.31 Relationship between W_p/W_{tot} and h_f/h_m

	Al HE15 (Ref. V)	Al HE15 (Ref. U)	Brass 60/40	Copper	Steel
h_f/h_m	0.9034	0.9178	0.9441	0.9590	0.9729
W_p/W_{tot}	0.8732	0.8930	0.9266	0.9484	0.9646

Table 5.32 Relationship between h_f/h_m and H_{IT}/E^*

	Steel	Copper	Brass 60/40	Al HE15 (Ref. U)	Al HE15 (Ref. V)
H_{IT}/E^*	5.217e-3	6.843e-3	0.0108	0.01625	0.0189
h_f/h_m	0.9729	0.9590	0.9441	0.9178	0.9034

Table 5.33 Relationship between H_{IT}/E^* and W_e/W_{tot}

	Steel	Copper	Brass 60/40	Al HE15 (Ref. U)	Al HE15 (Ref. V)
W_e/W_{tot}	0.0354	0.0516	0.0734	0.1070	0.1268
H_{IT}/E^*	5.217e-3	6.843e-3	0.0108	0.0162	0.0189

$$\frac{W_p}{W_{tot}} = 1.3044\frac{h_f}{h_m} - 0.3044 \quad for \ \frac{h_f}{h_m} > 0.4 \tag{5.27}$$

$$\frac{h_f}{h_m} = 1 - 5.1573\frac{H_{IT}}{E^*} \tag{5.28}$$

$$\frac{H_{IT}}{E^*} = 0.1484\frac{W_e}{W_{tot}} \tag{5.29}$$

Equations (5.27)-(5.29) provide a good fit to the calculated values. They are of the same form as used by Cheng and Cheng (2002), i.e. Equations (5.21) to (5.23), although the values for the curve-fitted constants are somewhat different. These differences most probably arise from the inclusion of friction in the present analyses. The assumption by Cheng and Cheng of frictionless contact does not seem to be a good approximation to actual test conditions.

5.16 Summary

In order to establish a reliable and effective FEM indentation model, the relevant factors, e.g. mesh size, model size, friction coefficient, applied load, indenter tip radius, indenter angle, and indenter rigidity, were investigated first using a 2D axisymmetric FEM model. ABAQUS was found to be the most appropriate FE software package to model the hardness indentation problem after comparison with four other general FE software packages.

The effect of material properties of the substrate was also studied. Subsequently, the loading behaviour and the unloading behaviour were investigated based on five materials. The methods for calculating the elastic modulus were discussed and modified versions were proposed. A comparison between a 2D model and a 3D model was undertaken. It was found that H_{IT}, $H_{IT} = F/(\pi R_c^2)$, from the 2D model is equivalent to the Vickers hardness, $HV = \frac{2F\sin 68^\circ}{d^2}$, from the 3D model. In addition, HM, $HM = F/(26.03h^2)$, from the 2D model is equivalent to HM, $HM = F/(26.424h^2)$, from the 3D model.

Finally, a dimensional analysis of the relationships between H/E^*, W_p/W_{tot} and h_f/h_m was implemented.

CHAPTER 6
FE MODELLING OF HARDNESS TESTS ON MgO

As noted in Chapter 1, one of the main objectives of this research is to be able to use FE modelling of ceramic materials to be able to quantify not only the hardnesses but also other relevant mechanical properties. Hardness testing of single crystal MgO has been the subject of many experimental investigations (Brookes, 1983, 1986; Armstrong and Elabn, 1989; Khan et al, 1992; Guillou, 1992; Ren et al, 2002). These have identified the qualitative aspects of the deformation and fracture in MgO. Therefore MgO is a good material model to use to develop an improved interpretation of hardness test results. The detailed geometry of the deformation and fracture in single crystal MgO is very complex. Thus, the purpose of the studies presented in this chapter is primarily to demonstrate an application of the procedures developed in Chapters 4 and 5 to the deformation of a ceramic material, and to lay the foundations for a more detailed FE study in the future.

6.1 Material model for MgO

6.1.1 Anisotropic elastic properties of MgO

For a crystalline solid, when the periodic and repeated arrangement of atoms is perfect or extends throughout the entirety of the specimen without interruption, the result is a *single crystal*. The physical properties of single crystals of some substances depend on the crystallographic direction in which the measurements are taken. For example, the elastic modulus, the electrical conductivity, and the index of refraction may have different values in the <1 0 0> and <1 1 1> directions. This directionality of properties is termed anisotropy, and it is associated with the variance of atomic or ionic spacing with crystallographic direction.

For the face centred cubic ceramic single crystal MgO, the anisotropic material properties need to be considered in order to reflect the actual situation (Tables 6.1, 6.2).

Table 6.1 Stiffness constants and compliances of MgO (Kelly and Groves, 1970)

Single crystal MgO					
Stiffness constants (GPa)			Compliances($10^{-12}N^{-1}m^2$)		
C_{11}	C_{12}	C_{44}	S_{11}	S_{12}	S_{44}
289	88	155	4.03	-0.94	6.47

Table 6.2 Elastic and shear moduli of MgO (Kelly and Groves, 1970)

Single crystal MgO							
A'	ν	Tensdile modulus (GPa)			Shear modulus (GPa)		
		$E_{<100>}$	$E_{<110>}$	$E_{<111>}$	μ_{100}	μ_{110}	μ_{111}
1.54	0.23	248	316.2	348	154.6	121.9	113.8

Note: A' is the anisotropy ratio. $A' = 2c_{44}/(c_{11} - c_{12})$, *cf* appendix A.

6.1.2 MgO plastic material model

The indentation hardness test has been used to obtain information concerning the plastic deformation behaviour of ceramics and ultrahard materials since it is generally not possible to test these in conventional uniaxial tensile or compressive tests. Magnesium oxide has been used for many studies on indentation behaviour since the dislocation patterns can be revealed by etch pitting. The hardness of single crystal MgO measured on the cube face, {001}, is markedly dependent on the orientation of the indenter. For example typically for a Knoop indenter it would vary between 4000 and 8000 MPa in the <100> and <110> directions, respectively. The results of Hulse and Pask (1960) in uniaxial compression gave a compressive yield stress of 120 MPa, and a plastic modulus of 468 MPa, with a true strain at failure of 0.08 at 26°C. If these values are used in a similar model to that used for steel, the hardness value calculated by FEM is only about 560 MPa, which is much lower than the measured single crystal value. The physical reason for this is that in uniaxial compression, the dislocations move on parallel slip planes and do not intersect. However, around an indentation, there is slip on multiple slip planes. Thus dislocation interaction, and particularly the formation of sessile locks, occurs rapidly. Therefore, this needs to be taken into consideration when developing a suitable material model to describe the deformation behaviour around an indentation.

The form of the stress strain relationship that has been proposed (Griffiths et al, 2001) assumes that the material has a low initial yield stress, i.e. 124 MPa, based on the results of Hulse and Pask (1960). This will be followed by a short region of easy glide, i.e. low work hardening rate, again based on the observations of Hulse and Pask. However this region will not be as extensive as for uniaxial conditions. It is proposed that the strain in this region is relatively limited, e.g. ~0.001, which results in the start of dislocation locking. This dislocation locking will prevent further dislocation motion until the local stress is sufficiently high to either initiate new dislocation sources or overcome the

barriers presented by the sessile dislocation locks. In this part of the stress-strain curve there will thus be a rapid, almost elastic, increase in the stress until it reaches in effect an 'upper yield stress'. The value for this cannot be determined with precision. It has been proposed that for ionically bonded materials that this 'second yield stress' may be as much as fifteen times the initial yield stress (Kelly & Groves, 1970). This stress value is likely to have a significant influence on the calculated hardness values. A value of 1116 MPa has been assumed in the present analyses. The strain for this region is assumed to be 0.004. This will be followed by a region of high work hardening rate as the dislocations multiply and intersect. The local dislocation densities around indentations in MgO have been observed to be very high, which will result in a very high strain hardening rate, since this rate is proportional to the (dislocation density)$^{1/2}$. This high work hardening rate will probably continue until saturation occurs, which will be at a high local strain. It is difficult to predict a value for this, but again given the exceedingly high local dislocation densities, it is possible that this strain could be as high as ~ 0.1. For strains greater than this, it can be assumed that since saturation has occurred, that the work hardening rate becomes very low. In the present instance, it has been assumed that for strains above ~0.1 that the work hardening rate can be taken as zero. The postulated stress-strain curve is shown in Figure 6.1.

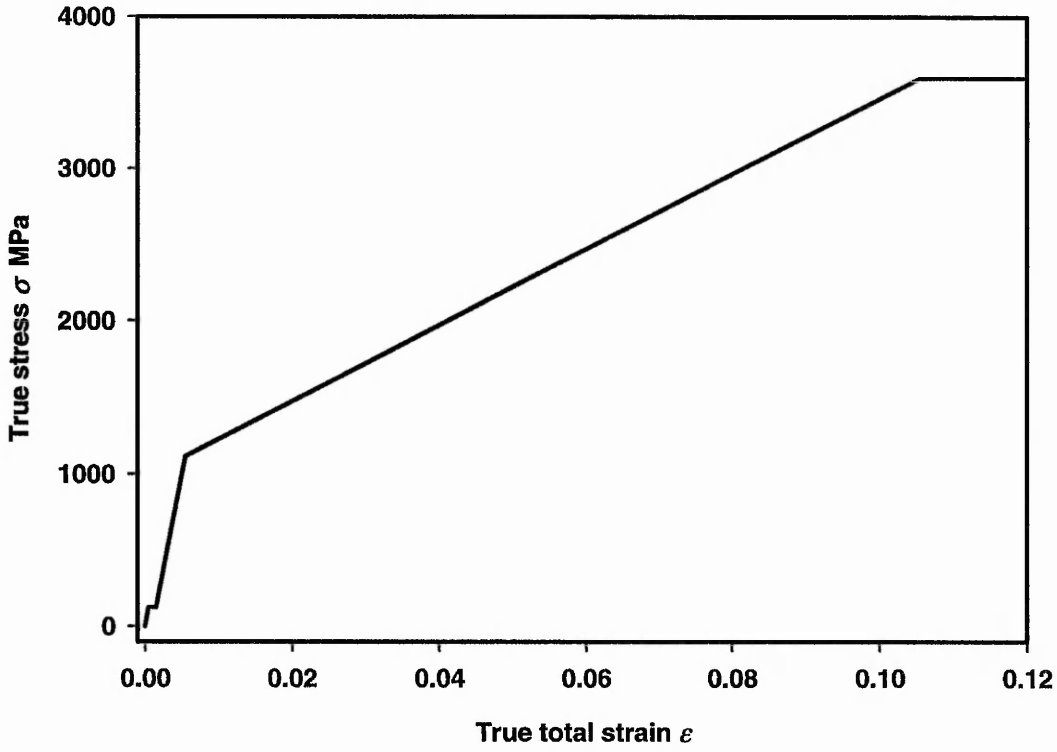

Figure 6.1 Multiaxial material model for single crystal MgO

6.2 Modelling process

Two 2D axisymmetric models were established to reflect the anisotropic elasticity of MgO. In the first case the test plane, i.e. substrate surface, is (001), and the X and Z axes in ABAQUS correspond to <100> and $<0\bar{1}0>$ respectively. This model was effectively an isotropic model, since the elastic moduli along the three directions were the same. In the second case the test plane was the same, i.e. (001), but the X and Z axes corresponded to <110> and $<1\bar{1}0>$ respectively. This model was in effect anisotropic, but did not have the same elastic anisotropy as MgO, since this is actually more complex than can be incorporated in a straightforward manner in ABAQUS. In addition a conventional equivalent stress criterion was assumed for the yield surface. This does not describe the actual anisotropy of plastic deformation in a single crystal. However to fully model the plastic anisotropy would require the resolution of the stresses onto the primary and secondary slip systems, which was not considered to be useful or appropriate in the present instance.

A sharp rigid indenter was used. The FE model is similar to that described in section 5.1. The applied force was 3.13 N and the friction coefficient was taken as 0.15.

6.3 Hardness results for MgO

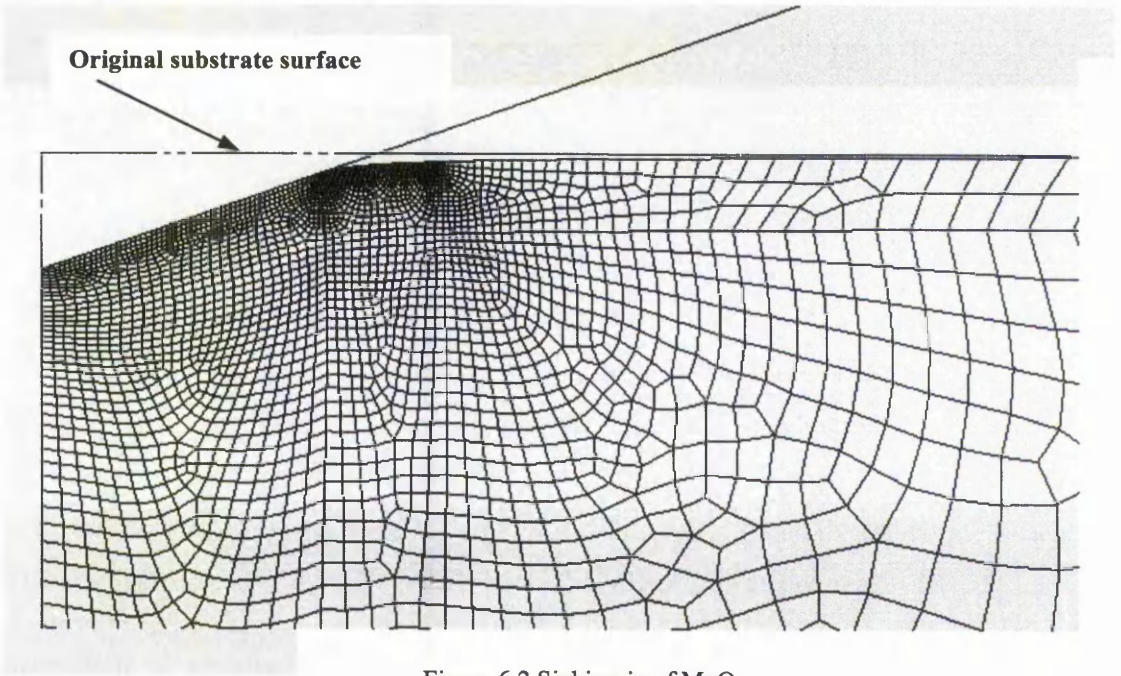

Figure 6.2 Sinking-in of MgO

Figure 6.2 shows the deformed mesh in MgO at full load. The contact edge can clearly be seen to be below the original substrate surface, i.e. 'sinking-in' has occurred.

Table 6.3 MgO calculated Hardness values

Material		HM MPa	H_{IT} MPa
Isotropic MgO	under load	5103	7525
	unloaded	6350	7361
'Anisotropic' MgO	under load	5194	7630
	unloaded	6462	7476

Table 6.3 shows that the hardness values of isotropic MgO and anisotropic MgO are very close. This shows that the contribution of the elastic anisotropy of MgO to the observed hardness anisotropy is negligible, which implies that the anisotropy of the slip deformation is mainly responsible for the observed anisotropy.

The experimental Knoop hardness values are 4072 MPa for MgO (001) <100> and 7656 MPa for MgO (001) <110> (Ren et al, 2002). Thus, the above stress-strain data (section 6.1.2) proposed by Griffiths et al (2001) is applicable to MgO (001) <110> only. For MgO (001) <100>, the stress-strain data need to be adjusted with the consideration of the hardness anisotropy. The initial yield stress and the flow stress at ε_p =0.001, where ε_p is the true plastic strain, were the same as those for MgO (001) <110>. The following equation was proposed to estimate the flow stresses at ε_p =0.005 and 0.105:

$$\sigma_{<100>} = \frac{HK_{<100>}}{HK_{<110>}} \sigma_{<110>} \qquad (6.1)$$

Table 6.4 The flow stress vs. plastic strain data for MgO (001) <100>

Flow stress MPa	True plastic strain
124	0
124.5	0.001
594	0.005
1913	0.105

Table 6.5 Calculated Hardness values for MgO (001) <100> using the material model in Table 6.4

	HM MPa	H_{IT} MPa
under load	3141	4178
unloaded	3555	4126

This corresponds to a modified flow stress vs. plastic strain relationship for MgO (001) <100> as presented in Table 6.4. These values were used to re-calculate the hardness as

shown in Table 6.5. These data are now closer to the measured experimental hardness values.

These results also demonstrate that it is not always possible to use uniaxial stress-strain data to model the complex multiaxial deformation which occurs beneath an indenter. It is sometimes necessary to understand the physical deformation processes that are occurring and to take account of these in the modelling.

6.4 Summary

FE modelling of hardness tests on MgO was implemented primarily in this chapter. A simplified anisotropic material model was used and a specific plastic material model was assumed for MgO (Griffiths et al, 2001). The results show that the contribution of the elastic anisotropy of MgO to the observed hardness anisotropy is negligible. The calculated hardness values for MgO (001) <100> and MgO (001) <110) agree well with the experimental results based on the proposed material model. The results also demonstrate that it is not always possible to use uniaxial stress-strain data to model the complex multiaxial deformation which occurs beneath an indenter.

CHAPTER 7

FE MODELLING OF THE HARDNESS OF ALTERNATING Al AND TiB_2 MULTILAYER COATINGS

In this chapter, FE modelling has been performed for multilayer coatings comprising alternating aluminium and titanium diboride, TiB_2, layers. The dependence of the hardness and elastic modulus on the structure of the multilayer coating have been investigated and compared with experimental results from the literature (Hancock et al, 2002). The different methods of calculating the hardness and elastic modulus were compared and analysed. The variations of hardness and elastic modulus with number of layers were calculated. As noted above, section 2.6.1.7, an explicit method for the FE analysis of hardness using ABAQUS has been proposed on the basis that it substantially reduces the required computational times (Yoo et al, 2004). Therefore, it was decided to investigate if a modified form of this approach could be used for the analyses described in this chapter.

7.1 Introduction

The use of protective coatings on substrates of traditional materials has developed into many application areas, such as wear resistant layers on cutting tools and corrosion protection of gas turbine blades. Although such coatings are very successful, there are still technical issues, particularly concerning the adhesion and lack of ductility in some cases. There has recently been an increase in interest in the deposition of multiple layers of alternating materials. By interspersing layers of ductile metallic coatings, not only can the erosion resistance be improved, because the lengths of through thickness cracks in the ceramic are limited to the depth of a single layer in the multilayer coating whereas in monolayer ceramic coatings the cracks can run from the surface to the substrate (Hancock et al, 2002), but the hardness of the coating can also be controlled. Using solely an experimental methodology, it is only possible to investigate the properties of a small range of the potential combinations of material composition, layer thicknesses and numbers of layers. This situation is a clear example where the use of numerical modelling can be used to guide the selection of those parameters that should be taken to the stage of fabrication and characterization.

Hancock et al (2002) addressed the problem of measuring the mechanical properties of multilayer surface coatings by nanoindentation by examining specimens with multilayers of alternate titanium diboride TiB_2, (as a hard erosion/wear resistant material) and aluminium (as a ductile interlayer to resist crack propagation and aid adhesion) on a steel substrate. The same system has been studied using nanoindentation FE modelling in this chapter.

7.2 FE model

A standard Berkovich diamond indenter was used in the experimental study (Hancock et al, 2002). A 2D axisymmetric model has been developed in this investigation to enable the analyses to be performed with a sufficiently refined mesh adjacent to the indenter. The indenter was modelled as a sharp, rigid cone with semi-apical included angle of 70.3°.

The simulations were carried out with the finite element analysis software ABAQUS. The FE model is shown in Figure 7.1. Figure 7.2 shows a typical detailed mesh of the coatings under the indenter. The radius and the thickness of the substrate were 200 μm. The radius and the total thickness of the multilayer coatings were 200 μm and 5 μm respectively. The multilayer coating was composed of 25 pairs of alternate layers of TiB_2 and Al, i.e. each pair (TiB2 plus Al) was 200 nm thick and each coating contained 50 individual layers. The layer next to the steel was always aluminium, to improve the

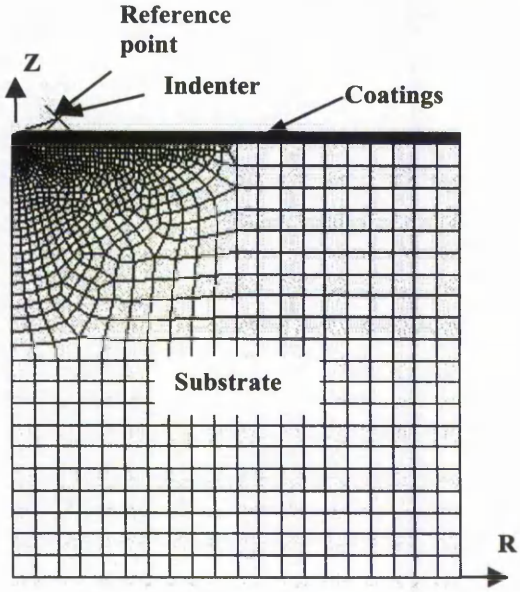

Figure 7.1 FE model

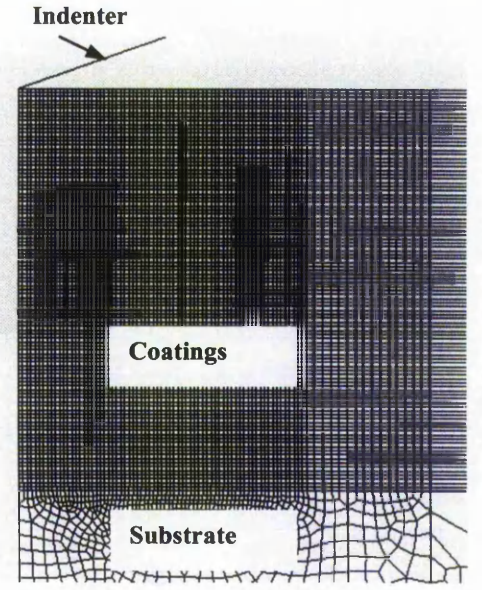

Figure 7.2 A typical detailed mesh of the coatings

adherence to the substrate steel, and the top layer was always TiB_2 to give an enhanced wear resistant surface (Hancock et al, 2002).

Three types of specimen were produced with the following individual coating thicknesses (Hancock et al, 2002):

(i) 25%TiB_2: with Al layers of 150 nm and TiB_2 layers of 50 nm

(ii) 50%TiB_2: with Al layers of 100 nm and TiB_2 layers of 100 nm

(iii) 75%TiB_2: with Al layers of 50 nm and TiB_2 layers of 150 nm

All percentages are expressed by volume. A typical example of the mesh for the 75% TiB_2 coating is shown in Figure 7.2.

The coatings were assumed to be bonded perfectly with each other. A surface-to-surface contact pair was established between the indenter and the coating. For the tangential behaviour, the penalty friction formulation was used. The friction coefficient was assumed to be 0.15; for the normal behaviour, the 'hard' contact option that allows separation after contact was used. The bottom line (z=0) of the substrate was constrained along the Z and R directions and the axisymmetric line (r=0) was constrained along the R direction only. A velocity 'load' was applied to the reference point of the rigid indenter.

7.3 Material properties

The material properties of TiB_2 and Aluminium used in this chapter are shown in Table 7.1. The elastic properties and densities were obtained from the MEMS and Nanotechnology Exchange (Anon., 2004a), with the yield stress for aluminium being based on typical values (Tsui et al, 1999), and that for TiB_2 was estimated from the bulk hardness (Anon., 2004a). An isotropic elastic perfectly-plastic material model was assumed for both TiB_2 and Aluminium.

The elastic modulus, Poisson's ratio and density of AISI 1095 steel are 205GPa, 0.29 and 7850 kg/m^3 respectively (Anon., 2004b). A typical uniaxial true plastic stress vs. true plastic strain curve (Lease, 2002) is shown in Figure 7.3. Its initial yield stress is

Table 7.1 Material properties of TiB2 and Aluminium

	Elastic modulus GPa	Poisson's ratio	Yield stress GPa	Density kg/m^3
TiB_2	366.9	0.22	10	4550
Aluminium	70	0.34	0.28	2700

0.569 GPa. The indentation hardness of the AISI 1095 steel is approximately 3.415 GPa.

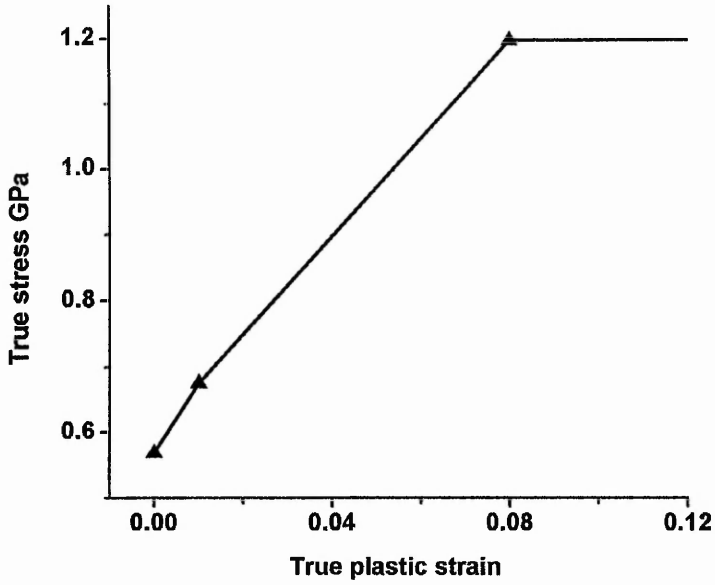

Figure 7.3 True plastic stress vs. true plastic strain of AISI 1095 steel (Lease, 2002)

7.4 Measurements of hardness and elastic modulus

The Indentation Hardness defined in the ISO standard (BS EN ISO 14577, 2002) is usually calculated based on the indentation depth in contact, h_c, i.e.

$$H_{IT}(h_c) = P_{\max} / A_p(h_c) \qquad (7.1)$$

However, the projected contact area in Equation (2.4) can be calculated from the contact radius R_c directly in FEA. Thus, the Indentation Hardness can also be calculated from the following equation,

$$H_{IT}(R_c) = P_{\max} / A_p(R_c) \qquad (7.2)$$

Hancock et al (2002) used Oliver and Pharr's method (1992) to process their nanoindentation results. The corresponding equation used to calculate the elastic modulus is

$$E(h_c) = \sqrt{\pi}(1-\nu^2)S_c/(2\sqrt{A_p(h_c)}) \qquad (7.3)$$

where S_c is the contact stiffness. Equation (5.16) provides an alternative calculation for the elastic modulus, which can be rewritten as follows,

$$E(R_c) = S_c(1-\nu^2)/(2\gamma_h R_c) \qquad (7.4)$$

where γ_h was determined based on the simplified modified indenter shape method (Equation (5.19)).

7.5 FE modelling process

The implicit method has been used generally in the indentation modelling in this study, with the results from such implicit analyses generally agreeing well with the experimental results. However, the computational time using the implicit method is usually much longer than that using the explicit method, which is performed by introducing mass scaling into the model and applying an appropriate virtual velocity to the indenter. Moreover, convergence difficulties were often encountered when using the implicit method.

In order to determine if it were possible to save on computational time and reduce, or eliminate, convergence difficulties, ABAQUS/EXPLICIT has been used initially to carry out the load step computation for the indentation modelling of the multilayer coatings. Subsequently, ABAQUS/STANDARD was used to implement the unloading step computation in order to obtain the correct unloading force-displacement response. The reason for this was that when using the explicit analysis method only to run the whole load and unload modelling, the unloading force-displacement response was found to be inaccurate. This methodology has been shown to be beneficial in the spring-back modelling field for sheet metal working, and has been termed the explicit-to-implicit method in this area.

There are two loading methods to set up the intermediate step, i.e. a ramp load method or a step load method. For the ramp load method, the deformed location of the rigid indenter needs to be defined, whereas for the step load method, the original location of the rigid indenter needs to be defined. The ramp load method was preferred since it was found to yield more consistent and accurate results than the step load method.

7.6 Comparison between the explicit-to-implicit method and the implicit method

In order to verify the reliability of the above mentioned explicit-to-implicit method, the pure implicit method was used here to carry out the verification by running an indentation model for bulk TiB_2.

The element type used for the implicit analysis method was CAX4I, a 4-node bilinear axisymmetric quadrilateral element with incompatible modes. For the explicit analysis method, the applied element type was CAX4R, a 4-node bilinear axisymmetric quadrilateral reduced integration element with hourglass control.

Figures 7.4(a) and (b) give the load-displacement curves obtained from the TiB_2 indentation modelling using the implicit method and the explicit-to-implicit method

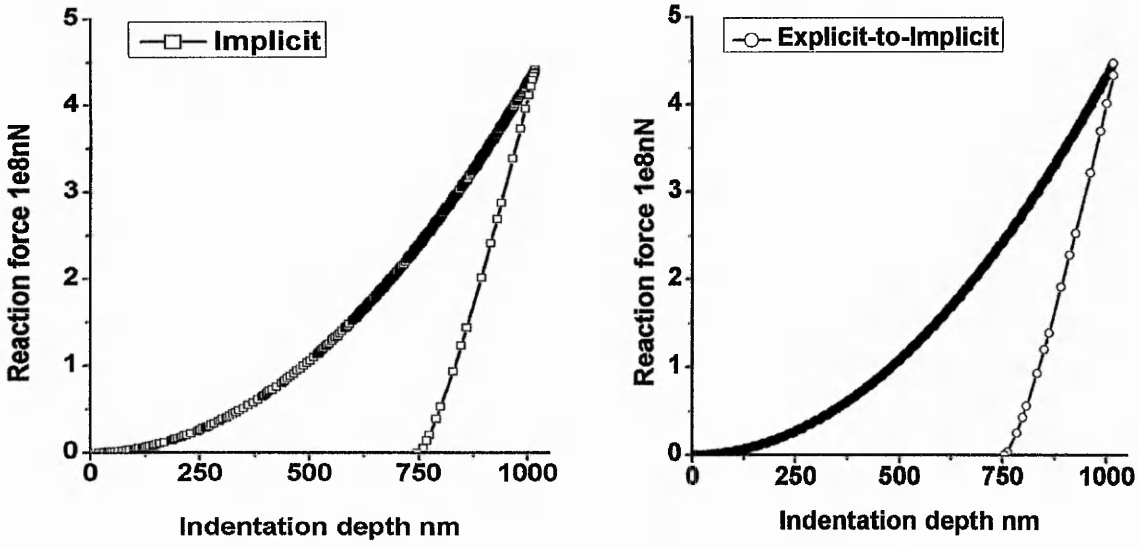

(a) (b)

Figure 7.4 The load-displacement curves for (a) the implicit method and (b) the explicit-to-implicit method

respectively. They are in good agreement with each other. Furthermore, Table 7.2 and Table 7.3 give the Indentation Hardness and elastic modulus comparison for TiB_2 using the two different methods.

Table 7.2 Hardness comparison between the implicit and explicit-to-implicit methods

Indentation depth nm		118	263	521	1016
$H_{IT}(R_c)$ GPa	Implicit	30.35	26.52	25.48	24.70
	Explicit-to-implicit	30.93	26.76	25.91	24.94
	Relative difference %	1.9	0.9	1.7	1.0
$H_{IT}(h_c)$ GPa	Implicit	24.1	24.4	24.0	24.3
	Explicit-to-implicit	24.8	24.6	24.4	24.6
	Relative difference %	2.9	0.82	1.7	1.2

Table 7.3 Elastic modulus comparison between the implicit and explicit-to-implicit methods (Note: the input value was 366.9 GPa)

Indentation depth nm		118	263	521	1016
$E(R_c)$ GPa	Implicit	379.8	375.2	373.8	379.0
	Explicit-to-implicit	379.1	373.7	372.2	371.4
	Relative difference %	0.18	0.41	0.43	1.97
$E(h_c)$ GPa	Implicit	370.0	389.9	397.7	410.2
	Explicit-to-implicit	370.6	390.6	395.0	402.9
	Relative difference %	0.19	0.19	0.68	1.8

The maximum relative difference of Indentation Hardness and elastic modulus between the two methods is less than 3%.

The values of h_c in Table 7.2 and Table 7.3 were obtained based on the method proposed in the ISO standard (BS EN ISO 14577, 2002), i.e.

$$h_c = h_m - c_h(h_m - h_r) \tag{7.5}$$

where, h_m is the maximum indentation depth at $P_{\max}$; c_h is the correction factor for the indenter geometry; h_r is derived from the force-displacement curve and is the intercept of the tangent to the unloading cycle at $P_{\max}$ with the displacement axis.

By comparing the values of hardness between $H_{IT}(R_c)$ and $H_{IT}(h_c)$ in Table 7.2, it can be seen that there are marked differences between the two calculation methods. These arise because for this material model, which exhibits sinking-in under indentation, the value of h_c calculated based on Equation (7.5) is greater than the true value of h_c. Consequently, $H_{IT}(h_c)$ is less than $H_{IT}(R_c)$ for this material model.

Now, denoting the value of h_c that is obtained based on R_c from FEA as h_{rc}, where $h_{rc} = R_c / \tan\theta$ then the relationship between $H_{IT}(h_c)$ and $H_{IT}(R_c)$ can be obtained from Equations (7.1) and (7.2) as

$$\frac{H_{IT}(R_c)}{H_{IT}(h_c)} = \left(\frac{h_c}{h_{rc}}\right)^2 \tag{7.6}$$

Consider now some examples. For the first case of a small indentation, i.e. h_m=118 nm, then h_c=98.3 nm, and h_{rc} =88 nm, thus:

$$\frac{H(R_c)}{H(h_c)} = \left(\frac{98.3}{88}\right)^2 \cong 1.248$$

which compares to the corresponding values of 1.259 for the implicit method and 1.247 for the explicit-to-implicit method as calculated from the data in Table 7.2.

In the second example, consider a deeper indentation, i.e. h_m=1016 nm, then h_c=861 nm, and h_{rc} =855.2 nm, thus:

$$\frac{H(R_c)}{H(h_c)} = \left(\frac{861}{855.2}\right)^2 \cong 1.014$$

which compares to the corresponding values of 1.016 for the implicit method and 1.014 for the explicit-to-implicit method as calculated from the data in Table 7.2.

In order to compare between $E(h_c)$ and $E(R_c)$, Equations (7.3) and (7.4) can be rewritten as

$$E(h_c) = \frac{(1-\nu^2)S_c}{2\tan\theta}\frac{1}{h_c} = C_s / h_c \tag{7.7}$$

where, $C_s = \frac{(1-\nu^2)S_c}{2\tan\theta}$, and h_c was calculated from Equation (7.5).

$$E(R_c) = \frac{(1-\nu^2)S_c}{2\tan\theta}\frac{1}{\gamma_h h_{rc}} = C_s /(\gamma_h h_{rc}) \tag{7.8}$$

From Equations (7.7) and (7.8),

$$\frac{E(R_c)}{E(h_c)} = \frac{h_c}{\gamma_h h_{rc}} \tag{7.9}$$

Consider now the situation at h_m=118 nm, with h_c=98.3 nm, h_{rc} =88 nm, and γ_h=1.09185, then

$$\frac{E(R_c)}{E(h_c)} = \frac{98.3}{1.09185*88} \cong 1.023$$

which compares to the corresponding values of 1.026 and 1.023 for the implicit and the explicit-to-implicit methods respectively as calculated from the data in Table 7.3. Also, for deeper indentations, i.e. h_m=1016 nm, h_c=861 nm, h_{rc} =855.2 nm, and γ_h=1.09185, then

$$\frac{E(R_c)}{E(h_c)} = \frac{861}{1.09185*855.2} \cong 0.922$$

which compares to the corresponding values of 0.924 and 0.922 for the implicit and the explicit-to-implicit methods respectively as calculated from the data in Table 7.3.

Table 7.3 also shows that the Oliver-Pharr method only worked well at shallow indentation depths, and it over-estimated the elastic modulus when the indentation depth was greater than 118 nm.

7.7 Results

7.7.1 Deformation of the coatings

Figure 7.5 shows the deformation of the three types of multilayer coatings. The mesh was specifically designed for each case because it was found that an indentation size effect can be reflected by adjusting the mesh size. The mesh sizes along the radial

direction were the same for all three cases. They were different though along the thickness direction as shown in Figure 7.5.

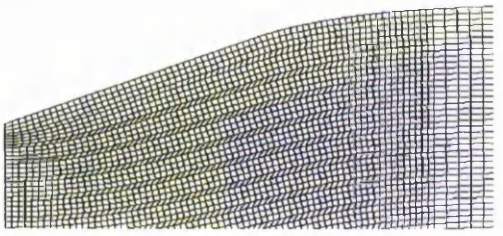

(a) Deformation of the 75% TiB_2 coatings

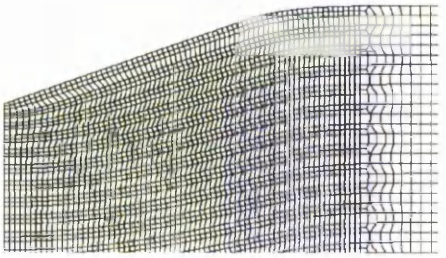

(b) Deformation of the 50% TiB_2 coatings

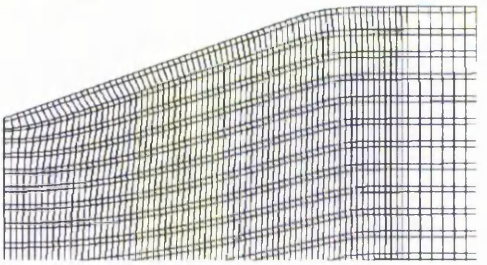

(c) Deformation of the 25% TiB_2 coatings

Figure 7.5 Deformation of the multilayer coatings

7.7.2 Equivalent stress

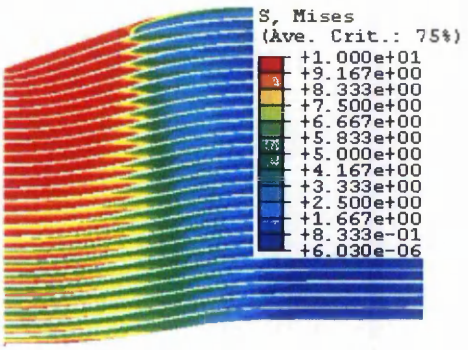

(a) The Mises stress contour for TiB_2

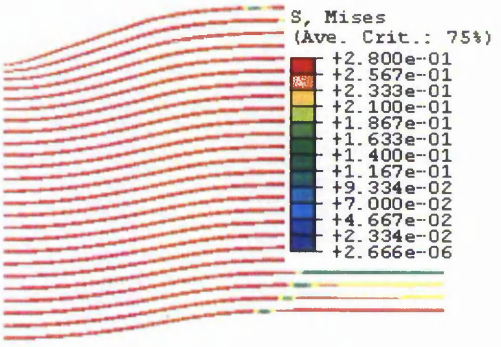

(b) The Mises stress contour for Al

Figure 7.6 Von Mises stress contours for 75% TiB_2 coating (h = 1016 nm)

Figure 7.6 shows the equivalent stresses for the different TiB_2 and Al layers in the 75% TiB_2 coating (h =1016 nm). The equivalent stress and equivalent strain results show that all of the aluminium layers under the indenter deform plastically, whereas only a small segment of the TiB_2 layers have plastic deformation at 1016 nm indentation depth.

7.7.3 Equivalent Plastic Strain in the substrate

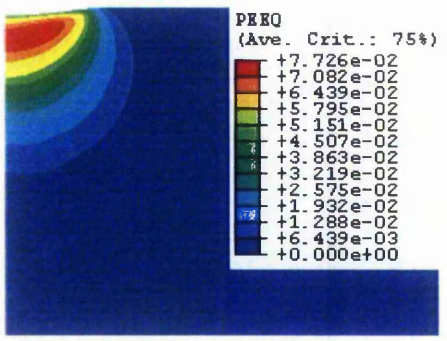

(a) 25% TiB_2 coating

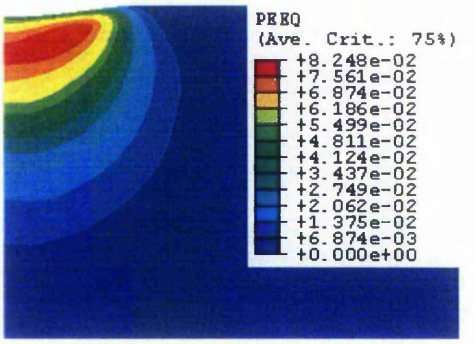

(b) 50% TiB_2 coating

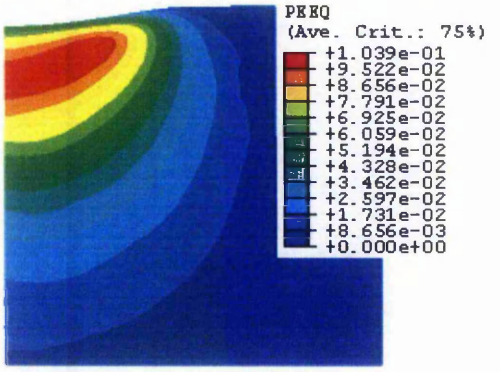

(c) 75% TiB_2 coating

Figure 7.7 Equivalent plastic strain contours in the substrate for the three types of coatings (h = 1016 nm)

The substrate has a noticeable influence on the measured properties of the coatings when plastic deformation occurs within the substrate. Figure 7.7 shows that the plastic deformation in the substrate increased with increasing percentage of TiB_2. This means that the influence of the substrate should be the most marked for the 75% TiB_2 coating system.

7.8 Hardness and elastic modulus

The results of the calculated hardness and elastic modulus are shown in Figures 7.8 and 7.11 respectively, where the hardness and elastic modulus values are plotted against depth of indentation for the three types of coatings. The results show that the values of hardness and elastic modulus for any depth of indentation increase as the percentage of TiB_2 increases from 25 to 75%. For the 75% TiB_2 and 50% TiB_2 coatings, the hardness values fall as the indentation depth increases. For the 25% TiB_2 coating, the hardness decreases first, and then increases gradually as the indentation depth increases.

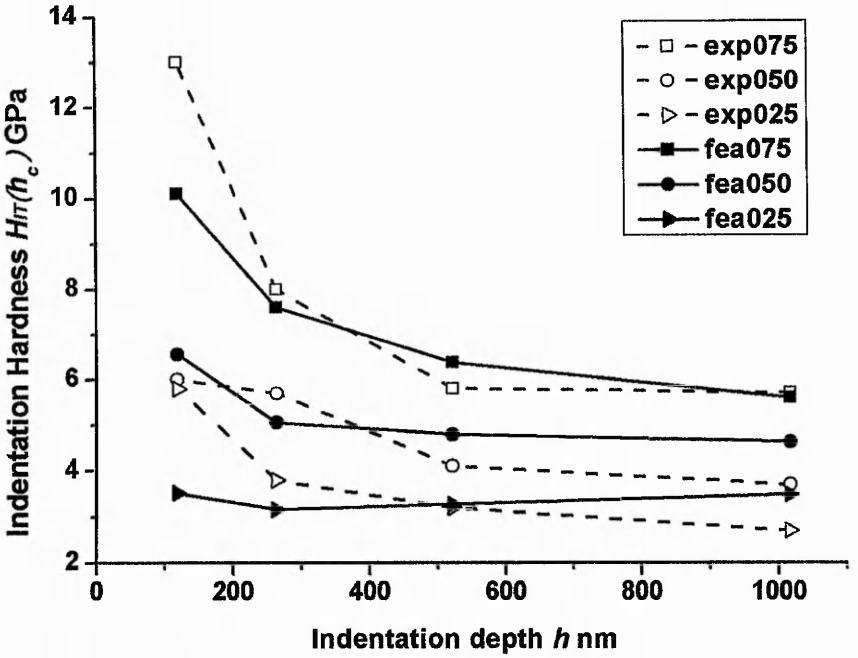

Figure 7.8 Comparison of hardness, based on h_c, between experimental and FEA [exp = experimental, fea = FEA and the number represents the volume fraction of TiB_2 in the coating, e.g. 025 = 25%]

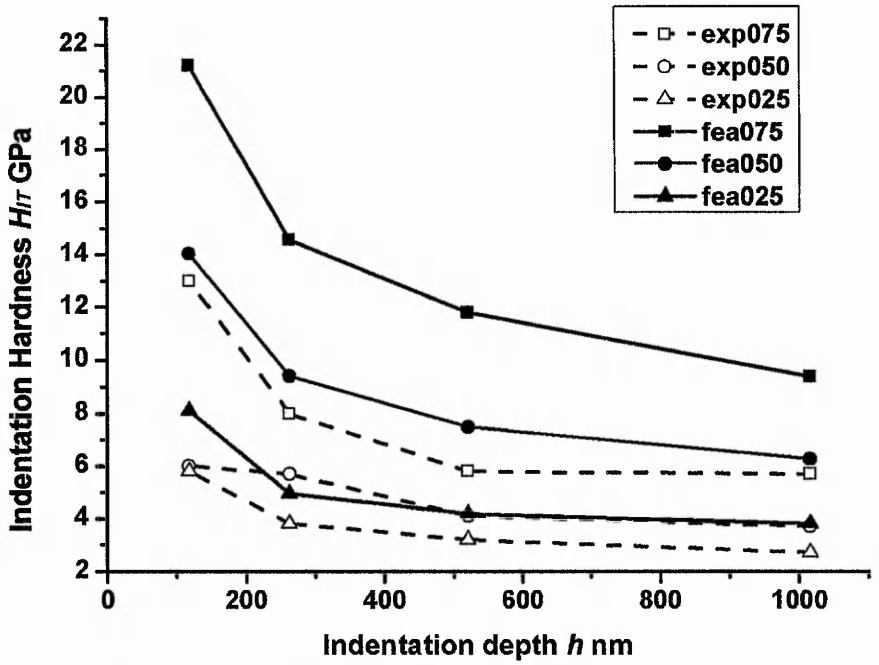

Figure 7.9 Comparison of experimental hardness and FEA values based on R_c [exp = experimental, fea = FEA and the number represents the volume fraction of TiB_2 in the coating, e.g. 025 = 25%]

Figure 7.8 shows that for the 75% TiB_2 coating and the 50% TiB_2 coating, the values of Indentation Hardness $H_{IT}(h_c)$ obtained from FEA agree reasonably well with those

from the experiments. For the 25% TiB_2 coating, there are some discrepancies between FEA and experimental values.

Figure 7.9 shows that the values of $H_{IT}(R_c)$ from FEA are significantly higher than the equivalent $H_{IT}(h_c)$ values shown in Figure 7.8. The difference is greatest at low indentation depths, being a factor of ~2 for 118 nm indentations, decreasing to ~1.4 for the 1016 nm indentations. The reason for this discrepancy is that the values of h_c calculated based on Equation (7.5) were markedly larger than the values of h_c indirectly obtained from FEA. For example, for the 75% TiB_2 coatings, at h_m=118 nm, h_c=100 nm, h_{rc}=69.37 nm, from Equation (7.6), the relationship between $H_{IT}(R_c)$ and $H_{IT}(h_c)$ can be obtained, i.e. $H_{IT}(R_c) \cong 2.078 H_{IT}(h_c)$. The $H_{IT}(R_c)$ values are generally higher than the experimental hardnesses, which are based on the measured h_c data although the trends are generally similar in both cases.

Figures 7.10 and 7.11 show that the values of elastic moduli $E(h_c)$ and $E(R_c)$ obtained from FEA are substantially different from the values of elastic modulus $E(h_c)$ obtained from the experiments. The reason for this is not clear at present. The difference between the elastic moduli $E(h_c)$ and $E(R_c)$ from FEA, is because the values of h_c from

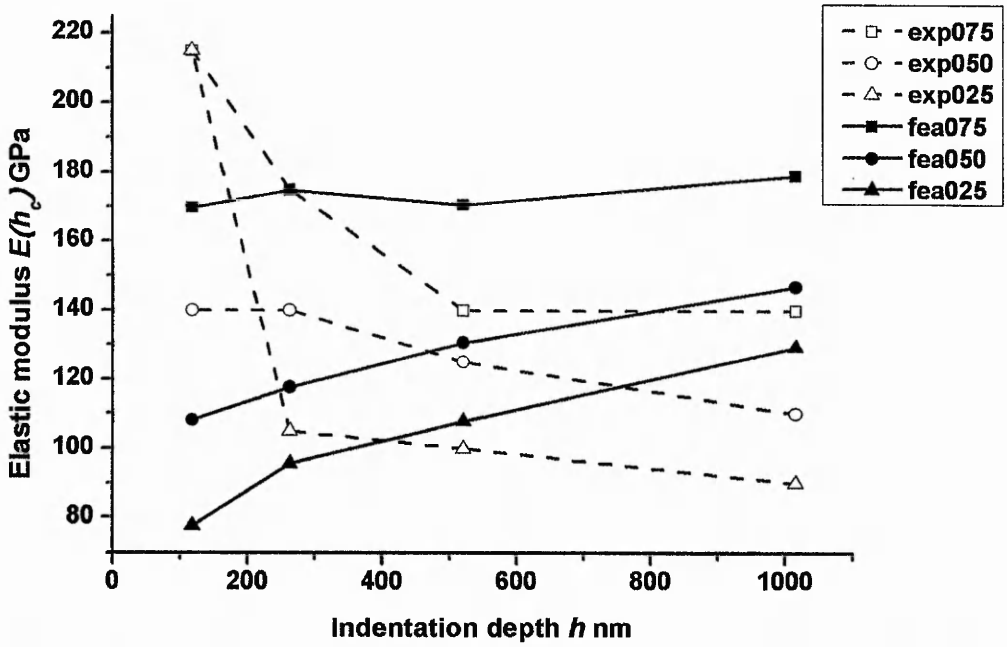

Figure 7.10 Comparison of elastic modulus, based on h_c, between experiments and FEA [exp = experimental, fea = FEA and the number represents the volume fraction of TiB_2 in the coating, e.g. 025 = 25%]

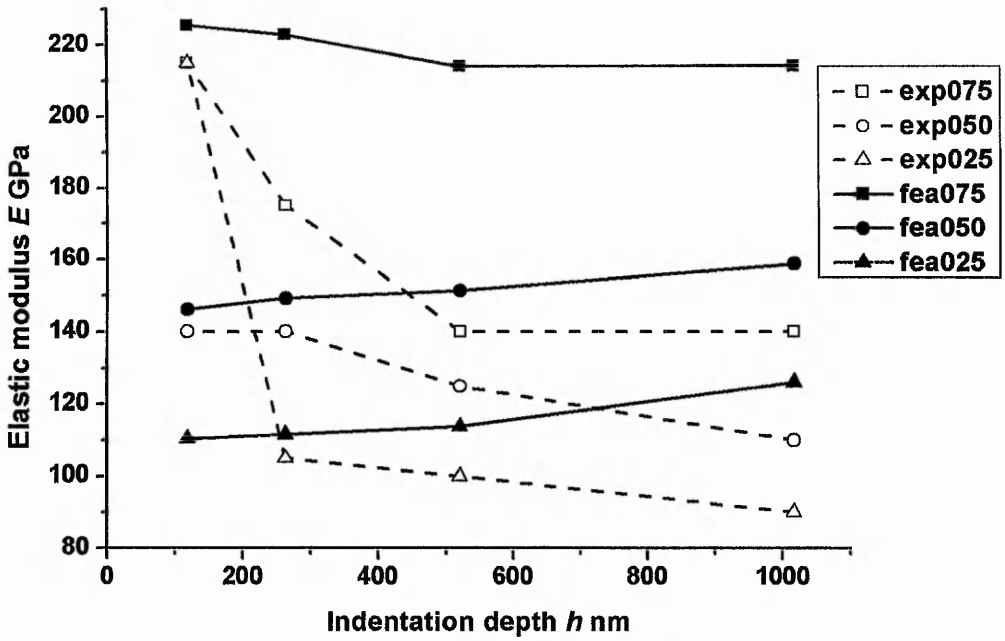

Figure 7.11 Comparison of experimentally determined elastic modulus values and the FEA values based on R_c, [exp = experimental, fea = FEA and the number represents the volume fraction of TiB_2 in the coating, e.g. 025 = 25%]

Equation (7.5) are markedly larger than those of $\gamma_h h_{rc}$, where h_{rc} was indirectly obtained from FEA. For example, for 75% T_iB_2 coatings, at h_m=1016 nm, h_c=934 nm, h_{rc}=721 nm, and γ_h=1.08523, thus from Equation (7.8), the relationship between $E(R_c)$ and $E(h_c)$ can be obtained, i.e. $E(R_c) = 1.194E(h_c)$.

The results also show that the influence of the substrate becomes more marked as the indentation depth increases. This can also be demonstrated by the increasing plastic deformation of the substrate as noted in section 7.7.3. At a shallow indentation depth, the properties are primarily determined by the structure and materials in the multilayer coatings. At greater indentation depths, the properties reflect the influence of a combination of the multilayer coatings and the substrate.

7.9 Hardness and elastic modulus variations with number of layers

7.9.1 Hardness variation with number of layers

The experimental study was based on a total of 25 layers, with each Al + TiB_2 layer having a thickness of 200 nm. This seems an arbitrary arrangement to give a total layer thickness of 5 μm. It is probable that as the number of layers increases, there is more disruption to the deposition process, and thus a cost penalty. Therefore it was decided to investigate, using FEA alternative total layer thicknesses, and thus number of layers, whilst maintaining a constant total coating thickness of 5 μm.

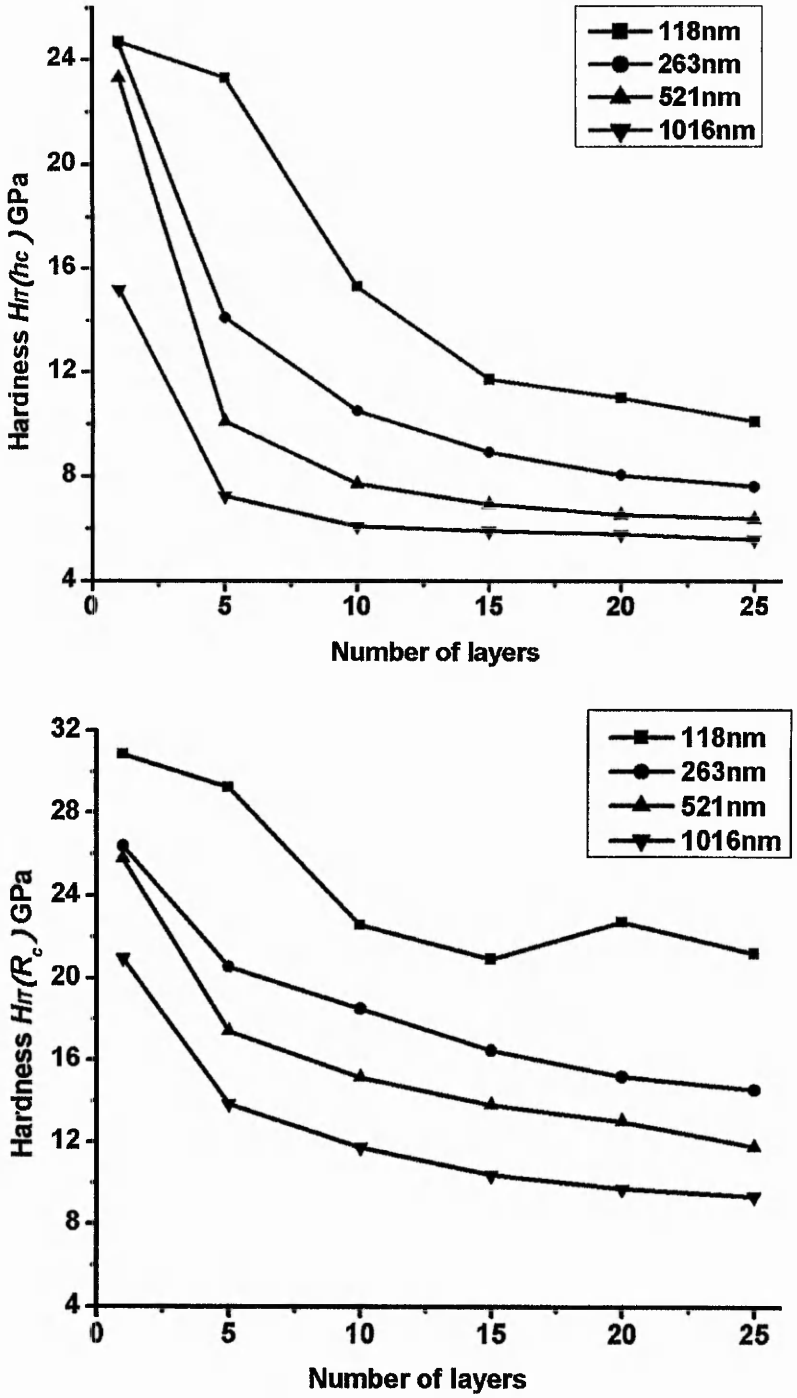

(a) 75% TiB2 coating

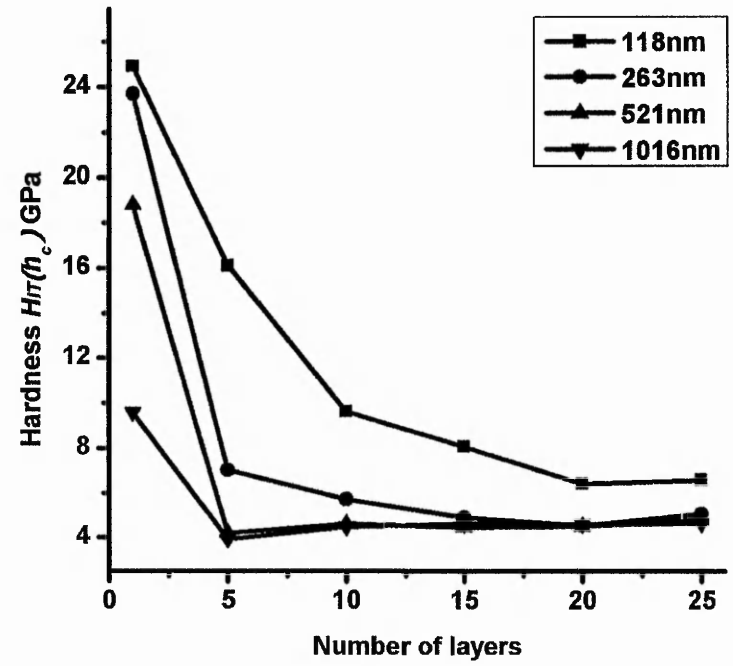

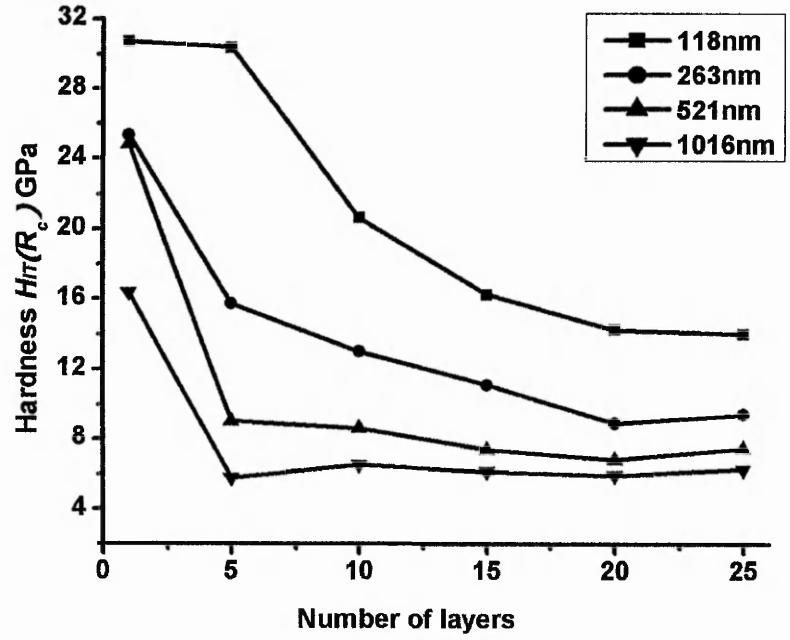

(b) 50% TiB_2 coating

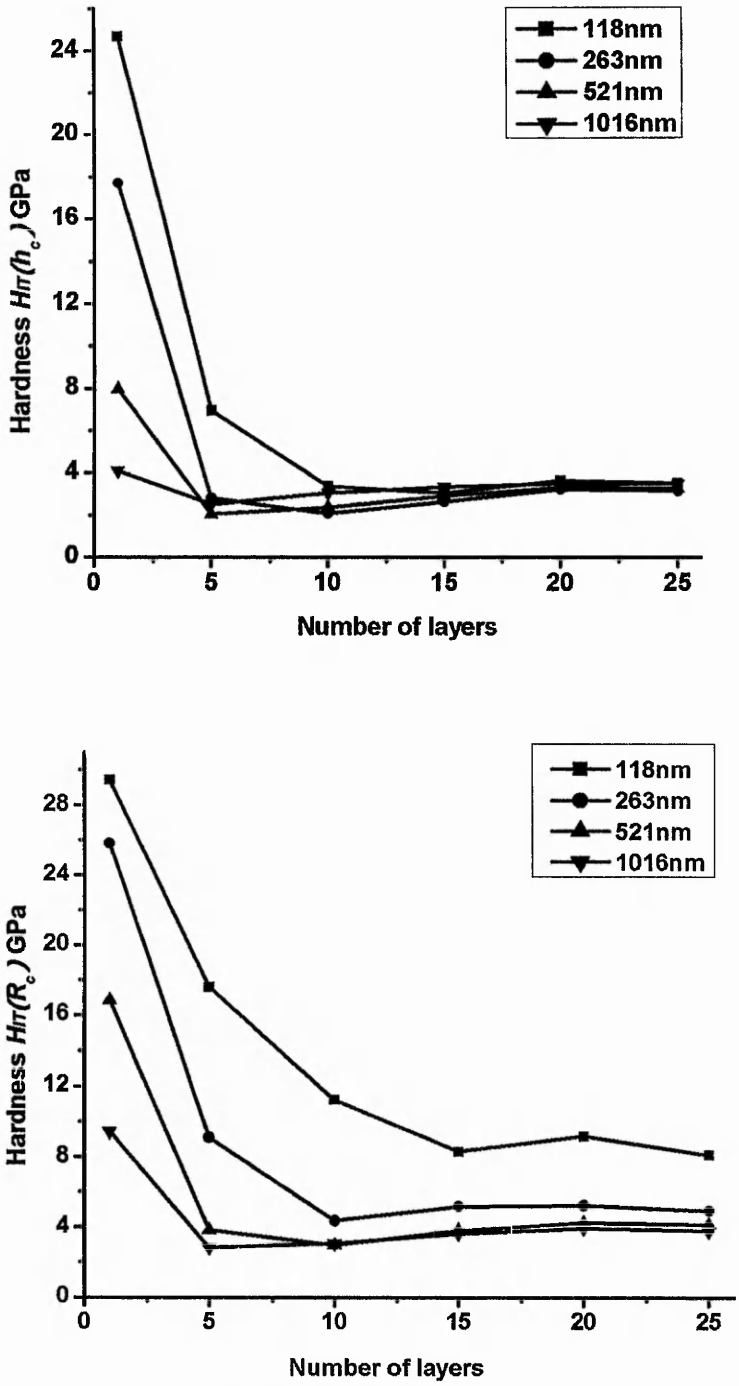

(c) 25% TiB2 coating

Figure 7.12 Hardness variation with number of layers

Figure 7.12 shows the calculated hardness values ($H_{IT}(h_c)$ and $H_{IT}(R_c)$), at the same depths as used previously, with number of layers for the three different compositions of multilayer coatings. For all the three compositions, the hardness decreased initially and then approached a constant value as the number of layers increased from 1 to 25. In

general the values of $H_{IT}(h_c)$ are lower than the equivalent $H_{IT}(R_c)$ values, for the reason discussed above, and the number of layers required for the latter to level off is generally considerably greater. For a given calculation method, the number of layers at which the hardness approached a constant value depended on two factors, i.e. indentation depth and percentage of TiB_2. The hardness approached a constant value with fewer layers when the indentation depth was greater and/or the percentage of TiB_2 was less. Thus, the desired hardness can be controlled by adjusting the percentage of TiB_2 with fewer layers. These results would suggest that it should be possible to save time and cost to produce a particular multilayer coating system.

7.9.2 Elastic modulus variation with number of layers

Figure 7.13 shows that the elastic modulus has the same tendency as the hardness, i.e. it also decreased initially and then approached a constant value as the number of layers increased from 1 to 25. The number of layers for which the elastic modulus approached a constant value also depends on two factors, i.e. indentation depth and percentage of TiB_2. Thus, the elastic modulus can also be controlled by adjusting the percentage of TiB_2, with the number of layers being minimised.

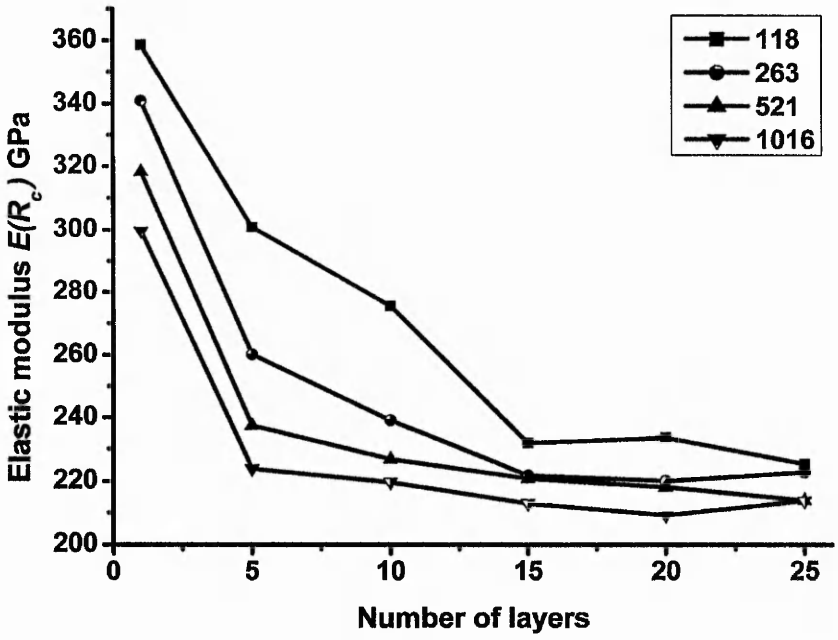

(a) 75% TiB_2 coating

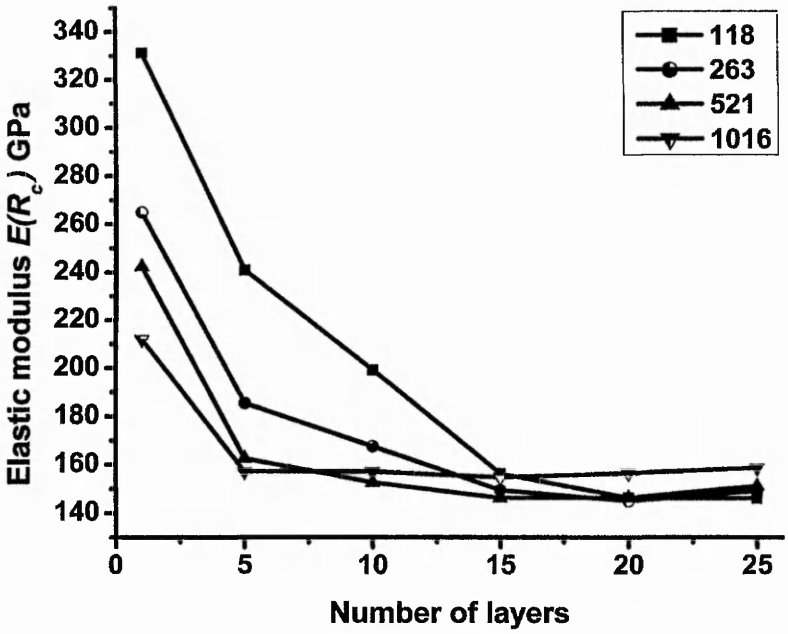

(b) 50% TiB2 coating

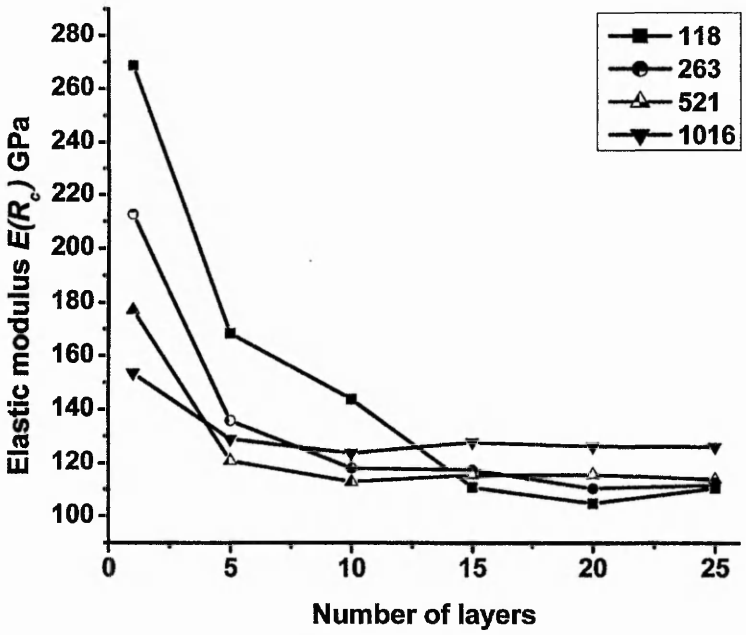

(c) 25% TiB_2 coating

Figure 7.13 Elastic modulus variation with number of layers

7.10 Summary

1) The explicit-to-implicit analysis method can be used to give equivalent load/unload force-displacement data, hardness and elastic modulus results as the pure implicit analysis method. The advantage of the explicit-to-implicit

analysis method over the pure implicit analysis method is computational time saving and relative ease of convergence.

The calculated values of Indentation Hardness and elastic modulus can be markedly different due to different calculation methods. Hardness and elastic modulus calculated based on the contact radius R_c obtained from FEA would give more precise results than those based on the contact depth h_c obtained from Equation (7.5).

2) For the sinking-in bulk material TiB_2, the value of h_c calculated based on Equation (7.5) is larger than the true value of h_c. So $H_{IT}(h_c)$ is less than $H_{IT}(R_c)$ for this model.

3) For the elastic modulus, a relationship between $E(R_c)$ and $E(h_c)$ was obtained, i.e. $\frac{E(R_c)}{E(h_c)} = \frac{h_c}{\gamma_h h_{rc}}$.

4) For the multilayer coatings of TiB_2 and Al, the extent of plastic deformation in the substrate increased with increasing percentage of TiB_2.

5) For the 75% TiB_2 and 50% TiB_2 25-layer coatings, the hardness values based on h_c decreased as the indentation depth increased. For the 25% TiB_2 coating, the hardness $H_{IT}(h_c)$ decreased initially and then increased gradually as the indentation depth increased. For all three types of coatings, $H_{IT}(R_c)$ decreased as the indentation depth increased. The values of Indentation Hardness $H_{IT}(h_c)$ obtained from FEA agreed reasonably well with those from the experiments.

6) For the multilayer coatings of alternating TiB_2 and Al, $E(h_c)$ is much lower than $E(R_c)$. This is because for indentations in this type of multilayer coating, the values of h_c calculated based on Equation (7.5) were markedly larger than the values of $\gamma_h h_{rc}$, where h_{rc} was indirectly obtained from FEA.

7) For all three compositions of multilayer coating systems, the hardness decreased first and then approached a constant value as the number of layers increased from 1 to 25 for a constant overall total coating thickness of 5 μm. For a given hardness calculation method, the number of layers for which the

hardness approached a constant value depended on two factors, i.e. indentation depth and percentage of TiB_2.

8) By analysing the hardness variation with the number of layers, the desired hardness can be controlled by adjusting the percentage of TiB_2 with fewer layers. This would save time and cost to produce a particular multilayer coating system.
9) The elastic modulus variation with number of layers has the same trend as the hardness variations. Thus, the elastic modulus can also be controlled by adjusting the percentage of TiB_2 and number of layers.

CHAPTER 8
RIGID INDENTATION CREEP MODELLING

Most of the mechanical property data that are available for ceramics have been measured at short times. However, in many operational situations the materials are required to operate for long periods. It is usually assumed that since most ceramics are relatively hard this means that there will be little time dependence of the mechanical properties at modest temperatures. In contact situations however, the localized stresses can be relatively high, and this may lead to time dependent plastic deformation at relatively low temperatures (Ashby & Frost, 1982; Carter et al 1988a, 1988b; Ren et al, 2001). It is experimentally difficult to determine the creep properties of ceramics, since the manufacture and testing of uniaxial tensile specimens is very expensive. Therefore it is appropriate to consider those tests which are experimentally straightforward and less costly to implement, but are more difficult to interpret, as a means of obtaining quantitative time dependent deformation data in ceramics. The aim of the research presented in this chapter is to investigate the application of FEA modelling of rigid indentation creep in ceramics. The analyses have been based on yttria stabilized cubic zirconia, YCZP, and single crystal MgO, since there exists a reasonable amount of data over a range of temperatures and times for these two ceramics.

Firstly, the modified dislocation creep model and the power law breakdown creep model were applied to the indentation creep deformation analyses for YCPZ at temperatures from 290 K to 1073 K. A FE indentation creep modelling procedure was proposed and implemented. The basic parameters, i.e. the activation energy for YCPZ and the stress index in the creep model were predicted from the analytical indentation creep analyses. This provides the basis to be able to predict the time dependent deformation for YCPZ in this temperature range for any applied stress state.

Secondly, the modified dislocation creep model and the power law breakdown creep model were used in the indentation creep deformation analyses for single crystal MgO at temperatures varying from 293 K to 873 K. A FE indentation creep modelling procedure was proposed and implemented. In this case, the activation energy, the 0 K shear flow stress of single crystal MgO and the stress index in the creep model were predicted based on the analytical indentation creep analyses.

8.1 Finite element modelling of diamond indentation creep in YCPZ

8.1.1 Introduction

Based on the analytical models, it was found, as outlined in section 8.1.2.1, that the modified plasticity (dislocation glide) creep and the power law breakdown (glide plus climb) creep models were the most suitable for the modelling of indentation creep at low temperatures. The indentation creep FE modelling has been implemented for YCPZ at low temperatures by programming the two creep models as ABAQUS creep user subroutines.

8.1.2 Indentation creep modelling procedure

8.1.2.1 Analytical Approach

A preliminary study of the analytical modelling of the indentation creep data in YCPZ using the equation from Ashby and Frost (1982), i.e. Equation (8.1a), for glide controlled dislocation deformation showed that this was not able to model the experimental data well over the complete temperature range (Hu and Henshall, to be published). Therefore, it is now proposed that the relevant rate controlling equation can be modified by incorporating a stress constant α and a reference temperature T_{ref} into this constitutive equation. Thus, this modified dislocation glide creep rate equation has been termed the Reference Temperature creep model and can be written as Equation (8.1b),

$$\dot{\varepsilon}_{cr} = \frac{A}{\sqrt{3}}\dot{\gamma}_p\left(\frac{\sigma}{\sqrt{3}\mu_s}\right)^n \exp\left\{-\frac{\beta_p \Delta F_p}{KT}\left[1-\left(\frac{\sigma}{\sqrt{3}\hat{\tau}_p}\right)^p\right]^q\right\} \qquad (8.1a)$$

$$\dot{\varepsilon}_{cr} = \frac{A}{\sqrt{3}}\dot{\gamma}_p\left(\frac{\alpha\sigma}{\sqrt{3}\mu_s}\right)^n \exp\left\{-\frac{\beta_p \Delta F_p}{KT_{ref}}\left(\frac{T_{ref}}{T}\right)^m\left[1-\left(\frac{\sigma}{\sqrt{3}\hat{\tau}_p}\right)^p\right]^q\right\} \qquad (8.1b)$$

where, following Ashby and Frost (1982), $p = 0.75$, $q = 4/3$, $\Delta F_p = \gamma\mu_s b^3$, $\dot{\varepsilon}_{cr}$ is the equivalent creep strain rate, σ is the equivalent stress, ΔF_p is the activation energy, $\hat{\tau}_p$ is the flow stress at $T = 0$ K, μ_s is the shear modulus, $\dot{\gamma}_p$ is the pre-exponential of lattice-resistance-controlled glide, b is the Burgers vector, T is temperature, T_{ref} is the reference temperature, K is the Boltzman constant, and A, α, β_p, γ, m and n are adjustable constants.

For YCPZ, $b = 3.22e-10$ m, $\mu_s = 71$ GPa, and $\hat{\tau}_p = 5680$ MPa, (taken from Carter et al,

1988a). α was assumed to be 2000 (Frost and Ashby, 1982). A was assumed to be 1.0 and T_{ref} was assumed to be 273 K. Values for the other parameters, i.e. $m = 0.57$, $\gamma = 0.27$, and $\beta_p = 0.8$, were obtained based on the analytical indentation creep analysis in the present study.

Assuming $\sigma = H / C_{cr}$, where C_{cr} is a constant, and replacing σ with the indentation hardness H, the hardness rate equation (Li et al, 1991) can be obtained based on Equation (8.1b),

$$\dot{H} = -\frac{\sqrt{3}}{6}(1+k)^3 H\dot{\varepsilon}_{cr}$$
$$= -\frac{A}{6}(1+k)^3 H\dot{\gamma}_p\left(\frac{\alpha H}{\sqrt{3}C_{cr}\mu_s}\right)^n \exp\left\{-\frac{\beta_p \Delta F_p}{KT_{ref}}\left(\frac{T_{ref}}{T}\right)^m [1-(\frac{H}{\sqrt{3}C_{cr}\hat{\tau}_p})^p]^q\right\} \quad (8.2)$$

where, $k = c/a$, is a material constant during the indentation process (Johnson, 1970); c is the radius of elastic-plastic zone, and a is the contact radius under load.

The power law breakdown creep model was found to be an alternative appropriate creep model for the indentation creep of YCPZ at low temperatures. The creep strain rate equation in this case is,

$$\dot{\varepsilon}_{cr} = \frac{A}{\sqrt{3}}[\sinh(\frac{\alpha_p \sigma}{\sqrt{3}\mu_s})]^n \exp(-\frac{Q_{cr}}{RT}) \quad (8.3)$$

where, α_p is a constant, $Q_{cr} = \gamma Q_v$, Q_{cr} is the activation energy for creep, Q_v is the activation energy for extrinsic diffusion, γ is a constant and R is the universal gas constant.

For YCPZ, $A = 10$, $\alpha_p = 300$, and $Q_v = 243$ KJ/mol.

The corresponding hardness rate equation can be obtained as,

$$\dot{H} = -\frac{A}{6}(1+k)^3 H[\sinh(\frac{\alpha_p H}{\sqrt{3}C\mu_s})]^n \exp(-\frac{Q_{cr}}{RT}) \quad (8.4)$$

8.1.2.2 Formulation of procedure to apply to experimental data

The Knoop hardness values at several time points were obtained from the Knoop indentation creep tests. In the present investigation, the indentation hardness values at the corresponding time points were calculated from 2D axisymmetric FE creep indentation modelling. An elastic perfectly plastic material model was assumed, with the yield stress Y being assumed to be $HK/3.1$, based on the correlation found

previously, section 5.9.1. The indentation hardness, H_{IT0}, can be calculated from the indentation modelling. The ratio of the Knoop hardness to the indentation hardness at time $t = 0$ was then used to calculate the indentation hardness at subsequent times in the indentation creep process,

$$\lambda_0 = \frac{HK_0}{H_{IT0}} \tag{8.5}$$

For $t = 100$, $t = 1000$ and $t = 10000$,

$$H_{IT100} = \frac{HK_{100}}{\lambda_0}, H_{IT1000} = \frac{HK_{1000}}{\lambda_0}, H_{IT10000} = \frac{HK_{10000}}{\lambda_0} \tag{8.6}$$

Based on above method, the Knoop hardness obtained from experiments were changed to the indentation hardness, which can be used to represent the experimental results and be compared to the indentation hardness from the 2D axisymmetric FE creep indentation modelling.

The ratio, C_{HY}, of the indentation hardness to the yield stress can be calculated as

$$C_{HY} = \frac{H_{IT0}}{Y} \tag{8.7}$$

The constant k can also be determined from the FE indentation modelling.

8.1.2.3 Calculate 'constants' from experimental data

Based on the indentation hardness values that were calculated from the experimental Knoop hardness values at different time points, the constants, e.g. ΔF_p, Q_{cr} and n in the rate equations can be determined from the analytical indentation hardness rate models, as shown in section 8.1.3.

8.1.2.4 Implementation of the creep model in ABAQUS

In order to implement in ABAQUS/Standard the creep models described above, the user creep subroutines were programmed. $\partial \Delta \varepsilon_{cr} / \partial \sigma$ was required in the user creep subroutine.

For the glide controlled creep model,

$$\frac{\partial \Delta \varepsilon_{cr}}{\partial \sigma} = \frac{A \Delta t}{\sqrt{3}} \dot{\gamma}_p \{ n (\frac{\alpha \sigma}{\sqrt{3}\mu_s})^{n-1} \frac{\alpha}{\sqrt{3}\mu_s} \exp\left\{ -\frac{\beta_p \Delta F_p}{K T_{ref}} \left(\frac{T_{ref}}{T} \right)^m [1 - (\frac{\sigma}{\sqrt{3}\hat{\tau}_p})^p]^q \right\} +$$

$$(\frac{\alpha \sigma}{\sqrt{3}\mu_s})^n \exp\left\{ -\frac{\beta_p \Delta F_p}{K T_{ref}} \left(\frac{T_{ref}}{T} \right)^m [1 - (\frac{\sigma}{\sqrt{3}\hat{\tau}_p})^p]^q \right\} \bullet$$

$$[-\frac{\beta_p \Delta F_p}{KT_{ref}}\left(\frac{T_{ref}}{T}\right)^m q[1-(\frac{\sigma}{\sqrt{3}\hat{\tau}_p})^p]^{q-1}[-p(\frac{\sigma}{\sqrt{3}\hat{\tau}_p})^{p-1}\frac{\alpha}{\sqrt{3}\hat{\tau}_p}]\} \tag{8.8}$$

For the power law breakdown creep model,

$$\frac{\partial \Delta\varepsilon_{cr}}{\partial\sigma} = \frac{An\alpha\Delta t}{3\mu_s}\cosh(\frac{\alpha\sigma}{\sqrt{3}\mu_s})[\sinh(\frac{\alpha\sigma}{\sqrt{3}\mu_s})]^{n-1}\exp(-\frac{Q_{cr}}{RT}) \tag{8.9}$$

Using the initial values of the constants obtained from the analytical creep model, the FE indentation creep modelling was carried out. Then the constants were adjusted slightly by comparing the values of the indentation hardness from FEA with those from the experiments.

8.1.3 Analytical indentation creep analysis in YCPZ

Indentation creep tests were implemented with the temperature varying from 290K to 1073K for YCPZ by Henshall et al (1989). Given the complexity of the analytical equations, it is not possible to use a simple linear regression analysis to determine the values of the unknown constants, i.e. γ, β_p and n in the reference temperature creep model, and γ and n in the power law breakdown creep model. Consequently, the hardness values were calculated at each temperature for a range of values of the constants, and the values obtained Tables 8.1 and 8.2, were the values which gave the closest fits to the experimental data.

The hardness variations with time using the two analytical creep models for YCPZ are shown in Figures 8.1 and 8.2. These figures show that both the reference temperature creep model and the power law breakdown creep model can deliver similar results of

Table 8.1 Constants in the reference temperature creep model for YCPZ

Temperature K	290	473	573	673	773	873	973	1073
DFP KJ	$0.27\mu_s b^3$	$0.27\mu_s b^3$	$0.27\mu_s b^3$	$0.27\mu_s b^3$	$0.27\mu_s b^3$	$0.27\mu_s b^3$	$0.27\mu_s b^3$	$0.27\mu_s b^3$
Stress index n	3.33	3.24	3.49	4.73	4.06	4.01	4.17	4.06

Table 8.2 Constants in the power law breakdown creep model for YCPZ

Temperature K	290	473	573	673	773	873	973	1073
Q_{cr} KJ/mol	0.5* 243	0.72* 243	0.72* 243	0.72* 243	0.806* 243	0.806* 243	0.806* 243	0.806* 243
Stress index *n*	4.83	5.55	5.08	5.7	6.0	6.0	6.0	6.0

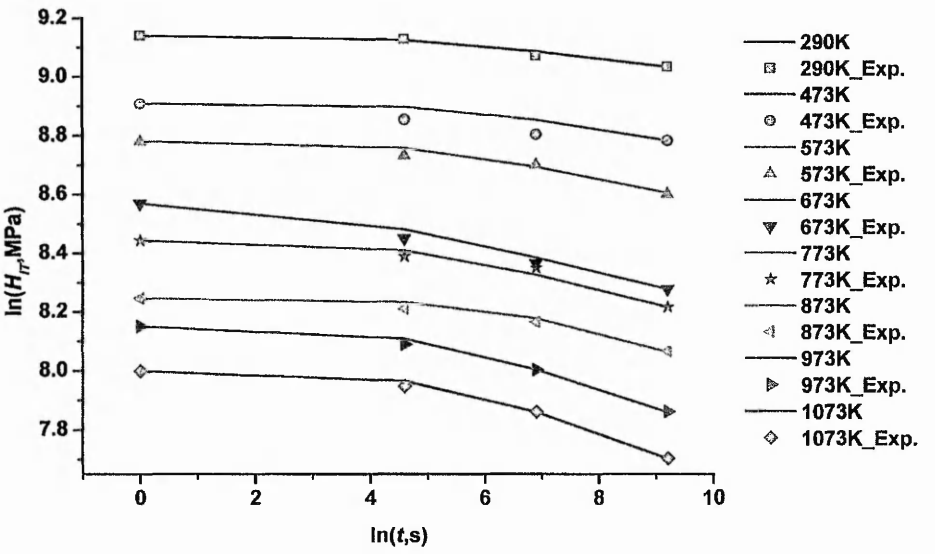

Figure 8.1 Analytical hardness variation with time using the reference temperature creep model for YCPZ

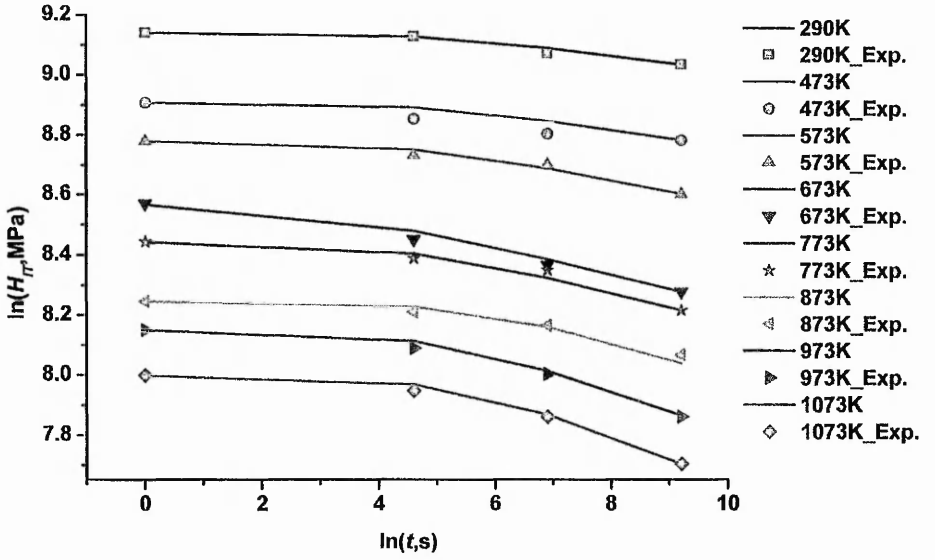

Figure 8.2 Analytical hardness variation with time using the power law breakdown creep model for YCPZ

hardness variations with time for YCPZ. It should be noted that values of the parameters have been used which appear to give the best fit to the data at a particular temperature and have been allowed to vary with temperature. This variation may be either due to a slight change in the physical mechanism, or inaccuracies in the experimental data.

8.1.4 FE MODELLING OF INDENTATION CREEP in YCPZ

8.1.4.1 FE model

A 2D axisymmetric model, which is similar to that described in section 5.1, was used to enable the analyses to be performed with a sufficiently refined mesh adjacent to the indenter. The indenter was modelled as a sharp, rigid cone with semi-apical included angle of 70.3°. Yttria stabilized cubic polycrystalline ceramic, YCPZ, was used as the substrate.

The static indentation modelling was carried out first, and then the applied force load, $F_Z = -2.94$ N, on the reference point of the rigid indenter, was maintained for the required period of time.

8.1.4.2 Results

Determining constants

In the FE analysis the values for the relevant parameters, apart from the stress index, n, were the same as those presented in sections 8.1.2 and 8.1.3. It was found that the value for n determined from the analytical analysis usually needed to be adjusted slightly in the FE analysis in order to fit the experimental results of hardness variation with time. Tables 8.3 and 8.4 give the adjusted constants for YCPZ that were obtained by comparing the hardness values from FEA and those from the experiments at different times.

Table 8.3 Adjusted constants in the reference temperature creep model for YCPZ

Temperature K	290	473	573	673	773	873	973	1073
Stress index n	5.76	4.58	4.59	5.00	4.61	4.63	4.55	4.30

Table 8.4 Adjusted constants in the power law breakdown creep model for YCPZ

Temperature K	290	473	573	673	773	873	973	1073
Stress index n	4.97	5.95	5.28	5.9	6.2	6.0	6.0	6.0

Hardness variation with time

Figure 8.3 shows the comparison of hardness variation with time from the FEA using the reference temperature creep model and the experimental data. Figure 8.4 shows the comparison of hardness variation with time for the FEA using the power law breakdown creep model and the experimental data. The results show that the hardness variations with time from FEA agree well with those from the experiments.

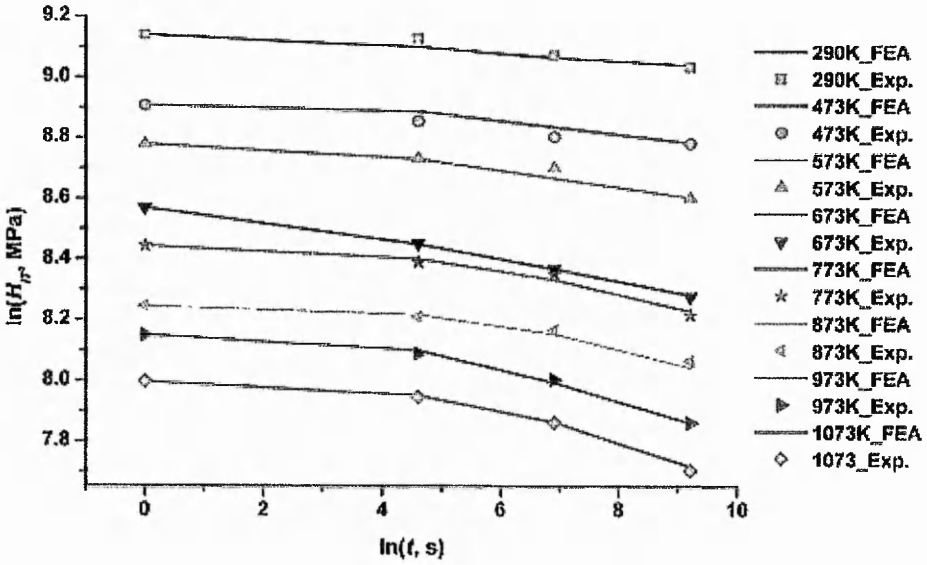

Figure 8.3 Comparison of hardness variation with time for the FEA using the reference temperature creep model and the experimental data

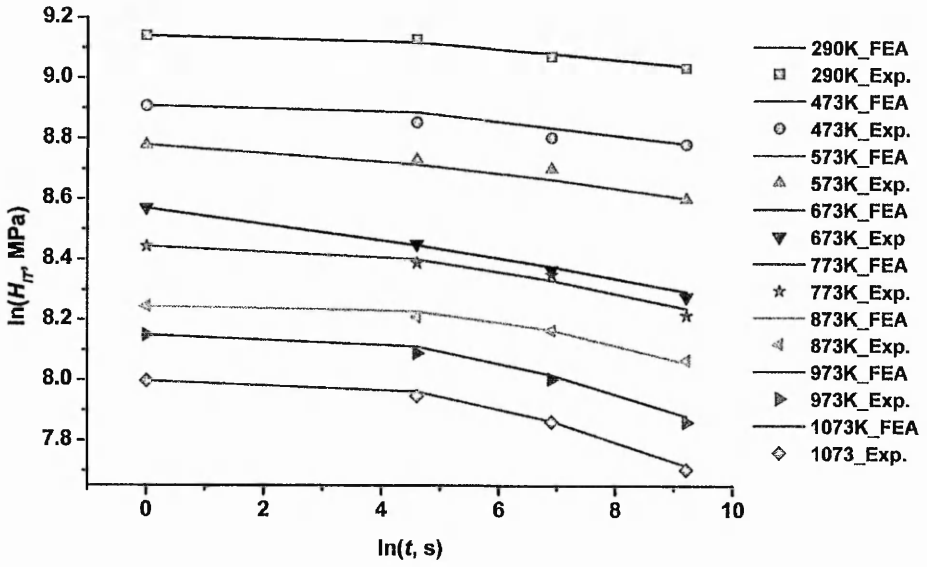

Figure 8.4 Comparison of hardness variation with time for the FEA using the power law breakdown creep model and the experimental data

Creep strain evolution with time

Figures 8.5 to 8.8 show the evolution of creep strain with time in YCPZ using the power law breakdown creep model at T=290 K and T=1073 K respectively. These figures

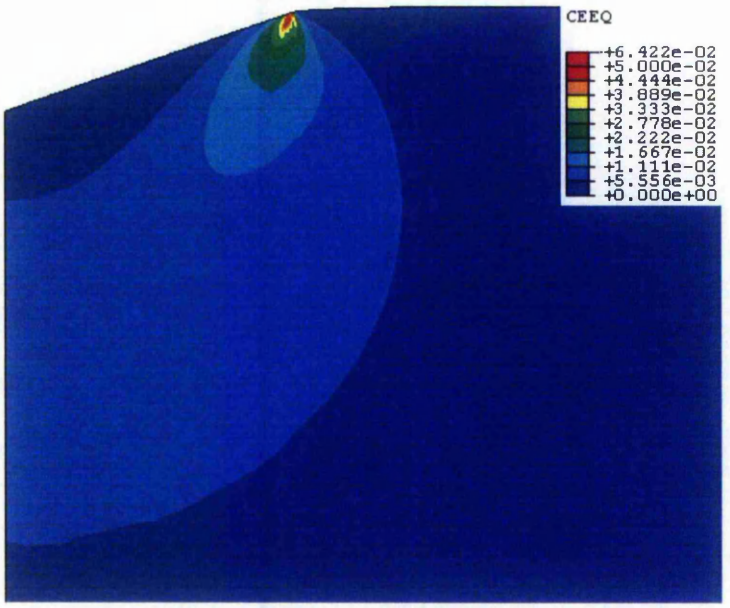

Figure 8.5 Creep strain contours at t = 1000 s using the power law breakdown creep model for YCPZ (T = 290 K)

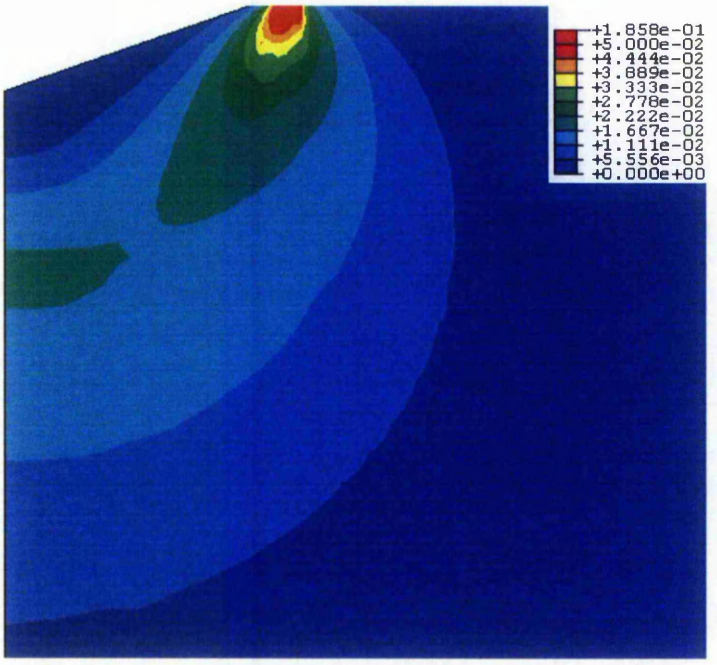

Figure 8.6 Creep strain contours at t = 10000 s using the power law breakdown creep model for YCPZ (T = 290 K)

show that the creep deformation originates from the contact edge, followed by extension into the substrate towards the central region. However, the central region that is just beneath the indenter has little creep deformation. It can also be seen that the creep deformation at higher temperature is more marked than that at the lower temperature.

This pattern in the evolution of the creep deformed zone provides a probable explanation for the slight differences in stress indices between the analytical models and the FE results, *cf* Tables 8.1 and 8.2 vs. 8.3 and 8.4 respectively, since the analytical model assumes that there is a uniform hemispherical creep zone from the outset (Li et al, 1991). The FE results clearly indicate that this is not the case.

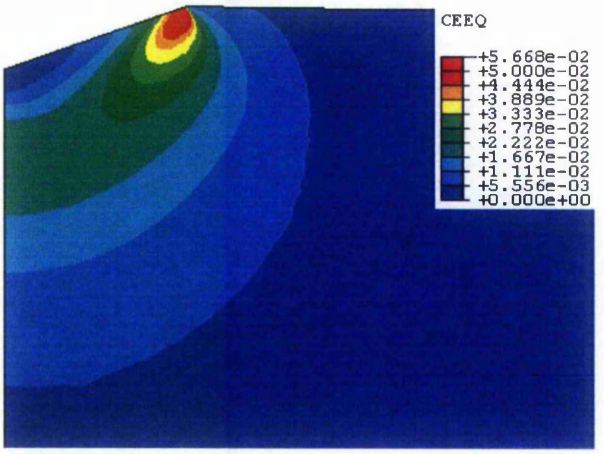

Figure 8.7 Creep strain contours at t = 1000 s using the power law breakdown creep model for YCPZ (T = 1073 K)

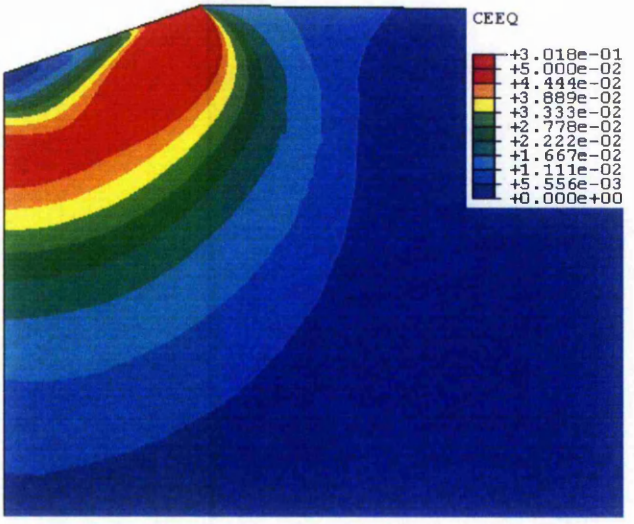

Figure 8.8 Creep strain contours at t = 10000 s using the power law breakdown creep model for YCPZ (T = 1073 K)

8.1.5 Summary for FE indentation creep modelling in YCPZ

1) The reference temperature creep model and the power law breakdown creep model were both suitable to be used for indentation creep deformation at low temperature.
2) An indentation creep modelling procedure was formulated.

3) Analytical indentation creep analyses for YCPZ were implemented. The physical constants, such as the activation energy for creep can be estimated.
4) FE indentation creep modelling for YCPZ was implemented. The results of hardness variation with time from FEA agree well with those from the experiments.
5) The FE indentation creep models showed that the creep deformation in YCPZ originates from the contact edge, then it extends into the substrate towards the central region. However, the central region just beneath the indenter has little creep deformation. It can also be seen that creep deformation at higher temperatures is more marked than that at lower temperatures.

8.2 Finite element modelling of diamond indentation creep in MgO

Indentation creep FE modelling has been implemented for single crystal MgO at low temperatures by programming the two creep models as ABAQUS creep user subroutines.

8.2.1 Indentation creep modelling procedure

8.2.1.1 Analytical approach

A similar approach has been used to model indentation creep in the (001) cube face of single crystal MgO in the <100> and <110> directions. In this case it was found that the data could be fitted to a modified form of Equation (8.1a) in which only the adjustable parameter α is required, rather than a reference temperature (8.1.2.1), i.e. the resultant equation is:

$$\dot{\varepsilon}_{cr} = \frac{A}{\sqrt{3}}\dot{\gamma}_p\left(\frac{\alpha\sigma}{\sqrt{3}\mu_s}\right)^n \exp\left\{-\frac{\Delta F_p}{KT}\left[1-\left(\frac{\sigma}{\sqrt{3}\hat{\tau}_p}\right)^p\right]^q\right\} \qquad (8.10)$$

where, $n=2$, $p=0.75$, $q=4/3$, $\Delta F_p = \gamma\mu_s b^3$, $\hat{\tau}_p = \beta\mu_s$, $\dot{\varepsilon}$ is the equivalent creep strain rate, σ is the equivalent stress, ΔF_p is the activation energy, $\hat{\tau}_p$ is flow stress at $T=0$ K, μ_s is the shear modulus, $\dot{\gamma}_p$ is the pre-exponential of lattice-resistance-controlled glide (s^{-1}), b is the Burgers vector, T is temperature, K is the Boltzman constant and A, α, γ, and β are adjustable constants.

For MgO, $\mu_s = 126$ GPa, $b = 2.98e-10$ m and α was assumed to be 2000 (Frost and Ashby, 1982). A was assumed to be 1.0.

Using the same approach as described in section 8.1.2.1, the hardness rate equation based on Equation (8.10) becomes,

$$\dot{H} = -\frac{\sqrt{3}}{6}(1+k)^3 H\dot{\varepsilon}_{cr}$$
$$= -\frac{A}{6}(1+k)^3 H\dot{\gamma}_p\left(\frac{\alpha H}{\sqrt{3}C\mu_s}\right)^n \exp\left\{-\frac{\Delta F_p}{KT}\left[1-\left(\frac{H}{\sqrt{3}C\hat{\tau}_p}\right)^p\right]^q\right\} \qquad (8.11)$$

The power law breakdown creep model was found to be an alternative suitable creep model for the indentation creep of MgO at low temperatures. The creep strain rate equation in this case is the same as Equation (8.3), i.e.

$$\dot{\varepsilon}_{cr} = \frac{A}{\sqrt{3}}\left[\sinh\left(\frac{\alpha_p \sigma}{\sqrt{3}\mu_s}\right)\right]^n \exp\left(-\frac{Q_{cr}}{RT}\right) \qquad (8.12)$$

where in this instance, $Q_{cr} = \gamma Q_v$, Q_{cr} is the activation energy for creep, Q_v is the activation energy of the extrinsic diffusion, γ is a constant and R is the universal gas constant.

For MgO, $\alpha_p = 2000$, and $Q_v = 261$ KJ/mol, from Frost and Ashby (1982). A was assumed to be 20.0 in this model.

The corresponding hardness rate equation is given as above by Equation (8.4).

8.2.1.2 Formulation of procedure to apply to experimental data

The same procedure as outlined in section 8.1.2.2 was used for the MgO indentation creep data, with the only slight difference that in this case the yield stress Y was initially taken as $HK/3$.

8.2.1.3 Calculate 'constants' from experimental data

The same procedure as described in section 8.1.2.3 was used to give estimates for the relevant parameters in the creep rate equations based on fitting the analytical equations to the results as described in section 8.2.2.

8.2.1.4 Implementation of the creep model in ABAQUS

The same procedure as described in section 8.1.2.4 was used. In this case though, the user creep subroutine for the modified dislocation glide creep model is,

$$\frac{\partial \Delta\varepsilon_{cr}}{\partial\sigma} = \frac{A\Delta t}{\sqrt{3}}\dot{\gamma}_p\left\{n\left(\frac{\alpha\sigma}{\sqrt{3}\mu_s}\right)^{n-1}\frac{\alpha}{\sqrt{3}\mu_s}\exp\left\{-\frac{\Delta F_p}{KT}\left[1-\left(\frac{\sigma}{\sqrt{3}\hat{\tau}_p}\right)^p\right]^q\right\}+\right.$$

$$(\frac{\alpha\sigma}{\sqrt{3}\mu_s})^n \exp\left\{-\frac{\Delta F_p}{KT}[1-(\frac{\sigma}{\sqrt{3}\hat{\tau}_p})^p]^q\right\}\bullet[\frac{\Delta F_p}{KT}q[1-(\frac{\sigma}{\sqrt{3}\hat{\tau}_p})^p]^{q-1}[-p(\frac{\sigma}{\sqrt{3}\hat{\tau}_p})^{p-1}\frac{\alpha}{\sqrt{3}\hat{\tau}_p}]\} \quad (8.13)$$

Equation (8.9) is again used for the power law breakdown creep model.

In a similar manner to that discussed in section 8.1.2.4, the constants obtained from the analytical creep model were used as initial values in the FE indentation creep modelling. The constants were then adjusted slightly by comparing the values of the indentation hardness from FEA with the experimental values.

8.2.2 Analytical indentation creep analysis in MgO

Indentation creep tests were implemented with the temperature varying from 293K to 873K for single crystal MgO by Ren et al (2002). Using the procedures described in sections 8.1.2.3, 8.1.3 and 8.2.1.3, the unknown constants, i.e. γ and β in the modified dislocation creep model, and γ and n in the power law breakdown creep model, for MgO <100> and MgO <110> can be obtained, Tables 8.5 to 8.8.

Table 8.5 Modified dislocation glide creep model for MgO (001) <100>

Temperature K	293	373	473	673	873
DFP KJ	$0.17\,\mu_s b^3$	$0.195\,\mu_s b^3$	$0.226\,\mu_s b^3$	$0.251\,\mu_s b^3$	$0.246\,\mu_s b^3$
$\hat{\tau}_p$ MPa	$0.013\,\mu_s$	$0.013\,\mu_s$	$0.013\,\mu_s$	$0.013\,\mu_s$	$0.013\,\mu_s$

Table 8.6 Power law breakdown creep model for MgO (001) <100>

Temperature K	293	373	473	673	873
Q_{cr} KJ/mol	0.75*261	1.0*261	1.0*261	1.0*261	0.90*261
Stress index n	5.4	6.24	4.98	4.02	3.58

Table 8.7 Modified dislocation glide creep model for MgO (001) <110>

Temperature K	293	373	473	673	873
DFP KJ	$0.171\,\mu_s b^3$	$0.186\,\mu_s b^3$	$0.207\,\mu_s b^3$	$0.232\,\mu_s b^3$	$0.233\,\mu_s b^3$
$\hat{\tau}_p$ MPa	$0.023\,\mu_s$	$0.020\,\mu_s$	$0.018\,\mu_s$	$0.016\,\mu_s$	$0.016\,\mu_s$

Table 8.8 Power law breakdown creep model for MgO (001) <110>

Temperature K	293	373	473	673	873
Q_{cr} KJ/mol	0.75*261	0.90*261	0.90*261	0.90*261	0.73*261
n	3.02	3.67	3.38	3.10	2.11

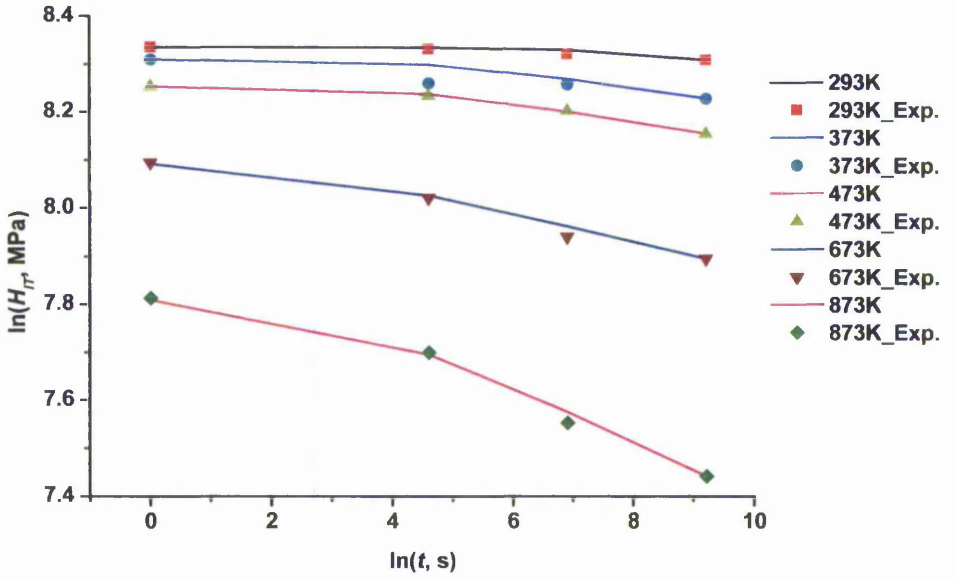

Figure 8.9 Analytical hardness variation with time using the glide controlled creep model for MgO <100>

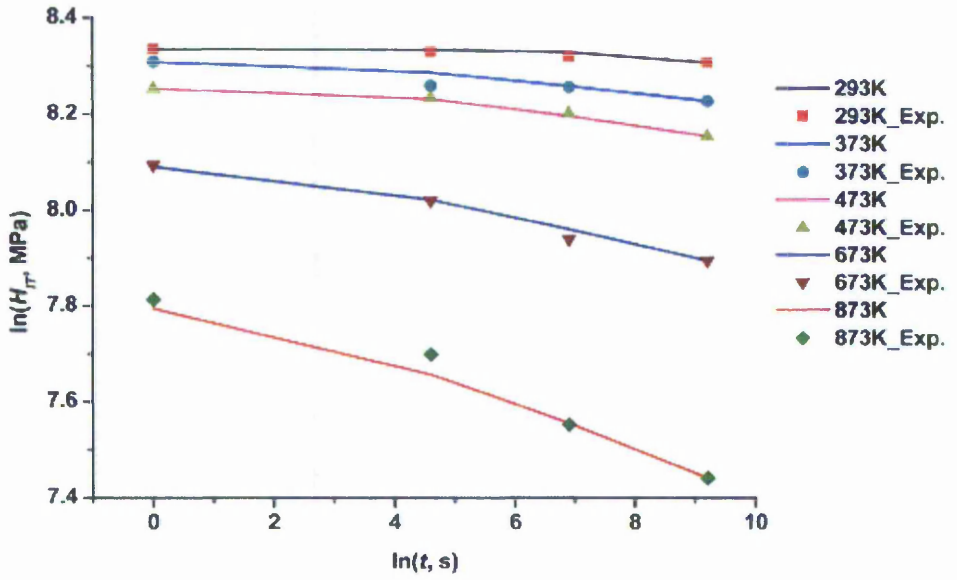

Figure 8.10 Analytical hardness variation with time using the power law breakdown creep model for MgO <100>

The analytical hardness variations with time using the two creep models for MgO <100> and MgO <110> are shown in Figures 8.9 to 8.12. These figures show that both the modified dislocation creep model and the power law breakdown creep model can provide similar results for the hardness variations with time for MgO <100> and MgO <110>.

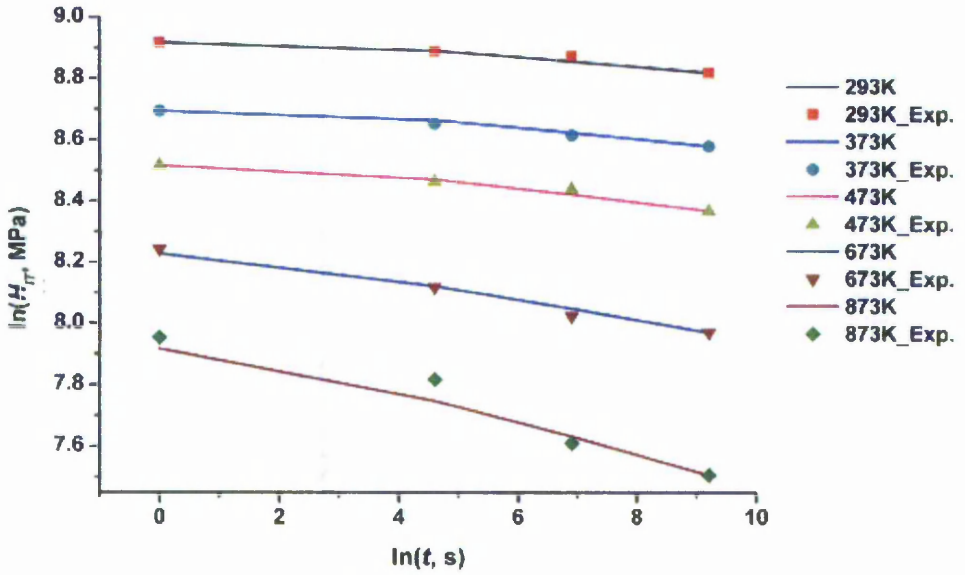

Figure 8.11 Analytical hardness variation with time using the glide controlled creep model for MgO <110>

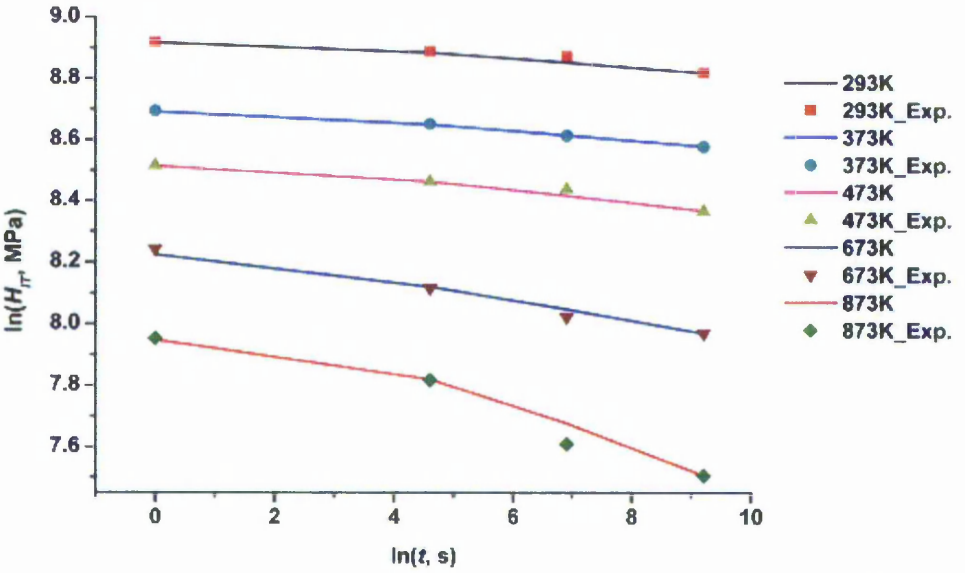

Figure 8.12 Analytical hardness variation with time using the power law breakdown creep model for MgO <110>

8.2.3 FE modelling of indentation creep in MgO

8.2.3.1 FE model

The FE model was similar to that described in section 8.1.4.1, with the exception that single crystal MgO was used as the substrate.

A static indentation analysis modelling was carried out first, then the applied force load, $F_Z = -3.13\text{N}$, on the reference point of the rigid indenter, was maintained for a period of time for the creep.

8.2.3.2 Results

Determining constants

In this case the FE modelling was based on the power-law breakdown creep model only. The same procedure was used as previously outlined in section 8.2.3.2, i.e. in the FE analysis the values for the relevant parameters, apart from the stress index, n, were the same as those presented in sections 8.2.1 and 8.2.2. Once again, it was found that the value for n determined from the analytical analysis, usually needed to be adjusted slightly in the FE analysis in order to fit the experimental results of hardness variation with time. Tables 8.9 and 8.10 give the adjusted constants for MgO <100> and MgO <110> respectively, that were obtained by comparing the hardness values from FEA and those from the experiments at different times.

Table 8.9 Power law breakdown creep model for MgO (001) <100>

Temperature K	293	373	473	673	873
Stress index n	5.4	6.34	5.03	4.08	3.6

Table 8.10 Power law breakdown creep model for MgO (001) <110>

Temperature K	293	373	473	673	873
Stress index n	3.07	3.77	3.46	3.17	2.17

Hardness variation with time

Figures 8.13 and 8.14 show the comparison of the hardness variation with time from FEA using the power law breakdown creep model and the experimental data. The results show that the hardness variations with time from FEA agree well with those from the experiments.

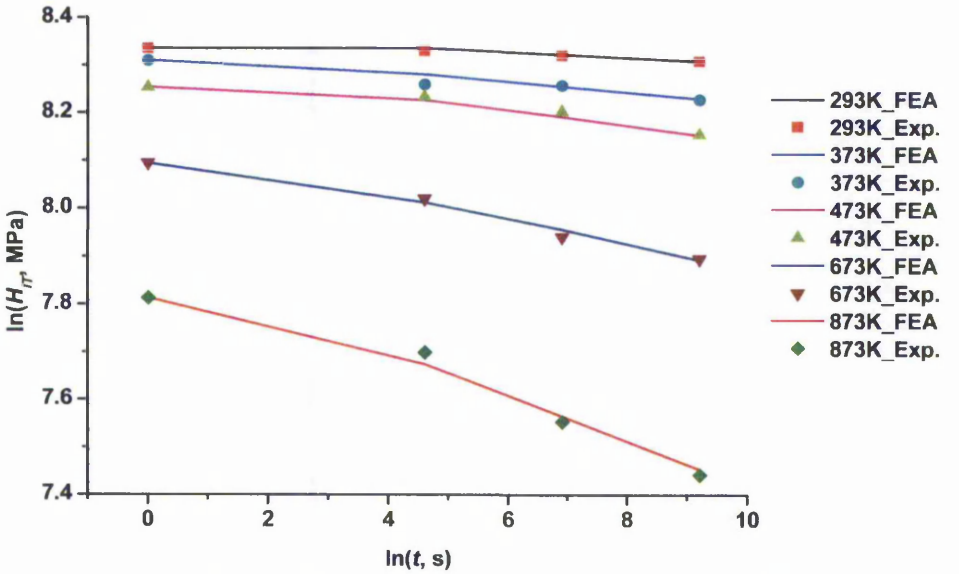

Figure 8.13 Comparison of hardness variation with time between FEA and experiments using the power law breakdown creep model for MgO <100>

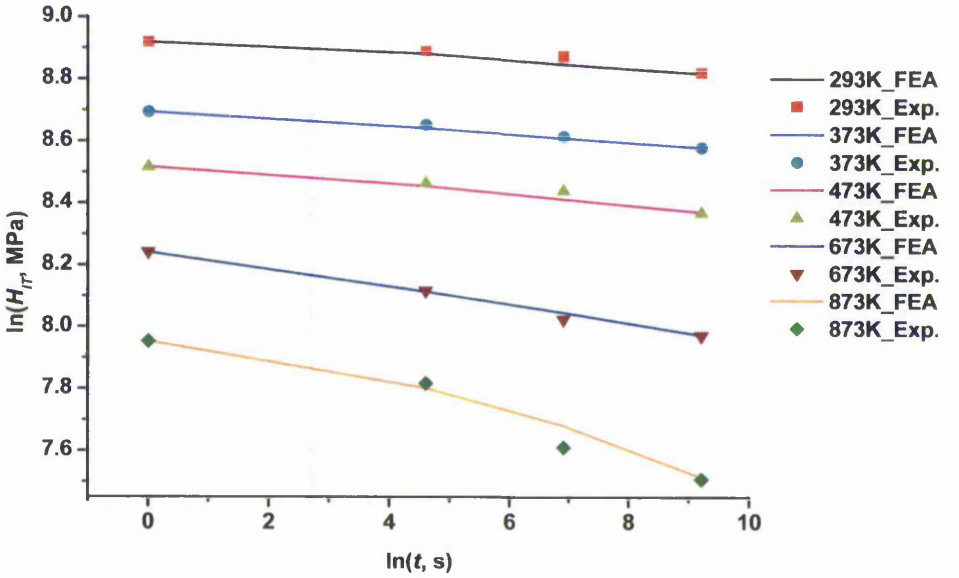

Figure 8.14 Comparison of hardness variation with time between FEA and experiments using the power law breakdown creep model for MgO <110>

The evolution of creep strain with time

Figures 8.15 to 8.18 show the evolution of the creep strain with time in MgO <110> using the power law breakdown creep model at T = 293 K and T = 873 K respectively. These figures show that the creep deformation again originates from the contact edge, then it extends into the substrate towards the central region. However, the central region just beneath the indenter has little creep deformation. It can also be seen that the creep

deformation at the higher temperature is more marked than that at the lower temperature. The general pattern for the evolution of the creep deformation is similar to that found for YCPZ. Thus the differences between the analytical and FE derived values for n are probably linked with the differences in the shapes of the deformed zones as discussed in section 8.1.4.2.

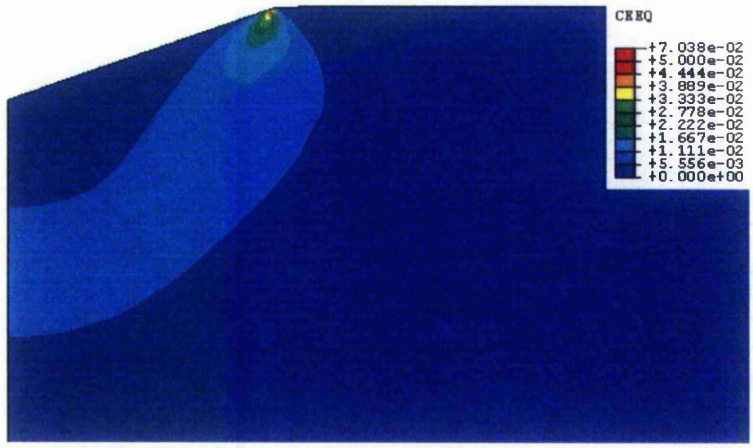

Figure 8.15 Creep strain contours at t = 100 s using the power law breakdown creep model for MgO <110> (T = 293 K)

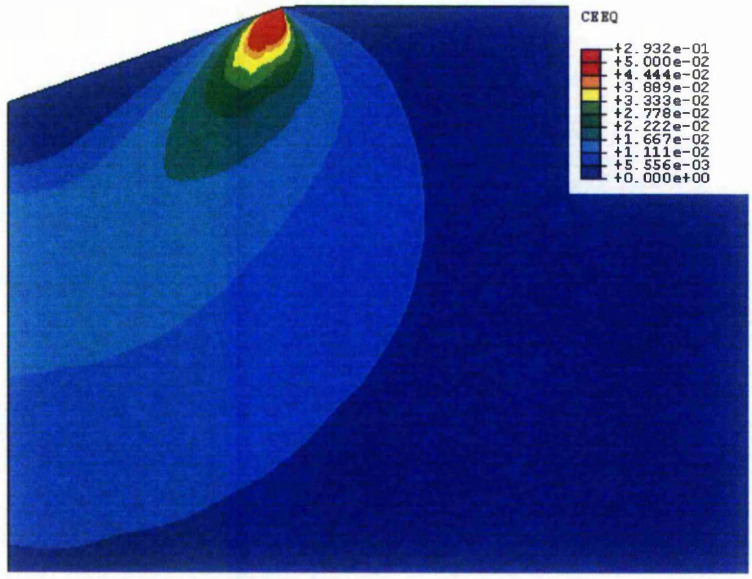

Figure 8.16 Creep strain contours at t = 10000 s using the power law breakdown creep model for MgO <110> (T = 293 K)

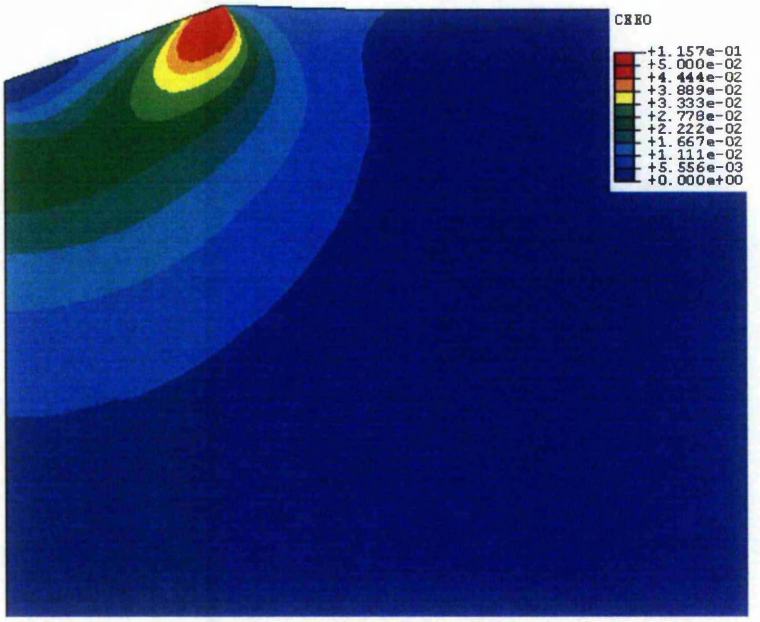

Figure 8.17 Creep strain contours at t = 100 s using the power law breakdown creep model for MgO <110> (T = 873 K)

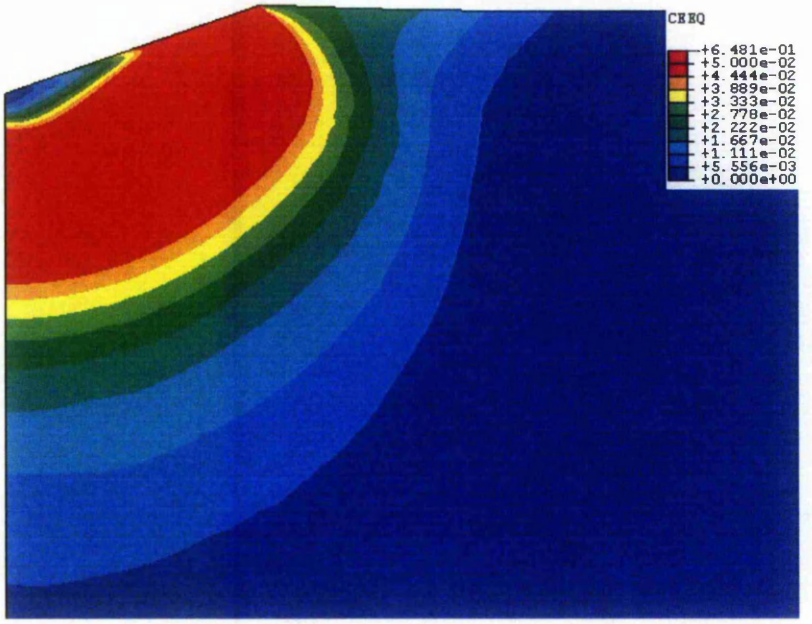

Figure 8.18 Creep strain contours at t = 10000 s using the power law breakdown creep model for MgO <110> (T = 873 K)

8.2.4 Summary for the FE indentation creep modelling in MgO

1) The modified dislocation creep model and the power law breakdown creep model were suitable to be used in the modelling of indentation creep deformation at low temperatures.
2) Analytical indentation creep analyses for MgO <100> and MgO <100> were implemented. The physical constants, such as the activation energy for creep and the 0 K shear flow stress of single crystal MgO were calculated.
3) The FE indentation creep modelling for MgO <100> and MgO <110> was implemented. The results of the hardness variation with time from FEA agree well with those from the experiments.
5) The FE indentation creep modelling showed that the creep deformation in MgO <110> originates from the contact edge, then it extends into the substrate towards the central region. However, the central region just beneath the indenter has little creep deformation. It can also be seen that creep deformation at higher temperatures is more marked than that at lower temperatures.

8.3 Summary

The FE indentation creep modelling in YCPZ and MgO has been implemented in this chapter. The indentation creep modelling procedure was formulated. The modified dislocation creep model and the power law breakdown creep model were both found to be suitable to use in the modelling of indentation creep deformation for ceramic materials at low temperatures. With the aid of the analytical indentation creep analyses, the physical constants, such as the activation energy for creep, can be calculated. The FE indentation creep modelling showed that the creep deformation in ceramic materials, such as YCPZ and MgO, originates from the contact edge, then it extends into the substrate towards the central region. However, the central region just beneath the indenter has little creep deformation. It can also be seen that creep deformation at higher temperatures is more marked than that at lower temperatures.

CHAPTER 9

SOFT IMPRESSER MODELLING

In this chapter finite element analyses for the soft impresser test methodology will be developed. The first step in the modelling was to develop appropriate meshes for both the substrate and the soft impresser. The models used are primarily 2D axisymmetric. In addition to the overall stress distribution, the parameters which were considered to be of most importance with regard to describing the behaviour of the substrate are: (a) the contact pressure, (b) the maximum tensile stress, and (c) the maximum shear stress. Secondly, the effects of friction on the radial stress and the contact pressure were studied for an elastically deforming substrate. Thirdly, the influence of the material properties of the soft impresser was considered. These results form the preliminary modelling phase for the soft impresser analyses.

After the preliminary analyses, the situation of firstly loading a soft impresser cone at one place on the substrate, and then lifting and moving the deformed cone to a new position on the substrate was modelled. The next step was to address the cyclic loading of a soft impresser, which is relevant to the study of the fatigue properties of a material. Finally, the case of a soft impresser sliding over the surface of a substrate was considered for a single traverse.

9.1 Soft impresser test

As outlined above, section 2.3, the soft impresser test involves placing a 'sharp' cone in contact with a flat substrate and applying a load sufficient to cause the cone to plastically deform to conform to the surface of the substrate. This test method enables the elucidation of the mechanical properties of materials which are very difficult to determine by other means, and has been principally applied to the study of ceramic and ultrahard materials. The majority of the analyses that have been presented to date (Brookes et al, 1990; Maerky et al, 1997; Fagan et al, 2000) have assumed that the loading due to the soft impresser can be considered as a uniform pressure, which is simply the applied load divided by the contact area. Some preliminary FE modelling of

the actual contact situation would suggest that this approximation is not generally correct (Henshall et al, 1999). The number of geometric and material variables associated with this test procedure is too great to be able to address the analyses using a comprehensive parametric approach. Therefore the analyses that have been performed have been strongly guided by the experimental work that has already taken place (Brookes et al, 1990; Maerky et al, 1997; Henshall et al, 1999). The cone has been modelled with a 120° apical angle, which is generally as used experimentally. Also practically, there are some advantages in being able to load a cone at one site on a substrate, and use the same cone at different positions, and with different loads, at other points. However Maerky (1997) found that there appears to be a different response for a MgO substrate with a steel cone, dependent upon whether the impresser was conical, i.e. unused, or previously flattened against the same substrate. The most comprehensive data set for fatigue using the soft impresser are those for Ceria stabilized Tetragonal Zirconia with steel cones (Guillou, 1996). Therefore the material properties used as the basis for the majority of the FE analyses in this chapter are those which are relevant to these two materials.

9.2 Preliminary Modelling

The preliminary analyses were carried out to determine the basic aspects of the soft impresser modelling, e.g. the mesh geometry. The necessity of including a model for the soft impresser, instead of using the constant pressure assumption, was also demonstrated.

9.2.1 Mesh Formulation

In addition to the standard mesh requirements, there are several particular considerations about the meshes to be used for soft impresser modelling. Firstly, for the substrate, a stress concentration occurs around the contact edge. Therefore, the mesh around the contact edge should be fine enough to capture the stress gradient. In the present instance, the mesh in the substrate was considered to be appropriate when the finite element results are consistent with the analytical results for a constant pressure applied to an elastic substrate. Secondly, for the soft impresser, the region around the

conical apex becomes highly deformed. Thus, the mesh around the apex of the cone should be fine enough to capture the plastic deformation. Thirdly, because the soft impresser will be in contact with the substrate after deformation, the mesh shape and the mesh size in the contact region should be appropriate to guarantee that no penetration occurs between the two bodies (section 9.2.2).

9.2.1.1 Substrate Mesh

A suitable mesh for the substrate was formulated using the situation of a circular constant applied pressure on a semi-infinite elastic body. Love (1929) has presented a rigorous analytical treatment for this situation, which has been used as the comparator for the present FE analyses. A constant pressure, p_{uni} = 4873.6 MPa, was applied to the surface over a circular area of radius a = 42.5 μm. The elastic modulus and Poisson's ratio of the substrate were 200 GPa and 0.27 respectively. This is similar to the analysis outlined in section 4.1 using ANSYS, but has been reconsidered herein in much more detail using ABAQUS.

A 2D axisymmetric model was used to enable a sufficiently refined mesh to be used within the overall limit on the numbers of elements and nodes. The axisymmetric element type CAX4I was used, which is a 4-node bilinear element with the incompatible mode.

Figure 9.1 shows the geometric partitioning of the substrate such that control of the element sizes could be achieved more effectively. The radius and height of the substrate were both 10000 μm. The axis of symmetry was along the left hand edge. The lower surface of the substrate, i.e. the bottom line in Figure 9.1, was constrained in both the radial and axial directions and the axisymmetric line was constrained in the radial direction only. The maximum principal stress outside the contact edge is one of the more difficult features of the stress distribution for the FEA to be able to match, and is also of particular relevance to the testing of ceramics. Therefore, the mesh size was adjusted gradually and was finally considered to be appropriate when the FE value of the maximum principal stress outside the contact edge agreed well with the analytical value. The final mesh is shown in Figure 9.2. This figure shows that the mesh is finest

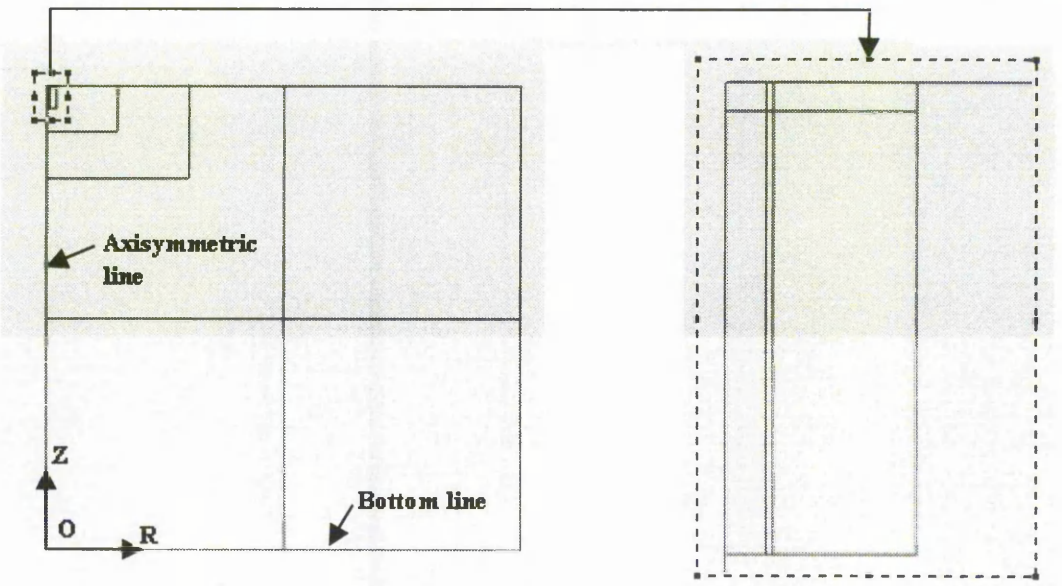

Figure 9.1 Geometric partition of the substrate

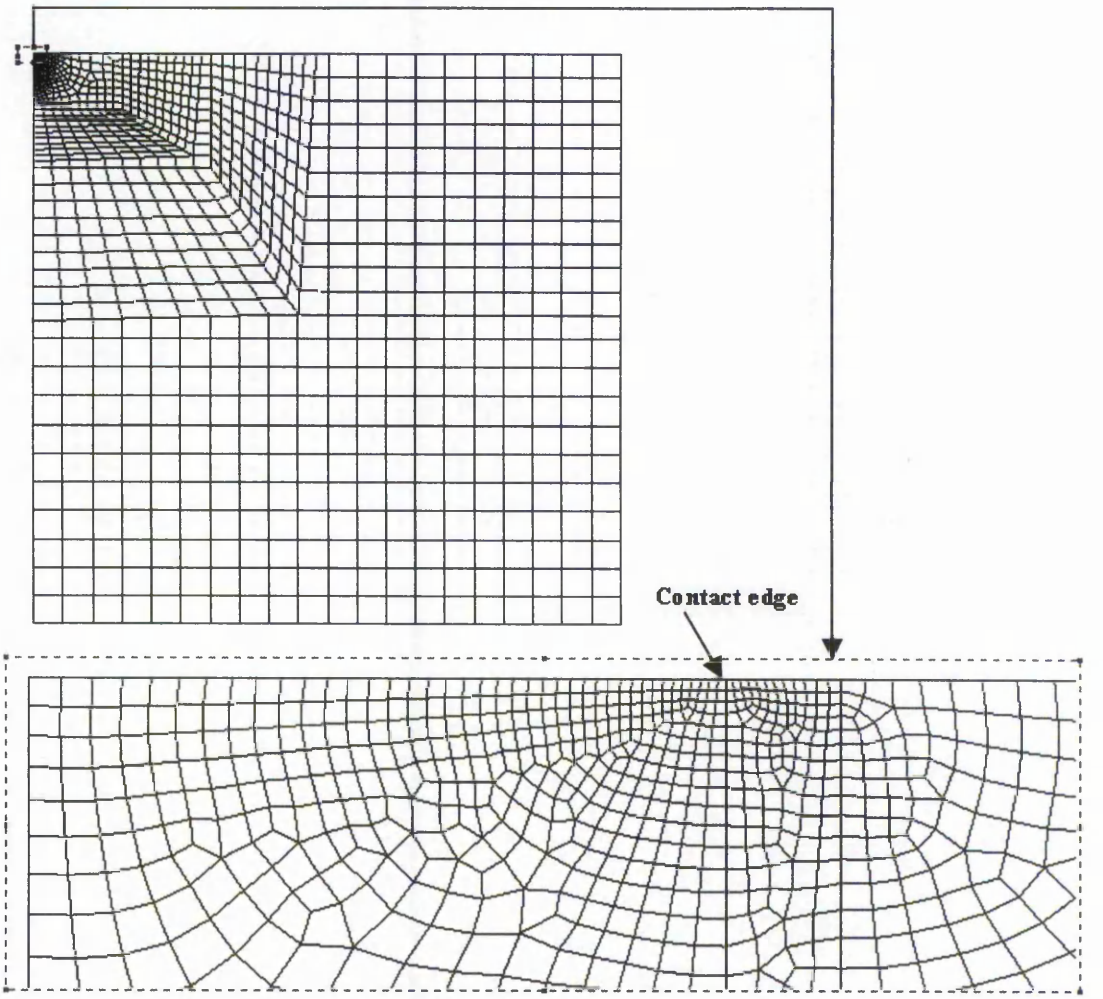

Figure 9.2 Mesh model for the substrate

around the contact edge and the mesh size increased gradually from the contact edge to the other regions. In total, there were 2271 elements and 2403 nodes in the substrate mesh. Figure 9.3 shows the radial stress contours for the constant pressure model. The constant pressure is applied to the surface between the symmetry axis and the point where there is a high stress gradient, i.e. where all the colours converge. The stress pattern has the general form predicted by Love's analytical model.

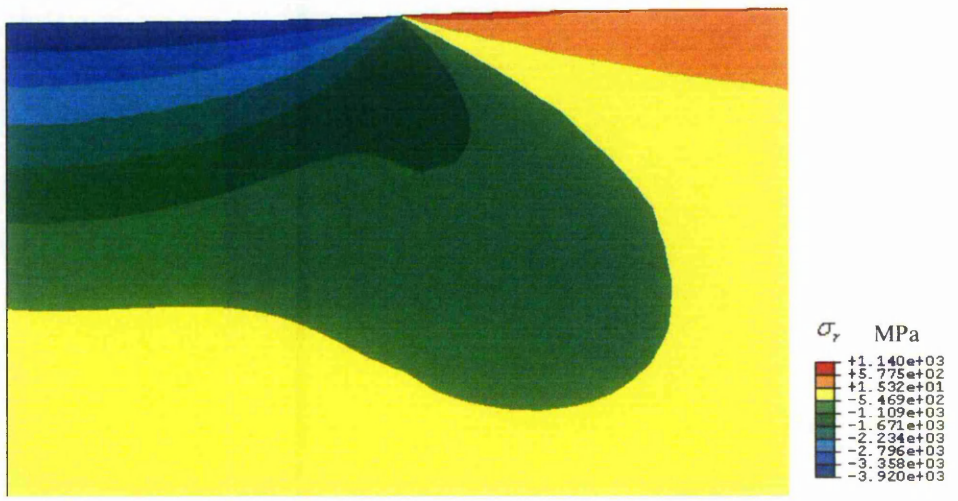

Figure 9.3 Radial stress contours for the constant pressure model

Figures 9.4 to 9.7 show more detailed comparisons between the analytical and FEA values for the radial stress, σ_r, and the axial stress σ_z on the top surface and also along the axisymmetric centreline of the substrate. The stress results were normalized by the applied pressure, p_{uni}. The distances along the radial, r, and symmetry axis, z, were normalized by the radius of the circle of the applied pressure, a. As can be seen from these figures, the analytical and FEA values generally agree well. In Figure 9.4 it can be noted that there is some difference between the analytical and FEA results for the radial stress at the surface in the region $r < a$. This could arise either as a result of the surface deforming elastically, and therefore not being absolutely flat as in the analytical model, or a result of numerical effects arising from the surface nodes being at a free boundary. The results for the radial stress in this region are not critically important.

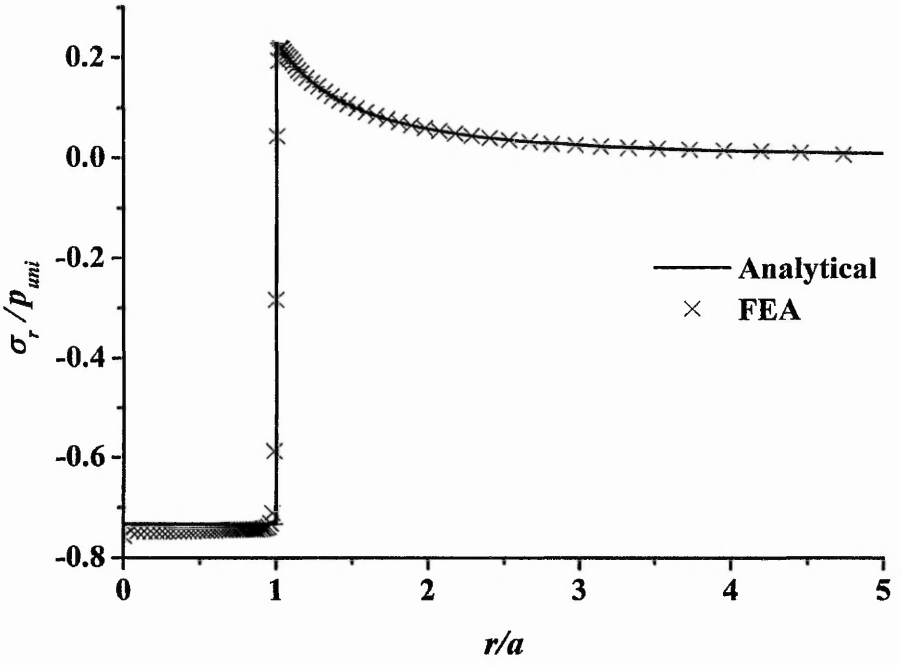

Figure 9.4 Comparison between theory and FEA for the radial stress on the surface of the substrate

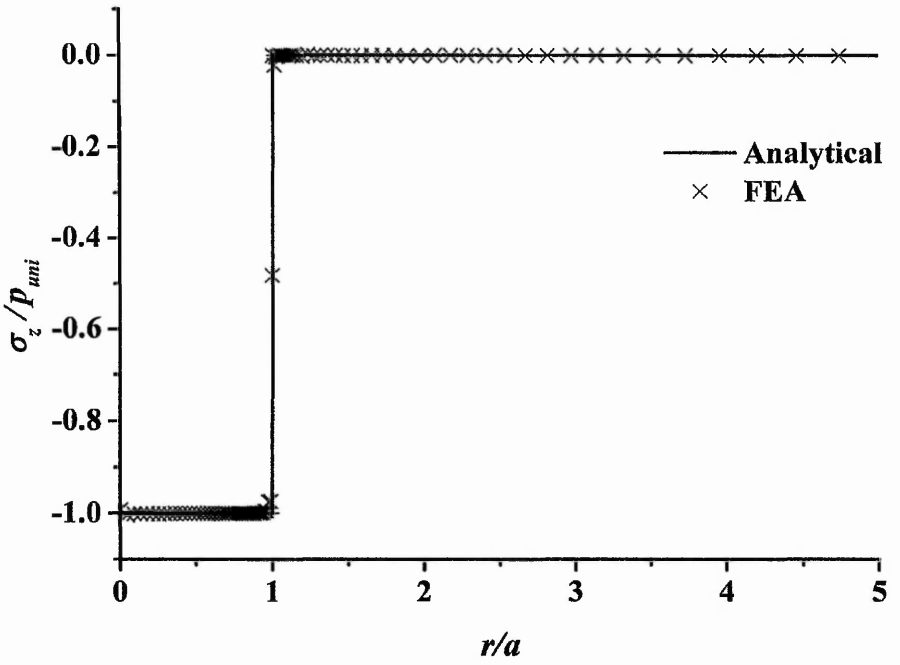

Figure 9.5 Comparison between theory and FEA for the axial stress on the surface of the substrate

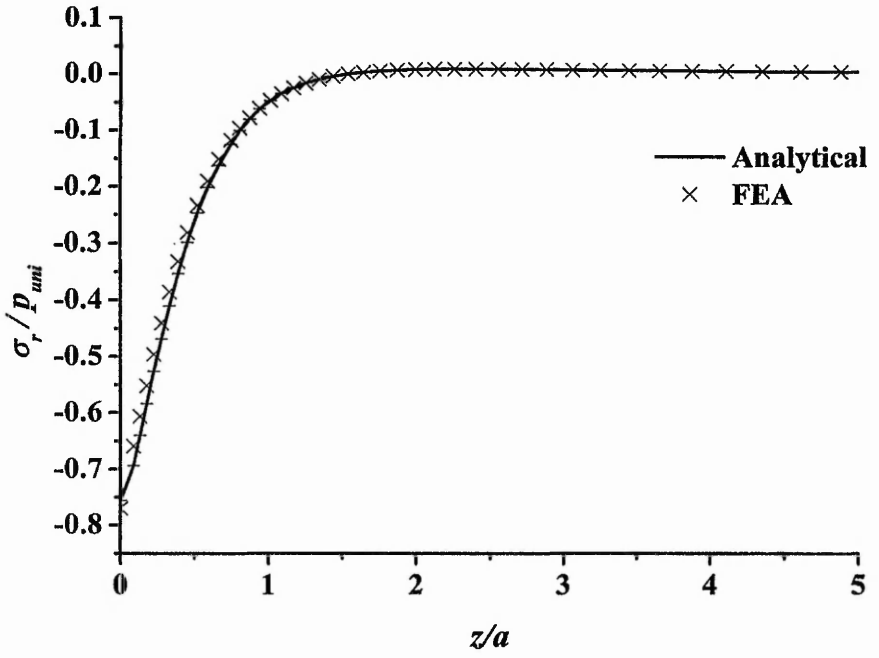

Figure 9.6 Comparison between theory and FEA for the radial stress along the axisymmetric centerline of the substrate

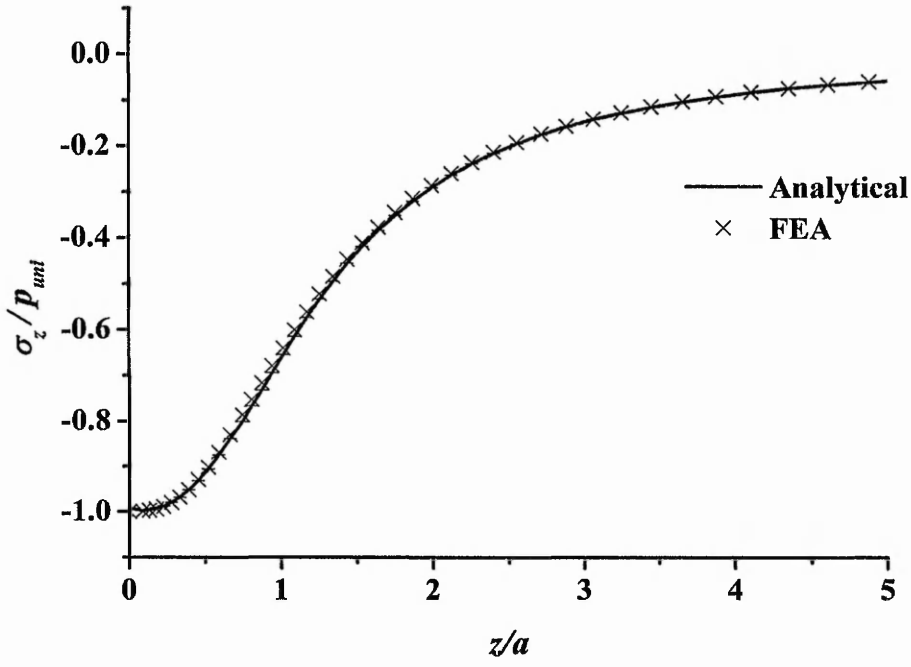

Figure 9.7 Comparison between theory and FEA for the axial stress along the axisymmetric centerline of the substrate

Therefore it is considered that these results indicate that the mesh was appropriate to satisfy the accuracy requirements.

9.2.1.2 Soft Impresser Mesh

The soft impresser was modelled using 2D axisymmetric elements as a sharp cone with semi-apical included angle of 60°, Figure 9.8. The mesh around the apex of the cone must be fine enough to capture the substantial plastic deformation. If the deformed element size along the edge of the cone which comes into contact with the substrate is larger than the surface mesh size of the substrate within the contact region, then 'penetration' of the substrate into the deformed cone will occur, leading to incorrect analyses. Therefore, the element size for the cone within the contact region should be smaller than the surface mesh size of the substrate within this region. In order to control the element size in this region, the apex region of the cone was partitioned by three lines (Figure 9.8). Line AB was used to control the mesh size for the apex region. Line CD was used to control the mesh size for the contact edge. Line EF was used to separate the large deformation region from the small deformation region in which a coarse mesh was used. Figure 9.9 shows the mesh for the soft impresser.

Since the element at the tip will be compressed severely when under load, the ratio of height to the width of this element should be greater than 1. Otherwise, penetration may occur between the soft impresser and the substrate for the frictionless case (Figure 9.13(a)). Figure 9.10 shows an example of the shape of the elements around the tip of the soft impresser before deformation. The symmetry axis was constrained in the radial direction. The motion in the axial direction of the nodes on the top surface was coupled to a reference node. A fixed displacement, or a designated concentrated force, in the axial direction, was applied to the reference node.

An isotropic bilinear work hardening material model was assumed for the soft impresser. The material properties for the soft impresser are shown in table 9.1. Conventional J_2 plasticity theory was used.

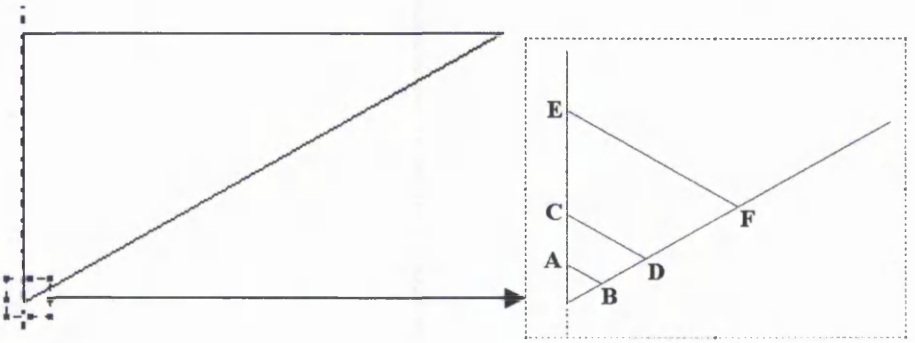

Figure 9.8 Geometric partition of the soft impresser

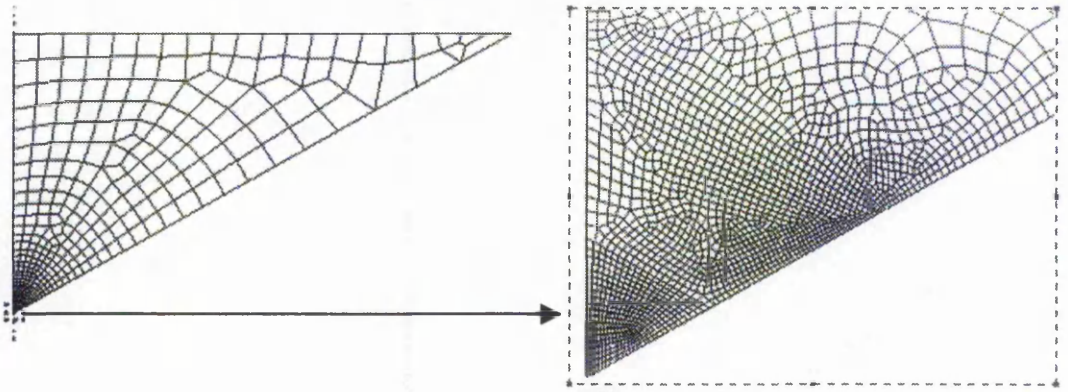

Figure 9.9 Mesh model for the soft impresser

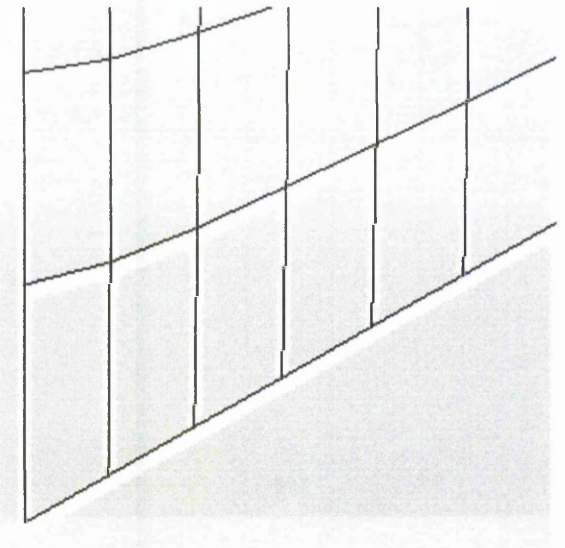

Figure 9.10 The shape of the elements around the tip of the cone before loading.

Table 9.1 Material properties for the soft impresser

Elastic modulus GPa	Poisson's ratio	Isotropic Bilinear Plastic Flow Stress vs. Plastic Strain Data	
		Flow Stress MPa	Plastic Strain
206	0.3	2054.05	0
		2466.05	1.00997

9.2.2 Effect of Friction Coefficient

Once the appropriate meshes have been determined for the substrate and impresser, the effect of friction coefficient on soft impresser indentation was studied. Figure 9.11 is the geometric model and Figure 9.12 is the mesh model, which were determined on the basis of the previous mesh formulations. A surface-to-surface contact pair was established between the impresser and the substrate. For the tangential behaviour, the penalty friction formulation was used; for the normal behaviour, the Lagrange formulation was used. A force load, F_z = -29.4 N, was applied to the reference node (*cf* section 9.2.1.2). The material properties for the substrate and soft impresser were the same as those presented in sections 9.2.1.1 and 9.2.1.2 respectively. The surface of the soft impresser was designated as the contact surface, and the surface of the substrate as the target surface, when defining the contact elements for the two meshes. It was found that the analyses for the frictionless case were the most difficult to perform. This arises from the fact that the deformation of the elements adjacent to the interface is very substantial. This has the effect of not only causing numerical difficulties within these elements, but can also lead to penetration of contact surface by the target surface, as shown in Figure 9.13(a). It is possible to modify the mesh to obviate this problem, Figure 9.13(b). For even relatively low values of friction coefficient, the deformation is much less localized, Figure 9.13(c), and convergence of the numerical solution is quicker. This is consistent with the results for the rigid impresser, as discussed in section 5.7.1.

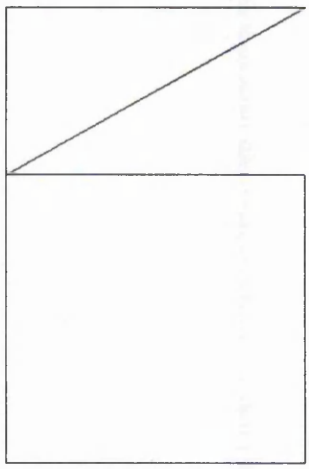

Figure 9.11 Geometric model

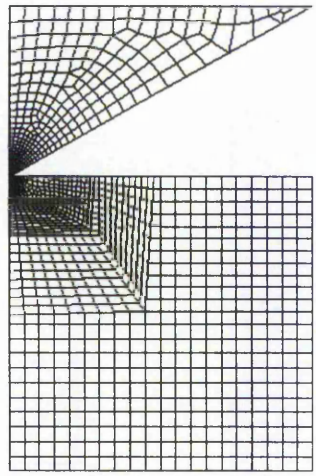

Figure 9.12 Mesh model

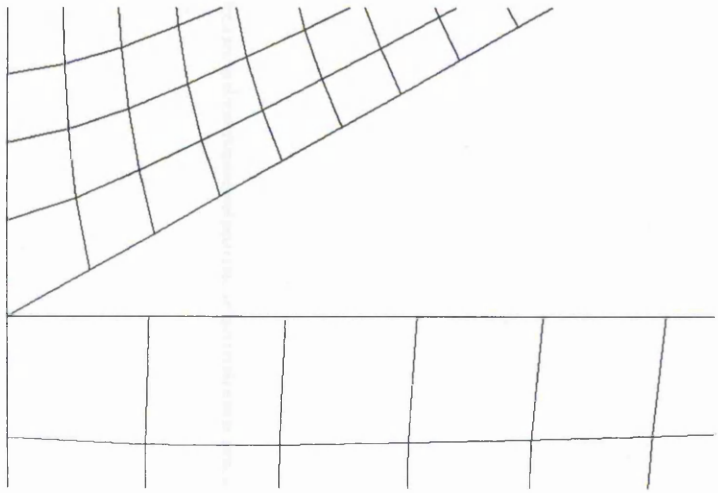

Before deformation

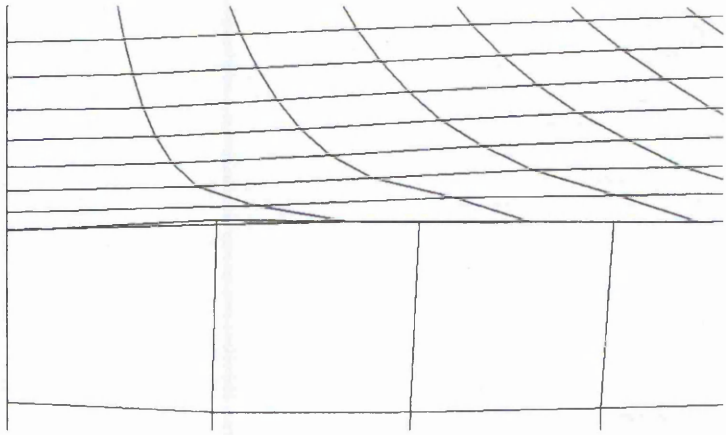

After deformation

(a) μ =0 penetration of the contact surface occurs

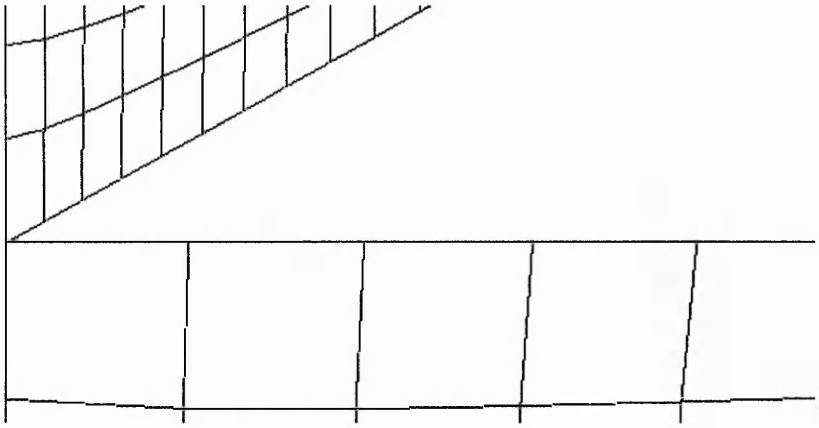

Before deformation

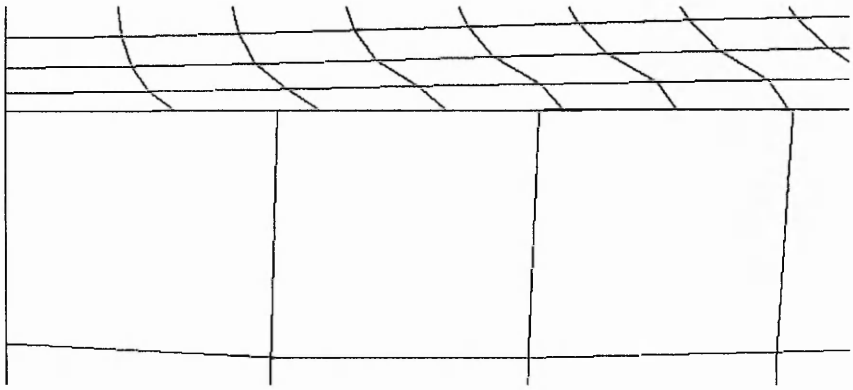

After deformation

(b) μ =0 There is no penetration of the contact surface into the target surface

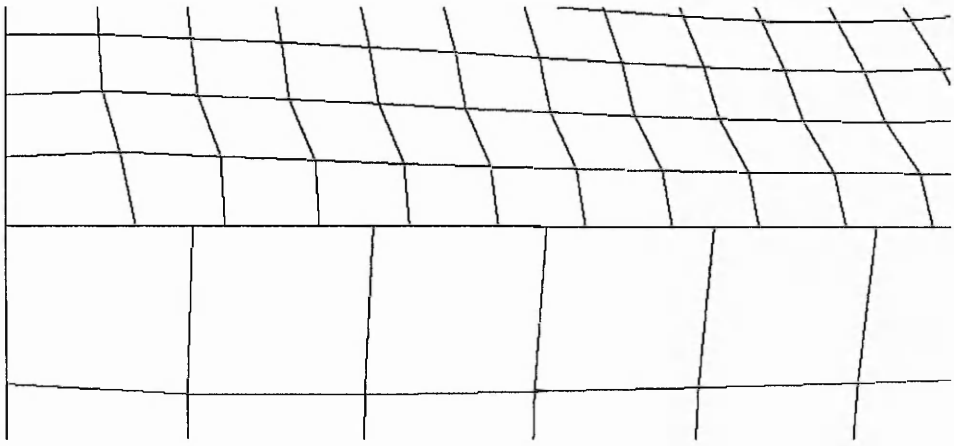

(c) μ =0.1 There is no penetration of the contact surface into the target surface

Figure 9.13 These figures show the deformed mesh at the interface of the impresser and substrate for (a) μ=0 with penetration occurring between the two surfaces, (b) μ =0 with no penetration, and (c) μ =0.1 with no penetration.

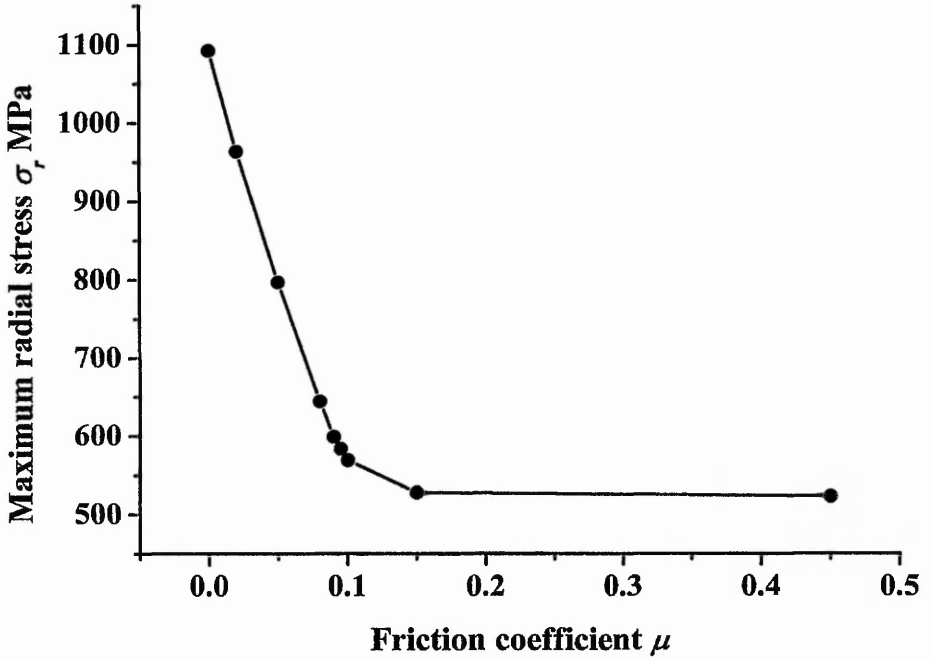

Figure 9.14 Effect of friction coefficient on the maximum radial stress

Figure 9.14 shows that the maximum radial stress is dependent on friction coefficient. There is a sharp, almost linear, decrease in the maximum radial stress as the friction coefficient increases from 0 to 0.1. The maximum radial stress becomes almost independent of the friction coefficient for values greater than 0.15.

Figures 9.15 and 9.16 show the radial stress contours in the substrate for the cases of μ=0 and μ=0.45 respectively. The main differences between the two cases appear to occur along the top surface of the substrate. Therefore the radial and axial stress distributions on the surface of the substrate for the cases of μ=0 and μ=0.45 are shown in Figures 9.17 to 9.20. From these figures it can be observed that there is a noticeable effect of friction coefficient on both the radial and axial stress distributions. The effect of friction on the radial stresses outside the contact zone is to both reduce the maximum magnitude and to move the position of the maximum away from the edge of contact. In both cases, the radial stress outside the contact zone is tensile. With regard to the axial stresses inside the contact zone, the effect of friction induces a greater variation, with the values generally increasing in magnitude from the axisymmetric centre line toward the contact edge, Figures 9.19 and 9.20.

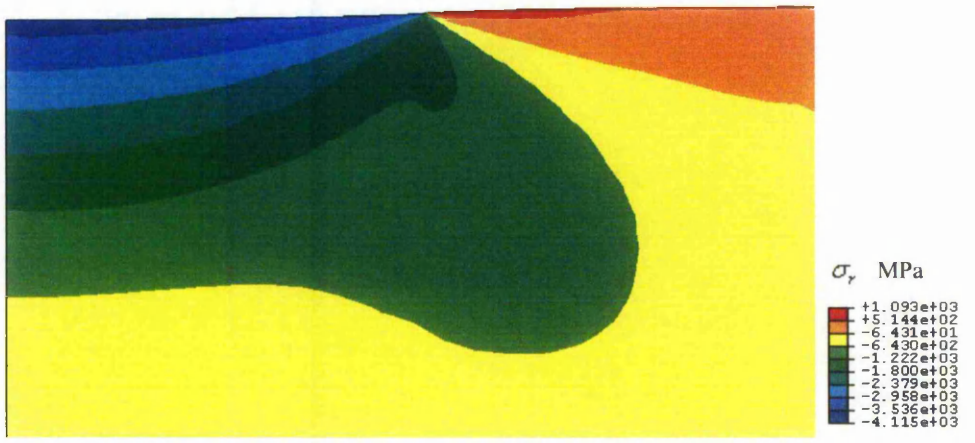

Figure 9.15 Radial stress contours in the substrate (μ =0)

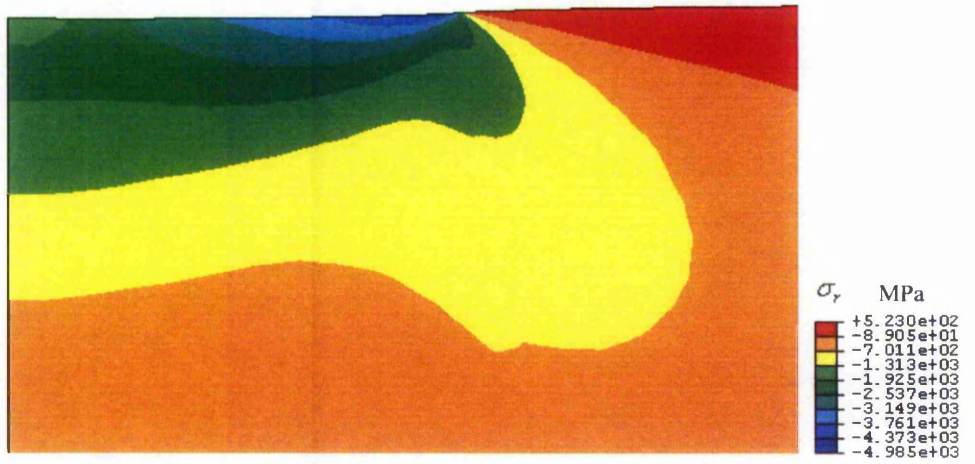

Figure 9.16 Radial stress contours in the substrate (μ =0.45)

Figure 9.21 shows in more detail that the location of the maximum radial stress moves outward from the edge of contact as the friction coefficient increases. When the friction coefficient reaches 0.095, the location of the maximum radial stress has moved to $r/a \approx$ 1.18. It then remains at almost the same location for the higher friction values.

For the constant pressure analytical model, the radial stress outside the contact edge is $\sigma_r = \frac{1-2*0.27}{2} * 4873.6 = 1120.9\,\text{MPa}$, which is very close to $\sigma_r = 1093.1\,\text{MPa}$ from FEA in the soft impresser frictionless case. This would perhaps be expected since there are no tangential surface tractions in the constant pressure case.

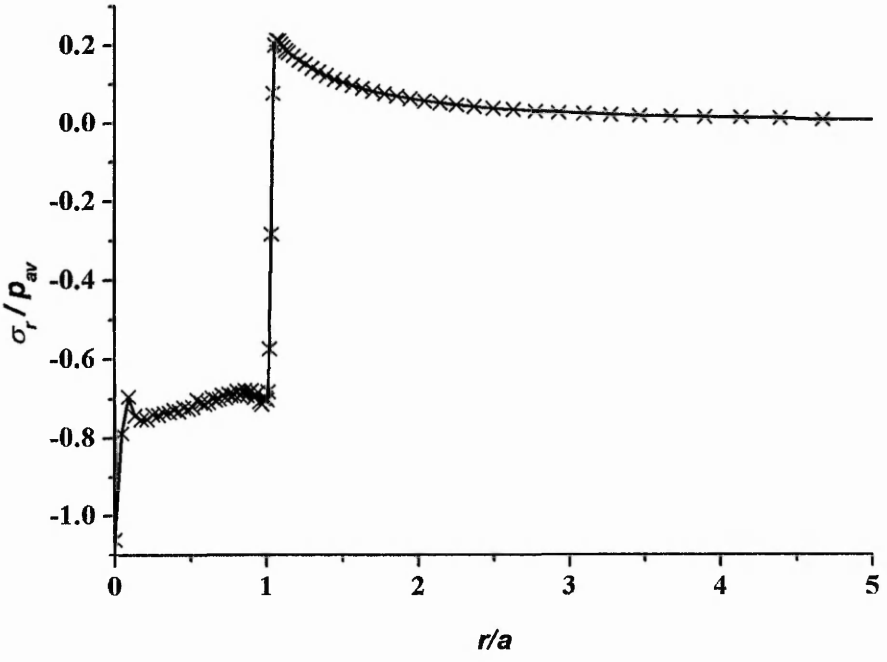

Figure 9.17 Radial stress distribution on the surface of the substrate (μ=0)

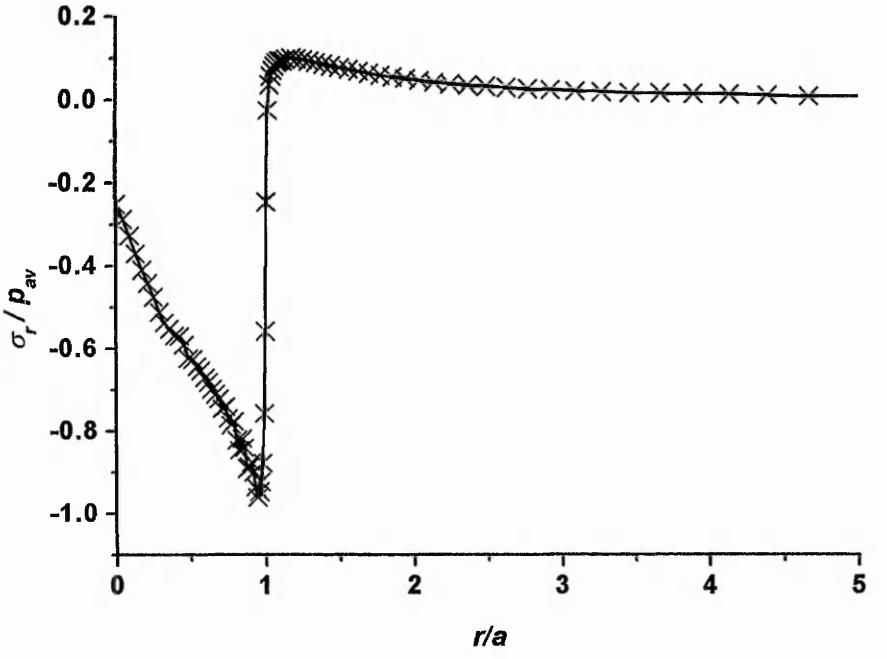

Figure 9.18 Radial stress distribution on the surface of the substrate (μ=0.45)

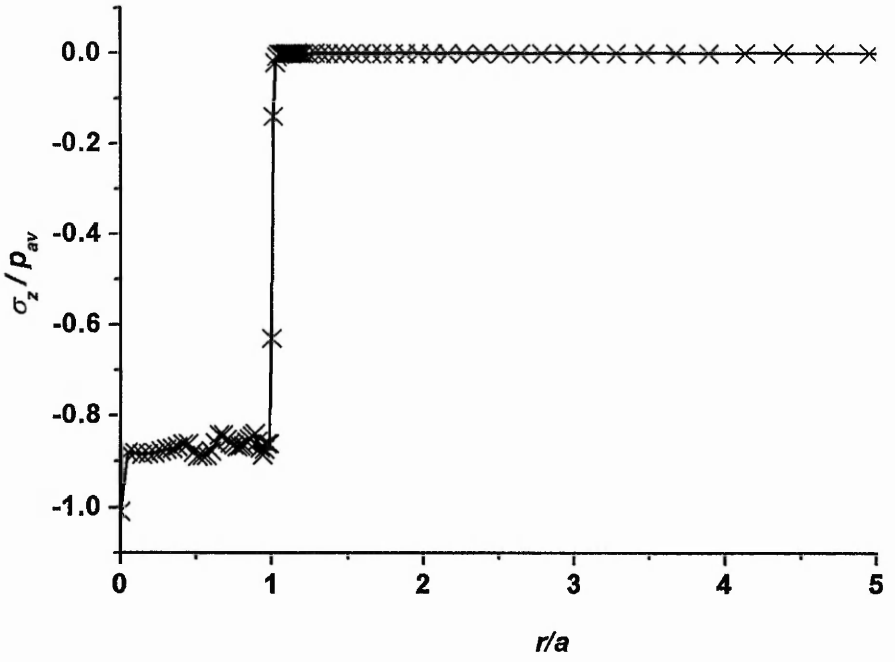

Figure 9.19 Axial stress distribution on the surface of the substrate (μ=0)

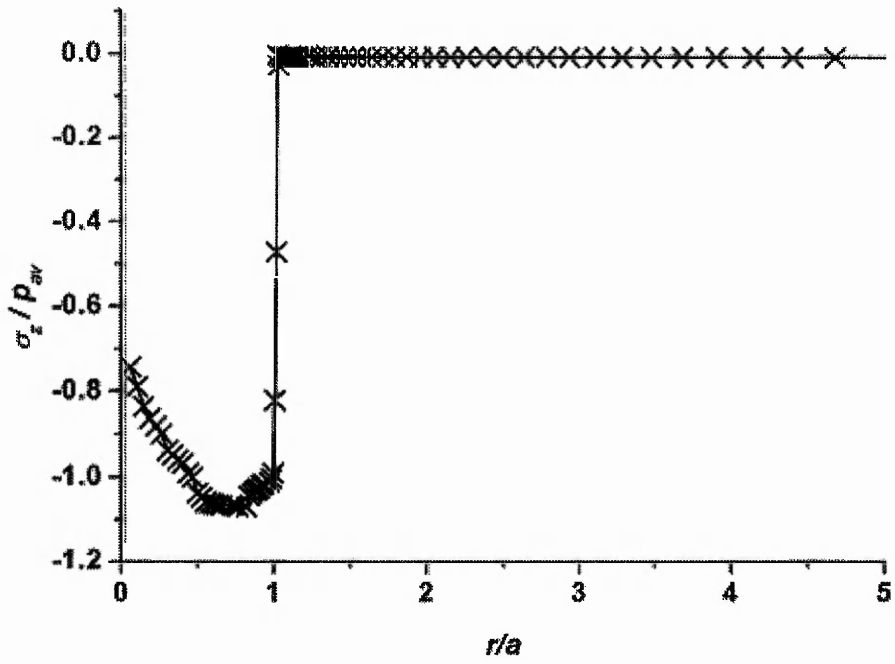

Figure 9.20 Axial stress distribution on the surface of the substrate (μ=0.45)

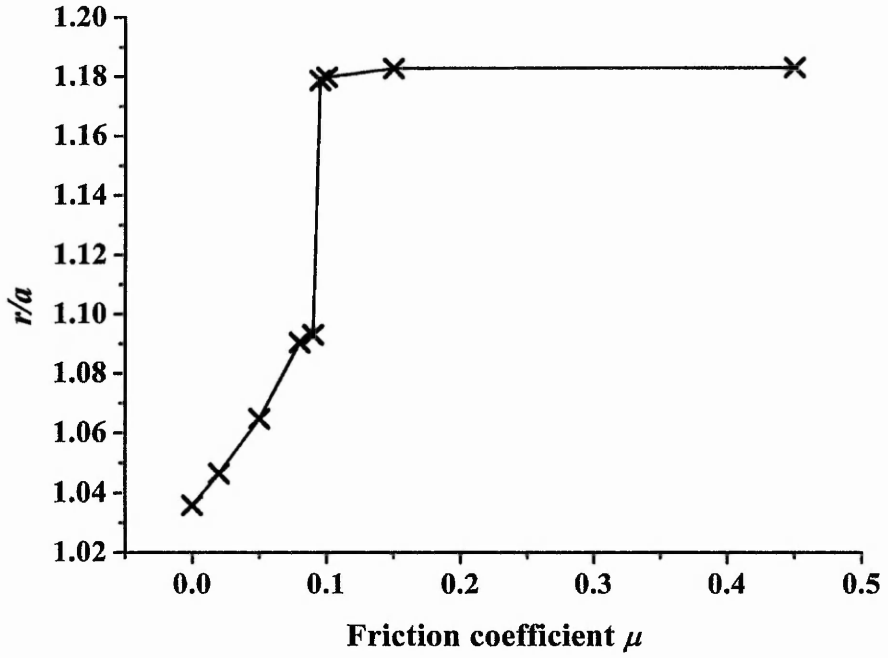

Figure 9.21 Effect of friction coefficient on the location of the maximum radial stress

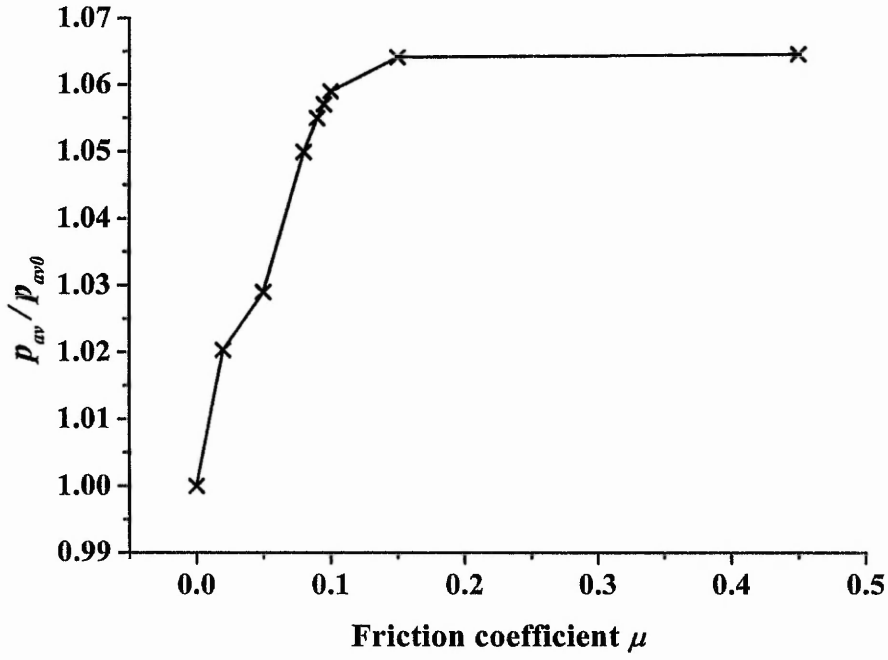

Figure 9.22 Effect of friction coefficient on the average contact pressure

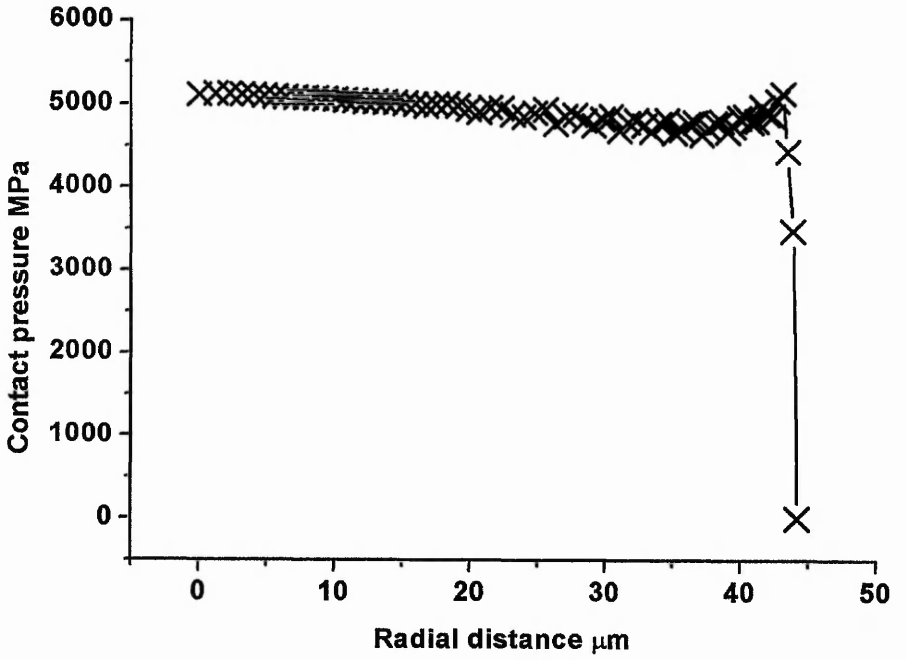

Figure 9.23 Contact pressure distribution along the radial direction for friction coefficient μ=0

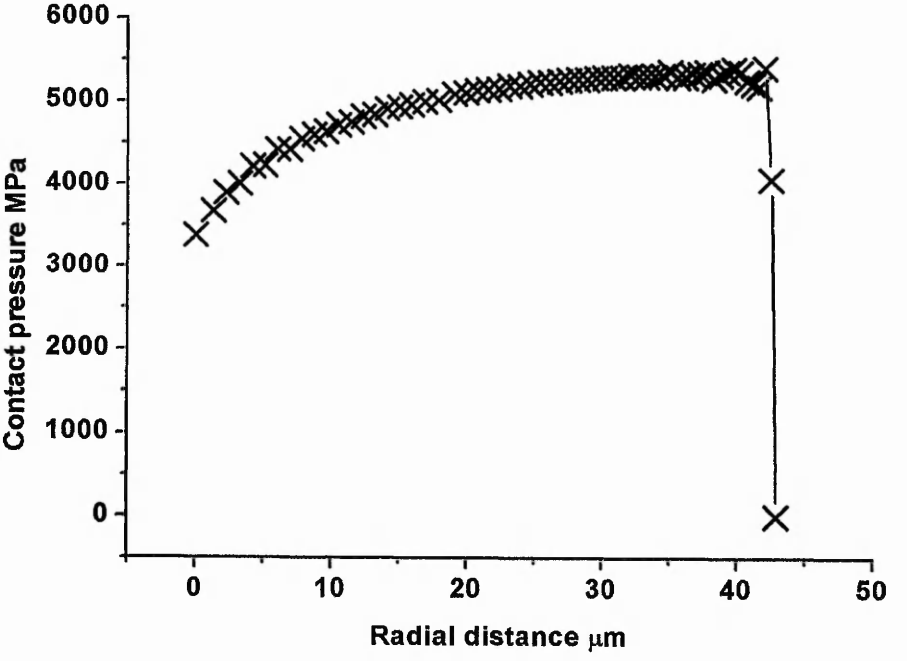

Figure 9.24 Contact pressure distribution along the radial direction for friction coefficient μ=0.45

Figure 9.22 shows the effect of friction coefficient on the average contact pressure, for a constant normal applied load. The variation of the average contact pressure with friction

coefficient is within 7%. The minimum average contact pressure occurs for μ=0. It then increases markedly as the friction coefficient increases. When the friction coefficient is 0.15 or greater, then the average contact pressure remains constant.

Figures 9.23 and 9.24 show the contact pressure distribution on the surface of the substrate along the radial direction for friction coefficients μ = 0 and μ = 0.45 respectively. For the frictionless situation, the contact pressure decreases gradually along the radial direction from the axisymmetric centre line toward the contact edge. For the high friction coefficient situation, the contact pressure increases gradually from the axisymmetric centre line toward the contact edge.

9.2.3 Effect of soft impresser material properties

In this section the substrate is the same as in the previous sections, i.e. an elastic material with Young's modulus equal to 200 GPa and Poisson's ratio equal to 0.27. Two friction coefficients, i.e. 0 and 0.15, were used. An isotropic bilinear work hardening material model was assumed for the soft impresser.

9.2.3.1 Effect of soft impresser elastic modulus

As noted above in section 9.1, much of the experimental testing with the soft impresser has used steel cones, with aluminum being the lowest elastic modulus non-polymer and silicon carbide and cubic boron nitride representing the highest elastic moduli. Hence the material properties used in this section are the same as those presented in Table 9.1

Table 9.2 Effect of soft impresser elastic modulus (μ =0)

Elastic modulus GPa	Contact radius μm	Average contact pressure p_{av} MPa	$\sigma_{r\max}$ MPa	Radial location of $\sigma_{r\max}$ μm	$\frac{\sigma_{r\max}}{p_{av}}$
68.7	43.98	4838.5	1092	45.39	0.2257
206	43.82	4873.6	1093	45.39	0.2242
618	44.44	4739.2	1082	45.98	0.2283

Table 9.3 Effect of soft impresser elastic modulus (μ =0.15)

Elastic modulus GPa	Contact radius μm	Average contact pressure p_{av} MPa	$\sigma_{r\max}$ MPa	Radial location of $\sigma_{r\max}$ μm	$\frac{\sigma_{r\max}}{p_{av}}$
68.7	43.85	4868	1319	44.84	0.2710
206	42.48	5186	528	50.24	0.1017
618	42.41	5204	428	53.56	0.0823

In contrast, when the friction coefficient is 0.15, it can be seen from Table 9.3 that the contact radius decreases slightly, and thus the average contact pressure increases, with increasing elastic modulus. The location of the maximum radial stress moves from being close to the contact edge to being some way from this point, and thus its value decreases markedly as the elastic modulus is increased. This value of friction coefficient is likely to be typical of experimental situations where there is some form of boundary lubrication between the impresser and substrate surfaces. Therefore in practice it should be noted that the elastic modulus of the impresser will have a noticeable effect on the average contact pressure, and also a very substantial effect on the maximum tensile stress.

9.2.3.2 Effect of soft impresser work hardening rate

The material properties for the soft impresser are the same as shown in Table 9.1 except that the second data points for the flow stress at the higher plastic strain were varied to be 2219, 2466, 2878 and 3702 MPa, which correspond to four different work hardening moduli, i.e. 164.8 MPa, 412 MPa, 824 MPa and 1648 MPa respectively. The applied load was 19.6 N, as previously used. Table 9.4 shows that for frictionless contact as the work hardening rate increases the contact radius decreases, due to the higher flow stress, and the average contact pressure increases concomitantly. The location of the maximum radial stress lies just outside the contact edge, and its value increases to be approximately a constant proportion of the average contact pressure.

For the analyses with $\mu = 0.15$, a comparison of Tables 9.4 and 9.5 shows that the effect of friction is to decrease the contact radius for a given work hardening rate, and thus to increase the average contact pressure. Also, as the work hardening rate increases, the location of the maximum radial stress moves closer to the contact edge, and its value increases absolutely, but decreases as a proportion of the average pressure. However, the values are always less than for frictionless contact. These results, albeit relatively limited, would indicate that it would be preferable to use a material with a reasonably high work hardening rate for the soft impresser.

Table 9.4 Effect of soft impresser work hardening rate (μ =0)

Plastic Work Hardening Modulus MPa	Contact radius μm	Average contact pressure p_{av} MPa	$\sigma_{r\max}$ MPa	Radial location of $\sigma_{r\max}$ μm	$\frac{\sigma_{r\max}}{p_{av}}$
164.8	44.97	4627.1	1041	45.98	0.2252
412	43.82	4873.6	1093	45.39	0.2242
824	42.57	5164.1	1164	43.84	0.2252
1648	41.10	5540.6	1207	43.39	0.2179

Table9.5 Effect of soft impresser work hardening rate (μ =0.15)

Plastic Work Hardening Modulus MPa	Contact radius μm	Average contact pressure p_{av} MPa	$\sigma_{r\max}$ MPa	Radial location of $\sigma_{r\max}$ μm	$\frac{\sigma_{r\max}}{p_{av}}$
164.8	43.10	5038	489	50.24	0.1393
412	42.79	5186	528	50.24	0.1147
824	41.76	5365	615	46.64	0.1017
1648	40.46	5716	796	43.87	0.09709

9.2.4 Preliminary Modelling Summary

The results presented in section 9.2 have shown that for the limited range of variables examined that for an elastically deforming substrate:

1) A suitable mesh has been obtained for the substrate and soft impresser, and appropriate contact conditions established.
2) For frictionless contact, the assumption of a constant pressure distribution is a good approximation.
3) As the friction coefficient between the substrate and impresser increases in the range 0 to 0.15, the contact pressures, and stress distributions, increasingly differ from the constant pressure assumption. When the friction coefficient is 0.15 or greater, then the results appear to reach a plateau.
4) The elastic modulus and the work hardening rate of the impresser have very little effect on the pressures and stress distributions in frictionless contact, but have a very marked effect for the values of friction coefficient that would be expected in practice.

9.3 Soft Impresser Flattening and Re-locating Analysis

As noted above, there are advantages experimentally in being able to flatten a given soft impresser against the surface of substrate and subsequently re-locating the flattened cone to another position on the same substrate. The analysis of the mechanics of this procedure has not been undertaken. Therefore, in this section, two loadings were implemented sequentially onto two substrate locations. The first loading uses a sharp soft impresser to impress the first position on the substrate. After this first loading, the sharp soft impresser becomes 'flattened'. Subsequently, the flattened soft impresser was re-located to the top surface of the second, remote, position on the same substrate and re-loaded to the same value of the applied load to impress the second soft substrate. The differences of the results from the two loadings are compared and analyzed.

9.3.1 Geometric model and FE model

Figures 9.25 and 9.26 are the geometric model and FE model respectively for this simulation. The meshes are very similar to those used in the previous sections. The loading sequence is described in detail below. The boundary conditions are the same as those used previously.

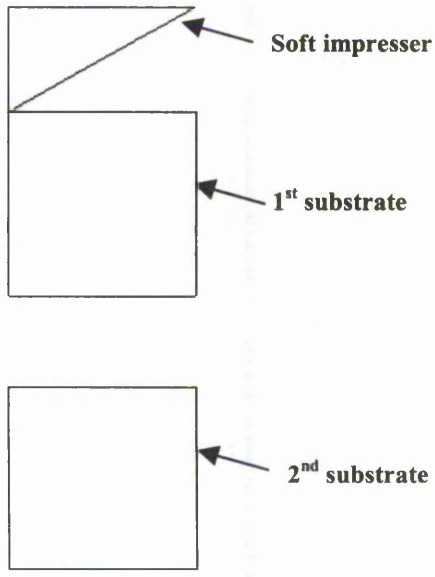

Figure 9.25 Geometric model

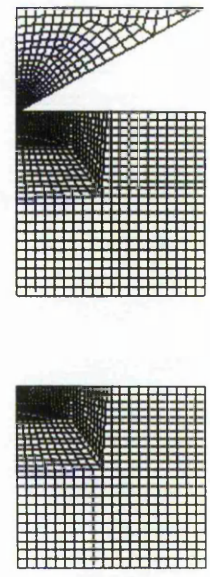

Figure 9.26 FE model

9.3.2 Material model

An isotropic bilinear work hardening material model was used for the soft impresser, with the material properties as detailed in Table 9.1. Two situations have been considered for the substrate, i.e. elastic only and elastic-plastic. In both cases, the elastic properties are those given in Table 9.6, which also includes the details for the plastic properties in the second set of analyses.

Table 9.6 Material properties for the substrate

Elastic modulus GPa	Poisson's ratio	Isotropic Bilinear Plastic Yield stress vs. Plastic Strain Data	
		Yield Stress MPa	Plastic Strain
200	0.27	2700	0
		3100	1.0135

9.3.3 Modelling procedure

The modelling procedure for the two substrates' soft indentation modelling problem is:

Step 1: Impress onto the first substrate

The required force load, generally 29.4 N maximum, was applied gradually to the impresser to indent the first substrate. At this step, the predefined contact pair between the impresser and the second substrate was deactivated and all the DOFs of nodes of the second substrate were constrained to zero. The output for the second substrate was excluded at this step to decrease the size of the results file.

Step 2: Re-location.

After the first step had been finished, the force load was removed and the displacement load, which was obtained from the calculated axial displacement of the pivot node of the impresser, was applied to the impresser. The impresser was then unloaded and relocated onto the top surface of the second substrate. At this step, the contact pair between the impresser and the first substrate was deactivated, so that the impresser can pass through the first substrate. The predefined contact pair between the impresser and the second substrate was reactivated. The first substrate was fixed in position and the

Table 9.7 Modelling procedure

Step 1	Objective	Impress onto the first substrate	
	Load method	Force	
	Contact pair status	Active	Soft impresser vs. 1st substrate
		deactivated	Soft impresser vs. 2nd substrate
	DOF	The nodal DOFs of the 2nd substrate were constrained to zero	
	Output control	Included	1st substrate and the soft impresser
		Excluded	2nd substrate
Step 2	Objective	Re-location	
	Load method	Change from force load to displacement load	
	Contact pair status	Deactivated	Soft impresser vs. 1st substrate after unloading from step 1
		Activated	Soft impresser vs. 2nd substrate
	DOF	The nodal DOFs of the 2nd substrate were released and new appropriate boundary conditions were applied; The nodal DOFs of the 1st substrate were fixed to their current positions from this step.	
	Output control	Included	2nd substrate and the soft impresser
		Excluded	1st substrate after unloading from step 1
Step 3	Objective	Impress onto the 2nd substrate	
	Load method	Increase the displacement load first until it is close to the required force load. Change from displacement load method to force load method and then increase the force load to the required force.	
	Contact pair status	Active	Soft impresser vs. 2nd substrate
		Deactivated	Soft impresser vs. 1st substrate
	Output control	Included	2nd substrate and the soft impresser
		Excluded	1st substrate

DOFs of nodes of the second substrate were released. New boundary conditions for the second substrate need to be applied. The output for the first substrate was excluded from this step to decrease the size of the results file. The output for the second substrate was included from this step.

Step 3: Impress onto the second substrate

When the impresser was relocated on the top surface of the second substrate, the displacement load on the impresser was applied to load the second substrate. At this point the maximum reaction force on the impresser was less than the final required force. Then, the displacement load on the impresser was replaced by a force load, the value of which was obtained from the calculated reaction force on the pivot node of the impresser. Then the force load was increased to that required to complete the whole modelling process of indenting two substrates.

Table 9.7 summarizes the modelling procedure for the two substrates impresser modelling problem.

9.3.4 Results

9.3.4.1 Results for two elastic substrates

In this section the substrate deforms elastically only. The friction coefficient between the impresser and both substrate positions was set to the same value of either zero or 0.15.

1) Frictionless case

The results for the two loading steps for the frictionless case are presented in Tables 9.8 and 9.9.

Table 9.8 Results for two elastic substrates for the first loading step (μ =0)

Applied load N	Contact radius μm	Average contact pressure MPa	$\sigma_{r\max}$ MPa	Radial location of $\sigma_{r\max}$ μm	$\sigma_{rz\max}$ MPa
9.8	25.5	4785	1074.3	27.3	1490
19.6	35.8	4857	1103.7	37.8	1510
24.9	40.4	4868	1101.3	41.7	1540
29.4	43.8	4875	1102.4	45.4	1515

Table 9.9 Results for two elastic substrates for the second loading step (μ =0)

Applied load N	Contact radius μm	Average contact pressure MPa	$\sigma_{r\max}$ MPa	Radial location of $\sigma_{r\max}$ μm	$\sigma_{rz\max}$ MPa
9.8	36.3	2371	502	37.9	733
19.6	42.4	3466	766	43.5	1055
24.9	43.5	4189	925	44.9	1264
29.4	43.8	4874	1092	45.4	1514

2) Friction coefficient=0.15

The results for the two loading steps for the frictional case are presented in Tables 9.10 and 9.11.

Table 9.10 Results for two elastic substrates for the first loading step (μ =0.15)

Applied load N	Contact radius μm	Average contact pressure MPa	$\sigma_{r\max}$ MPa	Radial location of $\sigma_{r\max}$ μm	$\sigma_{rz\max}$ MPa
9.8	24.6	5172	534	29.3	1705
19.6	35.0	5094	535	40.8	1839
24.9	39.2	5152	537	46.7	1890
29.4	42.5	5186	529	50.2	1922

Table 9.11 Results for two elastic substrates for the second loading step (μ =0.15)

Applied load N	Contact radius μm	Average contact pressure MPa	$\sigma_{r\max}$ MPa	Radial location of $\sigma_{r\max}$ μm	$\sigma_{rz\max}$ MPa
9.8	35.8	2428	485	37.3	762
19.6	41.3	3659	749	42.7	1164
24.9	42.2	4456	916	43.9	1416
29.4	43.0	5059	739	46.0	1724

9.3.4.2 Results for the elasto-plastic substrates

In this section the substrate undergoes elasto-plastic deformation. The friction coefficient between the impresser and both substrate positions was set to the same value of either zero or 0.15.

1) Frictionless case

The results for the two loading steps for the frictionless case are presented in Tables 9.12 and 9.13.

Table 9.12 Results for two elasto-plastic substrates at the first loading step (μ =0)

Applied load N	Contact radius μm	Average contact pressure MPa	$\sigma_{r\max}$ MPa	Radial location of $\sigma_{r\max}$ μm	$\sigma_{rz\max}$ MPa
9.8	25.4	4846	974	27.4	1449
19.6	35.6	4917	1072	37.2	1471
24.9	40.5	4830	1195	41.3	1556
29.4	43.9	4860	965	44.4	1528

Table 9.13 Results for two elasto-plastic substrates at the second loading step (μ =0)

Applied load N	Contact radius μm	Average contact pressure MPa	$\sigma_{r\max}$ MPa	Radial location of $\sigma_{r\max}$ μm	$\sigma_{rz\max}$ MPa
9.8	33.1	2847	586	35.2	942
19.6	40.9	3729	880	42.3	1139
24.9	42.8	4317	1245	43.9	1269
29.4	43.9	4852	1976	44.4	1393

2) Friction coefficient = 0.15

Table 9.14 Results for two elasto-plastic substrates at the first loading step (μ =0.15)

Applied load N	Contact radius μm	Average contact pressure MPa	$\sigma_{r\max}$ MPa	Radial location of $\sigma_{r\max}$ μm	$\sigma_{rz\max}$ MPa
9.8	24.4	5219	76.8	53.7	1527
19.6	34.8	5146	76.3	69.8	1523
24.9	39.5	5076	74.7	83.3	1534
29.4	42.7	5136	74.1	87.3	1519

Table 9.15 Results for two elasto-plastic substrates at the second loading step (μ =0.15)

Applied load N	Contact radius μm	Average contact pressure MPa	$\sigma_{r\max}$ MPa	Radial location of $\sigma_{r\max}$ μm	$\sigma_{rz\max}$ MPa
9.8	31.6	3123	561	33.6	988
19.6	38.8	4153	1098	39.6	1278
24.9	41.1	4695	1799	42.3	1383
29.4	43.2	5007	1892	43.5	1534

The results for the two loading steps for the frictional case are presented in Tables 9.14 and 9.15.

9.3.5 Analysis of results

Tables 9.16 and 9.17 give summaries of the results (*cf* Tables 9.8-9.15) for the first loading and the second loading respectively. For the second loading, the contact radius increased with increasing load until it became approximately constant above ~ 50-66% of maximum load. Full contact is defined as the contact radius achieving a similar value to that at the end of the 1st loading.

It can be seen from these results that for frictionless conditions it is possible to flatten an impresser at one position on an elastic substrate and then move it to a second position and apply a load, which as a general rule should be no less than 66% of the initial load, with a reasonable knowledge of the resultant contact pressure and stress distributions. If there is friction between the impresser and substrate, or plastic deformation in the substrate, then it is not possible to use the constant pressure analytical results to estimate the actual stress values.

9.3.6 Summary for the soft impresser flattening and re-locating analysis

The soft impresser flattening and re-locating analysis was implemented in this section. The results show that if there is friction between the impresser and substrate, or plastic deformation in the substrate, it is not possible to use the constant pressure analytical results to estimate the actual stress values. In these cases, the stress fields are quite different between the first and second loadings. This implies that the response should be

different using an unused conical impresser or a previously flattened impresser, which agrees with the experimental observation by Maerky (1997).

Table 9.16 Summary for the first loading

1st loading	Elastic substrate	Elasto-plastic substrate
Friction coefficient μ=0	$\sigma_{r\max}$ is approximately constant. It is always situated close to the edge of contact as the load is increased, and has a closely similar value to that from the constant pressure model.	$\sigma_{r\max}$ is approximately constant, similar to the values from the elastic substrate model and with similar location.
	$\sigma_{rz\max}$ is approximately constant with increasing load.	$\sigma_{rz\max}$ values are closely similar to the values from the elastic model.
Friction coefficient μ=0.15	$\sigma_{r\max}$ is approximately constant, but only about 50% of the value for the elastic frictionless case, and situated further from the contact edge.	$\sigma_{r\max}$ is markedly different from all the other situations. It is compressive at the edge of contact, with a relatively low tensile value (< 10% of frictionless, elastic values) and is situated more than the contact radius away from the edge of contact.
	$\sigma_{rz\max}$ varies slightly with increasing load and is up to 25% higher than the frictionless situation.	$\sigma_{rz\max}$ values are similar to the frictionless, elastic values.

Table 9.17 Summary for the second loading

2nd loading	Elastic substrate	Elasto-plastic substrate
Friction coefficient μ=0	$\sigma_{r\max}$ becomes proportional to the applied load once full contact is achieved and is situated just outside the edge of contact. At the maximum load, it is similar to the 1st loading value.	$\sigma_{r\max}$ is not proportional to the applied load even after full contact occurs. The increase in $\sigma_{r\max}$ is greater than would be expected as the applied load is increased.
	$\sigma_{rz\max}$ is proportional to the applied load once full load has been achieved and the value at maximum load is closely similar to the 1st loading value.	$\sigma_{rz\max}$ is not proportional to the applied load, with the rate of increase in $\sigma_{rz\max}$ being less than would be expected. The value at maximum load is 8% less than the frictionless, elastic value.
Friction coefficient μ=0.15	$\sigma_{r\max}$ is again proportional to the applied load once full contact occurs and are similar to the frictionless values.	$\sigma_{r\max}$ increases with increasing load once full contact occurs, but not in a uniform manner. At full load, it is 73% higher than the frictionless, elastic value.
	$\sigma_{rz\max}$ is proportional to the applied load once full contact occurs, with the values being approximately 12 % higher than the frictionless ones.	$\sigma_{rz\max}$ at full load is close to the frictionless, elastic value, but the values at lower loads are higher than the equivalent frictionless elastic values.

9.4 Cyclic Soft Impresser Modelling with Reference to CeTZP

As noted in section 9.1, the results presented in this section were intended to provide further insight and understanding to the data and observations presented previously on soft impresser cycle fatigue of Ceria stabilized Tetragonal Zirconia, CeTZP (Guillou et al, 1996). Details of the fatigue behaviour are presented in Guillou's paper. In brief, it was noted that fatigue occurred at the edge of the contact zone, with several small cracks initiating and then propagating to form a cracked zone around the contact edge.

The main focus of the present analysis is concerned with the initial fatigue crack formation stage. Therefore, two stresses are considered in this section, i.e. the maximum principal stress and maximum shear stress at, or near to, the contact edge, since it was observed that the fatigue cracking initiated in this region. The material properties used in this section for the substrate are shown in Table 9.18.

The FE model for the soft impresser was the same as that described in the previous sections.

Table 9.18 Material properties used to represent the CeTZP substrate

Elastic modulus GPa	Poisson's ratio	Isotropic Bilinear Plastic Yield stress vs. Plastic Strain Data	
		Yield Stress MPa	Plastic Strain
200	0.27	2700	0
		3100	1.0135

9.4.1 Modelling procedure

The modelling procedure for the cyclic soft impresser modelling problem is:

* The force was applied to the top surface of the soft impresser until the maximum required force had been achieved.
* Subsequently, the force was decreased until the minimum cyclic force was applied.
* Then the applied force was increased again and cycled between the minimum and maximum values for a total of ten cycles.

Three values of load cycle were applied, i.e. 19.6 ± 9.8 N, 39.2 ± 9.8 N and 29.4 ± 19.6 N. The contact pair between the soft impresser and the substrate was established. The friction coefficient was assumed to be 0.15. Different material properties were used for the soft impresser in order to achieve the same average contact pressure under the maximum load as that measured in the experiments.

9.4.2 Results

9.4.2.1 Variation of the maximum principal stress

1) Load case 1:

The test conditions for this load case are shown in Table 9.19. The material properties of the soft impresser for this load case are shown in Table 9.20.

Table 9.19 Test conditions for load case 1

Material of the soft impresser	Applied load N	Maximum contact pressure GPa
Steel No. 1	19.6 ± 9.8	3.75

Table 9.20 Material properties for the soft impresser

Elastic modulus GPa	Poisson's ratio	Isotropic Bilinear Plastic Yield stress vs. Plastic Strain Data	
		Yield Stress MPa	Plastic Strain
206	0.3	1533	0
		1945	1.01

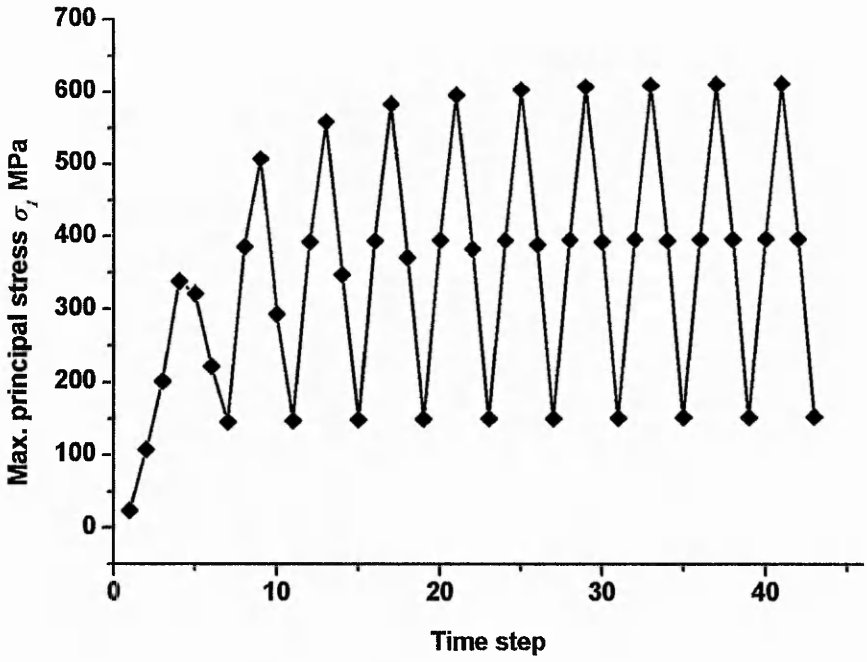

Figure 9.27 Variation of the maximum principal stress with time step for load case 1

Figure 9.27 shows the variation of the maximum principal stress just outside the contact region for load case 1. This figure shows that the stress at the lowest applied load is essentially constant after the first full load cycle has been applied. The stress at the

maximum applied load increased markedly with number of cycles for the first three cycles, then more gradually for the next three cycles, and was essentially constant thereafter. At the tenth cycle, the amplitude of the maximum principal stress, $\Delta\sigma_1$, and the corresponding mean maximum principal stress, σ_{1m}, are:

$$\Delta\sigma_1 = 230.2 \text{ MPa}, \quad \sigma_{1m} = 382.6 \text{ MP}a.$$

2) Load case 2:

Table 9.21 Test conditions for load case 2

Material of the soft impresser	Applied load N	Maximum contact pressure GPa
Steel No. 2	39.2 ± 9.8	4.45

The test conditions for this load case are shown in Table 9.21. The material properties of the soft impresser for this load case are shown in Table 9.22. As previously noted, the material properties for the impresser needed to be adjusted slightly to represent the actual observed deformation of the heat treated steels by Guillou et al (1996).

Table 9.22 Material properties for the soft impresser

Elastic modulus GPa	Poisson's ratio	Isotropic Bilinear Plastic Yield stress vs. Plastic Strain Data	
		Yield Stress MPa	Plastic Strain
206	0.3	1769	0
		2181	1.01

Figure 9.28 shows the variation of the maximum principal stress outside the contact region for load case 2. The results exhibit a very similar pattern to those for load case 1, except that the value at the minimum applied load requires three cycles to attain steady state. At the tenth cycle, the amplitude of the maximum principal stress, $\Delta\sigma_1$, and the corresponding mean maximum principal stress, σ_{1m}, are:

$$\Delta\sigma_1 = 119.6 \text{ MPa}, \quad \sigma_{1m} = 353.8 \text{ MPa}.$$

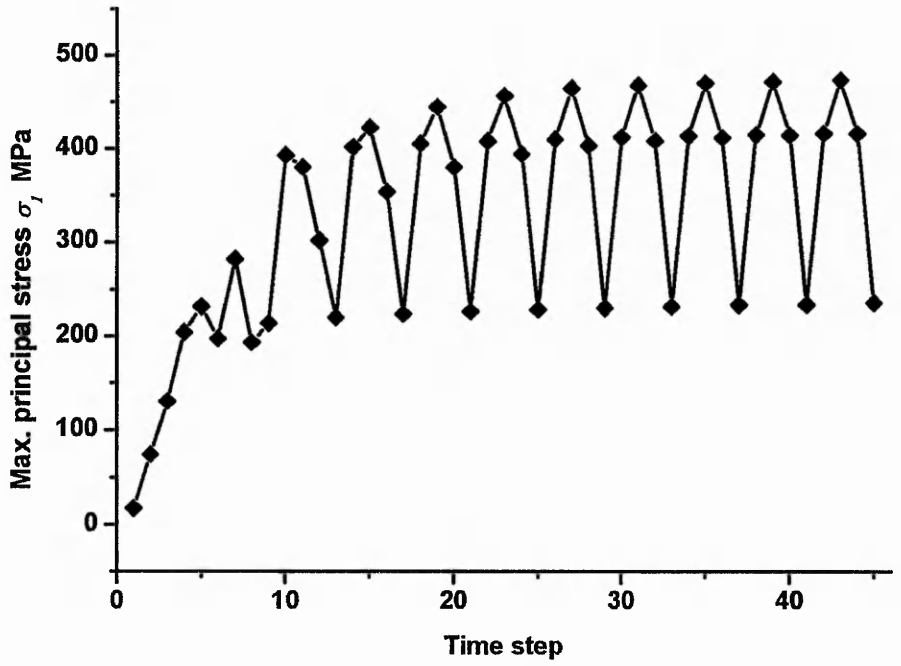

Figure 9.28 Variation of the maximum principal stress with the time step for load case 2

3) Load case 3:

The test conditions for this load case are shown in Table 9.23. The material properties of the soft impresser for this load case were the same as those in Table 9.20 for load case 1.

Table 9.23 Test conditions for load case 3

Material of the soft impresser	Applied load N	Maximum contact pressure GPa
Tempered steel No. 3	29.4 ± 19.6	3.88

Figure 9.29 shows the variation of the maximum principal stress outside the contact region for load case 3. The variation is again very similar to that for load cases 1 and 2; the only slight difference being that the stress at maximum load was still increasing by a small amount for the later cycles. At the tenth cycle, the amplitude of the maximum principal stress, $\Delta\sigma_1$, and the corresponding mean maximum principal stress, σ_{1m}, are:

$$\Delta\sigma_1 = 291.9 \text{ MPa}, \quad \sigma_{1m} = 394.4 \text{ MPa}.$$

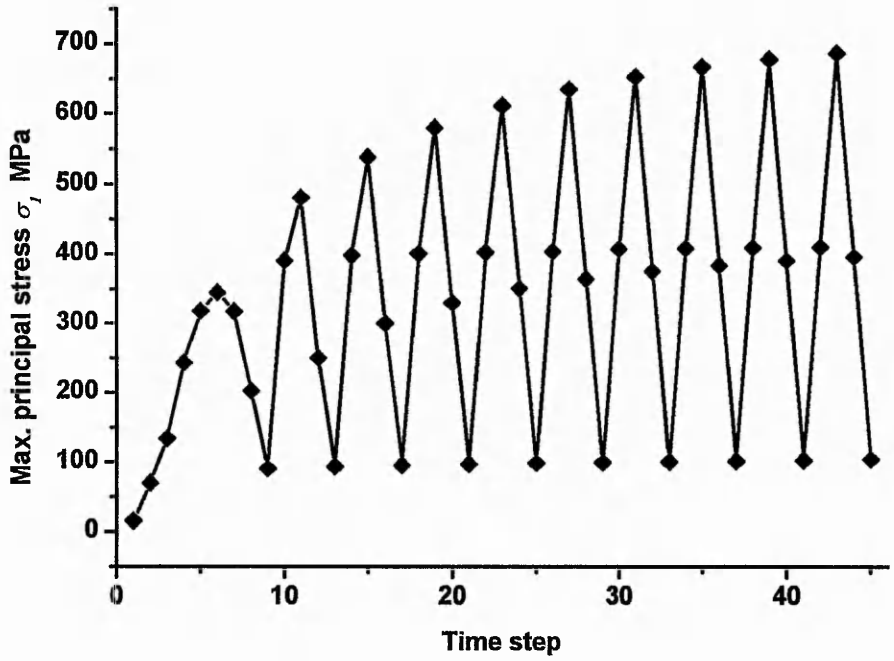

Figure 9.29 Variation of the maximum principal stress with time step for load case 4

4) Load case 4:

The test conditions for this load case are shown in Table 9.24. The material properties of the soft impresser for this load case are given in Table 9.25.

Table 9.24 Test conditions for load case 4

Material of the soft impresser	Applied load N	Maximum contact pressure GPa
Steel No. 1	29.4 ± 19.6	6.44

Table 9.25 Material properties for the soft impresser

Elastic modulus GPa	Poisson's ratio	Isotropic Bilinear Plastic Yield stress vs. Plastic Strain Data	
		Yield Stress MPa	Plastic Strain
206	0.3	2533	0
		3563	1.012

Figure 9.30 shows the variation of the maximum principal stress outside the contact region for load case 4. Again, the stress variation is generally very similar to the previous load cases. The only slight difference is that the stress at the maximum load

becomes constant at an early stage, whereas the stress at the minimum load changes slightly for the first six cycles. At the tenth cycle, the amplitude of the maximum principal stress, $\Delta\sigma_1$, and the corresponding mean maximum principal stress, σ_{1m}, are:

$$\Delta\sigma_1 = 453.9 \text{ MPa}, \quad \sigma_{1m} = 913.0 \text{ MPa}.$$

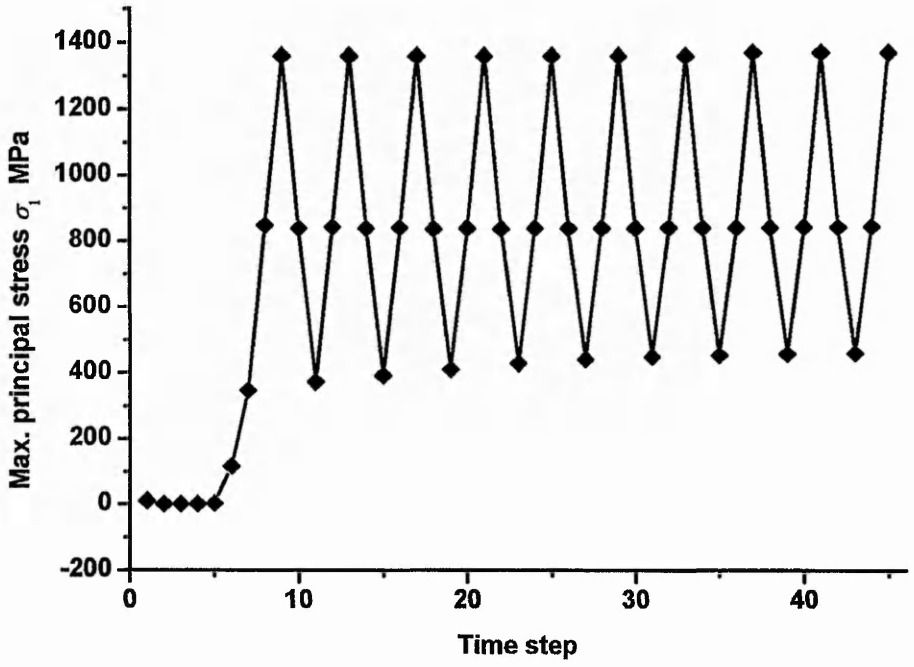

Figure 9.30 Variation of the maximum principal stress with time step for load case 4

9.4.2.2 Variation of the shear stress

1) Load case 1:

Figure 9.31 shows the variation of the maximum shear stress near the contact edge for load case 1. In this instance, the shear stress at the minimum load is effectively constant after the first full cycle, and the stress at maximum load decreases for the first five cycles and is constant thereafter. At the tenth cycle, the amplitude of the shear stress, $\Delta\sigma_{rz}$, and the corresponding mean shear stress, σ_{rzm}, are:

$$\Delta\sigma_{rz} = 501.6 \text{ MPa}, \quad \sigma_{rzm} = 669.6 \text{ MPa}.$$

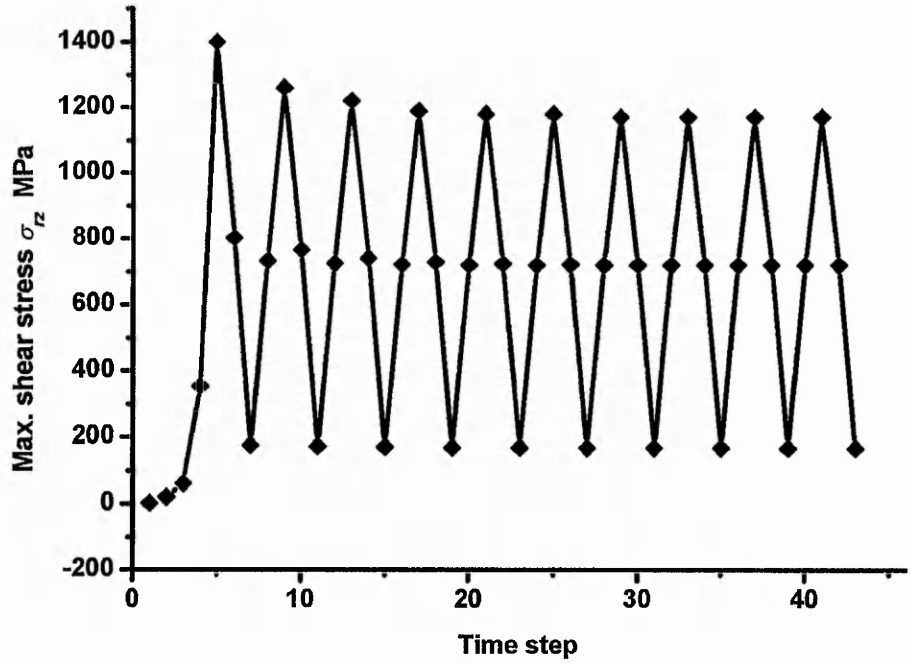

Figure 9.31 Variation of the maximum shear stress with time step for load case 1

2) Load case 2:

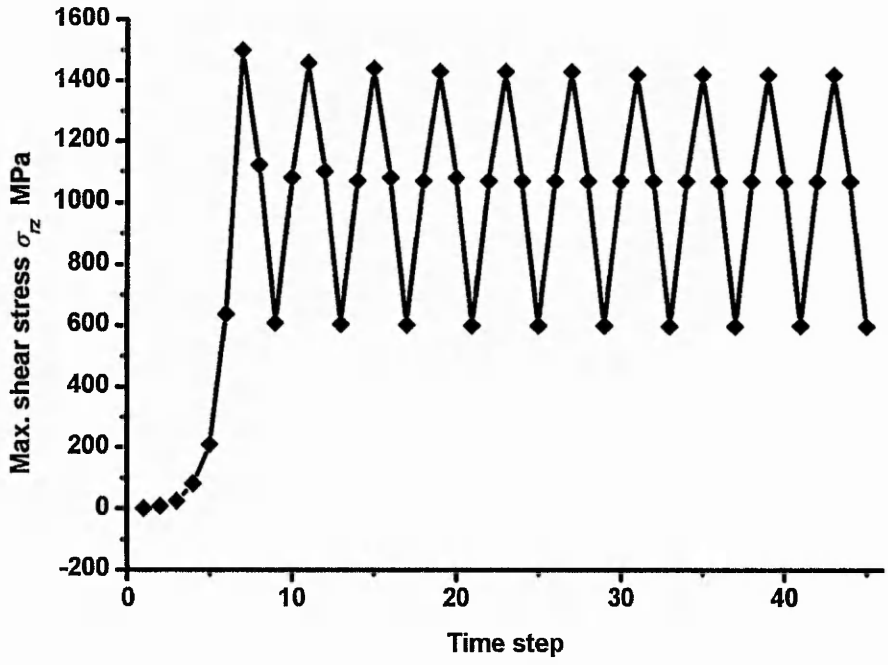

Figure 9.32 Variation of the maximum shear stress with time step for load case 2

Figure 9.32 shows the variation of the maximum shear stress for load case 2. The trend is very similar to load case 1, with a constant stress range occurring from the fifth load cycle onwards. At the tenth cycle, the amplitude of the shear stress, $\Delta\sigma_{rz}$, and the corresponding mean shear stress, σ_{rzm}, are:

$$\Delta\sigma_{rz} = 411.5 \text{ MPa}, \quad \sigma_{rzm} = 1010 \text{ MPa}.$$

3) Load case 3:

Figure 9.33 shows the variation of the maximum shear stress for load case 3. The trend is very similar to load cases 1 and 2, with the initial decrease in the stress at maximum load being slightly greater in this case. At the tenth cycle, the amplitude of the shear stress, $\Delta\sigma_{rz}$, and the corresponding mean shear stress, σ_{rzm}, are:

$$\Delta\sigma_{rz} = 547.0 \text{ MPa}, \quad \sigma_{rzm} = 578.3 \text{ MPa}.$$

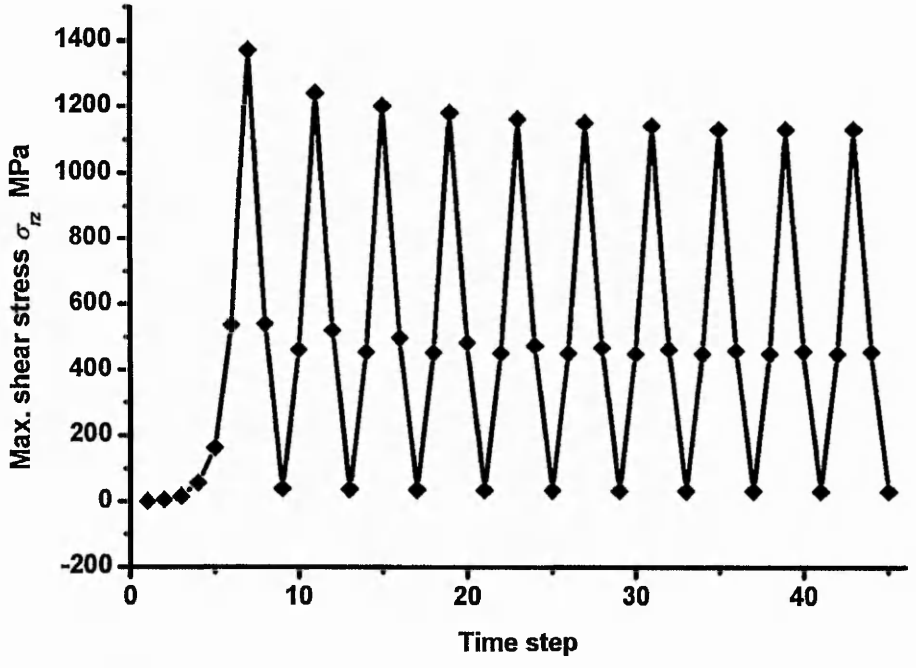

Figure 9.33 Variation of the maximum shear stress with time step for load case 3

4) Load case 4:

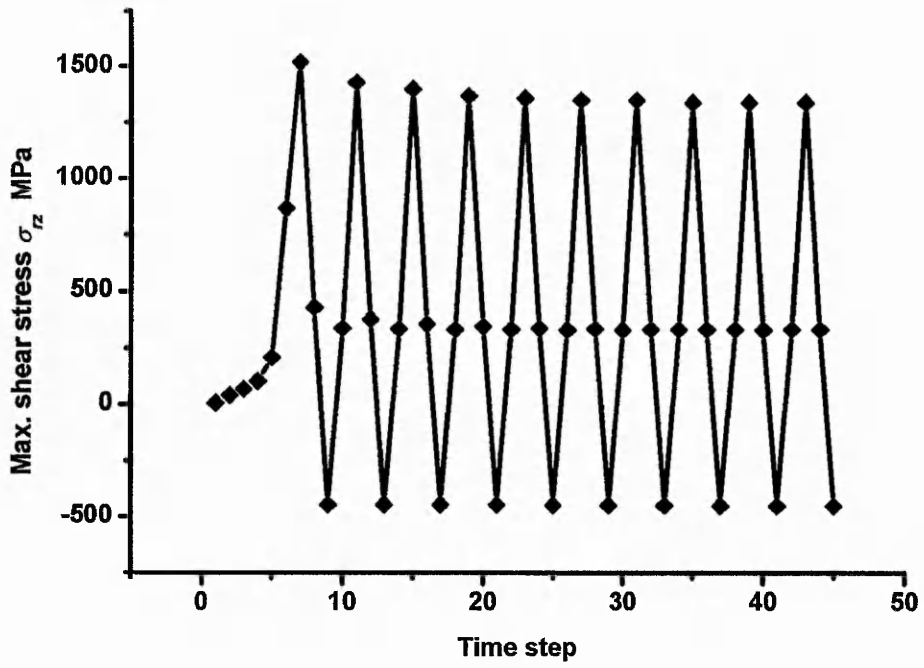

Figure 9.34 Variation of the maximum shear stress with time step for load case 4

Figure 9.34 shows the variation of the maximum shear stress for load case 4. The trend is similar to the previous load cases, with steady state being achieved after six cycles to give the amplitude of the shear stress, $\Delta\sigma_{rz}$, and the corresponding mean shear stress, σ_{rzm}, as:

$$\Delta\sigma_{rz} = 895.2 \text{ MPa}, \quad \sigma_{rzm} = 443.4 \text{ MPa}.$$

9.4.2.3 Comparison between experimental observations and FEA results

One of the objectives for using the soft impresser method in fatigue is to be able to generate data which can be used quantitatively in design, particularly for materials which are difficult to test by conventional means and with relevance to operational conditions involving contact between two bodies. By analogy with conventional fatigue, it is of interest to determine if the fatigue results of Guillou et al (1996) can be presented in the form of a classical 'S-N' fatigue curve. These are normally determined from fatigue tests performed in rotating bending, i.e. with zero mean stress. It is therefore necessary to obtain equivalent zero mean stress values for the present data. The most

commonly used approaches to account for mean stress effects are the Goodman and Gerber formulae (Suresh, 1992). In this case the Goodman approach will be used, since there is not sufficient general fatigue data for ceramic materials to be able to provide guidance as to which approach is likely to be more appropriate. Using the present notation, the Goodman equation is:

$$\frac{\Delta\sigma_m}{\Delta\sigma_0}+\frac{\sigma_m}{\sigma_{TS}}=1 \qquad (9.1a)$$

or,

$$\Delta\sigma_0=\Delta\sigma_m/(1-\sigma_m/\sigma_{TS}) \qquad (9.1b)$$

where $\Delta\sigma_0$ is the equivalent zero mean stress amplitude and σ_{TS} is the tensile strength of the material.

The tensile strength, σ_{TS}, of CeTZP can be estimated using (Knott and Withey, 1993):

$$\sigma_{TS}=\frac{1}{Y_c}\frac{K_{IC}}{\sqrt{\pi\, a_c/Q}} \qquad (9.2)$$

where, K_{IC} is the critical value of the stress intensity factor, also known as an alternative measure of fracture toughness; a_c is the length of an edge crack; Y_c is a dimensionless parameter depending on both the specimen and crack geometries; and Q is the flaw shape and orientation parameter. Guillou et al (1996), report a value of 15.8 MPa $m^{1/2}$ for K_{IC} and from the micrographs presented in their paper, the flaw size at the edge of the contact zone is approximately the grain size, which is typically ~ 5 μm, and also Y and Q are both taken as unity. Thus,

$$\sigma_{TS}=\frac{15.8}{\sqrt{\pi*5e-6}}=3990 \quad \text{MPa}$$

Normally in fatigue a test is terminated when the specimen fractures. This definition is not appropriate in the present case where the fatigue effects are localized to a relatively small surface area. Therefore, in this instance, the relevant fatigue life, N_f, is taken as the number of cycles to the formation of a full ring crack around the periphery of the

contact zone. Guillou et al (1996) have tabulated this data for their tests. Thus using Equation (9.1) with the maximum principal stress values presented in section 9.4.2.1, and the fatigue life data from Guillou et al (1996), the results shown in Table 9.26 are obtained.

Table 9.26 Fatigue stress amplitude and cycles to failure for CeTZP

	$\Delta\sigma_m$ MPa	σ_m MPa	$\Delta\sigma_0$ MPa	N_f
1	230.2	382.6	254.7	150000
2	119.6	353.8	131.3	500000
3	291.9	394.4	324.0	100000
4	453.9	913.0	588.7	5000

These data are presented graphically in Figure 9.35. It can be seen that there appears to be a similar form to the results as would be expected for conventional fatigue data.

It is possible to fit the data with an equation of the form:

$$\Delta\sigma_0 = c_5 + c_6 * \exp(-c_7 N_f) \qquad (9.3)$$

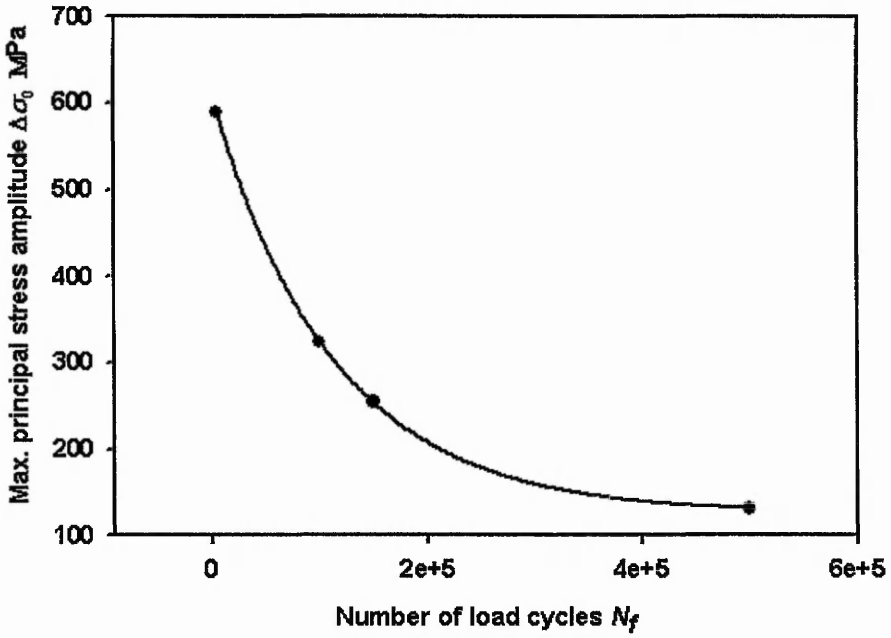

Figure 9.35 Relationship between $\Delta\sigma_0$ and N_f for CeTZP

The present results give the following values values for c_5 = 125.76, c_6 = 483.84, and c_7 = 8.872e-6, with the stresses in MPa. Thus it is now possible to use this equation to

predict the fatigue life to the formation of a full 'ring' crack in CeTZP under cyclic contact loading conditions.

9.4.3 Cyclic Soft Impresser Modelling Summary

Cyclic soft impresser modelling in CeTZP has been implemented with particular respect to the fatigue observations presented in Guillou et al (1996). The variation of the maximum principal and shear stresses outside the contact region with applied load was obtained for four load cases. It was found that the stresses at maximum and minimum load settled to constant values after between 3 and 7 cycles. Finally, a relationship between $\Delta\sigma_0$ and N_f was obtained for the CeTZP data presented in Guillou et al (1996).

9.5 Sliding

Brookes et al (1990) have shown that repeated sliding of a soft impresser across a flat substrate can be used to investigate the deformation and wear mechanisms in ceramics and ultrahard materials. The constant pressure - elastic substrate has been used in their work to estimate the stresses. The objective in this section is to investigate the possibility of using FEA to provide more detailed and accurate stress data. Since the FEA analyses take a considerable length of time to produce results, the modelling in this section has been implemented for a single forward traverse only. A plane strain model was assumed for the geometric model so that the modelling can be implemented in a 2D FE analysis. The substrate used was an elastic material, with elastic modulus and Poisson's ratio of 200 GPa and 0.27 respectively. The material properties for the soft impresser were the same as those in Table 9.1.

9.5.1 Geometric model and FE model

Figure 9.36 is the geometric model used. The symmetry line OO' of the soft impresser was constrained along the x direction. A constant force was applied on the top surface AB of the soft impresser. Lines CE, EF and FD on the substrate were constrained along the y direction and the displacement along the x direction was applied on lines CE, EF and FD to control the movement of the substrate.

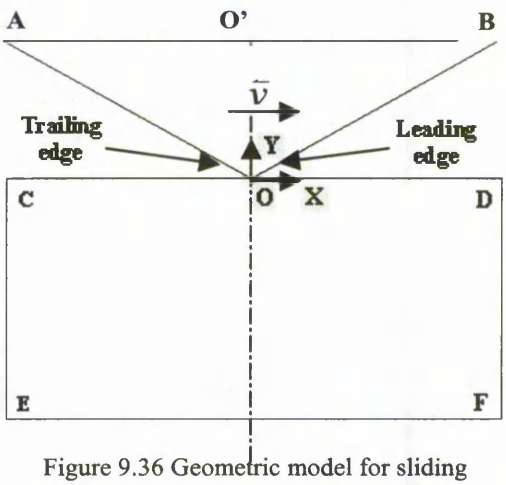

Figure 9.36 Geometric model for sliding

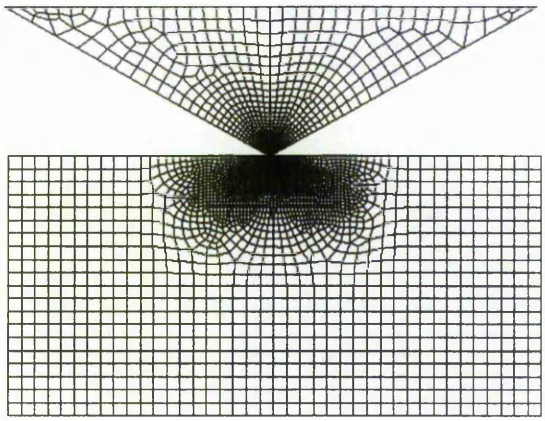

Figure 9.37 FE model for sliding

Figure 9.37 is a general view of the FE model, and Figure 9.38 is the detailed mesh model in the high deformation region. A surface to surface contact pair was defined between the soft impresser and the substrate.

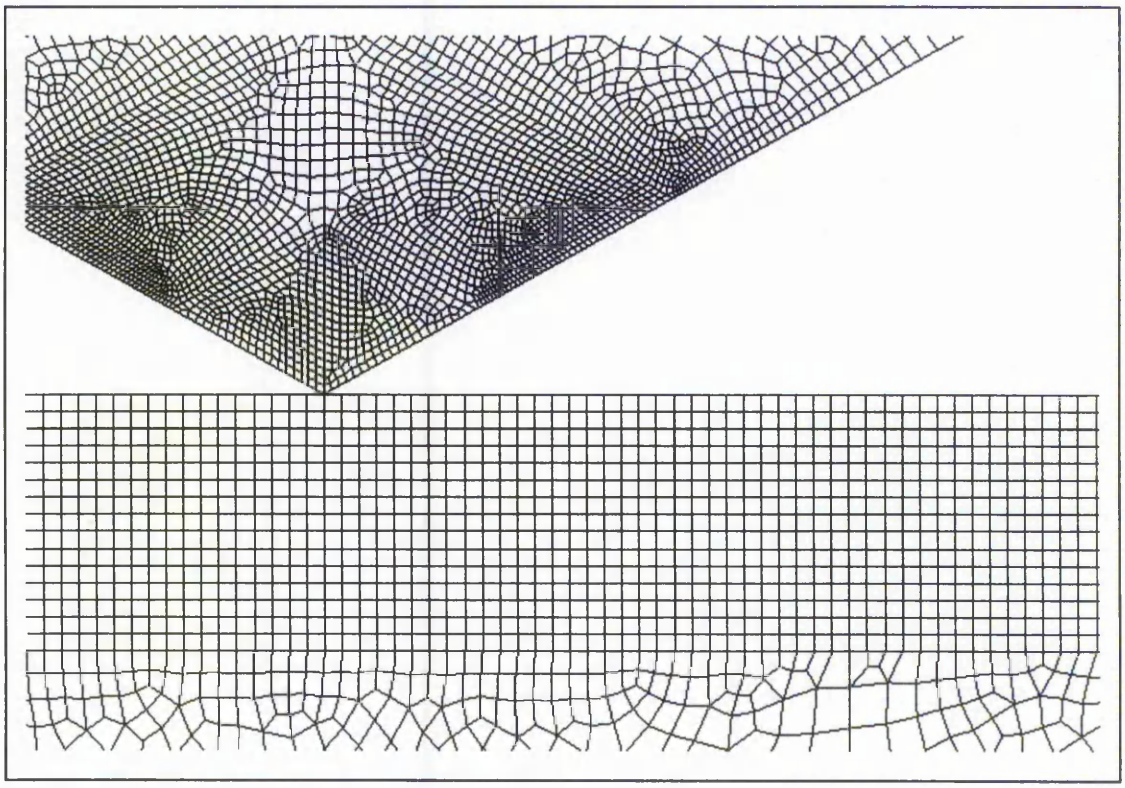

Figure 9.38 Detailed FE model close to the contact region

9.5.2 Modelling procedure

The modelling procedure for the sliding model was:

Step 1:

Apply a force load on the top surface of the soft impresser. After the maximum force has been achieved, the soft impresser will be flattened. The displacement along the x direction on the boundary lines of the substrate was set to zero.

Step 2:

Maintain the maximum force load on the top surface of the soft impresser and apply non-zero displacement along the x direction on the boundary lines of the substrate. The horizontal displacement applied to the substrate was increased gradually until the required sliding displacement had been achieved.

9.5.3 Results

Figure 9.39 shows the variation of σ_x* with sliding distance on the two sides of the impresser for the frictionless case. When there is no friction between the soft impresser and the substrate, the maximum σ_x in the substrate on both sides of the soft impresser are tensile.

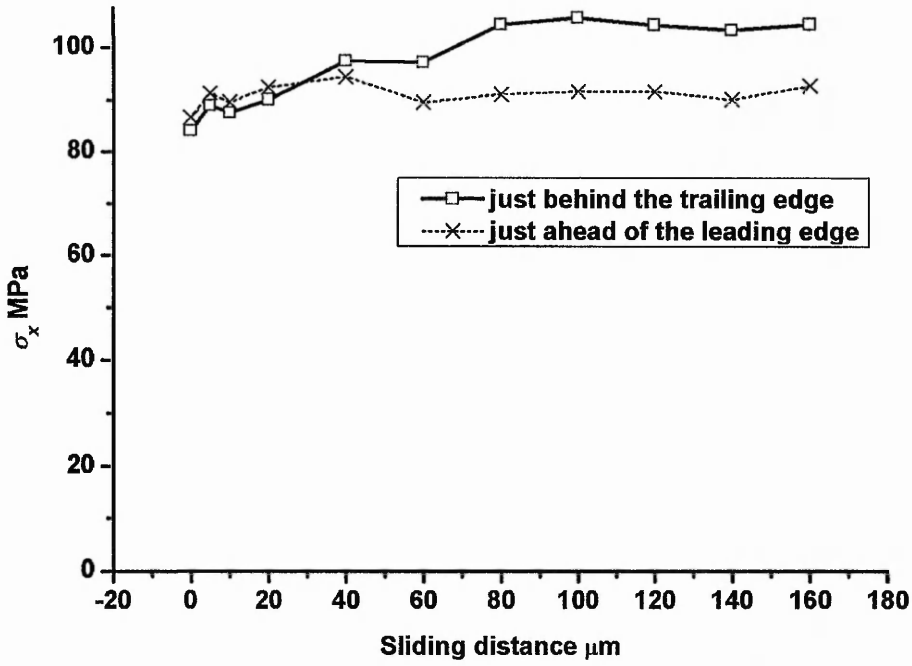

Figure 9.39 Variation of stresses in the substrate with sliding distance for both sides of the flattened cone ($\mu = 0$)

* Note: For Figures 9.39 – 9.42, the maximums are obtained from the results for the tensile stresses. For Figures 9.40 – 9.42, the compressive stresses are obtained from the symmetric location of the maximum tensile stresses with the centreline of the soft impresser as the symmetric line.

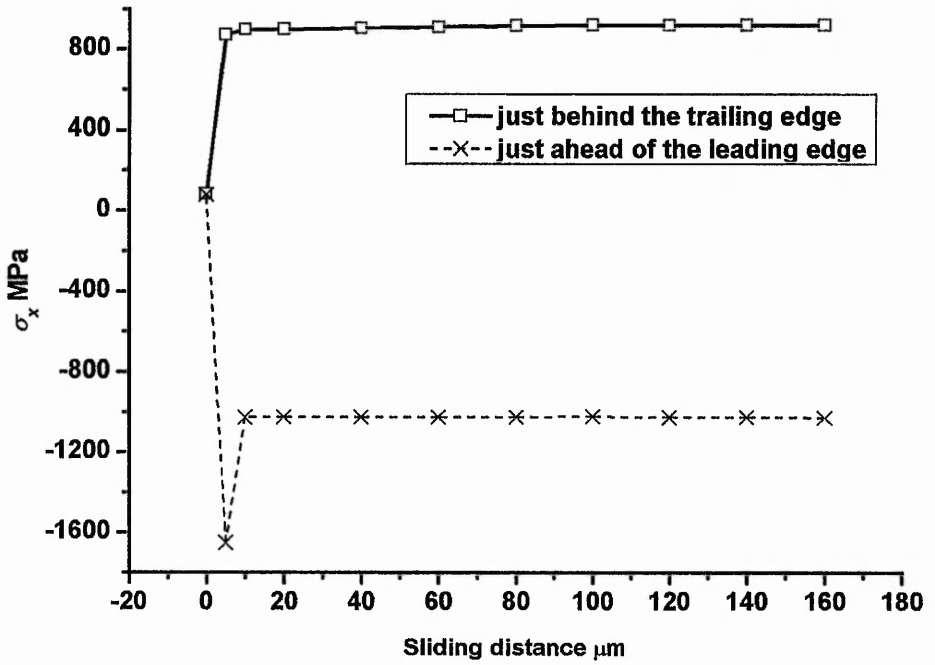

Figure 9.40 The variation of σ_x in the substrate with sliding distance for both sides of the flattened cone ($\mu = 0.1$)

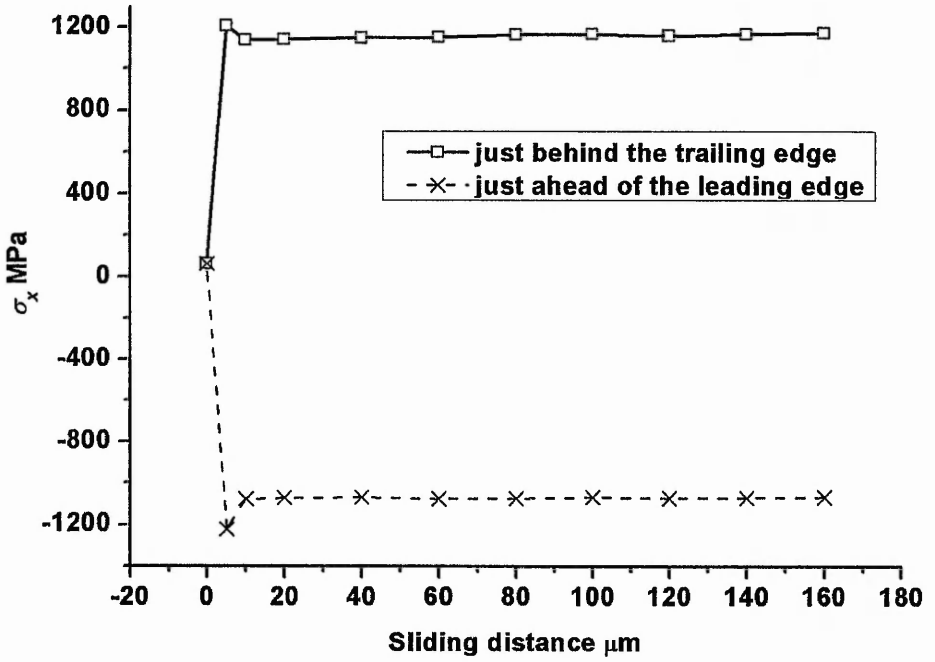

Figure 9.41 Variation of σ_x in the substrate with sliding distance for both sides of the flattened cone ($\mu = 0.15$)

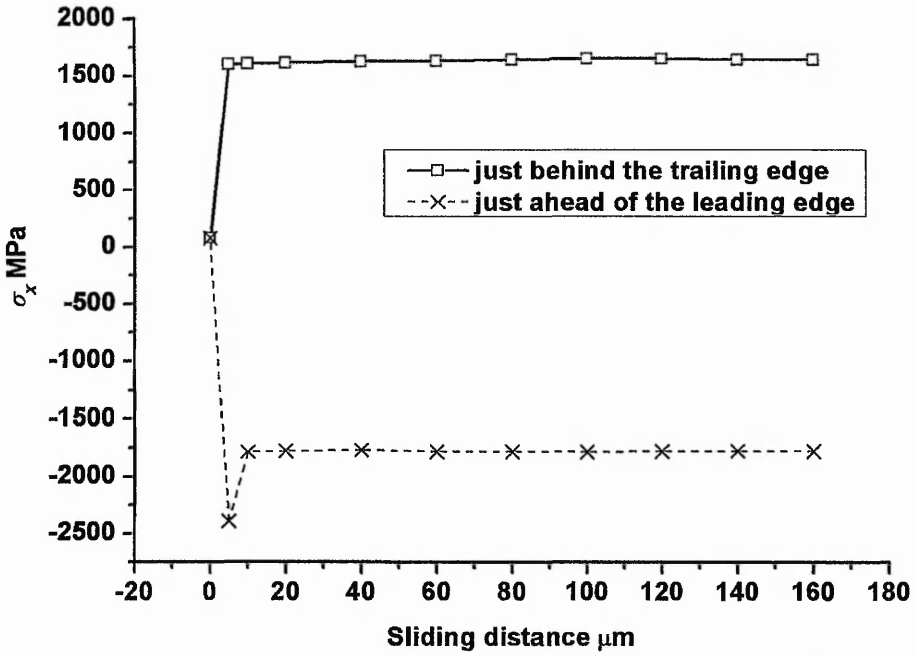

Figure 9.42 The variation of σ_x in the substrate with sliding distance for both sides of the flattened cone ($\mu = 0.2$)

It can also be seen that the maximum σ_x in the substrate just behind the trailing edge (Figure 9.36) is slightly greater than that just ahead of the leading edge (Figure 9.36).

Figures 9.40 to 9.42 show the variation of σ_x in the substrate with sliding distance for both the leading and trailing edges for $\mu = 0.1$, $\mu = 0.15$ and $\mu = 0.2$ respectively. For the three cases, the maximum σ_x in the substrate on the trailing edge of the soft impresser are tensile and the stresses along the x direction in the substrate on the leading edge of the soft impresser are compressive during the sliding process. σ_x in the substrate, on both sides of the soft impresser, becomes constant when the sliding distance is greater than one third of the contact radius.

The results show that the maximum tensile stress, i.e. $\sigma_{x\max}$, on the trailing edge of the substrate increases with increasing friction coefficient. Furthermore, using the regression method, for these particular results, the variation between the maximum tensile stress $\sigma_{x\max}$ and the friction coefficient is observed to be approximately linear (Figure 9.43), i.e.

$$\sigma_{x\max} = (0.0231 + 1.515 * \mu) p_{av} \qquad (9\text{-}4)$$

where the stress is in MPa, and $p_{av} = 4970$ MPa in the present case.

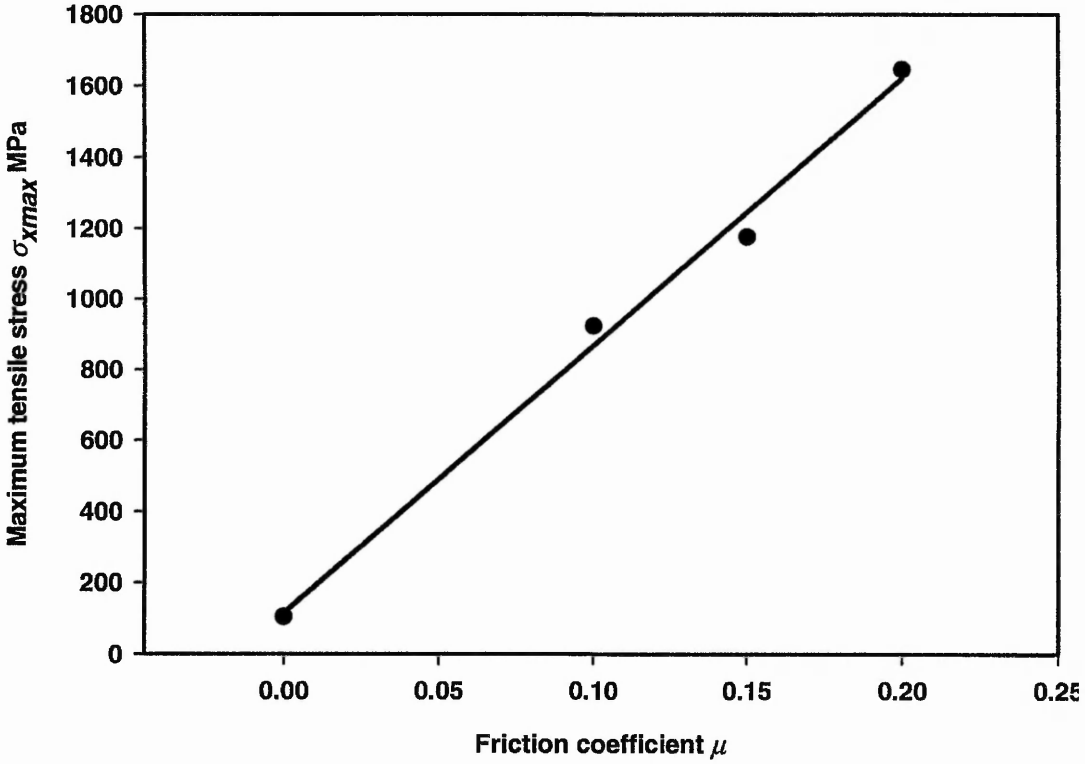

Figure 9.43 The relationship between the maximum tensile stress and the friction coefficient

That the friction coefficient value has a marked effect on the maximum tensile stress value revealed that the friction coefficient would have a marked influence on cracking for brittle materials, and thus the wear rate.

When higher friction coefficients were input, e.g. 0.5, it was found that the solution did not converge, even after several days run time. Experimentally, for soft impresser sliding at room temperature, a lubricant is always used. Thus the experimental friction coefficient values would lie in the range 0.01 - 0.14.

Figures 9.44 to 9.46 show the stress contours of σ_x at the beginning and the end of sliding for $\mu = 0$, $\mu = 0.1$ and $\mu = 0.2$ respectively. It can be seen that the asymmetry in the stress distribution after sliding increases as the friction coefficient increases.

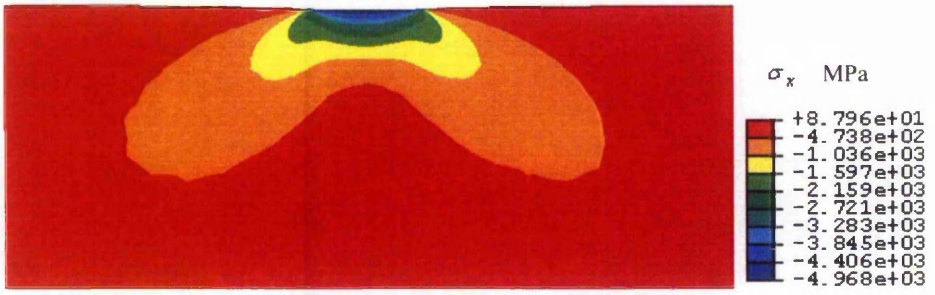

a) σ_x contours in the substrate at the beginning of sliding ($\mu = 0$)

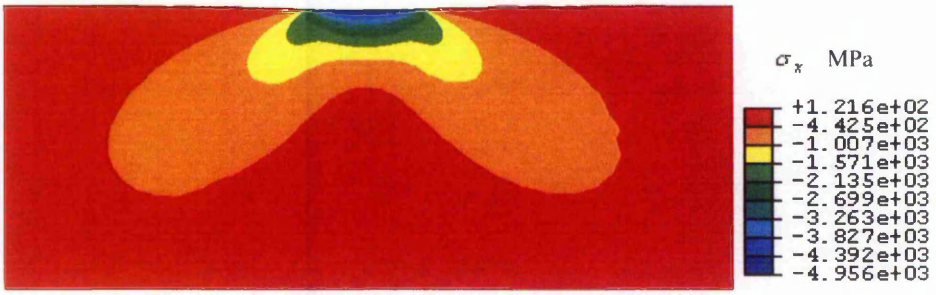

b) σ_x contours in the substrate at the end of sliding ($\mu = 0$)

Figure 9.44 σ_x contours in the substrate for $\mu = 0$

a) σ_x contours in the substrate at the beginning of sliding ($\mu = 0.1$)

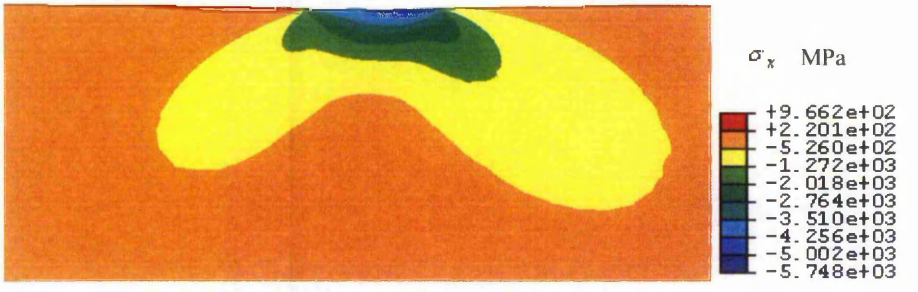

b) σ_x contours in the substrate at the end of sliding ($\mu = 0.1$)

Figure 9.45 σ_x contours in the substrate for $\mu = 0.1$

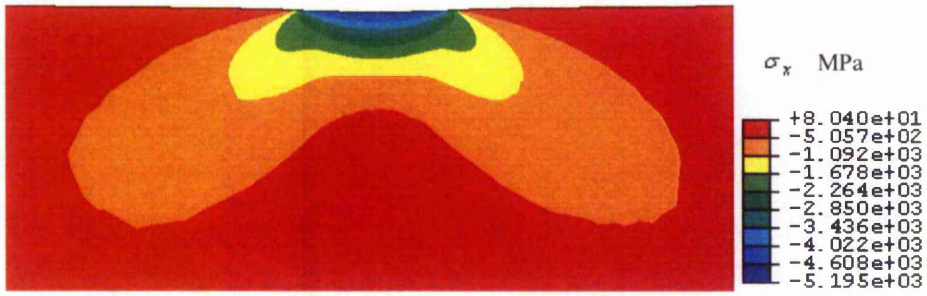

a) σ_x contours in the substrate at the beginning of sliding ($\mu = 0.2$)

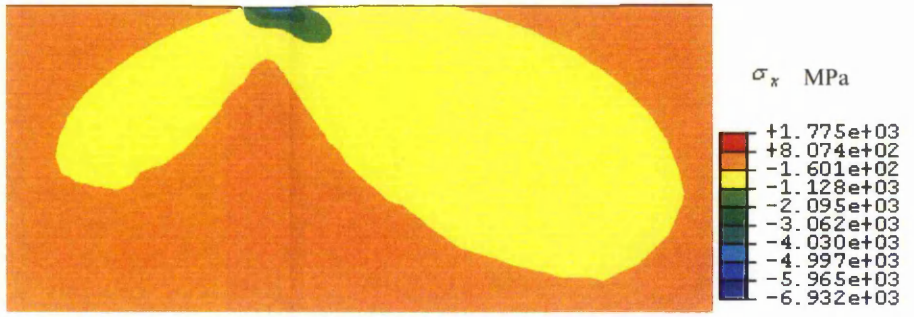

b) σ_x contours in the substrate at the end of sliding (μ=0.2)

Figure 9.46 σ_x contours in the substrate for $\mu = 0.2$

9.5.4 Soft Impresser Sliding Summary

The analysis and results for modelling the sliding of a soft impresser against an elastic substrate for a single traversal are reported in this section. The variations of the stresses along the x direction in the substrate with sliding distance for both the leading and trailing edges for the frictionless case and the frictional case were obtained.

When there is no friction between the soft impresser and the substrate, the maximum stress along the x direction in the substrate on both sides of the soft impresser are tensile. Also, the maximum stress along the x direction in the substrate on the trailing edge of the soft impresser is slightly greater than that on the leading edge.

For the frictional case, the maximum stresses along the x direction in the substrate on the trailing side of the soft impresser are tensile, whereas the stresses along the x direction in the substrate on the leading edge of the soft impresser are compressive during the sliding process. The stress along the x direction in the substrate on both sides of the soft impresser become constant when the sliding distance is greater than one sixth

of the contact length. The results also show that the tensile stress in the substrate on the trailing edge increases markedly with increasing friction coefficient.

9.6 Extracting the elastic modulus

The elastic modulus of a material may be estimated using an instrumented hard indentation test (section 5.13). However, it was found that the indenter rigidity has no effect on the calculated elastic modulus (section 5.8.2), which implies that the soft impresser indentation testing may also be applicable to measure the elastic modulus of a material. It is of interest to investigate this hypothesis. In this section, three materials, i.e. MgO, CeTZP and En08, were used to extract the elastic modulus from the soft impresser modelling. The other details of the analysis are as described in section 9.2.1. The material models for MgO, CeTZP and En08 were presented in section 6.1, Table 9.6 and section 5.2.1 respectively. The material properties of the soft impresser for CeTZP were presented in Table 9.1. The material properties of the soft impresser for MgO were presented in Table 9.27. The friction coefficient was taken as 0.15. Equation (5.1) was applied to calculate the elastic modulus of the substrate.

Table 9.27 Material properties of the soft impresser for MgO

Material	Elastic modulus GPa	Poisson's ratio	Isotropic Bilinear Plastic Flow Stress vs. Plastic Strain Data	
			Flow Stress MPa	Plastic Strain
HE 30 Aluminium	70	0.33	370.968	0
			510.968	1.0

The results (Tables 9.28-9.30) demonstrate that the soft impresser technique can be used to measure the elastic modulus of a material. For all of the cases studied in this section, the constant γ_h is close to 0.99, which implies that the constant γ_h is independent of the material properties of the substrate and the soft impresser. For the models with different impresser angles and coarser mesh for the impresser (section 5.8.2), the values

of the constant γ_h are slightly different, which means that γ_h is dependent on the impresser geometry and the precision of the model.

Table 9.28 Calculated elastic modulus for CeTZP

Impresser	Elastic	Elasto-plastic (En08)
Elastic modulus of the impresser GPa	206	206
Hardness ratio	∞	0.83
γ_h	0.99	0.99
E GPa	200.8	200.5
Relative difference	0.41 %	0.24 %

Table 9.29 Calculated elastic modulus for MgO

Impresser	Elastic	Elasto-plastic (HE 30 Al)	Elasto-plastic (MgO)
Elastic modulus of the impresser GPa	70	70	248
Hardness ratio	∞	0.15	1
γ_h	0.99	0.99	0.99
E GPa	246.3	247.7	248.2
Relative difference	- 0.69 %	0.10 %	0.08 %

Table 9.30 Calculated elastic modulus for En08

Impresser	Elasto-plastic (HE 30 Al)	Elasto-plastic (En08)
Elastic modulus of the impresser GPa	70	206
Hardness ratio	0.47	1
γ_h	0.99	0.99
E GPa	205.3	207.8
Relative difference	0.33 %	0.88 %

9.7 Summary

1) It has been demonstrated in this chapter that FEA can be used to good effect to provide knowledge of the stress distributions in soft impresser contact conditions. The formulation of the mesh requires considerable care to ensure the necessary accuracy in the results.
2) With frictionless contact between the impresser and an elastic substrate, it has been found that the stress distributions are reasonably close to the values predicted by Love's analysis (Love, 1929) for an applied constant pressure over a circular area on the surface of the substrate. When the contact is not frictionless, or there is plastic deformation in the substrate, then the maximum stress values become very different from those predicted using Love's analysis. Similar results have been obtained for the situation of flattening a cone at one position on a substrate and relocating and reloading the flattened cone at a different point on the substrate's surface. When the substrate is elastic and the contact is frictionless, for a second applied load which is at least 66% of the initial load to flatten, then the stresses can be estimated using the analytical equations for a constant pressure. When the substrate deforms plastically, and/or there is friction between the substrate and impresser, then the resultant stresses are different for the first and subsequent loadings. The values are also very different to the analytical estimates for the stress. Given the differences between the FEA stress results and those obtained using the constant pressure analytical approximation, it is clearly preferable generally to undertake FEA analysis of soft impresser test to derive quantitative materials information.
3) The results for the cyclic loading FEA analyses have demonstrated that an improved interpretation and understanding of the experimental data can be obtained.
4) It has also been demonstrated that FEA can be used to model the situation of a soft impresser sliding over the surface of a flat substrate. The limited

results obtained show that in this case too, friction can significantly affect the stress distribution in the substrate.

5) The soft impresser technique can be used to measure the elastic modulus of a material. The value of the constant γ_h is independent of the material properties of the substrate and the soft impresser. However, γ_h is dependent on the impresser geometry and the precision of the model.

CHAPTER 10
DISCUSSION

10.1 Introduction

The finite element method has been used extensively in the modelling of indentation testing since 1968 (Akyus and Merwin, 1968), although by far the majority of papers have appeared within the last 4 years or so. There has tended to be a concentration on the topics studied, such as the load-penetration depth relationship (Bhattacharya and Nix 1988; Giannakopoulos et al, 1994; Larsson et al, 1996; Murakami and co-workers, 1994 and 1997), estimation of the mechanical properties such as Young's modulus, compressive yield strength, strain hardening exponent and hardness (Jayaraman et al, 1998; Giannakopoulos and Suresh 1999; Futakawa et al, 2001; Cao and Lu, 2004b), the scaling relationships for the loading and unloading curves, contact depth, and hardness for indentation in elastic-plastic solids with work hardening (Cheng and Cheng, 1999 and 2004), indenter geometries (Lichinchi et al, 1998; Yu Ning et al, 2004), mesh effects (Lausen and Simo, 1992), effects of material properties (Matsuda, 2002), friction (Tsou et al, 2004; Bolzon et al, 2004; Mata and Alcalá, 2004), sliding (Krichen et al, 1996; McColl et al, 2004), coatings (Tsui et al, 1999; He and Veprek, 2003; Panich and Sun, 2004; Yoo et al, 2004), creep (Becker et al, 1994; Yue et al, 2000), or indentation cracking (Larsson and Giannakopoulos, 1998; Zhang and Subhash, 2001; Muchtar et al, 2003).

The above studies have been concerned with modelling the penetration of a softer substrate by a rigid/harder indenter. Very few papers, e.g. Lacerda et al (1999), Henshall et al (1999), and Fagan et al (2000), have been concerned with soft impresser modelling, and have only covered very limited aspects.

The literature review showed that the majority of the hard impresser modelling to date has concentrated on metals and reproducing the macroscopic aspects of the behaviour, principally indentation depth, using 2-D axisymmetric models. Thus further the analysis of the hard indenter modelling in ceramic materials was required. This form of testing is particularly relevant for ceramic materials since their mechanical properties are difficult to measure using other conventional methods, such as uniaxial tension. The majority of the soft impresser modelling that has been presented to date (Brookes et al, 1990; Maerky et al, 1997; Fagan, 2000) have assumed that the loading due to the soft

impresser can be considered as a uniform pressure, which is simply the applied load divided by the contact area. Some preliminary FE modelling of the actual contact situation suggested that this approximation is not generally correct (Henshall et al, 1999). Therefore further analysis of the mechanics of this test method was required.

10.2 Development of the finite element models

It was necessary to investigate the accuracy and validity of the finite element modelling parameters and procedures prior to being able to have confidence in the results obtained for the range of FE models considered in this work. Thus, the FEM results were initially verified in Chapter 4 using ANSYS by comparison with available analytical and/or experimental results. For the problem of a circular region of constant pressure applied to a flat semi-infinite solid, the stresses generally could be determined without much difficulty, but it was quite difficult to obtain reasonably good estimates of the radial stress on the surface at the boundary between the applied pressure and free surface, table 4.1. However it did prove possible to achieve good agreement when using an appropriate mesh and element type. Furthermore, a suitable finite element model was developed by taking into consideration the effect of mesh (*cf* sections 5.3.1, 7.7.1, 9.2.1 and 9.2.2), element type (section 4.1.3), model size (section 5.5), contact element type (sections 4.2.2 and 5.1), FE software package (section 5.3.2), and dimensions of the model (section 5.14).

These observations highlighted the fact that for contact situations the mesh in the substrate around the contact edge should be sufficiently refined to capture the local stresses, since the stress around the contact edge is of major interest and it also has a high stress gradient. Most of the researchers (e.g. Giannakopoulos et al, 1994; Murakami, 1994; Cheng & Cheng, 1999; Dao et al, 2001; Strange & Varshneya, 2001; Mata, 2004; Bolzon, 2004; Yu, 2004) have used a uniform mesh in the contact region. Using this approach, the precision of the computed stresses cannot be guaranteed unless the mesh size around the whole contact region is small enough. However, in this case, the total number of elements will increase dramatically, whereas only the mesh in the location where there exists a high stress gradient, needs to be fine enough. In the present instance, the mesh in the substrate was considered to be appropriate when the finite element results are consistent with the analytical results for a constant pressure applied to an elastic substrate (sections 5.3.1, 9.2.1 and 4.1.3). This consideration is applicable to both the hard indenter modelling and the soft impresser modelling.

In practical situations, a general problem may not have an analytical solution. In this case, the results from the FE model must be verified by experiments, otherwise, the reliability of the results cannot be guaranteed. Thus, in the situations where the analytical solutions cannot be obtained, the mesh was considered to be appropriate when the finite element results are consistent with the experimental results.

For the soft impresser, the region around the apex of the cone becomes highly deformed. Thus, the mesh around the apex of the cone should be fine enough to capture the plastic deformation (section 9.2.1). Because the soft impresser will be in contact with the substrate after deformation, the mesh size in the contact region should be appropriate to guarantee that no interpenetration occurs between the two bodies. A 4-node bilinear axisymmetric quadrilateral element with enhanced strain option (ANSYS), or incompatible mode (ABAQUS), is the most robust element. These give maximum radial stress values close to the analytical results. Moreover, these elements are not as sensitive with regard to the mesh size as compared with the other possible elements (section 4.1.3). In the literature, a study of the use of this type of element in the indentation FE modelling field, and the comparison between different types of elements, does not appear to have been reported (e.g. Giannakopoulos et al, 1994; Cheng & Cheng, 1999; Dao et al, 2001; Strange & Varshneya, 2001; Bucaille et al, 2003; Mata, 2004; Bolzon, 2004; Yu, 2004).

A surface-to-surface contact pair was established between the indenter/impresser and the substrate. For the tangential behaviour, the penalty friction formulation was used; for the normal behaviour, the augmented Lagrange formulation was used (section 5.1). This kind of contact pair was preferred to that in the early version of ANSYS (section 4.2.2) since it improves convergence and it is more straightforward to implement.

The model size (section 5.5) has only a limited influence on the calculated hardness values, especially when the model size is more than 20 times the indentation depth. However, tables 5.6 and 5.8 show that model size may have a marked influence on the calculated elastic modulus (the method for calculating the elastic modulus is described in detail in section 5.13). The relative differences between the input and calculated elastic modulus values are less than 5% when the ratio of the model size to the indentation depth is greater than 50. These results show that a model size of more than one hundred times the indentation depth is required to give accurate elastic modulus values, and would suggest that experimentally tested specimens should also have a thickness of more than one hundred times the indentation depth. In the literature

concerned with the FE modelling of hardness and elastic modulus, various ratios of the model size to the indentation depth have been used (Table 5.9). A model size of only about 10 times (Table 5.9) the indentation depth, which has been conventionally mentioned as being sufficient, may not give good results. Moreover, the effect of the model size on the calculated elastic modulus does not appear to have been reported in the literature.

A comparison between a 2D model and a 3D model was undertaken in Section 5.14. It was found that H_{IT} [$H_{IT} = F/(\pi R_c^2)$] from the 2D model is equivalent to the Vickers hardness [$HV = \frac{2F\sin 68^\circ}{d^2}$] from the 3D model. In addition, HM [$HM = F/(26.03h^2)$] from the 2D model is equivalent to HM [$HM = F/(26.424h^2)$] from the 3D model. Moreover, Lichinchi et al (1998) found that the axisymmetric model with a conical indenter, which has the same area function as the 3D Berkovich indenter, can give an identical loading-unloading curve as that from the 3D model. Thus, it was decided that using a 2D axisymmetric FEM model instead of a 3D model is more appropriate, since a 2D model can use a more detailed mesh, and save substantial computing time with regard to a 3D model.

Table 5.3(a), based on the model described in section 5.3.1 with En08 as the substrate and friction coefficient = 0.5, shows values for selected parameters as examples to demonstrate that many of the FE results are very similar for ABAQUS and ANSYS, when using the same geometrical model, although the material model may need to be adjusted. However, table 5.3(b) shows that the calculated values for the maximum principal stress from ANSYS exhibit a much greater variation than the values calculated by ABAQUS. Furthermore, Table 5.3(c) shows that for ANSYS versions from 5.7 to 9.0 do not apply this material model (Table 5.3(d)) with sufficient accuracy. Thus it is considered that the results from ABAQUS are more reliable and robust. Moreover, it is much easier to implement the user subroutine in ABAQUS than in ANSYS, since ABAQUS has much more detailed help documentation. Therefore ABAQUS was selected as the preferred FE package, although a substantial amount of modelling was also undertaken in ANSYS prior to ABAQUS being available for use by the author. In the literature, ABAQUS is also the most commonly used commercially available software in the indentation modelling field (*cf* section 2.6.1).

When using the implicit analysis method to carry out the indentation modelling of multilayer coatings (Chapter 7), it was very difficult to obtain a converged solution. For some cases, the solutions just diverged even after several days' computation. The difficulty in convergence arose due to the extensive localised deformation in the aluminium layers. The explicit-to-implicit analysis method, which is widely used in the spring-back analysis of sheet metal, was introduced into the indentation modelling field (section 7.5). It was found to give essentially the same results as an implicit procedure, but could overcome the convergence difficulty of the implicit method. This method has previously been used successfully by the author to resolve the spring-back modelling problem for an auto-door cover panel using ANSYS/LSDYNA (Sun & Hu, 1999). As noted above, section 2.6.1.7, an explicit method for the FE analysis of hardness using ABAQUS was also proposed on the basis that it substantially reduces the required computational times (Yoo et al, 2004).

10.3 FE modelling of rigid indentation hardness

FEM modelling can be used to quantitatively estimate material hardness and evaluate the deformation properties, such as elasto-plastic deformation and creep, of materials. In order to establish a reliable and effective FEM indentation model, some relevant factors, such as the mesh size, model size, friction coefficient, applied load, indenter tip radius, indenter angle, indenter rigidity, etc., were investigated (Chapter 5) using a 2D axisymmetric FEM model in most cases. Either piling-up or sinking-in of the substrate material along the face of a rigid indenter is usually encountered during experimental indentation testing. Two typical materials, i.e. En08 and MgO, were used for this study since the En08 steel is a well characterised piling-up material, whereas MgO is a not-as-well-characterised sinking-in material.

Two measures of hardness (section 2.1.1), i.e. the Martens Hardness *HM* and the Indentation Hardness H_{IT}, were used in this study. Based on the results presented in this thesis it is considered that the indentation hardness is a better measure of a material's hardness than the Martens hardness, since the Martens hardness definition does not take into account any sinking-in or piling-up of material around the indenter. In the literature, the indentation hardness H_{IT} is the most commonly used measure of hardness (section 2.6.1).

The effect of the indenter angle was studied in section 5.4.1. Although there is a significant difference in the actual indentation hardness values between the present FEA

and Johnson's model (Johnson, 1970), the trend of the variation in hardness with indenter angle is broadly similar. However, the results based on Cheng and Li's analysis (Cheng and Li, 2000) appear to be very different. Overall, these results would indicate that it is not possible to use a simplified equation to predict quantitatively the variation of hardness with indenter angle. It is also of interest to note that the FEA results give a value of $H/Y = 3.9$, which is very close to the 'rule-of-thumb' estimate for steels of $H/Y = 4$.

The effects of indentation size and indenter tip radius on the hardness were studied for En08 and MgO in section 5.6. Xue et al (2002) concluded that the effect of indenter tip radius on indentation hardness disappears once the contact radius exceeds one half of the indenter radius. In this work, the minimum ratio of the contact radius to the indenter radius was equal to 0.93 for MgO when the indenter radius is 3 μm and the indentation depth is 1 μm. Thus the conclusion in the present study with regard to the effect of the indenter tip radius on H_{IT} agrees with Xue et al (2002). No indentation size effect was found in the present investigation, which is different from the results of Xue et al (2002). This is possibly because classical continuum plasticity theory, which was used in this work, may not be appropriate for modelling the observed indentation size effect (Xue et al, 2002).

The effect of friction coefficient was studied in section 5.7. Figures 5.8 and 5.9 give a comparison of the effect of friction coefficient on H_{IT} between FEA and the analytical results (Mata, 2004) for En08 and MgO respectively. For En08, the results from the FEA agree well with those from the analytical analysis. However, for MgO, the results exhibit a significant difference between FEA and the analytical analysis (Mata, 2004), which is not surprising since the analytical analysis (Mata, 2004) was developed for metallic materials. The friction coefficient has usually assumed to be zero in many papers in the literature (e.g. Laursen & Simo, 1992; Cheng & Cheng, 1999; Dao et al, 2001; Strange, 2001; He & Veprek, 2003; Yu et al, 2004) and has been considered to have no effect on the indentation process (Laursen & Simo, 1992; Yu et al, 2004). However, the results from the present study show that for a ductile material, the relative difference in the indentation hardness between a frictionless model and a frictional one may be as great as 10% to 15%. It is only for a hard material that the effect of friction coefficient on the indentation hardness is negligible. Thus, the assumption of frictionless contact between a rigid indenter and softer substrate is not appropriate for a ductile material.

The following relation (Pharr et al, 1992) has most frequently been used to derive the elastic modulus of a material from instrumented indentation test data,

$$S_c = \frac{2}{\sqrt{\pi}} \frac{E(h_c)}{(1-\nu^2)} \sqrt{A(h_c)} \tag{10.1}$$

However, this relation was derived based on elasticity theory (Snedon, 1965) and thus it was assumed that there is sinking-in of the material instead of pileup. Some insight into the causes of overestimation of Young's modulus is provided by the work of Hay, Bolshakov and Pharr (1999). For a rigid conical indenter, they derived a corrected relationship

$$S_c = \gamma_h \frac{2}{\sqrt{\pi}} \frac{E(h_c)}{(1-\nu^2)} \sqrt{A(h_c)} \tag{10.2}$$

However, Strange and Varshneya (2001) found that the corrections derived by Hay, Bolshakov and Pharr (1999) for a conical indenter are not applicable to a true three-dimensional Vickers indentation in aluminium. Since a 2D axisymmetric model with a conical indenter, which has the same area function as the 3D Vickers indenter, can give the same results as a 3D model (section 5.14), the conclusion from Strange and Varshneya (2001) implies that the corrections derived by Hay, Bolshakov and Pharr (1999) for a conical indenter may not be generally applicable to a 2D axisymmetric model as well. Another observation by Strange and Varshneya (2001) is that if the appropriate area of contact is used in the calculation, then Sneddon's solution for calculating Young's modulus can be accurate, even for highly plastic materials.

In this work, three modifications were applied. Firstly, the basic assumption, i.e. $h_c / h = 2/\pi$ (which is not true generally), has been used to derive Equations (10.1) and (10.2) was replaced by a more general assumption, i.e. $R_c / h = \text{C}''$ instead (section 5.13). Secondly, the correction derived by Hay, Bolshakov and Pharr (1999) was adopted. Thirdly, the contact area was calculated using R_c, which can be interpolated based on the contact pressure of the last two contact nodes in FEA directly instead of h_c. Thus, the following equation was finally derived as

$$S_c = \gamma_h \frac{2E(R_c)}{1-\nu^2} R_c \tag{10.3}$$

In section 7.6, both the Oliver and Pharr method (1992) and the present method were applied to calculate the elastic modulus for bulk TiB_2. Table 7.3 shows that the Oliver-Pharr method (1992) only worked well at shallow indentation depths, which is expected since the Oliver-Pharr method (1992) was derived based on elasticity theory; and it

over-estimated the elastic modulus by up to 11.8% when the indentation depth was greater than 118 nm. The relationship between $E(R_c)$ and $E(h_c)$ was obtained as

$$\frac{E(R_c)}{E(h_c)} = \frac{h_c}{\gamma_h h_{rc}} \tag{10.4}$$

Equation (10.4) clearly shows that the difference between $E(h_c)$ and $E(R_c)$ occurs due to the values of h_c being calculated using different methods and that the constant γ_h was used in Equation (7.8).

The maximum relative difference between the inputted elastic modulus value and the calculated one for this model is 3.5%. A relatively coarse mesh was used for these analyses since the main purpose of the results presented in section 7.6 was to compare the differences between the implicit method and the explicit-to-implicit method. Actually, when a finer mesh was used, the maximum relative difference between the input value and the calculated one can be less than 1% (Tables 5.25-5.26).

The above analysis with regard to extracting the Young's modulus of a material from instrumented indentation test or modelling data was implemented based on the rigid indenter assumption. For a deformable indenter, the reduced modulus should be used to compensate for the elastic deformation of the indenter (Oliver and Pharr, 1992). Thus, Equation (10.1) can be rewritten as

$$S_c = \frac{2}{\sqrt{\pi}} E_r(h_c)\sqrt{A(h_c)} \tag{10.5}$$

Similarly, Equations (10.2) and (10.3) can be rewritten respectively as

$$S_c = \gamma_h \frac{2}{\sqrt{\pi}} E_r(h_c)\sqrt{A(h_c)} \tag{10.6}$$

$$S_c = 2\gamma_h R_c E_r(R_c) \tag{10.7}$$

It was found (section 5.8.2) that the method proposed by Hay, Bolshakov and Pharr (1999) to calculate the constant γ_h is not applicable to the case with a deformable indenter. In section 5.8.2, γ_h was calculated based on the FE indentation modelling for the elastic indenter case. Then the same value of γ_h was applied to the elasto-plastic indenter cases. Since the indenter rigidity has virtually no effect on the calculated elastic modulus, the methods (Equation (10.7)) for calculating the elastic modulus of a material can be extended to the elasto-plastic indenter case, which implies that the soft impresser indentation testing may be able to be used to measure the elastic modulus of a material as well, especially for a hard material. This was further discussed and demonstrated in

section 9.6. Moreover, it was found that in this case the constant γ_h is independent of the material properties, although it is dependent on the impresser geometry and the precision of the model.

Although the indenter rigidity has no significant effect on the calculated elastic modulus, it does have a marked effect on the calculated indentation hardness (section 5.8.1). The magnitude of the effect of the indenter rigidity depends on the hardness of the studied material and the hardness ratio of the indentation hardness of the indenter to that of the substrate material. For both En08 and MgO, when the hardness ratio is equal to 1, the calculated indentation hardness values were substantially lower than the true values. For En08, when the hardness ratio is greater than 1.5, the indenter rigidity has no effect on the calculated indentation hardness. However, for MgO, for the case with hardness ratio = 2, although the indenter exhibits exceedingly limited plastic deformation, the calculated indentation hardness is still about 3.3% lower than that for the rigid indentation case. This arises from the elastic deformation of the indenter, since it is equal to the value from the elastic indenter case with the same elastic modulus. Only in the elastic indenter case with the same material properties as a diamond, can the equivalent indentation hardness value as that from the rigid indentation case be obtained for MgO. Lo and Bogy (1999) also obtained lower hardness values for very hard materials when the elastic deformation of the indenter was taken into account.

A limited investigation into the effects of variations in the elastic modulus, yield stress and tangent modulus for the substrate was undertaken in section 5.9. The hardness value increases with increasing yield stress, as well as with increasing tangent modulus, which is expected. The values calculated for *HM* are higher when unloaded than loaded, which is expected as a result of the elastic recovery. In contrast, the values calculated for H_{IT} are essentially the same for both the loaded and unloaded cases.

The ratio of hardness to yield stress increases with the increasing tangent modulus for both *HM* and H_{IT} for a work hardening material. For an elastic perfectly plastic material, both *HM/Y* and H_{IT}/Y increase with increasing *E/Y*. However, the variation of *HM/Y* is different from that for H_{IT}/Y. When *E/Y* increases from 50 to 1030, *HM/Y* varies from 1.97 to 4.04 and H_{IT}/Y varies from 2.72 to 3.13 when under load (Tables 5.19 and 5.21). *HM/Y* has a larger variation than H_{IT}/Y, as well between the loaded status and the unloaded status. For a relatively low *E/Y* ratio, e.g. *E/Y*=50, *HM/Y* increased from 1.97

(under load) to 3.16 (unloaded), where, H_{IT}/Y only decreased from 2.72 (under load) to 2.63 (unloaded).

Dimensional analysis can provide additional helpful interpretations of the mechanics of the indentation process; thus the basic theory of dimensional analysis was given in section 2.4. A limited investigation into the dimensional analysis of the rigid indentation results was undertaken in section 5.15, based on Cheng and Cheng's work (2002). In the present study the friction coefficient, which was assumed to be 0.15 for a general practical situation, was taken into account. Based on the FE analyses, the relationships between H_{IT}/E^*, W_p/W_{tot} (W_e/W_{tot}) and h_f/h_m were determined using regression. The values for the curve-fitted constants in Equations (5.20) – (5.22) are somewhat different from the values in Equations (5.14) – (5.16) (Cheng and Cheng, 2002), which may imply that friction does have an influence on H_{IT}/E^*, W_p/W_{tot} (W_e/W_{tot}) and h_f/h_m, and it cannot be neglected in practical situations.

10.4 FE modelling of hardness tests on MgO

FE modelling of hardness tests on single crystal MgO was implemented primarily in Chapter 6. A simplified anisotropic material model was used and a specific plastic material model was assumed for MgO (Griffiths et al, 2001). The results show that the contribution of the elastic anisotropy of MgO to the observed hardness anisotropy is negligible, which implies that the anisotropy of the slip deformation is mainly responsible for the observed anisotropy. Thus, a specific plastic material model is applicable to a specific slip system only. An equation (Equation (6.1)) was proposed based on the hardness anisotropy to correlate the flow stresses along different slip directions. The calculated hardness values for MgO (001) <100> and MgO (001) <110> agree reasonably well with the experimental results based on the proposed material model. The results also demonstrate that it is not always possible to use uniaxial stress-strain data to model the complex multiaxial deformation which occurs beneath an indenter.

In sections 8.1.2.2 and 8.2.1.2, an elastic perfectly plastic material model was assumed for YCPZ and MgO respectively at different temperatures. Obviously, this is only an approximate estimation of the material model. More accurate estimation of the material model, as discussed in Chapter 6, could be applied instead in future work.

10.5 FE modelling of the hardness of alternating Al and TiB_2 multilayer coatings

In Chapter 7, FE modelling has been performed for multilayer coatings comprising alternating aluminium and titanium diboride, TiB_2, layers. The dependence of the hardness and elastic modulus on the structure of the multilayer coating were investigated and compared with experimental results from the literature (Hancock et al, 2002). The different methods of calculating the hardness and elastic modulus were compared and analysed. The variations of hardness and elastic modulus with number of layers were calculated. The agreement between the FE results and the experimental observations was good in some cases, but there were significant discrepancies (> 50%) in some cases. This could be due the assumptions made in the modelling, e.g. it was assumed that the aluminium and titanium diboride were perfectly bonded together, which is unlikely to be the case in practice, scatter in the experimental data, or a different elasto-plastic constitutive equation being required for such thin layers, e.g. strain gradient hardening. The number of layers, and thus relative thicknesses, had been arbitrarily selected in the experimental study. The present numerical investigation of the number of layers in the coating, for a constant overall coating thickness, showed that this parameter was probably not optimal in the experimental study.

FE modelling of the hardness of single layer coatings has received considerable attention in the literature (e.g. Tsui et al, 1999; He and Veprek, 2003; Panich and Sun, 2004; Yoo et al, 2004), but FEA of alternating multilayer coatings does not appear to have been reported in the literature to date. Tsui et al (1999) have studied the indentation plastic displacement field around Knoop indentations made in multilayered coatings. However, in their FE analysis, the multilayered coatings were modelled as a monolithic layer.

Čekada and Panjan (2001) experimentally evaluated the microhardness and elastic modulus of multilayer hard coatings by micro-indentation. Their results on the variation of elastic modulus and hardness with number of layers revealed that the elastic modulus approaches a constant value when the number of layers is greater than 8 and the hardness has negligible changes when the number of layers is greater than 6, which are close to the conclusions obtained in the present study. The variation in hardness values does not seem to be consistent with the elastic moduli in their results, which might be due to measurement error since the calculated values of Indentation Hardness and elastic modulus are very sensitive to calculation methods (section 7.6).

10.6 Rigid indentation creep modelling

The modelling of time dependent deformation under rigid indentation conditions was considered in chapter 8. A modified dislocation glide model and the power law breakdown creep model were applied to the indentation creep deformation analyses for YCPZ at temperatures from 290 K to 1073 K (section 8.1) and for single crystal MgO at temperatures from 293K to 873K (section 8.2) respectively. A FE indentation creep modelling procedure was proposed and implemented (sections 8.1.2 and 8.2.1). The basic material parameters, i.e. the activation energy for YCPZ and MgO were predicted based on the analytical indentation creep analyses. This provided the basis to be able to predict the time dependent deformation for YCPZ and MgO in this temperature range for any applied stress state.

Prior to modelling the rigid indentation creep process, the hardness testing and the analytical analysis were required to be undertaken. The hardness testing provided the hardness values at different temperatures. Thus the yield stress at the different temperatures can be estimated from the hardness values (sections 8.1.2.2 and 8.2.1.2). Some constants (sections 8.1.2.1 and 8.2.1.1) in the creep model can be determined from the analytical analysis. In the subsequent FE indentation creep analysis, the stress index n needs to be adjusted slightly so that the variation of the hardness with time from FEA can agree with that from the experimental hardness testing.

Two forms of modified glide controlled dislocation creep models were proposed based on analytical analysis and the experimental results in sections 8.1.2.1 and 8.2.1.1 respectively. Both of these creep models can give similar results to the power law breakdown creep model, especially at lower temperatures (sections 8.1.3 and 8.2.2). These creep models were subsequently implemented in ABAQUS to carry out FE analysis. The results from the FEA agreed well with the experimental results in general, with only a few data points providing relatively weaker agreement. From the FEA the evolution of creep strains with time for YCPZ and MgO show that the creep deformation originates from the contact edge, followed by extension into the substrate towards the central region. However, the central region just beneath the indenter exhibits little creep deformation. This is different from the analytical assumption since the analytical model assumes that there is a uniform hemispherically shaped creep zone from the outset (Li et al, 1991). It can also be seen that the creep deformation at a higher temperature is more marked than that at a lower temperature, which is expected.

10.7 Soft impresser modelling

In Chapter 9, finite element analyses for the soft impresser test methodology were developed. Preliminary analyses (section 9.2) were implemented first to a) develop appropriate meshes, for both the substrate and the soft impresser; b) study the effects of friction on the radial stress and the contact pressure; and c) consider the influence of the material properties of the soft impresser. After the preliminary analyses, the situation of firstly loading a soft impresser cone at one place on the substrate, and then lifting and moving the deformed cone to a new position on the substrate was modelled (section 9.3). Subsequently, the cyclic loading of a soft impresser, which is relevant to the study of the fatigue properties of a material, was addressed. Finally, the case of a soft impresser sliding over the surface of a substrate was considered for a single traverse.

The procedure to determine an appropriate mesh for the substrate and soft impresser has been presented in detail in section 9.2.1. In the soft impresser model, the mesh formulation for the substrate is based on the same considerations as those in the hard impresser model, which has been discussed in section 10.2. For the soft impresser, the region around the conical apex becomes highly deformed and the soft impresser will be in contact with the substrate after deformation. Thus, the mesh around the apex of the cone should be fine enough to capture the plastic deformation and the mesh shape and size in the contact region should be appropriate to guarantee that no penetration occurs between the two bodies.

Preliminary analyses of the effects of friction on the radial stress (section 9.2.2) reveal that for an elastically deforming substrate, for frictionless contact, the assumption of a constant pressure distribution is a good approximation. As the friction coefficient between the substrate and impresser increases in the range 0 to 0.15, the contact pressures, and stress distributions, increasingly differ from the constant pressure assumption. The soft impresser flattening and re-locating analysis reveals that if there is plastic deformation in the substrate, the actual stress values cannot be estimated based on the constant pressure analytical assumption. This is not surprising since the constant pressure analysis was developed from elasticity theory, without considering friction effects. Thus, it is necessary to include a model for the soft impresser, instead of using the constant pressure assumption, to implement the soft impresser modelling for real situations with friction between the soft impresser and the substrate, or plastic deformation in the substrate.

The soft impresser flattening and re-locating analysis was implemented in section 9.3. Only for frictionless conditions is it possible to flatten an impresser at one position on an elastic substrate and then move it to a second position and apply a load, which as a general rule should be no less than 66% of the initial load, with a reasonable knowledge of the resultant contact pressure and stress distributions. If there is friction between the impresser and substrate, or plastic deformation in the substrate, then it is not possible to use the constant pressure analytical results to estimate the actual stress values. The stress fields are different between the first loading and the second loading (section 9.3.4). This implies that the response should be different using an unused conical impresser or a previously flattened impresser against the same substrate, which agrees with the experimental observation by Maerky (1997).

Cyclic soft impresser modelling in CeTZP was implemented in section 9.4. The variation of the maximum principal and shear stresses outside the contact region with applied load was obtained for four load cases. It was found that the stresses at maximum and minimum load settled to constant values after between 3 and 7 cycles. Finally, a relationship between the alternating stress amplitude, $\Delta\sigma_0$, and number of cycles to failure, N_f, was obtained for the CeTZP data presented in Guillou et al (1996). The maximum principal stress was used to derive the relationship between the equivalent zero mean stress amplitude and the fatigue life in this study. However, the maximum shear stress may be more appropriate to be used since it was observed that the shear stress values can be calculated with more confidence than the maximum principal stresses.

CHAPTER 11

CONCLUSIONS and FURTHER WORK

11.1 Conclusions

In this section the conclusions have been based upon the aims and objectives of the research as outlined in section 1.2. The finite element method has been applied to model the classical indentation process involving penetration of a pointed rigid indenter into metals and ceramics, and the soft impresser test technique. The following specific conclusions can be drawn from this work:

1.1* ABAQUS was found to be the most appropriate FE software package to model the hardness indentation problem after a comparative study utilising four other general FE software packages, i.e. ANSYS, MSC.MARC, ADINA and LSDYNA (section 5.3.2).

2.1 The 4-node bilinear axisymmetric quadrilateral element with incompatible mode (CAX4I in ABAQUS), or enhanced strain option (PLANE 182 in ANSYS), has been determined to be the most robust element for indentation/impresser modelling. It gives a maximum radial stress value close to the analytical result; moreover, it is not as sensitive with regard to the mesh size as compared with the other elements (section 4.1.3).

2.2 A surface-to-surface contact pair was established between the indenter/impresser and the substrate. For the tangential behaviour, the penalty friction formulation was used; for the normal behaviour, the augmented Lagrange formulation was used (section 5.1). This kind of contact pair was preferred to that in the early version of ANSYS (section 4.2.2) as it improves convergence and precision and it is more straightforward to implement since the contact constants do not need to be adjusted by the user.

2.3 The model size (section 5.5) has limited influence on the calculated hardness values, especially when the model size is more than 20 times the indentation depth. However, as shown in tables 5.6 and 5.8 the model size has a marked influence on the calculated elastic modulus (the method for calculating the elastic modulus is described in detail in section 5.13). The relative difference in

* Note: The first number in this list refers to the objective number in section 1.2, i.e. 1.1 indicates the first conclusion made with regard to objective number 1.

the calculated elastic modulus is less than 5% when the ratio of the model size to the indentation depth is greater than 50. These results show that a model size of more than one hundred times the indentation depth is required to give accurate elastic modulus values, and would suggest that experimentally tested specimens should also have a thickness of more than one hundred times the indentation depth.

2.4 For the substrate, the mesh around the contact edge should be fine enough to capture the stress gradient. In the present instance, the mesh in the substrate was considered to be appropriate when the finite element results are consistent with the analytical results for a constant pressure applied to an elastic substrate (sections 5.3.1, 9.2.1 and 4.1.3). This consideration is applicable to both the hard indenter modelling and the soft impresser modelling.

For the soft impresser, the region around the conical apex becomes highly deformed. Thus, the mesh around the apex of the cone should be fine enough to capture the plastic deformation (section 9.2.1). Because the soft impresser will be in contact with the substrate after deformation, the mesh size and the mesh shape in the contact region should be appropriate to guarantee that no significant penetration occurs between the two bodies.

2.5 A comparison between a 2D model and a 3D model was undertaken. It was found that H_{IT} $[H_{IT} = F/(\pi R_c^2)]$ from the 2D model is equivalent to the Vickers hardness $[HV = \frac{2F\sin 68^\circ}{d^2}]$ from the 3D model. In addition, HM, $[HM = F/(26.03h^2)]$ from the 2D model is equivalent to HM, $[HM = F/(26.424h^2)]$ from the 3D model. Thus, it was decided that using a 2D axisymmetric FEM model instead of a 3D model is more appropriate, since a 2D model can use a considerably more detailed mesh and save substantial computing time with respect to a 3D model.

2.6 The explicit-to-implicit analysis method can be used to give equivalent loading/unloading force-displacement data, hardness and elastic modulus results to the implicit only analysis method. The advantage of the explicit-to-implicit analysis procedure over the implicit only analysis method is computational time saving and relative ease of convergence.

2.7 The indentation hardness is a better measure of hardness than the Martens hardness since the Martens hardness by definition does not take into account any sinking-in or piling-up of material around the indenter. In the literature, the indentation hardness H_{IT} is the most commonly used measure of hardness (section 2.6.1).

2.8 The calculated values for *HM* increase markedly with an increase in the indenter tip radius, although the effect becomes less significant as the indentation depth increases, whereas H_{IT} is hardly affected (section 5.6). Xue et al (2002) concluded that the effect of indenter tip radius on the indentation hardness disappears once the contact radius exceeds one half of the indenter radius. In this work, the minimum ratio of the contact radius to the indenter radius is equal to 0.93 for MgO when the indenter radius is 3 μm and the indentation depth is 1 μm. Thus the conclusion of the present study with regard to the effect of the indenter tip radius on H_{IT} is in agreement with Xue et al (2002).

When the indenter tip radius equals zero, there is no indentation size effect for either the Martens hardness *HM* or the Indentation Hardness H_{IT}. For an indenter tip radius equal to 1, 2 or 3 μm, H_{IT} still exhibits no indentation size effect; however, *HM* has a marked indentation size effect. There was no indentation size effect for H_{IT} found in the present analyses (section 5.6), which is different from the results of Xue et al (2002), in which the theory of mechanism-based strain gradient (MSG) plasticity was used. They have proposed that the reason for this discrepancy is that classical continuum plasticity theory, which was used in this work, cannot explain the observed indentation size effect (Xue et al, 2002).

2.9 An investigation of the effect of the included angle for a conical indenter showed that although there was a significant difference in the actual indentation hardness values between FEA and Johnson's model (Johnson, 1970), the variation in form is generally the same (section 5.4.1). However, the results based on Cheng and Li's analysis appear to be very different (Cheng and Li, 2000). These results would indicate that it is not possible to use a simplified equation to predict quantitatively the variation of hardness with indenter angle. It was found that a conical semi-apical angle of 70.3° gave the best consistency between the 2D H_{IT} values, calculated 3D Vickers hardness and experimental

Vickers hardness values. This is consistent with the results generally reported in the literature (Lichinchi et al, 1998; Carlsson and Larsson, 2001). It is also of interest to note that the FEA results gave a value of $H/Y = 3.9$, which is very close to the 'rule-of-thumb' estimate for steels of $H/Y = 4$.

2.10 For a hard material, the assumption generally made in the literature of frictionless contact between the indenter and the substrate appears to be acceptable. However, for a ductile material, it does not appear to be appropriate (section 5.7). The results from this work show that for a ductile material, the relative difference in the indentation hardness between a frictionless model and a frictional one may be as much as 10% to 15%.

2.11 The calculated value of the elastic modulus is very sensitive to the calculation method. The original method to calculate the elastic modulus proposed by Pharr et al (1992) tends to overestimate the true elastic modulus (Equation (5.13)), especially for piling-up materials. A modified equation (Equation (5.17)) was proposed and when an appropriate FE model is used, the maximum relative difference between the input value and the calculated one can be less than 1% (Tables 5.25-5.26) using the modified equation (Equation (5.17)).

2.12 The indenter rigidity has a marked effect on the calculated indentation hardness (section 5.8.1). The extent of the effect of the indenter rigidity depends on the hardness of the studied material and the hardness ratio of the indentation hardness of the indenter to the one of the studied material. For both En08 and MgO, when the hardness ratio is equal to 1, the calculated indentation hardness values were substantially lower than the true values. For En08, when the hardness ratio is greater than 1.5, the indenter rigidity has no effect on the calculated indentation hardness. However, for MgO, for the case with hardness ratio = 2, though the indenter experiences virtually no plastic deformation, the calculated indentation hardness is still about 3.3% lower than that for the rigid indentation case. This occurs as a result of the elastic deformation of the indenter, since it is equal to the value from the elastic indenter case with the same elastic modulus. Only in the elastic indenter case with the same material properties as a diamond, can the equivalent indentation hardness value be obtained as that for the rigid indentation case for MgO.

2.13 The indenter rigidity has virtually no effect on the calculated elastic modulus (section 5.8.1). The method (Equations (5.18) – (5.20)) proposed by Hay,

Bolshakov and Pharr (1999) to calculate the constant γ_h (Equation (5.1)) is not applicable to the case with a deformable indenter.

2.14 The calculated values for *HM* are higher when unloaded than loaded. In contrast, the calculated values for H_{IT} are essentially the same for both the loaded and unloaded cases (section 5.9).

2.15 The ratio of hardness to yield stress increases with increasing tangent modulus for both *HM* and H_{IT} for a work hardening material (section 5.9). For an elastic perfectly plastic material, both *HM/Y* and H_{IT}/Y increase with increasing *E/Y*. However, the variation of *HM/Y* is different from that for H_{IT}/Y (section 5.9).

2.16 Based on the results of FE analyses incorporating the effects of friction, the relationships between the dimensionless groupings H_{IT}/E^*, W_p/W_{tot} (W_e/W_{tot}) and h_f/h_m were determined. The values for the curve-fitted constants in Equations (5.27) – (5.29) are somewhat different from the values in the equivalent Equations (5.21) – (5.23) (Cheng and Cheng, 2002) determined using frictionless contact, which may imply that friction does have an influence on the relationships between H_{IT}/E^*, W_p/W_{tot} (W_e/W_{tot}) and h_f/h_m and thus it cannot be neglected in practical situations.

3.1 The present FE results indicate that the contribution of the elastic anisotropy in MgO to the observed hardness anisotropy is negligible, which implies that the anisotropy of the slip deformation is mainly responsible for the observed anisotropy. Thus, a specific plastic material model is applicable to a specific slip system only. An equation (Equation (6.1)) was proposed based on the hardness anisotropy to correlate the flow stresses along different slip directions. The calculated hardness values for MgO (001) <100> and MgO (001) <110> agree reasonably well with the experimental results based on the proposed material model. The results also demonstrate that it is not always possible to use uniaxial stress-strain data to model the complex multiaxial deformation which occurs beneath an indenter.

4.1 It was found that for coated systems, the calculated values of Indentation Hardness and elastic modulus can be markedly different due to the different calculation methods (Chapter 7). The hardness and elastic modulus calculated

based on the contact radius R_c obtained from FEA would give more precise results than those based on the contact depth h_c obtained from equation (7.5).

4.2 For the multilayer coatings of TiB_2 and Al, the extent of plastic deformation in the substrate increased with increasing percentage of TiB_2 (Chapter 7).

4.3 For the 75% TiB_2 and 50% TiB_2 25-layer coatings, the hardness values fell as the indentation depth was increased (Chapter 7). For the 25% TiB_2 coating, the hardness decreased initially and then increased gradually as the indentation depth increased. The values of Indentation Hardness $H_{IT}(h_c)$ obtained from FEA agreed reasonably well with those from the experiments.

4.4 For all of the three compositions of multilayer coating systems investigated in Chapter 7, the hardness decreased first and then approached a constant value as the number of layers increased from 1 to 25, for a constant overall total coating thickness of 5 μm. The number of layers for which the hardness approached a constant value depended on two factors, i.e. the indentation depth and the percentage of TiB_2.

4.5 By analysing the hardness variation with the number of layers, the desired hardness can be controlled by adjusting the percentage of TiB_2 with fewer layers (Chapter 7). This would save time and cost to produce a particular multilayer coating system. The elastic modulus variation with number of layers has the same trend as the hardness variations. Thus, the elastic modulus can also be controlled by adjusting the percentage of TiB_2 and number of layers.

5.1 A procedure for modelling time dependent rigid indentation into ceramic substrates has been described in detail in Chapter 8. An appropriate mesh and associated geometric and contact conditions were developed to give sufficiently precise hardness and stress values with overall run times of 3 - 7 hours. The analyses were also more difficult to undertake due to the lack of appropriate independent material property data, e.g. the yield stresses had to be inferred from the experimental hardness values.

5.2 Two forms of modified glide controlled dislocation creep models were proposed respectively based on an analytical analysis and the experimental results in sections 8.1.2.1 and 8.2.1.1. Both of these creep models can give similar results to the power law breakdown creep model, especially at lower temperatures

(sections 8.1.3 and 8.2.2). The basic material parameters, i.e. the activation energy for YCPZ and MgO were predicted based on the analytical indentation creep analyses. The results from the FEA generally agreed well with the experimental results, except for a small percentage of the data points, i.e. ~5%.

5.3 The evolution of the creep strains with time from FEA for YCPZ (section 8.1.4.2) and MgO (section 8.2.3.2) show that the creep deformation originates from the contact edge, followed by extension into the substrate towards the central region. However, the central region just beneath the indenter exhibited little creep deformation. This is different from the analytical assumption since the analytical model assumes that there is a uniform hemispherical creep zone from the outset (Li et al, 1991). It can also be seen that the creep deformation at a higher temperature is more marked than that at a lower temperature, which would be expected.

6.1 A procedure has been described in Chapter 9 to use ABAQUS to model the soft impresser test technique, with particular reference to the deformation of a softer metallic cone of semi-apical angle 60°, against a flat ceramic substrate.

6.2 With frictionless contact between the impresser and an elastic substrate, it has been found that the stress distributions are reasonably close to the values predicted by Love's analysis (Love, 1929) for an applied constant pressure over a circular area on the surface of the substrate. When the contact is not frictionless, or there is plastic deformation in the substrate, then the maximum stress values become very different from those predicted using Love's analysis.

6.3 Similar results have been obtained for the situation of flattening a cone at one position on a substrate and relocating and reloading the flattened cone at a different point on the substrate's surface. When the substrate is elastic and the contact is frictionless, for a second applied load which is at least 66% of the initial load to flatten, then the stresses can be estimated using the analytical equations for a constant pressure. When the substrate deforms plastically, and/or there is friction between the substrate and impresser, then the resultant stresses are different for the first and subsequent loadings. The values are also very different to the analytical estimates for the stresses assuming a constant pressure.

6.4 Given the differences between the FEA stress results and those obtained using the constant pressure analytical approximation, it is clearly preferable generally

to undertake FEA analysis of soft impresser test to derive quantitative materials information. The response should be different for an unused conical impresser compared with that for a previously flattened impresser against the same substrate, since the stress fields are different between the first loading and the second loading (section 9.3.4), which agrees with the experimental observation by Maerky (1997).

7.1 Cyclic soft impresser modelling in CeTZP was implemented in section 9.4. The variation of the maximum principal and shear stresses outside the contact region with applied load was obtained for four load cases. It was found that the stresses at maximum and minimum load settled to constant values after between 3 and 7 cycles. Finally, a relationship between $\Delta\sigma_0$ and N_f was obtained for the CeTZP data presented in Guillou et al (1996).

7.2 It has also been demonstrated that FEA can be used to model the situation of a soft impresser sliding over the surface of a flat substrate (section 9.5). The limited results obtained show that in this case too, friction can significantly affect the stress distribution in the substrate.

When there is no friction between the soft impresser and the substrate, the maximum stress along the sliding direction in the substrate on both sides of the soft impresser are tensile. Also, the maximum stress along the sliding direction in the substrate on the trailing edge of the soft impresser is slightly greater than that on the leading edge.

For the frictional case, the maximum stress along the sliding direction in the substrate on the trailing side of the soft impresser is tensile, whereas the stress along the sliding direction in the substrate on the leading edge of the soft impresser is compressive during the sliding process. The stresses along the sliding direction in the substrate on both sides of the soft impresser become constant when the sliding distance is greater than one sixth of the contact length. The results also show that the tensile stress in the substrate on the trailing edge increases approximately linearly with increasing friction coefficient.

7.3 It has also been demonstrated that FEA can be used to model the situation of a soft impresser sliding over the surface of a flat substrate. The limited results obtained show that in this case too, friction can significantly affect the stress distribution in the substrate.

7.4 The soft impresser technique can be used to measure the elastic modulus of a material. The constant γ_h is independent of the material properties. However, γ_h is dependent on the impresser geometry and the precision of the model.

11.2 Further work

The work presented in this thesis provides a basis for future research on the numerical modelling of the rigid indentation and soft impresser tests. Future research might include the points listed below.

1) Verify the technique (Futakawa et al, 2001) for determining the constitutive equation of elastic-plastic materials by the indentation technique using multiple indenters with different apex angles. If possible, extend it or propose a new method to determine the material properties for brittle materials.
2) Construct a composite constitutive material model such as the composite constitutive material model for cast iron in ABAQUS for ceramic materials.
3) Extend the assumed specific plastic material model for MgO (Griffiths et al, 2001) to brittle materials at different temperatures for creep modelling.
4) Combine the cyclic loading FE analysis (ABAQUS) with fatigue analysis (FE-SAFE).
5) Implement time dependent soft impresser modelling, as well as soft impresser creep testing in brittle materials.
6) Use the theory of mechanism-based strain gradient (MSG) plasticity to study the indentation size effect.
7) Find or establish a feasible method to implement improved anisotropic models for single crystal MgO.

REFERENCES

Atkins A. G., Silverio A. and Tabor D. (1966). Indentation hardness and the creep of solids. *Journal of the Institute of Metals*, **94**, 369-378.

Akyus F. A. and Merwin J. E. (1968). Solutions of the nonlinear problems of elastoplasticity by finite element methods. *AIAA Journal,* **6**, 1825-1831.

Almond E. A. and Roebuck B. (1983). Extending the use of indentation tests. *Proceedings of the International Conference on the Science of Hard Materials,* Plenum press, New York, USA, 597-614.

Anon. (2004a). http://www.memsnet.org/material/titaniumboridetib2bulk/. The MEMS and Nanotechnology Exchange. Accessed on 14 12 2004.

Anon. (2004b). http://www.matweb.com/search/SpecificMaterial.asp. Accessed on 14 12 2004.

Armstrong R. W. and Elban W. L. (1989). Cracking at hardness micro-indentations in RDX explosive and MgO single crystals. *Materials Science and Engineering A*, **11**, 35-43.

Atkinson M. and Shi H. (1989). Friction effect in low load hardness testing of iron. *Materials Science and Technology*, **5**, 613-614.

Becker A. A., Hyde T. H. and Xia L. (1994). Numerical analysis of creep in components. *Journal of Strain Analysis*, **29**, 185-192.

Bolzon G., Maier G. and Panico M. (2004). Material model calibration by indentation, imprint mapping and inverse analysis. *International Journal of Solids and Structures*, **41**, 2957-2975.

BS EN ISO 14577. (2002). *Metallic materials instrumented indentation test method for hardness and materials parameters: Part 1 - Test method: Part 2 - Verification and calibration of testing machines: Part 3 - calibration of reference blocks*, British Standards Institute, London.

Brookes C. A. (1983). Hardness measurements in the evaluation of hard materials. *Proceedings of the International Conference on the Science of Hard Materials,* Plenum press, New York, USA, 181-199.

Brookes C. A. (1986). Mechanical properties of cubic boron nitride - a perspective view. *Proceedings of the Second International Conference on the Science of Hard Materials*, Adam Hilger Ltd, Bristol, England, 207-220.

Brookes C.A., Brookes E.J., Howes V.R., Roberts S.G. and Waddington C.P. (1990). A comparison of the plastic deformation and creep of type I, type II and synthetic diamonds at 1100°C under conditions of point loading. *Journal of Hard Materials*, **1**, 3-24.

Bucaille J. L., Stauss S., Felder E., and Michler J. (2003). Determination of plastic properties of metals by instrumented indentation using different sharp indenters. *Acta Materialia*, **51**, 1663-1678.

Buckingham E. (1914). On Physically Similar Systems: Illustrations of the Use of Dimensional Equations. *Physical Review*, **4,** 345-376.

Carlsson S. and Larsson P. –L. (2001). On the determination of residual stress and strain fields by sharp indentation testing. Part I: theoretical and numerical analysis. *Acta Materialia*, **49**, 2179-2191.

Cao Y. P. and Lu J. (2005a). Size-dependent sharp indentation-I. A closed-form expression of the indentation loading curve. *Journal of Mechanics and Physics of solids*, **53**, 33-48.

Cao Y. P. and Lu J. (2005b). Size-dependent sharp indentation-II: a reverse algorithm to identify plastic properties of metallic materials. *Journal of Mechanics and Physics of solids*, **53**, 49-62.

Carter G. M., Henshall J. L. and Hooper R. M. (1988a). Creep of Zirconia Ceramics Below 0.2 T_m. *2nd Int. Conf. on Materials and Engineering Desig., Inst. Of Metals*, London, G1-G3.

Carter G. M., Henshall J. L. and Hooper R. M. (1988b). Indentation Creep in Single Crystal Cubic Zirconia at Room Temperature. *Commun. Amer. Ceram. Soc.*, **71**, C270.

Čekada M. and Panjan P. (2001). Evaluation of microhardness and elastic properties of multilayer hard coatings by microindentation. Vacuum, **61**, 235-240.

Chen W.F. and Han D.J. (1998). *Plasticity for structural engineers,* Springer-Verlag New York Inc.

Cheng Y.-T. and Cheng C. M. (1997). Further analysis of indentation loading curves: Effect of tip rounding on mechanical property measurements. *Journal of Materials Research*, **13**, 1059-1064.

Cheng Y.-T. and Cheng C. M. (1998a). Analysis of indentation loading curves obtained using conical indenters. *Philosophical Magazine Letters*, **77,** 39-47.

Cheng Y.-T. and Cheng C. M. (1998b). Scaling approach to conical indentation in elastic-plastic solids with work hardening. *Journal of Applied Physics*, **84**, 1284-1291.

Cheng Y.-T. and Cheng C. M. (1999). Scaling relationships in conical indentation of elastic-perfectly plastic solids. *International Journal of Solids and Structures*, **36,** 1231-1243.

Cheng Y.-T. and Cheng C. M. (2000). What is indentation hardness? *Surface and Coatings Technology*, **133-134,** 417-424.

Cheng Y.-T. and Cheng C. M. (2001). Scaling relationships in indentation of power-law creep solids using self-similar indenters. *Philophical Magazine Letters,* **81**, 9-16.

Cheng Y.-T. and Cheng C. M. (2002). Scaling relationships for indentation measurements. *Philosophical Magazine A,* **82**, 1821-1829.

Cheng Y.-T. and Cheng C. M. (2004). Scaling, dimensional analysis and indentation measurements. *Materials Science and Engineering R,* **44**, 91-149.

Cheng Y.-T. and Li Z. (2000). Hardness obtained from conical indentations with various cone angles. *Journal of Materials Research*, **15**, 2830-2835.

Clough R. W. (1960). The finite element method in plane stress analysis. *Proc 2d ASCE Conf. Electronic Computation,* Pittsburgh, Sept., 345-378.

Cook R. D., Malkus D. S. and Plesha M. E. (1989). *Concepts and applications of finite element analysis*, John Wiley & Sons, Inc., 14.

Dao M., Chollacoop N., Van Vliet K.J., Venkatesh T.A. and Suresh S. (2001). *Acta Materialia,* **49,** 3899-3918.

Dieter G. (1976). *Mechanical Metallury*, Second ed., McGraw-Hill, New York.

Fagan M.J., Park S.J. and Wang L. (2000). Finite Element Analysis of the Contact Stresses in Diamond Coatings subjected to a Uniform Normal Load. *Diamond and Related Materials*, **9,** 26-36.

Frost H. J. and Ashby M. F. (1982). *Deformation-Mechanism Maps*, Pergamon Press, Oxford.

Futakawa M., Wakui T., Tanabe Y. and Ioka I. (2001). Identification of the constitutive equation by the indentation technique using plural indenters with different apex angles. *Journal of Materials Research*, **16**, 2283-2292.

Giannakopoulos A. E., Larsson P.–L. and Vestergaard R. (1994). Analysis of Vickers indentation. *International Journal of Solids and Structures,* **31**, 2678-2708.

Giannakopoulos A. E. and Suresh S. (1998). A three dimensional analysis of fretting fatigue. *Acta Materialia,* **46**, 177-192.

Giannakopoulos A. E. and Suresh S. (1999). Determination of elastioplastic properties by instrumented sharp indentation. *Scripta Materialia,* **40**, 1191-1198.

Griffiths C., Henshall J. L., Ren X. J. and Hooper R. M. (2001). FE modelling of micro-indentation testing. *Proceedings 9th Annual Conference of the Association for Computational Mechanics in Engineering*, April, Birmingham, ed H C Chan, 17-20.

Guillou M.-O. (1992). *Indentation deformation and fracture of hard ceramic materials*, Ph.D. Thesis, University of Exeter.

Guillou M.–O., Henshall J. L. and Hooper R. M. (1996). The measurement of surface contact fatigue and its application to engineering ceramics. *Material Science and Engineering*, **A209**, 116-127.

Hancock P., Vales da Silva M. F., and Nicholls J. R. (2002). Measurement of mechanical properties of multilayer coatings by nanoindentation. *Materials Science and Technology*, **18**, 827-831.

Hay J. C., Bolshakov A. and Pharr G. M. (1999). A critical examination of the fundamental relations used in the analysis of nanoindentation data. *Journal of Materials Research*, **14**, 2296-2305.

He J. L. and Veprek S. (2003). Finite element modeling of indentation into superhard coatings. *Surface and Coatings Technology*, **163-164**, 374-379.

Henshall J. L., Carter G. M. and Hooper R. M. (1989). Indentation creep in Zirconia ceramics between 290 K and 1073 K. *Mechanics of creep brittle materials*, 117-128.

Henshall J. L., Guillou M.–O. and Hooper R. M. (1996). The Assessment of Surface Fatigue Effects in Toughened Zirconia Using a New Point Contact Method. *Fatigue Fract. Engng Mater. Struct.*, **19**, 903-910.

Henshall J. L., Jiang W. G., Wrobel L. C., Lacerda L. A. and Hooper R. M. (1999). Calculations of stress distributions in diamond coatings under contact conditions. *50th Diamond Conference*, St. Catherine's College, OXFORD, July 4-7.

Hooper R. M. and Brookes C. A. (1984). Incubation periods and indentation creep in lead. *Journal of Materials Science*, **19**, 4057-4060.

Hulse C. O. and Pask J. A. (1960). Mechanical Properties of Magnesia Single Crystals in Compression. *J. Amer. Ceram., Soc.*, **43**, 373-378.

Jayaraman S., Hahn G. T., Oliver W. C., Rubin C. A. and Bastias P. C. (1998). Determination of monotonic stress-strain curve of hard materials from ultra-low-load indentation tests. *International Journal of Solids and Structures*, **35**, 365-381.

Johnson K.L. (1970). The correlation of indentation experiments. *Journal of the Mechanics and Physics of Solids*, **18**, 115-126.

Johnson K.L. (1985). *Contact Mechanics*, Cambridge University Press.

Kelly & Groves. (1970). Crystallography and crystal defects. Longman Group Limited, London, ISBN: 582 46001 8.

Khan M. Y., Brown L. M. and Chaudhri M. M. (1992). The effect of crystal orientation on the indentation cracking and hardness of MgO single crystals. *J. Phys. D: Appl. Phys.*, **25**, A257-A265.

Knott J. F. and Withey Paul. (1993). *Worked examples in fracture mechanics*, The Institute of Materials, London.

Krichen A., Kharrat M. and Chateauminois A. (1996). Experimental and numerical investigation of the sliding behaviour in a fretting contact between poly (methylmethacrylate) and a glass counterface. *Tribology International*, **29**, 615-624.

Kucherskii A. M. and Kaporovskii B. M. (1995). Test method problems in determining hardness of rigid rubbers. *Polymer Testing*, **14**, 253-262.

Lacerda L. A., Wrobel L. C., Jiang W. G. and Henshall J. L. (1999). Boundary element simulation of the soft impresser technique. *2nd UK Conference on Boundary Integral Methods,* Brunel, Sep. 13-14.

Larsson P.–L., Giannakopoulos A. E., Söderlund E., Rowcliffe D. J. and Vestergaard R. (1996). Analysis of Berkovich indentation. *International Journal of Solids and Structures,* **33**, 221-248.

Larsson P.–L. and Giannakopoulos A. E. (1998). Tensile stresses and their implication to cracking at pyramid indentation of pressure-sensitive hard metals and ceramics. *Materials Sciences and Engineering,* **A254**, 268-281.

Lausen T. A. and Simo J. C. (1992). A study of the mechanics of microindentation using finite elements. *Journal of Materials Research*, **7**, 618-626.

Lawn B. R. (1998). Indentation of ceramics with spheres: A century after Hertz. *J. Amer. Ceram. Soc.*, **81**, 1977-1994.

Lease K. (2002). http://ww2.mne.ksu.edu/classes/ME563/HWSet4data.pdf. Kansas State University. Accessed on 14 12 2004.

Li H. and Bradt R. C. (1992). The microhardness indentation size-load effect (ISE) in hard ceramic materials. *Journal of Hard Materials*, **3**, 403-419.

Li W. B., Henshall J. L., Hooper R. M. and Easterling K. E. (1991). The Mechanisms of indentation creep. *Acta Materialia*, **39**, 3099-3110.

Lichinchi M., Lenardi C., Haupt C. and Vitali R. (1998). Simulation of Berkovich nanoindentation experiments on thin films using finite element method. *Thin Solid Films,* **333**, 278-286.

Lo R. Y. and Bogy D. B. (1999). Compensating for elastic deformation of the indenter in hardness tests of very hard materials. *Journal of Materials Research*, **14**, 2276-2282.

Love A.E.H. (1929). The stress produced in a semi-infinite solid by pressure on part of the boundary. *Philosophical Transactions of the Royal Society*, **A228**, 377-420.

Mackerle J. (2001). Finite element and boundary element simulations of indentation problems. *Finite Elements in Analysis and Design*, **37**, 811-819.

Maerky C. (1997). *Analysis of the soft impresser technique with application to the fatigue of engineering ceramics,* Ph.D. Thesis, The University of Exeter, United Kingdom.

Maerky C., Henshall J. L., Hooper R. M. and Guillou M.-O. (1997). Cyclic Contact Fatigue of CaF_2: Stress Analysis and Experimental Results. *Journal of the European Ceramic Society*, **17**, 61-70.

Malkow Th., Arce-García I., Kolitsch A., Schneider D., Bull S. J. and Page T. F. (2001). Mechanical properties and characterisation of very thin CN_x films. *Diamond and related materials*, **10**, 2199-2211.

Mata M. and Alcalá J. (2004). The role of friction on sharp indentation. Journal of the Mechanics and Physics of Solids, **52**, 145-165.

Matsuda K. and Kaneta M. (1996). Analysis of the Vickers hardness of electroplated coatings. *Philosophical Magazine A*, **74**, 1171-1184.

Matsuda K. (2002). Prediction of stress-strain curves of elastic-plastic materials based on the Vickers indentation. *Philosophical Magazine A*, **82**, 1941-1951.

McColl I. R., Ding J. and Leen S. B. (2004). Finite element simulation and experimental validation of fretting wear. *Wear*, **256**, 1114-1127.

Mott B.W. (1956). *Micro-indentation hardness testing,* Butterworths Scientific Publications, London.

Muchtar A., Lim L. C. and Lee K. H. (2003). Finite element analysis of Vickers indentation cracking processes in brittle solids using elements exhibiting cohesive post-failure behaviour. *Journal of Materials Sciences,* **38**, 235-243.

Murakami Y. and Matsuda K. (1994). Analysis of Vickers hardness by the finite element method. *Journal of Applied Mechanics*, **61**, 822-828.

Murakami Y. and Itokazu M. (1997). Elastic-plastic analysis of a triangular pyramidal indentation. *International Journal of Solids and Structures,* **34**, 4005-4018.

Nix W. D. and Gao H. (1998). Indentation size effects in crystalline materials: a law for strain gradient plasticity. *Journal of the Mechanics and Physics of Solids*, **46**, 411-425.

Panich N. and Sun Y. (2004). Effect of penetration depth on indentation response of soft coatings on hard substrates: a finite element analysis. *Surface and Coatings Technology*, **182**, 342-350.

Peggs G. N. and Leigh I. C. (1983). Recommended procedure for micro-indentation Vickers hardness test. Report MOM 62, UK National Physical Laboratory.

Pharr G. M., Oliver W. C. and Brotzen F. R. (1992). On the generality of the relationship among contact stiffness, contact area, and elastic modulus during indentation. *Journal of Materials Research*, **7**, 613-617.

Ren, X. J. (2001). Private communication, University of Exeter.

Ren X. J., Hooper R. M., Griffiths, C. and Henshall J. L. (2001). The effect of indenter heating on indentation creep testing of MgO. *Journal of Materials Science Letters*, **20**, 1819-1821.

Ren X. J., Hooper R. M., Griffiths C. and Henshall J. L. (2002). Indentation-size effects in single-crystal MgO. *Philosophical Magazine A*, **82**, 2113-2120.

Robinson J. (1985). *Early FEM Pioneers*, Robinson & Associates, Dorset, England.

Strange D. J. and Varshneya A. K., (2001). Finite element simulation of microindentation on aluminium. *Journal of Materials Science*, **36**, 1943-1949.

Sun H. & Hu J. (1999). Forming Process Numerical Simulation of Auto-Door Cover Panel. Natural Science Funded Research Project of Hebei Province, China.

Sung Joon Park. (2000). *An investigation of the mechanical performance of diamond coated materials by finite element analysis*, PhD Thesis, Hull University.

Suresh S. (1992). *Fatigue of Materials*, Cambridge University Press.

Suresh S., Giannakopoulos A. E., and Alcala J. (1997). Spherical indentation of compositionally graded materials: theory and experiments. *Acta Materialia*, **45**, 1307-1321.

Suresh S. and Giannakopoulos A. E., (1998). Report Inst-2/98, Massachusetts Institute of Technology.

Tabor D. (1951). *The Hardness of Metals*, Clarendon Press, Oxford.

Tabor D. (1985). *Microindentation Techniques in Materials Science and Engineering* (edited by P.J. Blau and B. R. Lawn), ASTM Special Publ. 889, 129-159.

Tsou C., Hsu C. and Fang W. (2005). Interfaces friction effect of sliding contact on nanoindentation test. *Sensors and Actuators A.*, **117**, 309-316.

Tsui T. Y., Joost V. and Nix W. D. (1999a). Indentation plastic displacement field: Part I. The case of soft films on hard substrates. *Journal of Materials Research*, **14**, 2196-2203.

Tsui T. Y., Joost V. and Nix W. D. (1999b). Indentation plastic displacement field: Part II. The case of hard films on soft substrates. *Journal of Materials Research*, **14**, 2204-2209.

Turner M. J., Clough R. W., Martin H. C., and Topp L. J. (1956). Stiffness and deflection analysis of complex structures. *J. Aero. Sci.*, **23**, 805-823.

Walker W. W. (1973). *The Science of Hardness Testing and its Research Applications* (edited by J. H. Westbrook and H. Conrad), Am. Soc. Metals, Metals Park, Ohio, 258-273.

Washizu K. (1982). *Variational methods in elasticity and plasticity*, -3rd ed., Pergamon press.

Xiao J. and Li S. (1994). *Plastic deformation simulation theory*, Huazhong Science and Industry University Publication. China.

Xue Z., Huang Y., Hwang K. C. and Li M. (2002). The influence of indenter tip radius on the micro-indentation hardness. *Journal of Engineering Materials and Technology,* Transactions of the ASME, **124**, 371-379.

Yoo Y.-H., Lee W. and Shin H. (2004). Spherical nano-indentation of a hard thin film/soft substrate layered system: I. Critical indentation depth. *Modelling and Simulation in Materials Science and Engineering*, **12**, 59-67.

Yu N., Polycarpou A. and Conry T. (2004). Tip-radius effect in finite element modelling of sub-50 nm shallow nanoindentation. *Thin Solid Films*, **450**, 295-303.

Yue Z. F., Probst-Hein M. and Eggeler G. (2000). Determination of creep parameters from indentation creep experiments: a parametric finite element study for single phase materials. *Materials at high temperatures*, **17**, 449-456.

Zhang W. and Subhash G. (2001). Finite element analysis of interacting Vickers indentations on brittle materials. *Acta Materialia*, **49**, 2961-2974.

BIBLIOGRAPHY

ABAQUS Version 5.8. (1998). Hibbitt, Karlsson & Sorensen, Inc., 1080 Main Street, Pawtucket, Rhode Island 02860-4847, USA.

ANSYS manuals. (2001). ANSYS Inc.

He J. and Lin X. (1994). *Numerical solution of engineering structural nonlinear problems.* National Defence Industry Publication of China.

Wriggers P. (2002). Computational contact mechanics. John Wiley & Sons Ltd, England.

Smith I. M. (1995). Programming in Fortran 90. John Wiley & Sons Ltd, England.

Smith I. M. and Griffiths D. V. (2004). Programming the Finite Element Method 4th Edition. John Wiley & Sons Ltd, England.

APPENDIX A

Calculation of Elastic Constants for MgO

The elastic constants for MgO (Table 6.1) were taken from Kelly & Groves (1970) and subsequently used to calculate:

the anisotropy ratio $A = 2c_{44}/(c_{11} - c_{12})$,

the Poisson's ratio $\nu = c_{12}/(c_{11} + c_{12})$,

the Young's modulus (Zhang 1987),

$$1/E_{hkl} = S_{11} - 2\{(S_{11} - S_{12}) - \frac{1}{2}S_{44}\} * (\alpha^{*2}\beta^{*2} + \alpha^{*2}\gamma^{*2} + \beta^{*2}\gamma^{*2}) \qquad (A.1)$$

and the shear modulus (Zhang 1987),

$$1/\mu_{hkl} = S_{44} + 4\{(S_{11} - S_{12}) - \frac{1}{2}S_{44}\} * (\alpha^{*2}\beta^{*2} + \alpha^{*2}\gamma^{*2} + \beta^{*2}\gamma^{*2}) \qquad (A.2)$$

in different directions.

where α^*, β^*, and γ^* are the cosines of the three angles, which are between the considered direction and the <100> axis of the cubic crystal.

APPENDIX B_1

Fortran resource file of the analytical creep model for MgO

```
c       Fortran resource file: HardnesspowerlawAT1-3.for
c       Analytical power law breakdown creep model for MgO (001) <110>
        DIMENSION Hardness(10001),Hrate(10001),Temp1(10),H0(10),
     1          C1(10),AN(10),gama(10),sigma(10001),ecr(10001)
                                open(1,FILE='creepout.txt')
                                open(2,FILE='creepout2.txt')
                H0(1)=7467.2
                H0(2)=5963.19
                H0(3)=4996.05
                H0(4)=3795.66
                H0(5)=2844.36
                C1(1)=2.926057
                C1(2)=2.98757
                C1(3)=3.026198
                C1(4)=3.066539
                C1(5)=3.097869
                AN(1)=3.02
                AN(2)=3.6713
                AN(3)=3.384
                AN(4)=3.103
                AN(5)=2.112
                gama(1)=0.75
                gama(2)=0.9
                gama(3)=0.9
                gama(4)=0.9
                gama(5)=0.73
                DTIME=1
                R=8.3145
                A1= 20.
                A2=sqrt(3.)
                alpha=2000.
                AK1=2.
                AM=1.
                TREF=273
                TEMP1(1)=293.0
                TEMP1(2)=373
                TEMP1(3)=473
```

```
                TEMP1(4)=673
                TEMP1(5)=873
                AMU=1.2481e11
                AMU=AMU/1.0e6
                Qcr=261.e3
                DO I=1,1
                write(1,5) TEMP1(I)
        5       format('TEMPERATURE=',F10.1,'K')
                Qcr=gama(I)*261.e3
                QRT=(Qcr/(R*TREF))*(TREF/TEMP1(I))**AM
                QRTEXP=exp(-QRT)
                T12=alpha*H0(I)/(C1(I)*A2*AMU)
                T1=exp(T12)
                T2=exp(-T12)
                T12AN=((T1-T2)*0.5)**AN(I)
                Hrate(1)=-((1+AK1)**3/6.)*A1*H0(I)*T12AN*
   1            QRTEXP
c       ecr---- creep strain rate
                ecr(1)=A1*T12AN*QRTEXP/A2
                Hardness(1)=H0(I)
                sigma(1)=Hardness(1)/C1(I)
                Do J=1,10000
                Hardness(J+1) = Hardness(J)+DTIME*Hrate(J)
                sigma(J+1)=Hardness(J+1)/C1(I)
                T12=alpha*Hardness(J+1)/(C1(I)*A2*AMU)
                T1=exp(T12)
                T2=exp(-T12)
                T12AN=((T1-T2)*0.5)**AN(I)
                Hrate(J+1)=-(1+AK1)**3/6.*A1*Hardness(J+1)*T12AN*
   1            exp(-QRT)
                ecr(J+1)=A1*T12AN*QRTEXP/A2
c       write(2,40) sigma(J), ecr(J)
c40     Format(E13.6, ' ', E13.6)
        write(2,40) Hardness(J)
40      Format(E13.6)
        enddo
        write(2,45) Hardness(10001)
45      Format(E13.6)
C
        print*, QRT,QRTEXP
```

```
c       write(1,10) QRT, QRTEXP
c10     Format(F13.6,F13.6)
        print*
        print*, hrate(1),hrate(100),hrate(1000),hrate(10000)
c       write(1,20) hrate(1),hrate(100),hrate(1000),hrate(10000)
c20     Format('hrate(1)=',F13.6,' hrate(100)=',F13.6,' hrate(1000)=',
c   1   F13.6,' hrate(10000)=',F13.6)
c       write(1,*)
        print*
        print*, hardness(1),hardness(100),hardness(1000),hardness(10000)
        write(1,30) hardness(1), hardness(100), hardness(1000),
    1    hardness(10000)
30      Format('hardness(1)=',F10.1,' hardness(100)=',F10.1,
    2   ' hardness(1000)=',F10.1,' hardness(10000)=',F10.1)
c       write(1,*)
        Print*
        ENDDO
      END
```

APPENDIX B_2

Abaqus creep user subroutine for MgO at T=293K

```
c       ABAQUS creep user subroutine Power293.for (The power law breakdown creep
c       model for MgO (001) <110> at T = 293 K)


      SUBROUTINE CREEP(DECRA,DESWA,STATEV,SERD,EC0,ESW0,P,QTILD,
     1 TEMP,DTEMP,PREDEF,DPRED,TIME,DTIME,CMNAME,LEXIMP,LEND,
     2 COORDS,NSTATV,NOEL,NPT,LAYER,KSPT,KSTEP,KINC)
C
      INCLUDE 'aba_param.inc'
C
      CHARACTER*80 CMNAME
C
      DIMENSION DECRA(5),DESWA(5),STATEV(*),PREDEF(*),DPRED(*),
     1 TIME(2),COORDS(*)
C
C DEFINE CONSTANTS
C
C       K=Boltzman constant(J/K)
C       AK=1.38065812e-23
C       R=gas constant(J/mol/K)
        R=8.3145
        A1= 20.
        A2=sqrt(3.)
        AN1=3.074693
        alpha=2000.
C
C       AMU=shear modulus
        AMU=1.2481e11
        AMU=AMU/1.0e6
        Qcr=0.75*261.e3
        TEMP1=293.0
        QRT=Qcr/(R*TEMP1)
        QRTEXP=exp(-QRT)
C
        T12=alpha*QTILD/(A2*AMU)
        T1=exp(T12)
        T2=exp(-T12)
        T12AN=((T1-T2)*0.5)**AN1
```

```
C
      DECRA(1) = (A1*DTIME/A2)*((T1-T2)*0.5)**AN1*exp(-QRT)
      IF(LEXIMP.EQ.1) THEN
      DECRA(5) = A1*AN1*alpha*DTIME*0.5*(T1+T2)*exp(-QRT)*
     1                  (0.5*(T1-T2))**(AN1-1)/(3.*AMU)
      END IF
      RETURN
      END
```

APPENDIX C

Useful notes for the use of ABAQUS

I would like to append some useful notes based on the author's experience on ABAQUS during this period. I am sure that it would be helpful for the lucky followers.

C.1 How to create the ABAQUS scripting interface scripts.

The ABAQUS Scripting Interface is an application programming interface (API) to the models and data used by ABAQUS (ABAQUS Scripting User's Manual). The ABAQUS Scripting Interface is an extension of the Python object-oriented programming language; ABAQUS Scripting Interface scripts are Python scripts (ABAQUS Scripting User's Manual). The ABAQUS Scripting Interface can be used to do the following (ABAQUS Scripting User's Manual):

- Create and modify the components of an ABAQUS model, such as parts, materials, loads, and steps.
- Create, modify, and submit ABAQUS analysis jobs.
- Read from and write to an ABAQUS output database.
- View the results of an analysis.

The ABAQUS Scripting Interface is especially useful when a parametric study is to be implemented. It can be learned easily within several days with the aid of the ABAQUS Scripting User's Manual. The problem is how to create your own scripts. It is not feasible to write every line of the scripts manually for a new user. Even for an advanced user, it would be very hard work as well. The short cut to do this is applying the file, i.e. abaqus.rpy, which is created by ABAQUS automatically when ABAQUS/CAE or ABAQUS/VIEWER is used in the GUI (Graphic User Interface) mode. The procedure for this method is,

1) Start ABAQUC/CAE, several lines of the scripts have already been written to the abaqus.rpy file, e.g.

```
from abaqus import *
from abaqusConstants import *
session.Viewport(name='Viewport: 1', origin=(1.318359375, 1.3216145336628),
   width=194.0625, height=131.104161739349)
session.viewports['Viewport: 1'].makeCurrent()
from driverUtils import executeOnCaeStartup
```

```
executeOnCaeStartup()
Mdb()
#: A new model database has been created.
#: The model "Model-1" has been created.
session.viewports['Viewport: 1'].setValues(displayedObject=None)
```

You can copy them into a new text file, which was created and named by yourself, e.g. mu05.py.

2) Create the script gradually.

Remember that every operation that was carried out will be recorded into abaqus.rpy. You can open abaqus.rpy at any time and copy the correct scripts (Ignore the incorrect, useless or repeated ones) into your own scripting file, i.e. mu05.py. Create the scripting file gradually and make sure you are on the right way (run mu05.py from the sub-menu 'Run Script' within the 'File' menu at any time to verify it!). Thus after the whole model has been finished, you get your own scripting file as well.

C.2 The explicit-to-implicit method

The explicit-to-implicit method was normally used in the spring-back analysis of a sheet metal after forming. This method has been used successfully by the author about 6 years before using ANSYS/LSDYNA3D (Sun and Hu, 1999). It was introduced into the indentation modelling problem of multilayer coatings (Chapter 7) in order to eliminate the convergence difficulties. ABAQUS/EXPLICIT was used initially to carry out the load step computation for the indentation modelling. Subsequently, ABAQUS/STANDARD was used to implement the unloading step computation in order to obtain the correct unloading force-displacement response. This is because when using the explicit analysis method only to run the whole load and unload modelling, the unloading force-displacement response was found to be inaccurate. Some tips for the application of the explicit-to-implicit method in ABAQUS are:

1) noPartsInputFile=ON and explicitPrecision=DOUBLE

The 'JOB' part in the Python scripting file, e.g. 25-075exp-1016.py, was copied as follows:

```
import job
session.viewports['Viewport: 1'].assemblyDisplay.setValues(loads=OFF, bcs=OFF,
   fields=OFF, connectors=OFF)
mdb.Job(name='25-075exp-1016', model='Model-1', type=ANALYSIS,
   explicitPrecision=DOUBLE, nodalOutputPrecision=SINGLE, description='',
```

```
   parallelizationMethodStandard=TREE, parallelizationMethodExplicit=LOOP,
   multiprocessingMode=THREADS, numDomains=1, userSubroutine='', numCpus=1,
   preMemory=256.0, standardMemory=512.0, standardMemoryPolicy=MODERATE,
   scratch='', echoPrint=ON, modelPrint=OFF, contactPrint=OFF,
   historyPrint=ON)
mdb.models['Model-1'].setValues(noPartsInputFile=ON)
mdb.jobs['25-075exp-1016'].writeInput()
```

where, the command '**mdb.models['Model-1'].setValues(noPartsInputFile=ON)**' must be put in before writing the input file. If this command were to be omitted, the structure of the input file generated by ABAQUS will be different and thus cannot be processed in the subsequent implicit analysis. Initially, the author did not know of the existence of this command either and had to modify the input file manually, which was tough work.

By the way, the double precision (**explicitPrecision=DOUBLE**) must be used instead of the single precision for the explicit analysis. Otherwise, the accumulated error will affect the precision of the results.

2) Structure of the input file for the implicit analysis

The input file, e.g. 25-075exp-1016u.inp was attached as follows.

```
*Heading
** Job name: 25-075exp-1016u Model name: Model-1
*Preprint, echo=NO, model=NO, history=NO, contact=NO
*IMPORT,STEP=4,STATE=YES,UPDATE=YES
*IMPORT ELSET
bcy0, bcx0,
Part-1-1_substrate,
Part-1-1_film-al-1, Part-1-1_film-tib2-1,
..... (23 lines Omitted)
Part-1-1_film-al-25, Part-1-1_film-tib2-25,
__PickedSurf9_S4,
__PickedSurf9_S2
*IMPORT NSET
bcy0, bcx0
*Node
   15361,     20000.,    211145.,         0.
*Nset, nset=indenter-1-RefPt_
 15361,
*Surface, type=SEGMENTS, name=indenter-1_Surf-indenter
START,      20000., 211145.036747897
```

```
LINE,          0.,     203984.
*Rigid Body, ref node=indenter-1-RefPt_, analytical surface=indenter-1_Surf-indenter
*System
*Nset, nset=indenterrp
 15361,
*Surface, type=ELEMENT, name=Surf-substrate
__PickedSurf9_S2, S2
__PickedSurf9_S4, S4
** INTERACTION PROPERTIES
*Surface Interaction, name=IntProp-1
*Friction
 0.15,
*Surface Behavior, pressure-overclosure=HARD
** INTERACTIONS
** Interaction: Int-1
*Contact Pair, interaction=IntProp-1
Surf-substrate, indenter-1_Surf-indenter
** STEP: Step-1
*Step, name=Step-1, nlgeom, inc=100000, unsymm=YES
*Static
1., 1e-4, 1e-10, 1.
** BOUNDARY CONDITIONS
** Name: bcx0 Type: Displacement/Rotation
*Boundary
bcx0, 1, 1
** Name: bcy0 Type: Displacement/Rotation
*Boundary
bcy0, 1, 1
bcy0, 2, 2
** Name: BC-indenter Type: Displacement/Rotation
*Boundary
indenterrp, 1, 1
indenterrp, 2, 2, 0.
indenterrp, 6, 6
** OUTPUT REQUESTS
*Restart, write, frequency=999999
** FIELD OUTPUT: F-Output-1
*Output, field, frequency=100
*Node Output
RF, U, V
```

*Element Output
LE, PE, PEEQ, S
*Contact Output
CSTRESS,
** HISTORY OUTPUT: H-Output-1
*Output, history
*Node Output, nset=indenterrp
CF2, RF2, U2
*El Print, freq=999999
*Node Print, freq=999999
*End Step
** STEP: Step-2
*Step, name=Step-2, nlgeom, inc=100000, unsymm=YES
*Static
1., 1e-3, 1e-10, 1.
** BOUNDARY CONDITIONS
** Name: bcx0 Type: Displacement/Rotation
*Boundary
bcx0, 1, 1
** Name: bcy0 Type: Displacement/Rotation
*Boundary
bcy0, 1, 1
bcy0, 2, 2
** Name: vy1 Type: Displacement/Rotation
*Boundary
indenterrp, 1, 1
indenterrp, 2, 2, 2.
indenterrp, 6, 6
** OUTPUT REQUESTS
*Restart, write, frequency=999999
** FIELD OUTPUT: F-Output-1
*Output, field, frequency=100
*Node Output
RF, U, V
*Element Output
LE, PE, PEEQ, S
*Contact Output
CSTRESS,
** HISTORY OUTPUT: H-Output-1
*Output, history

```
*Node Output, nset=indenterrp
CF2, RF2, U2
*El Print, freq=999999
*Node Print, freq=999999
*End Step
```

There are four steps in the previous explicit analysis, the implicit analysis was restarted from the 4th step in the explicit analysis. Thus, STEP=4 in the *IMPORT command. Actually, the implicit analysis was required to be restarted from the previous three steps as well. So, three more input files, where STEP=1, 2 and 3 respectively, need to be generated in this case.

Subsequently, input the element sets and node sets from previous explicit input file using *IMPORT ELSET and *IMPORT NSET respectively.

Then generate the reference node and the surface segments for the rigid indenter and define the contact pair. There are two steps in the implicit analysis. The first step is to update from the explicit analysis to the implicit one. The second step is to implement the implicit unloading step. For the first step in the implicit analysis, the step load method can also been used. However, it was found that it did not work as well as the ramp load method.

C.3 Indentation creep modelling

The indentation creep modelling can be run sequentially, *cf* the following FORTRAN resource file batchrun.for.

```
C       Batchrun.for
        PROGRAM MAIN
        USE DFLIB
        LOGICAL(4)    RESULT
C       Run the indentation modelling first
        result=SYSTEMQQ('abaqus job=indentation293 interactive')
C       Run the creep modelling with the user subroutine power293.for
        result=SYSTEMQQ('abaqus job=power293 input=creep2
      1                 user=power293 oldjob=indentation293 interactive')
        END
```

where, the creep user subroutine power293.for can be found in Appendix B_2. The input file, i.e. creep2.inp, for the creep modelling was attached as follows. Certainly, these jobs can also be run in ABAQUS command mode, i.e. input 'abaqus

job=indentation293' and 'abaqus job=power293 input=creep2 user=power293 oldjob=indentation293' sequentially in ABAQUS command line.

```
** creep2.inp
*Heading
** Job name: creep Model name: Model-1
*restart,read,step=1
** STEP: Step-1
*Step, name=creep-1, nlgeom, inc=100000, unsymm=YES
*Visco, cetol=0.001
0.001, 100., 1e-08, 100.
** BOUNDARY CONDITIONS
** Name: BCx0 Type: Displacement/Rotation
*Boundary
bcx0, 1, 1
** Name: BCy0 Type: Displacement/Rotation
*Boundary
bcy0, 1, 1
bcy0, 2, 2
** Name: uy Type: Displacement/Rotation
*Boundary
indenterrp, 1, 1
indenterrp, 6, 6
*Amplitude, name=creep_AMP1
0., 1., 10000., 1.
** LOADS
** Name: Load-1   Type: Concentrated force
*Cload, amplitude=creep_AMP1
indenterrp, 2, -2.94e+06
** OUTPUT REQUESTS
*Restart, write, frequency=10000
** FIELD OUTPUT: F-Output-1
*Output, field, frequency=10
*Node Output
U, RF, CF
*Element Output
CE, CEEQ, CEMAG, CEP, ER, ELEN, ENER, LE, PE, PEEQ, PEMAG, S
*Contact Output
CSTRESS, CDISP
** HISTORY OUTPUT: H-Output-2
*Output, history
```

*Node Output, nset=indenterrp

U2,

** HISTORY OUTPUT: H-Output-1

*Output, history, variable=PRESELECT, frequency=99999

*End Step

** STEP: Step-2

*Step, name=creep-2, nlgeom, inc=100000, unsymm=YES

*Visco, cetol=0.001

0.001, 900., 1e-08, 100.

*Restart, write, frequency=10000

*End Step

** STEP: Step-3

*Step, name=creep-3, nlgeom, inc=100000, unsymm=YES

*Visco, cetol=0.001

0.001, 9000., 1e-08, 100.

*Restart, write, frequency=10000

*End Step

BIBLIOGRAPHY FOR APPENDICES

Sun H. and Hu J. (1999). Forming Process Numerical Simulation of Auto-Door Cover Panel. Natural Science Fund Research Project of Hebei Province, PRC.

Kelly and Groves. (1970). Crystallography and crystal defects. Longman Group Limited, London, SBN: 582 46001 8.

Zhang Q. (1987). Mechanical Property of Ceramic Materials. Science Publishing Company.